OFFICIAL JOURNAL OF THE SCIENTIFIC SOCIETY OF
ANATOMISTS, HISTOLOGISTS, EMBRYOLOGISTS AND
TOPOGRAPHIC ANATOMISTS OF UKRAINE

DOI: 10.31393
ISSN 1818-1295
eISSN 2616-6194

ВІСНИК МОРФОЛОГІЇ
REPORTS OF MORPHOLOGY

Vol. 30, №4, 2024

Scientific peer-reviewed journal in the fields of normal and pathological anatomy, histology, cytology and embryology, topographical anatomy and operative surgery, biomedical anthropology, ecology, molecular biology, biology of development

Published since 1993
Periodicity: 4 times a year

Vinnytsya • 2024

ВІСНИК МОРФОЛОГІЇ - REPORTS OF MORPHOLOGY

Founded by the "Scientific Society of Anatomists, Histologists, Embryologists, and Topographic Anatomists of Ukraine" and National Pyrogov Memorial Medical University, Vinnytsya in 1993

Certificate of state registration КВ №9310 from 02.11.2004

Professional scientific publication of Ukraine in the field of medical sciences in specialties 221, 222, 228, 229
According to the list of professional scientific publications of Ukraine, approved by the order of the Ministry of Education and Science of Ukraine No. 1188 of 24.09.2020
Professional scientific publication of Ukraine in the field of biological sciences in specialty 091
According to the list of professional scientific publications of Ukraine, approved by the order of the Ministry of Education and Science of Ukraine No. 1471 of 26.11.2020

Approved by the Academic Council of National Pyrogov Memorial Medical University, Vinnytsya, protocol №4 from 27.12.2024.

Indexation: Scopus, CrossRef, Index Copernicus, Google Schoolar Metrics, National Library of Ukraine Vernadsky

Address editors and publisher:
Pyrogov Str. 56,
Vinnytsya, Ukraine - 21018
Tel.: +38 (0432) 553959
E-mail: nila@vnmu.edu.ua

Computer page-proofs - Klopotovska L.O.
Translator - Gunas V.I.
Technical support - Levenchuk S.S.
Scientific editing - editorship

The site of the magazine - https://morphology-journal.com

CONTENT

Arshynnikov R. S., Kulygina V. N., Drohomyretska M. S., Poberezhna H. M., Polyanyk N. Y., Sukhomlynova T. Y.
Morphological study of hard dental tissue condition with various types of dental deposits **5**

Danylevych V. P., Guminskyi Yu. Y., Andriichuk V. M., Zalevskyi L. L., Prykhodko S. O., Danylevych A. V.
Modeling of intervertebral discs' parameters of the lumbar spine base on somatometric data **12**

Vynnychenko O. I., Moskalenko Yu. V., Yazykov O. V., Seleznov O. O., Sulaieva O. M., Moskalenko R. A.
GLUT1 expression in patients with non-small cell lung cancer and its impact on survival **21**

Ryabov T. V., Shinkaruk-Dykovytska M. M., Pylypiuk O. Yu., Muntian O. V., Drachevska I. Yu., Rokunets I. L., Burdeina L. V.
Modeling the parameters necessary for constructing the correct shape of the dental arch depending on the features of teleradiometric indicators using the Steiner or Tweed methods and computed tomography dimensions of teeth in Ukrainian young men and young women with physiological occlusion **29**

Yanko R. V., Safonov S. L., Levashov M. I.
Morphological features of white adipose tissue in rats with different levels of energy metabolism in visceral obesity **44**

Maievskyi O. Ye., Bobr A. M., Gunas I. V., Tkach G. F., Maslii V. P., Kyrychenko I. M., Ihnatishchev M. R.
Histological organization of the spleen of rats under conditions of acute intoxication with viper venom Vipera berus berus **52**

Oshurko A. P., Oliinyk I. Yu., Maystruk M. V., Sukhliak V. V., Tsurkan M. M., Ruskovoloshyn D. V.
Histo-morphometric evaluation of post-augmentation bone tissue of the human mandible **58**

Gunas M. M., Moskovko G. S., Nazarova M. S., Kyrychenko Yu. V., Prokopenko S. V., Ruban M.M.
Modeling, based on discriminant analysis, the possibility of occurrence and features of the course of multiple sclerosis in Ukrainian women depending on the features of the structure and sizes of the body **67**

Kulbitska V. V., Ohinska N. V., Slabyy O. B., Lisnychuk N. Ye., Trach Rosolovska S. V., Nebesnyi O. R., Nebesna Z. M.
Ultrastructure of adrenal glands endocrinocytes after thermal skin injury under conditions of correction with cryo-lyophilized xenograft skin substrate **74**

AL-Azzawie A. F., Ajeel M. A., AL -Bayti A. A. H.
Impact of gamma-aminobutyric acid receptors modulators on renal and liver functional, molecular and histological characteristics in white male mice **82**

DOI: 10.31393/morphology-journal-2024-30(4)-01 Reports of Morphology, Vol. 30, №4, Pages 5-11

ISSN 1818-1295 eISSN 2616-6194

REPORTS OF MORPHOLOGY

Official Journal of the Scientific Society of Anatomists, Histologists, Embryologists and Topographic Anatomists of Ukraine

journal homepage: https://morphology-journal.com

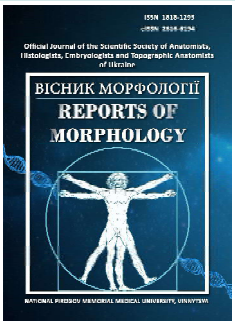

Morphological study of hard dental tissue condition with various types of dental deposits

Arshynnikov R. S.[1], Kulygina V. N.[2], Drohomyretska M. S.[1], Poberezhna H. M.[3], Polyanyk N. Y.[1], Sukhomlynova T. Y.[1]

[1]Shupyk National Healthcare University of Ukraine, Kyiv, Ukraine
[2]SHEI "Uzhhorod National University", Uzhhorod, Ukraine
[3]National Pirogov Memorial Medical University, Vinnytsya, Ukraine

ARTICLE INFO
Received: 28 March 2024
Accepted: 21 August 2024

UDC: 616.314-008.4:572.77

CORRESPONDING AUTHOR
e-mail: poberezhna16@gmail.com
Poberezhna H. M.

CONFLICT OF INTEREST
The authors have no conflicts of interest to declare.

FUNDING
Not applicable.

DATA SHARING
Data are available upon reasonable request to corresponding author.

Today, it has been established that the primary factor in preventing dental caries is controlling the level and type of dental deposits. However, the literature has not yet addressed the specific morphological changes in the hard dental tissues when non-mineralized and mineralized dental plaque is present on the tooth surface. The aim of this study was to examine the microscopic structure of the cuticle and hard dental tissues and to assess the X-ray spectral changes associated with different types of dental deposits. Epimicroscopic and X-ray spectral examinations were performed on 32 teeth with various types of supragingival deposits, extracted for orthodontic and surgical indications. Each tooth was cut in the vestibulo-oral direction using a diamond bur at low speed, then one half was polished, stained with PAS-Alcian blue, and photographed at different magnifications in epiprojection. Samples were carbon-coated in a vacuum chamber, and the inorganic components in the cuticle and mineralized deposits were assessed using the Link AN 10.85s micro X-ray analyzer. Thin sections of the other tooth halves were prepared, stained with PAS-Alcian blue, and examined under the "Olympus" microscope at various magnifications. Statistical analysis was performed using standard parametric methods with "Statistica 6.0" and "Microsoft Excel 2002" software. Significant findings in the hard dental tissues included the presence of non-mineralized (soft plaque, dental biofilm), mineralized (dental calculus), and smoker's plaque. In areas with soft plaque, enamel prisms remained intact, with no changes in the enamel-dentin junction or dentin, though the cuticle was nearly absent. In areas with dental biofilm, enamel thickening, the absence of characteristic enamel prism patterns, fragmentation of the reticular layer, and formation of interglobular dentin were observed. Morphological changes in mineralized deposits included enamel thinning, prism disorganization, localized hypermineralization, destroyed enamel-dentin junctions, and "dead tracts" in the dentin. In cases with smoker's plaque, nicotine pigment accumulated in Retzius line biomineralization zones, along with thickening of the reticular layer and "dead tracts" in the deeper dentin layers. A comparison of the main inorganic components (Ca, P, Mg, Ca/P) in the cuticle and mineralized deposits showed significant differences in phosphate, magnesium, and Ca/P ratios, indicating disrupted metabolic processes at the "enamel-oral fluid" interface, promoting calculus formation. Thus, the morphological and X-ray spectral changes observed in the enamel and surrounding tissues provide an objective assessment of tissue condition with various types of deposits. These findings should be considered in selecting a scaling method.

Keywords: *mineralized and non-mineralized dental deposits, morphological study.*

Introduction

The study of the etiology [25, 26, 27, 33] and pathogenesis [6, 14, 19, 31] of dental caries has a long history. Dentists' ongoing focus on this issue is associated with the widespread prevalence of dental caries globally [5, 17, 21, 29]. Currently, dental biofilm (a type of dental plaque) is considered a monoetiologic factor in the development and progression of dental caries [12, 22, 24, 34] and periodontal diseases (gingivitis, periodontitis) [1,

3, 11, 18]. According to many researchers [2, 7, 9, 23], colonies of oral microorganisms on the tooth surface within dental plaque are a fundamental cause of the destruction of both hard dental tissues and the soft and bone tissues of the periodontium.

To date, numerous morphological studies have investigated the role of various types of mineralized and non-mineralized dental deposits (soft plaque, dental biofilm, calculus, and smoker's plaque) in the etiology and pathogenesis of periodontal diseases and dental caries [12, 13, 34]. However, there is a lack of morphological studies focused on the condition of tooth enamel, its covering structures, particularly the cuticle, as well as the enamel-dentin junction and dentin, in the presence of different types of dental deposits.

According to reports by authors [32], immobilized alkaline phosphatase on the enamel surface retains its enzymatic activity, which contributes to the regulation of metabolic processes in enamel at the "enamel-saliva" interface. Alkaline phosphatase on the enamel surface binds calcium and phosphate ions, forming high concentrations that impact the processes of enamel mineralization and remineralization. Consequently, it is necessary to study the composition of inorganic chemical elements in the surface structures of enamel, as this is an indicator of the stability and resistance of hard tissues to potential damage during the application of different dental plaque removal methods, especially in individuals highly susceptible to dental caries. Additionally, the role of inorganic compounds and ions on the enamel surface in the formation of mineralized plaque has not been clarified.

The aim of this study is to investigate the microscopic structure of the cuticle and hard tissues of the tooth and to characterize X-ray spectral changes in the presence of various types of dental deposits.

Material and methods

The study was conducted under the initiative of the Department of Orthodontics at Shupyk National Healthcare University of Ukraine, titled "An Integrated Approach to the Diagnosis and Treatment of Orthodontic Patients with Comorbidities," in compliance with the ethical principles of the Declaration of Helsinki. The study was approved by the Ethics and Academic Integrity Committee of Shupyk National Healthcare University of Ukraine (Protocol No. 6/27 dated 28.06.2024).

To achieve the study's objectives, 32 teeth from the mandible (4 incisors, 6 canines, and 22 premolars and molars) with various supragingival dental deposits were examined. These teeth were extracted based on orthodontic and surgical indications. After extraction, the teeth were stored in a 10 % neutral formalin solution. The sample groups were distributed as follows: the first group (2 teeth) had soft plaque, the second group (10 teeth) had dental biofilm, the third group (10 teeth) had dental calculus, and the fourth group (10 teeth) had smoker's plaque. Five intact teeth without deposits, extracted for orthodontic reasons, served as controls.

Each tooth was sectioned in a vestibulo-oral direction into two halves using a diamond bur at low speed. One half of each tooth was polished and histochemically stained with PAS-Alcian blue. The crown fragments were then photographed at different microscope magnifications in epi-projection. Next, they were coated with carbon in a vacuum chamber, and the content of inorganic components in the cuticle and mineralized dental deposits was analyzed. The chemical composition of these structures was examined at the Kharkiv Research Institute "Monocrystal" using a Link AN 10.85s micro-X-ray analyzer.

Thin sections (15-20 microns) were prepared from the second half of each sample tooth and stained with PAS-Alcian blue. Different areas of these sections were studied and photographed at various magnifications using an "Olympus" microscope.

Statistical analysis of the inorganic component content in the cuticle and mineralized dental deposits was performed using standard parametric methods with "Statistica 6.0" and "Microsoft Excel 2002" statistical software. Mean values and standard errors were calculated. The significance of differences between the results was determined using Student's t-test [20].

Results

The first stage of the study was devoted to examining the histological structure of the enamel of intact teeth without dental deposits. Some specific features of the enamel structure were observed in the equator and cervical regions of the tooth. In particular, the enamel in the cervical region of the tooth crown is very thin but covered by a thick layer of cuticle (Fig. 1).

Figure 2 shows the structure of the enamel of an intact tooth without dental plaque. We have established that the outer layer of the cuticle contains alcian-positive structures,

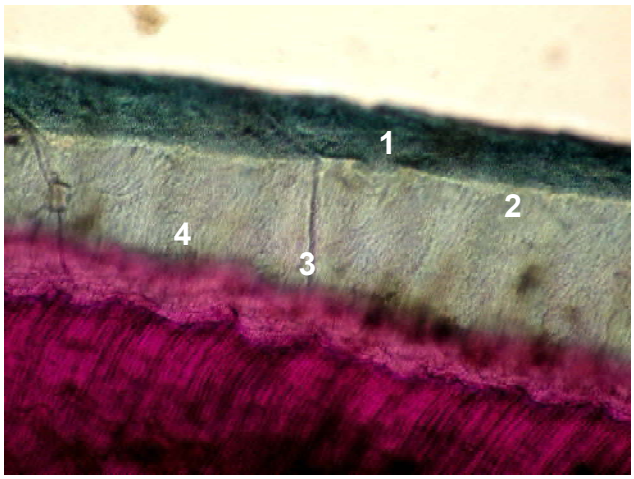

Fig. 1. Structure of the cuticle: 1 - outer layer of the cuticle; 2 - inner layer of the cuticle; 3 - lamella; 4 - enamel prisms. PAS-Alcian blue. x400.

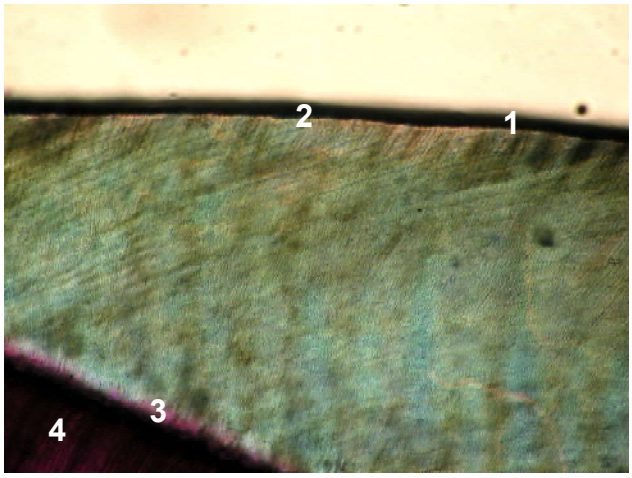

Fig. 2. Structure of enamel: 1 - cuticle; 2 - enamel; 3 - reticular layer; 4 - dentin. PAS-Alcian blue. x400.

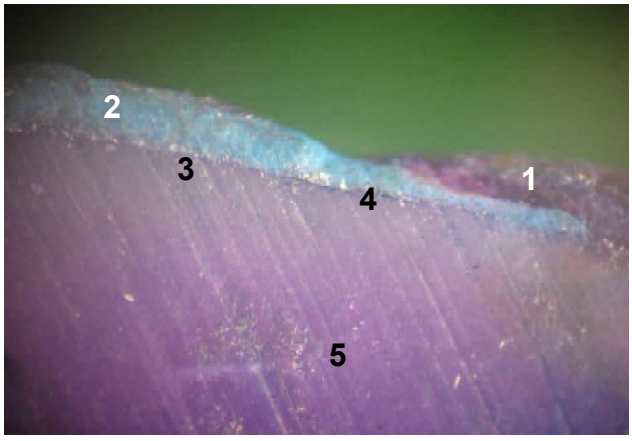

Fig. 3. Soft dental plaque in the cervical area: 1 - dental plaque; 2 - enamel; 3 - enamel-dentin junction; 4 - reticular layer; 5 - dentin. PAS-Alcian blue. x16.

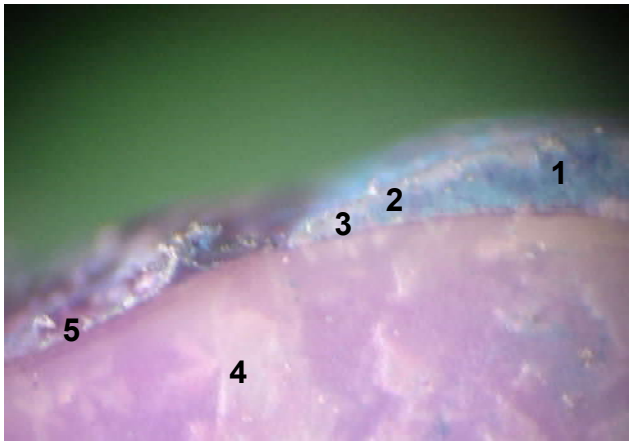

Fig. 4. Dental plaque: 1 - preserved enamel; 2 - destroyed enamel areas; 3 - fragmentation of the reticular layer; 4 - interglobular dentin; 5 - areas of destroyed cementum. PAS-Alcian blue. x16.

which include acidic glycosaminoglycans. Meanwhile, the inner layer consists of PAS-positive glycoproteins. In the cervical region of the tooth, the cuticle appeared as a thin strip, stained black. The inner layer (Nasmyth's membrane) has no distinct boundaries and merges into the enamel prisms. The entire thickness of the enamel (from the cuticle to the enamel-dentin junction) is permeated by well-defined lamellae, to which the Tomes' fibers, located in the dentinal tubules, are attached and stained red. In the equatorial region, the enamel is thickened, consisting of bundles of enamel prisms arranged in an S-shape (Hunter-Schreger bands) and stained blue. At a 30 ° angle to the cuticle, Retzius lines, stained brown, are visible. A faintly expressed network layer is located along the enamel-dentin junction.

In the second stage of the research, the morphological structure of different types of dental deposits and their inorganic chemical content were studied. Thick sections stained with PAS-alcian blue revealed the following types of dental deposits: soft dental plaque, dental plaque, dental calculus, and smoker's plaque.

Soft dental plaque appears in the cervical region of the tooth as a narrow strip stained in lilac (Fig. 3). The enamel structure and the pattern of enamel prisms remain intact, and the cuticle is almost completely absent on its surface. The enamel area is stained blue, dentin is stained pink, and cement is stained lilac. The structure of the enamel-dentin junction and dentin is undisturbed. The dentinal tubules, appearing as red parallel structures, have a clear direction.

In the presence of dental plaque in the cervical region of the tooth (Fig. 4), the enamel is thickened, and in its central part, the pattern of enamel prisms is absent. The prisms are replaced by pale pink homogeneous structures. Bundles of enamel prisms are preserved in the area of the enamel-dentin junction, but its boundary is disrupted in many areas (fragmentation of the reticular layer). Microscopic examination revealed changes in the dentin: the formation of interglobular dentin, which is stained white-pink.

In the area of formed supragingival dental calculus, enamel thinning is observed, which, when stained with PAS-Alcian blue, appears as a thin strip of blue color. In the

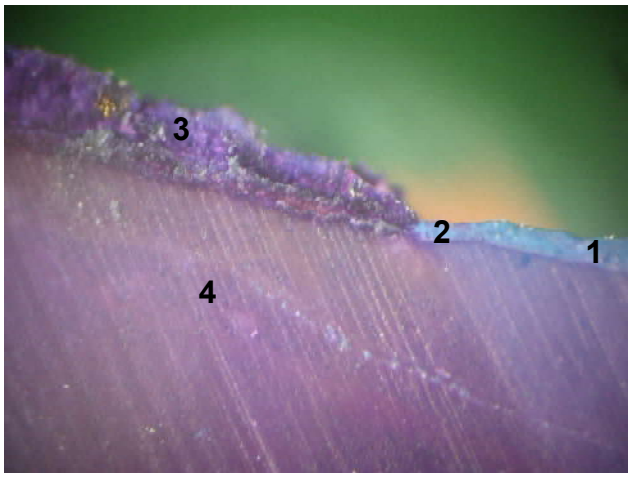

Fig. 5. Supragingival dental calculus: 1 - preserved enamel; 2 - destroyed enamel-dentin junction; 3 - dental calculus; 4 - "dead tracts in dentin". PAS-Alcian blue. x16.

Fig. 6. Smoker's dental deposits: 1 - preserved enamel; 2 - dental calculus with nicotine pigment; 3 - destroyed enamel-dentin junction; 4 - dentin. PAS-Alcian blue. x16.

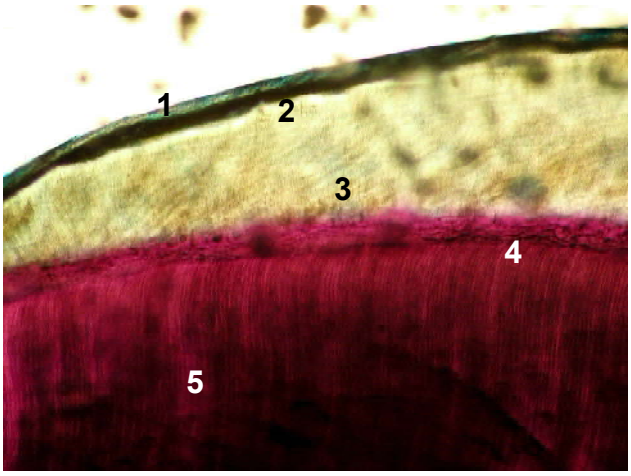

Fig. 7. Smoker's plaque: 1 - outer layer of the cuticle; 2 - inner layer of the cuticle; 3 - Retzius lines; 4 - reticular layer; 5 - dead tracts in dentin. PAS-Alcian blue. x400.

area of dental calculus, the enamel-dentin junction is completely destroyed. Dentin exhibits destruction of dentinal tubules and the formation of "dead paths", which, according to Hasyuk A. P. and co-authors [13], result from the fragmentation of odontoblast processes or their complete destruction (Fig. 5).

The most pronounced destructive changes in the enamel and dentin of the tooth were observed during microscopic examination of teeth with smoker's plaque, likely related to the toxic effects of nicotine pigment. Changes in the coloration of all components of the tooth's hard tissues were noted, presumably due to the penetration of nicotine pigment into the enamel and dentin (Fig. 6). On histochemically stained tooth sections, the preserved enamel is light green, dentin is dark orange, and the smoker's plaque is light yellow or dark brown.

A more detailed study of the nicotine pigment penetration level into the tooth tissues was conducted on thin sections under a microscope at x400 magnification (Fig. 7). When stained with PAS-Alcian blue, the outer layer of the cuticle appears as a light blue strip, while the Nasmyth's membrane (inner layer) appears dark brown. Pronounced changes were observed in the tooth enamel: most of the terminal sections of the enamel prisms are light yellow or brown, with intense nicotine pigment deposits in the Retzius lines. Additionally, the mesh layer at the dentin boundary is significantly thickened. Numerous "dead paths" were detected in the deep layers of the dentin.

The content of the main mineral components in the tooth cuticle and mineralized dental plaque, determined through micro X-ray spectral analysis, is presented in the table (Table 1). A comparison of the obtained results revealed significant differences in the ionic composition of the studied inorganic components. Specifically, the calcium ion (Ca^{2+}) content in the mineralized dental plaque tended to decrease compared to the tooth cuticle, and the difference was not statistically significant ($p>0.05$). In contrast, the magnesium cation level in the dental plaque was elevated and differed significantly from that in the cuticle with a high degree of reliability ($p<0.001$). It is noteworthy that the average phosphate content in the solid dental deposits was significantly higher compared to that in the tooth cuticle ($p<0.001$), while the Ca/P ratio was similarly reduced.

Discussion

The epimicroscopic studies of stained sections from extracted teeth aligned with literature data [11, 15, 16, 30] concerning the primary morphological formations on the tooth surface: soft plaque, dental biofilm, calculus, and smoker's plaque.

Our morphological findings on the structure of hard dental tissues, both in normal conditions and in the presence of non-mineralized and mineralized deposits, confirmed the findings of scientific publications [12, 13]. However, the studies of domestic and international authors [4, 8, 10, 12] have mainly focused on the morphological,

Table 1. Indicators of the content of the main macroelements in the areas of the cuticle of the tooth neck and mineralized dental deposits (tartar).

Field of study	The content of the main macroelements, % of dry weight				
	Ca^{2+}	PO_4^{3-}	Cl	Mg^{++}	Ca/P
Cuticle of the tooth	10.60±0.03	6.042±0.021	0.343±0.113	0.089±0.049	1.754±0.009
Tartar	10.54±0.22	7.381±0.124	0.154±0.024	0.668±0.092	1.352±0.021
p	p>0.05	p<0.001	p>0.05	p<0.001	p<0.001

Note: p - the significance level of the difference in macroelement content between the tooth cuticle and mineralized dental deposits.

biochemical, and microbiological features of dental deposits in the development of dental caries, fluorosis, and periodontal disease [13, 28, 30]. In contrast, our research is the first to establish that all types of supragingival dental deposits induce morphological changes in the tooth's hard tissues and its surface structures: the cuticle, enamel, enamel-dentin junction, and dentin. For instance, in teeth with soft plaque, we observed almost complete absence of the cuticle and no destructive changes in dentin. In extracted teeth with biofilm, the enamel was thickened, showing destruction of its surface prisms and fragmentation of the inner reticular layer. The dentin's response (in the form of excessive interglobular formation) seems to be an adaptive process. In cases with supragingival mineralized deposits (calculus), enamel thinning, prism disorganization, hypermineralization (an adaptive response), and complete destruction of the enamel-dentin junction were observed. The changes in dentin included fragmented and destroyed Tomes' fibers forming "dead tracts", as noted in studies [13] on dental caries progression. More pronounced morphological changes were seen in teeth with smoker's plaque: the presence of nicotine pigment in Retzius lines, slight destruction of enamel prisms, thickening of the aprismatic enamel layer, and "dead tracts" in the deeper dentin layers.

Our findings on the main chemical elements in the cuticle of intact teeth, obtained through micro-X-ray spectral analysis, established a Ca/P ratio of 1.754±0.009, which corresponds to the chemical formula of octacalcium phosphate crystal ($Ca_8(H_3PO_4)_2x5H_2O$) with a negative charge, as reported by [32]. This supports the literature [32], suggesting that this structural formation in teeth represents the initial stage of creating the inorganic matrix of enamel, as in an alkaline environment, octacalcium phosphate in Nasmyth's membrane can convert to hydroxyapatite under the influence of alkaline phosphatase. However, a similar ratio in mineralized plaque (1.352±0.021) corresponds to brushite crystal ($Ca^{2+}HPO_{4-}x2H_2O$) with a positive charge, as noted in [32]. Based on these results, we suggest that in the acidic oral environment, an electrochemical reaction occurs, depositing brushite crystals on the cuticle surface and forming dental calculus.

We believe that the observed decrease in calcium ions within the structure of mineralized dental deposits compared to the tooth cuticle, along with a substantial increase in magnesium ions, may result from their substitution.

Future research should focus on studying morphological changes in enamel and its adjacent tissues following different methods of dental deposit removal to determine the most optimal approach for various types of dental deposits.

Conclusions

1. It has been established that the primary morphological formations on the tooth surface are: soft plaque, dental biofilm, calculus, and smoker's plaque.

2. Morphological analysis revealed the following changes in the hard dental tissues associated with various types of deposits: absence of the cuticle in areas with soft plaque accumulation; enamel thickening, partial fragmentation of the reticular layer, and formation of interglobular dentin in adjacent regions with dental biofilm; enamel thinning, disorganization of enamel prisms, hypermineralization, destruction of the enamel-dentin junction, and "dead tracts" in the dentin with mineralized deposits; accumulation of nicotine pigment in Retzius biomineralization lines, thickening of the reticular layer, and "dead tracts" in dentin with smoker's plaque.

3. The results of morphological and X-ray spectral analyses of extracted teeth with various types of non-mineralized and mineralized plaque indicate the necessity for a differentiated approach to the removal of dental deposits.

References

[1] Abdulkareem, A. A., Al-Taweel, F. B., Al-Sharqi, A. J. B., Gul, S. S., Sha, A., & Chapple, I. L. C. (2023). Current concepts in the pathogenesis of periodontitis: from symbiosis to dysbiosis. *J Oral Microbiol,* 15(1), 2197779. doi: 10.1080/20002297.2023.2197779

[2] Al-Kamel, A., Baraniya, D., Al-Hajj, W. A., Halboub, E., Abdulrab, S., Chen, T., & Al-Hebshib, N. N. (2019). Subgingival microbiome of experimental gingivitis: shifts associated with the use of chlorhexidine and N-acetyl cysteine mouthwashes. *J Oral Microbiol,* 11(1), 1608141. doi: 10.1080/20002297.2019.1608141

[3] Azevedo, C. L., da Silva, L. R. V., Alencar, C. O., Braga, M. M., Biazevic, M. G. H., & Crosato, E. M. (2022). Is there a safe dental plaque index to prevent periodontal diseases related to plaque? A systematic review and meta-analysis. *Research, Society and Development,* 11(7), e27511730100. doi: 10.33448/rsd-v11i7.30100

[4] Bowen, W. H., Burne, R. A., Wu, H., & Koo, H. (2018). Oral biofilms: pathogens, matrix and polymicrobial interactions in microenvironments. *Trends Microbiol,* (26), 229-242. doi: 10.1016/j.tim.2017.09.008

[5] Daniltsiv, L. O., & Rozhko, M. M. (2022). Стоматологічний статус 15-річних школярів Івано-Франківської області [Dental status of 15-year-old schoolchildren in the Ivano-Frankivsk region]. *Клінічна Стоматологія=Clinical Dentistry,* (4), 39-43. doi: 10.11603/2311-9624.2021.4.12660

[6] De Carvalho, F. K., de Queiroz, A. M., Bezerra da Silva, R. A., Sawamura, R., Bachmann, L., Bezerra da Silva, L. A., & Nelson-Filho, P. (2015). Oral aspects in celiac disease children: clinical and dental enamel chemical evaluation. *Oral Surgery, Oral Medicine, Oral Pathology and Oral Radiology,* 119(6), 636-643. doi: 10.1016/j.oooo.2015.02.483

[7] Dienga, O. V., & Osadcha, A. O. (2022). Поширеність й інтенсивність карієсу зубів і захворювань пародонту у дітей 13-15 років, що займаються спортом вищих досягнень [Prevalence and intensity of dental caries and periodontal diseases in children aged 13-15 years engaged in high-level sports]. *Вісник стоматології=Journal of Dentistry,* 121(4), 68-73. doi: 10.35220/2078-8916-2022-46-4.12

[8] Earle, K. A., Billings, G., Sigal, M., Lichtman, J. S., Hansson, G. C., Elias, J. E., … & Sonnenburg, J. L. (2015). Quantitative

imaging of gut microbiota spatial organization. *Cell Host Microb,* 18(4), 478-488. doi: 10.1016/j.chom.2015.09.002

[9] Ebersole, J. L., Dawson, I. D., Emecen-huja, P., Emecen-Huja, P., Nagarajan, R., Howard, K., & Gonzalez, O. A. (2017). The periodontal war: microbes and immunity. *Periodontol,* 75(1), 52-115. doi: 10.1111/prd.12222

[10] Flemming, H.-C., & Wingender, J. (2010). Biofilm matrix. *Nat Rev Microbiol,* (8), 623-633. doi: 10.1038/nrmicro2415

[11] Godovanets, O. I., & Kitsak, T. S. (2022). Аналіз чинників ризику розвитку хронічного катарального гінгівіту в дітей, які страждають на дифузний нетоксичний зоб [Analysis of the risk factors promoting development of chronic catarrhal gingivitis in children suffering from simple diffuse goiter]. *Вісник стоматології=Journal of Dentistry,* 119(2), 78-82. doi: 10.35220/2078-8916-2022-44-2.14

[12] Grokholsky, A. P., Kodola, N. A., & Tsentilo, T. D. (2000). *Назубные отложения: их влияние на зубы, околозубные ткани и организм [Dental deposits: their effect on teeth, peri-dental tissues and the body].* Київ: Здоров'я=Kyiv: Health.

[13] Hasiuk, A. P., Shepitko, V. I., & Zhdan, V. M. (2008). *Морфо- та гістогенез основних стоматологічних захворювань [Morpho- and histogenesis of the main dental diseases].* Полтава=Poltava.

[14] Hodovanets, O. I., & Honcharenko, V. A. (2015). Особливості мінералізації емалі зубів у дітей хворих на дифузний нетоксичний зоб [Features mineralization of tooth enamel in children with diffuse nontoxic goiter]. *Профілактична та дитяча стоматологія=Preventive and Pediatric Dentistry,* 2(13), 14-17.

[15] Honcharuk-Khomin, M. Yu., Melnychuk, N. I., Tsuperyak, S. S., Pohoretska, H. V., & Patskan, L. O. (2019). Оцінка кількісних змін мікробіологічного профілю зубного нальоту з ділянки зубоясенної боріздки у пацієнтів із І стадією пародонтиту [Microbiological profile quantitative changes evaluation among patients with stage I periodontitis]. *Клінічна стоматологія=Clinical dentistry,* (3), 11-17. doi: 10.11603/23119624.2019.3.10571

[16] Hu, S., Mok, J., Gowans, M., Ong, D. E. H., Hartono, J. L., & Lee, J. W. J. (2022). Oral microbiome of Crohn's disease patients with and without oral manifestations. *Journal of Crohn's and Colitis,* 16(10), 1628-1636. doi: 10.1093/ecco-jcc/jjac063

[17] Jajam, M., Bozzolo, P., & Niklander, S. (2017). Oral manifestations of gastrointestinal disorders. *Journal of Clinical and Experimental Dentistry,* 9(10), e1242-e1248. doi: 10.4317/jced.54008

[18] Jarova, S. P., Novikova, K. V., & Jarov, Y. Y. (2019). Стан гігієни порожнини рота та структура патології пародонту у підлітків 15-16 років [The state of oral hygiene and the structure of periodontal pathology in adolescents aged 15-16 years]. *Клінічна Стоматологія=Clinical Dentistry,* (3), 56-61. doi: 10.11603/2311-9624.2019.3.10574

[19] Kaskova, L. F., Drozda, I. I., & Ulasevych, L. P. (2021). Швидкість салівації і вязкість ротової рідини у підлітків 15-18 років з різним ступенем активності карієсу [Speed salivation and viscosity of the oral fluid in teenagers 15-18 years old with varying degrees of activity caries]. *Вісник проблем біології і медицини=Bulletin of Problems Biology and Medicine*, 2(1), 303-306. doi: 10.29254/2077-4214-2021-2-160-303-306

[20] Kravchun, P. G., Babazhan, V. D., & Myasoyedova, V. V. (Eds.). (2020). *Методологія наукових досліджень в медицині: навчальний посібник [Methodology of scientific research in medicine: study guide].* Харків: ХНМУ=Kharkiv: KhNMU.

[21] Krut, A. G. (2022). Стан здоров'я порожнини рота населення за зверненнями до закладів третинної медичної допомоги стоматологічного профілю [The state oral health on appeals to tertiary medical care institutions of the dental profile]. Україна. *Здоров'я нації=Ukraine. The Health of the Nation,* 1(1), 66-72. doi: 10.24144/2077-6594.1.1.2022.254641

[22] Lebedyk, S. V., & Konovalenko, S. O. (2021). Ранній дитячий карієс - сучасна суспільна проблема [Early childhood caries - a modern social problem]. *Медсестринство=Nursing*, (4), 50-54. doi: 10.11603/2411-1597.2020.4.11875

[23] Ling, M. R., Chapple, I. L., & Matthews, J. B. (2015). Peripheral blood neutrophil cytokine hyper-reactivity in chronic periodontitis. *Innate Immun*, 21(7), 714-725. doi: 10.1177/1753425915589387

[24] Loban', G. A., Faustova, M. O., Chereda, V. V., & Ananieva, M. M. (2021). Epidemiological and etiological aspects of dental caries development. *Acta Facultatis Medicae Naissensis,* 38(1), 27-34. doi: 10.5937/afmnai38-27564

[25] Luchynskyi, M. A., & Rozhko, V. I. (2016). Особливості перебігу карієсу зубів у дітей із захворюваннями шлунково-кишкового тракту [The features of tooth decay in children with the diseases of gastrointestinal tract]. *Клінічна стоматологія=Clinical Dentistry,* (4), 66-69. doi: 10.11603/2311-9624.2016.4.7239

[26] Mantegazza, C., Paglia, M., Angiero, F., & Crippa, R. (2016). Oral manifestations of gastrointestinal diseases in children. Part 4: Coeliac disease. *European Journal of Paediatric Dentistry,* 17(4), 332-334. PMID: 28045325

[27] Matkulieva, S., Isakhodjaeva, K., & Khamidov, I. (2022). The incidence and structure of dental pathology in children with chronic viral hepatitis C. *Preventive Medicine and Health*, 1(1), 34-38. doi: 10.47689/2181-3663-vol1-iss1-pp34-38

[28] Nazarenko, I. V., & Gevkalyuk, N. O. (2022). Сучасні концепції лікування початкового карієсу зубів у дітей (огляд літератури) [Modern concepts of treatment of initial dental caries in children (literature review)]. *Клінічна Стоматологія=Clinical Dentistry,* (4), 44-51. doi: 10.11603/2319624.2021.4.12790

[29] Stanislav, N., Tolkachjov, M. D., Alison, J., & Bruce, M. D. (2017). Oral manifestations of nutritional disorders. *Clinics in Dermatology,* 35(5), 441-452. doi: 10.1016/j.clindermatol.2017.06.009

[30] Theodoro, L. H., Garcia, V. G., Ervolino, E., Holcroft, J., McCulloch, C. A. & Ganss, B. (2023). Role of junctional epithelium in maintaining dento-gingival adhesion and periodontal health. *Front Dent Med,* (4), 1144537. doi: 103389\fdmed.2023.1144537

[31] Udod, O. A., Kulish, A. S., & Gabshydze, N. O. (2018). Карієсрезистентність емалі та інтенсивність карієсу зубів у хворих на цукровий діабет [Enamel caries resistance and dental caries intensity in patients with diabetes mellitus]. *Вісник Проблем Біології і Медицини=Bulletin of Problems Biology and Medicine,* (4), 322-325. doi: 10.29254/2077-4214-2018-4-1-146-322-325

[32] Vavilova, T. P. (2019). *Биохимия тканей и жидкостей полости рта [Biochemistry of oral tissues and fluids].* Москва: ГЕОТАР-Медиа=Moscow: GEOTAR-Media.

[33] Watanabe, M., Nakatani, E., Yoshikawa, H., Kanno, T., Nariai, Y., Yoshino, A., & Sekine, J. (2017). Oral soft tissue disorders are associated with gastroesophageal reflux disease: retrospective study. *BMC Gastroenterology,* 17(1), 92. doi: 10.1186/s12876-017-0650-5

[34] Xu, Y., You, Y., Yi, L., Wu, X., Zhao, Y., Yu, J., … & Huang, C. (2022). Dental plaque-inspired versatile nanosystem for caries prevention and tooth restoration. *Bioact Mater,* (20), 418-433. doi: 10.1016/j.bioactmat.2022.06.010

МОРФОЛОГІЧНЕ ДОСЛІДЖЕННЯ СТАНУ ТВЕРДИХ ТКАНИН ЗУБІВ ПРИ РІЗНИХ ВИДАХ ЗУБНИХ НАШАРУВАНЬ

Аршинніков Р. С., Кулигіна В. М., Дрогомирецька М. С., Побережна Г. М., Поляник Н. Я., Сухомлинова Т. Я.

Сьогодні встановлено, що основним фактором профілактики каріозного ураження зубів являється контроль рівня і характеру зубних нашарувань. Проте, дотепер в літературі не висвітлені питання характеру морфологічних змін у твердих тканинах зуба при наявності на його поверхні немінералізованого та мінералізованого зубного нальоту. Метою проведеного дослідження було вивчення мікроскопічної будови кутикули і твердих тканин зуба та характер рентген-спектральних змін при наявності різних видів зубних нашарувань. Проведено епімікроскопічне та рентген-спектральне дослідження 32 зубів з різними видами над'ясенних зубних відкладень, видалених за ортодонтичними і хірургічними показаннями. Кожний зуб за допомогою алмазної фрези на малих обертах розрізали у вестибуло-оральному напрямку на дві половини, одну з яких полірували, забарвлювали ШИК-альціановим синім і фотографували при різних збільшеннях мікроскопа в епіпроекції. У подальшому напилювали вуглецем у вакуумній камері та визначали вміст неорганічних компонентів в кутикулі та мінералізованих зубних відкладеннях (на мікрорентгенівському аналізаторі Link AN 10.85s). З другої половини зуба виготовляли тонкі шліфи та забарвлювали ШИК-альціановим синім і вивчали при різних збільшеннях мікроскопу "Олімпус". Статистичну обробку результатів проводили з використанням загальноприйнятих параметричних методів із застосуванням пакета статистичних програм "Statistica 6.0" і "Microsoft Excel 2002". У твердих тканинах зубів з різними видами нальоту встановлені такі зміни: наявність немінералізованого (м`який зубний наліт, зубна бляшка), мінералізованого (зубний камінь) та нальоту курця. В ділянках накопичення м`якого зубного нальоту малюнок емалевих призм збережений, змін в емалево-дентинному з'єднанні та дентині не виявлено, проте кутикула майже повністю була відсутня. На ділянках емалі із зубною бляшкою виявлено її потовщення, відсутність характерного рисунку емалевих призм, фрагментація сітчастого шару та утворення інтерглобулярного дентину. Характерними морфологічними змінами при наявності мінералізованих зубних відкладень є: стоншення емалі, дезорганізація емалевих призм і підвищена мінералізація її окремих ділянок, зруйноване емалево-дентине з'єднання та "мертві шляхи" в дентині. У випадку наявності нальоту курця встановлено накопичення нікотинового пігменту в ділянках ліній біомінералізації Ретціуса, а також потовщення сітчастого шару емалі та "мертві шляхи" в глибоких шарах дентину. При порівнянні вмісту основних неорганічних компонентів (Ca, P, Mg, Ca/P) в кутикулі зуба та мінералізованих зубних відкладеннях встановлені істотні розбіжності вмісту фосфатів, магнію та співвідношенні Ca/P, котрі свідчили про порушення обмінних процесів на межі "емаль-ротова рідина", що сприяє утворенню зубного каменю. Таким чином, отримані результати морфологічних та рентген-спектральних змін в емалі зуба й прилеглих тканинах дають можливість об'єктивно оцінити стан досліджуваних тканин при наявності різних видів зубних нашарувань. Результати досліджень необхідно враховувати при виборі методу скейлінга.

Ключові слова: *мінералізовані та немінералізовані зубні нашарування, морфологічне дослідження.*

Author's contribution

Arshynnikov R. S. - conceptualization, research, writing of the original draft.
Kulygina V. N. - project administration.
Drohomyretska M. S. - methodology.
Poberezhna H. M. - research, review writing and editing.
Polyanyk N. Y. - software, resources.
Sukhomlynova T. Y. - formal analysis and validation.

DOI: 10.31393/morphology-journal-2024-30(4)-02 Reports of Morphology, Vol. 30, №4, Pages 12-20

ISSN 1818-1295 eISSN 2616-6194

REPORTS OF MORPHOLOGY

Official Journal of the Scientific Society of Anatomists, Histologists, Embryologists and Topographic Anatomists of Ukraine

journal homepage: https://morphology-journal.com

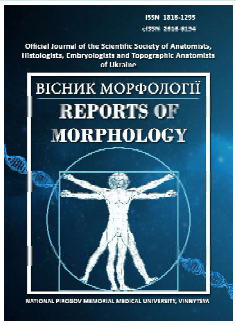

Modeling of intervertebral discs' parameters of the lumbar spine base on somatometric data

Danylevych V. P., Guminskyi Yu. Y., Andriichuk V. M., Zalevskyi L. L., Prykhodko S. O., Danylevych A. V.
National Pirogov Memorial Medical University, Vinnytsya, Ukraine

ARTICLE INFO
Received: 22 February 2024
Accepted: 23 August 2024

UDC: 611.721.1: 611.959:572.087

CORRESPONDING AUTHOR
e-mail: vidanlet@gmail.com
Danylevych V. P.

CONFLICT OF INTEREST
The authors have no conflicts of interest to declare.

FUNDING
Not applicable.

DATA SHARING
Data are available upon reasonable request to corresponding author.

The relevance of the study arises from the high prevalence of spinal column pathology and the rapid advancement of diagnostic technologies, which necessitate the refinement of criteria for identifying changes in the structural components of the spine, particularly one of its most vulnerable elementsm - the intervertebral discs. The reliance on subjective criteria for assessing intervertebral discs during magnetic resonance imaging (MRI) or computed tomography (CT) highlights the need for more objective, quantitative criteria to evaluate intervertebral disc changes. The aim of the study was to develop an optimal, practical model for calculating the total size index of intervertebral discs based on external body parameters, applicable in clinical practice, and to validate its effectiveness. To achieve this goal, lumbar spine MRI was performed on young women aged 16 to 26 years who were native residents of the Vinnytsia region. The main group consisted of 80 participants, including 52 young women aged 16-20 years and 28 women aged 21-26 years; the validation group included 65 females aged 16-26 years. Anthropometric measurements, including height and body weight, were recorded for all participants. Using data from the main group, mathematical modeling was conducted to determine the total size of lumbar intervertebral discs. The modeling process employed stepwise regression analysis based on somatodisc coefficients of individual intervertebral discs and anthropometric parameters. As a result, a model was developed to calculate somatodisc coefficients using body height and weight. Further algebraic transformations of the somatodisc coefficient yielded a formula for calculating individualized total disc size indicators, integrating vertical, sagittal, and transverse dimensions. The predictive accuracy of the obtained models ranged from 85 % to 91 %. When the actual total size measurements of intervertebral discs in the main group were compared to the mathematically modeled values, deviations did not exceed ±10 %. This mathematical model for calculating the total size of lumbar intervertebral discs based on somatometric data enables the determination of individualized normative metrics and the objective identification of early degenerative disc changes. When comparing clinical visual assessments of intervertebral disc changes using Pfirrmann grading with mathematical evaluations in the validation group, agreement was observed in 91 % of cases. Discrepancies were identified in 9 %, necessitating further analysis to prevent underdiagnosis or overdiagnosis of intervertebral disc changes. Thus, mathematical modeling serves as a tool for determining individualized normative metrics. The proposed mathematical models for calculating the total size of intervertebral discs based on body height and weight represent a powerful supplement to existing criteria for intervertebral disc assessment.

Keywords: *intervertebral disc, sum of dimensions, somato-disc coefficient, lumbar spine, modeling, individual norm.*

Introduction

Pathology of the musculoskeletal system worldwide is one of the leading causes of pain, temporary and permanent disability, and early mortality [35], causing significant economic and social problems that need to be addressed as quickly as possible [7]. According to age-standardized statistical data for 2017, low back pain (LBP) occurs in 7.5 % of the world's population. There is also a noted prevalence of LBP in women (8.01%), with the total number

of people experiencing LBP amounting to 577 million [34]. Researchers report that about 90 % of LBP cases are nonspecific, associated with osteochondrosis, chondrosis, and degenerative-dystrophic changes in the intervertebral disc [6]. Among the common causes of back pain are herniations of the intervertebral discs (IVD), which can be easily visualized during magnetic resonance imaging (MRI) [36]. However, it should be noted that lower back pain also occurs in children and adolescents [28] and is not necessarily discogenic. In Ukraine, chronic diseases of the musculoskeletal system are also among the most widespread problems. It has been established that among individuals residing in Ukraine, osteochondrosis occurs in 60-75 % of cases, including in people of working age [19]. Due to its prevalence (about 1 million people seek medical care annually) and temporary loss of ability to work, osteochondrosis is also a social problem. Osteochondrosis is a very insidious disease that, due to its masking of other conditions, causes the appearance of a whole range of symptoms. These facts complicate clinical non-instrumental diagnosis, especially when it comes to the early stages of IVD degeneration.

Most of the developed treatment procedures for disc degeneration do not have the desired effectiveness and, as a result of changes in the biomechanics of the spine, can cause alterations in adjacent segments [21]. Thus, approaches to the treatment of degenerative-dystrophic diseases of the IVD are increasingly leaning towards prevention and addressing the main etiological factors that alter the components of the disc matrix and its biomechanics. The effectiveness of such an approach depends on the ability to accurately and objectively assess the state of the matrix, biomechanics, and trends of their changes during treatment using non-invasive diagnostic methods, in particular through the use of quantitative MRI [23].

To determine the degree of changes in intervertebral discs in medical practice, MRI images are used, evaluated according to the Pfirrmann classification system [25, 27] and the modified system [10]. The assessment of IVDs according to the classical Pfirrmann classification is conducted by a radiologist and is based largely on visual criteria. These include: the degree of homogeneity and brightness of the MRI signal of the IVD nucleus pulposus; the presence and nature of changes in the vertebral endplates and the cartilage covering them; the integrity of the annulus fibrosus; and the height of the IVD.

The most objective parameter among the listed criteria is the height of the IVD. However, this parameter does not have clear normative values, which in most cases in clinical practice turns it into a subjective feature. It should also be noted that among the IVD parameters that change as a result of degeneration, height is an important but not the only parameter requiring evaluation [18]. It is noted that in addition to changes in IVD height, the sagittal and transverse dimensions of the IVD, and therefore the cross-sectional area and volume, also undergo changes [31]. The wide range of parameters presented in studies prompts a comprehensive approach to metric characteristics. Taking into account the somatometric parameters of each individual will allow objective personalization of the norm [11, 30]. At the same time, measuring and using a large number of additional somatometric parameters is a rather cumbersome task, which significantly limits their application in clinical practice.

The purpose of the study is to create an optimal workable model for calculating the IVD size sum indicator based on external body parameters, which can be used in medical practice, and to prove its effectiveness.

Material and methods

The main study group included 80 practically healthy young women and women aged 16 to 26 years (52 young women aged 16-20 years and 28 women aged 21-26 years) who were residents of the Vinnytsia region for at least three generations and consented to participate in the study. MRI of the lumbar spine was performed for these participants. Only individuals without IVD pathology detected on MRI were included in this group. Body height and weight measurements were recorded for all participants. The obtained MR images were used to measure the vertical dimensions (anterior, middle, and posterior heights), sagittal, and transverse dimensions of the lumbar IVDs.

For the first time in this study, the sum of IVD dimensions (the sum of sagittal, transverse, and averaged vertical dimensions of the IVD) and the somato-disc coefficient (the ratio of the body mass index to the sum of IVD dimensions) were used as parameters. Modeling was conducted within the main group based on the somato-disc coefficient, which was transformed algebraically into the sum of dimensions parameter. In subsequent analysis, a mathematical model for calculating the sum of IVD dimensions based on body height and weight was used, incorporating a normative range within 10 % of the calculated value.

The performance of the developed mathematical models was validated in an additional group of 65 young women and women aged 16-26 years, which included both practically healthy individuals and those with IVD changes detected on MRI. Individuals with significant pathological changes in the IVD identified on MR images were excluded from the validation group. Exclusion criteria included damage to the annulus fibrosus and vertebral endplates, pathological MRI signal changes in the bone marrow of adjacent vertebrae, and disruptions in alignment between adjacent vertebrae, such as listhesis. Consequently, the additional group consisted of previously examined individuals who, according to MRI data of the lumbar spine, exhibited Grades I, II, and III IVD changes as per Pfirrmann classification. Participants in the additional group also underwent height and weight measurements, and morphometric analysis of the IVD was performed on the

obtained MRI scans of the lumbar spine.

The Bioethics Committee of National Pirogov Memorial Medical University, Vinnytsya (protocol No. 4, dated May 18, 2023), confirmed that the study complied with the moral and legal requirements according to the Order of the Ministry of Health of Ukraine No. 66 of February 13, 2006, ethical standards, and the Helsinki Declaration on patient rights.

The study utilized a spine coil (SENSE-Spine), with participants positioned supine. MRI was performed on a Philips Achieva 1.5 Tesla scanner, obtaining MR images in sagittal and frontal planes:

- frontal plane slices, T1-SE: TR 577 ms, TE 9 ms, FA 45 °, matrix 512 x 256, 340 mm FOV, 11 slices with 4 mm thickness, interslice gap 0.4 mm, one repetition, scan time 1 minute 50 seconds.
- sagittal plane slices, T2-SE: TR 3007 ms, TE 100 ms, FA 45 °, matrix 512 x 256, FOV 340 mm, 13 slices with 4 mm thickness, interslice gap 0.4 mm, one repetition, scan time 1 minute 50 seconds.

Series of images in DICOM format were obtained. Measurements of the IVD were performed using DICOM files in the Radiant DICOM Viewer software by determining the heights, sagittal, and transverse dimensions.

Statistical processing of the results was conducted using the "Statistica 6.1" software package (license No. BXXR901E246122FA). A preliminary assessment of the distribution characteristics of the obtained variational series was performed, including the calculation of the arithmetic mean, standard error of the mean, standard deviation, median, the difference between the median and the mean, sample variance, distribution skewness, and coefficient of variation. Additionally, an evaluation of qualitative correlation relationships between magnetic resonance imaging linear parameters of the IVD and anthropometric body parameters was conducted using Pearson's parametric pairwise correlation. The quantitative nature of the relationships was determined using the method of direct stepwise regression analysis, involving modeling of the somato-disc coefficient of the IVD based on anthropometric parameters, Heath-Carter somatotype components, body mass composition indicators, and indices. Algebraic transformation of the derived regression models for somato-disc coefficients allowed for the formulation of final equations for calculating the sum of the IVD dimensions.

At the validation stage, calculations of the sum of the IVD dimensions were performed using the final equations based on individual indicators of body mass and height for the validation group. The calculated indicators were used for the mathematical evaluation of the IVD, which involved determining the difference between the mathematically predicted and the actually measured sums of the IVD dimensions. According to mathematical evaluation, an IVD is considered normal if the difference between the measured and mathematically predicted sums of the IVD dimensions is within ±10 %. Subsequently, a comparison of the mathematical evaluation results with the visual assessment of the IVD was conducted. It should be noted that visual assessment refers to the radiological conclusions of radiologists, who determined the presence or absence of IVD changes based on the commonly accepted Pfirrmann evaluation method.

Results

The mean age (A) of young women and women in the primary group was (A±SD) 19.93±2.93 years, while in the additional group it was 22.28±3.04 years. The mean body weight (M) of young women and women in the primary group was (M±SD) 56.94±7.98 kg, compared to 59.24±7.34 kg in the additional group. The mean height (H±SD) was 163.4±4.8 cm in the primary group and 165.1±4.9 cm in the additional group.

Correlation analysis conducted within the group of young women and women from the primary group revealed weak but significant correlations between IVD heights and circumferential body dimensions, with the highest correlation coefficient of 0.447. Notably, no significant

Table 1. The average absolute values of the correlation coefficients of linear dimensions, sums of dimensions and somato-disc coefficients of IVD with anthropometric parameters of the main group of young women and women in norm.

Indicator	Average absolute values of correlation coefficients	The relative indicator of the number of significant correlations out of the total number of correlations when r>0.3
Transverse size of IVD L_I-L_{II}, mm	0.149	0-26.9 %
Transverse size of IVD L_{II}-L_{III}, mm	0.148	
Transverse size of IVD L_{III}-L_{IV}, mm	0.076	
Transverse size of IVD L_{IV}-L_V, mm	0.123	
Sagittal size of IVD L_I-L_{II}, mm	0.139	
Sagittal size of IVD L_{II}-L_{III}, mm	0.140	
Sagittal size of IVD L_{III}-L_{IV}, mm	0.149	
Sagittal size of IVD L_{IV}-L_V, mm	0.141	
Height of IVD L_I-L_{II}, mm	0.198	
Height of IVD L_{II}-L_{III}, mm	0.102	
Height of IVD L_{IV}-L_V, mm	0.204	
Height of IVD L_{IV}-L_V, mm	0.177	
Sum of sizes of IVD L_I-L_{II}, mm	0.216	1.9-25.0 %
Sum of sizes of IVD L_{II}-L_{III}, mm	0.181	
Sum of sizes of IVD L_{III}-L_{IV}, mm	0.161	
Sum of sizes of IVD L_{IV}-L_V, mm	0.188	
Somato-disc coefficient of IVD L_I-L_{II}	0.471	77.4-81.1 %
Somato-disc coefficient of IVD L_{II}-L_{III}	0.453	
Somato-disc coefficient of IVD L_{III}-L_{IV}	0.497	
Somato-disc coefficient of IVD L_{IV}-L_V	0.514	

Table 2. Results of direct stepwise regression of IVD L1-L5 somato-disc coefficients on the basis of body length and weight in young women and women (16-26 years old) of the main group in the norm.

Somato-disc coefficient IVD	Results of direct stepwise regression									
	R	R^2	F	St.error estim.	Free index		Body length		Body weight	
					B	t(71)	B	t(71)	B	t(71)
L1-L2	0.932	0.868	217	0.275	7.238	6.462	-4.005	-5.777	0.064	20.81
L2-L3	0.922	0.850	190	0.266	7.096	6.610	-3.854	-5.788	0.058	19.44
L3-L4	0.940	0.884	251	0.221	6.816	7.553	-3.715	-6.651	0.055	22.36
L4-L5	0.949	0.901	299	0.203	6.361	7.702	-3.539	-6.923	0.056	24.42

correlations (with correlation coefficients >0.300) were observed between transverse and sagittal dimensions of the IVD and anthropometric parameters. Weak but significant correlations were identified between the sum of IVD dimensions and circumferential body dimensions, body surface area, body mass, and height, with a maximum value of 0.360.

Particular attention is drawn to the results of the correlation analysis of IVD somatodiscal coefficients with anthropometric parameters, which demonstrated a significant increase in the number and strength of correlations, including moderate to strong correlations. The highest correlation coefficients for somatodiscal coefficients were observed with body mass (0.835), upper arm circumference (0.788), ectomorphic component (-0.838), and body mass index (0.868). The average absolute values of correlation coefficients between linear dimensions, sums of dimensions, and somatodiscal coefficients of IVD with anthropometric parameters in the primary group under normal conditions are presented in Table 1.

Thus, the observed correlations between IVD dimensional parameters and external body dimensions provide a positive affirmation of proportional quantitative relationships. They also demonstrate both qualitative and quantitative enhancements in these relationships when using the somatodiscal coefficient. However, these correlations remain overly simplistic and straightforward, whereas the interconnections of polymorphic structures are far more complex. A more realistic approach to defining multiple correlations (covariates) involves regression analysis, which enables the identification of multidimensional correlations between IVD dimensions and a subset of anthropometric parameters. This method provides a more comprehensive and precise representation of the proportional relationships between human body parameters and IVD.

For regression-based modeling, the somatodiscal coefficient was used as the dependent variable, given its high number of correlations with anthropometric parameters. Anthropometric measures served as independent variables. Through regression analysis based on data from the primary group, the most optimal model was identified: the calculation of the somatodiscal coefficient using body mass and height. The final results of the stepwise linear regression for the somatodiscal coefficient of individual IVD segments (L1-L5) are presented in Table 2.

The coefficient of determination R2, as a measure of predictability, exceeds 85.0 %, indicating the expected predictive accuracy of the dependent variable. Therefore, the model's predictability ranges from 85.0 % for IVD L1-L2 to 90.1 % for IVD L4-L5.

The adequacy of the regression model was assessed by analyzing the difference between the predicted and actual values of the relative parameter in each sample. It was found that the maximum relative deviations were within ±10 %.

In the next stage, algebraic transformation of the obtained somatodiscal coefficient model was performed, leading to the final versions of the equations for calculating the sum of the dimensions of each IVD segment (L1-L5) based on body mass and height values:

IVD L1-L2 =K/(7.238 + 0.064 x m - 4.005 x H);

IVD L2-L3 =K/(7.096 + 0.058 x m - 3.854 x H);

IVD L3-L4 =K/(6.817 + 0.055 x m - 3.715 x H);

IVD L4-L5 =K/(6.361 + 0.056 x m - 3.539 x H).

where: IVD L1-L2 - IVD L4-L5 - sum of dimensions of the respective IVD (cm); K - mass-height coefficient (kg/m); m - body mass (kg); H - body height (m).

The obtained final formulas of the mathematical models allow the calculation of individualized sum of dimensions for individual IVD segments in the lumbar spine, based on body mass and height, with a deviation within ±10 %.

The next step involved work in the additional group to verify the functionality of the mathematical model in conditions close to practical medicine. This step aimed to compare the results of visual and mathematical assessments of IVD in the additional group, which are presented in Table 3.

Given the age characteristics of the individuals who participated in the study, the predominance of unchanged IVDs is understandable, which was confirmed by the comparison of mathematical and visual assessments (on average, 86.2 % of all examined individuals). Deviations from the norm were noted both in visual and mathematical assessments in 5.0 % of all examined.

In cases of discrepancies in assessment, two possibilities arise: either the absence of IVD changes visually, but their presence according to the mathematical

Table 3. Results of the analysis of the comparison of data from visual and mathematical assessment of IVD L1-L5 in the additional group.

Evaluation of data comparison	IVD L1-L2	IVD L2-L3	IVD L3-L4	IVD L4-L5	Σ
Assessment match (absence of IVD changes visually and mathematically)	84.6 %	89.2 %	84.6 %	86.2 %	86.2 %
Assessment match (presence of IVD changes visually and mathematically)	7.7 %	0.0 %	6.2 %	6.2 %	5.0 %
Discrepancy in assessment (absence of IVD changes visually, but presence by mathematical calculation)	7.7 %	10.8 %	4.6 %	0.0 %	5.8 %
Discrepancy in assessment (presence of IVD changes visually, but absence by mathematical calculation)	0.0 %	0.0 %	4.6 %	7.7 %	3.0 %

calculation, or vice versa. In the first case, the discrepancy between the mathematical and visual assessments indicates a deviation in the metric values from the calculated norm, suggesting changes in the linear parameters of the IVD that were not detected in the visual assessment (potential cases of underdiagnosis). This type of discrepancy was identified in an average of 5.8 % of cases. The second type, where visual assessment identified IVD changes but the mathematical calculation did not show deviations from the norm, is considered a case of overdiagnosis (on average, 3.0 % of cases).

Thus, the analysis of the obtained data showed that the agreement of results between visual and mathematical assessments occurred in 91.2 % of all assessments for both normal and pathologically altered IVDs. In other words, both mathematical and visual assessments simultaneously confirm the presence or absence of IVD changes.

Discussion

Accurate determination of the presence and degree of degeneration of the lumbar IVD is an important task for choosing the appropriate treatment strategy for spinal pathology.

Among the methods of evaluation, the Pfirrmann scale holds a leading position, which was used in our study. The identification of changes in the nucleus pulposus and intervertebral surfaces on MRI scans is subjective and depends on the scanning parameters and the "window" settings of the image viewing software. However, excessive attention to the nucleus pulposus area and, to a large extent, the superficial assessment of surrounding structures leads to a decrease in diagnostic accuracy. In the study by Tong N. et al. [32], a new approach to calibrating regional features for accurate and reliable assessment of degeneration was proposed. According to their data, the accuracy of the assessment reached 90.5 % with a sensitivity of 90.8 %, and it is fully automated. The use of artificial intelligence to assist doctors in detecting various diseases during complex diagnostic procedures, including MRI and CT scans, is becoming increasingly relevant [15, 16]. Automated assessment methods of IVD with damaged annulus fibrosus, aimed at verifying protrusions, herniations, osteophytes, and prolapses of vertebral endplates, are successfully being implemented [5, 26]. However, fully automated evaluation of IVD is a complex task due to the variability of discs and vertebrae [29]. The problem of correct recognition and clear delineation of the vertebral body contours, IVD, and spinal canal borders can be addressed by various approaches to automatic segmentation of the research area. Correctly defining the borders expands the capabilities of automated and semi-automated assessments of structures, enabling the determination of the degree of homogeneity of the structure, its average intensity, contour characteristics, and metric parameters [14]. Software that uses neural networks [20] assists in semi-automated assessment due to the wide range of adjustable parameters and brings it closer to automated evaluation by self-learning and considering previously analyzed data. The accuracy of such assessments can reach 90%, thus objectifying the diagnostic conclusions of specialists [24]. More complex systems include memory elements about surrounding tissues. The study by Han Z. et al. [13] demonstrates that MRI analysis should not be limited to just one structure. In 2021, Gong H. et al. [8] used an analysis of the surrounding spinal tissue features on axial MRI slices using an improved feature fusion module to create discriminative features for recognizing differences between normal and altered structures. The study showed that the module positively affected segmentation and diagnostic accuracy. Furthermore, the authors' results showed that Axial-SpineGAN had the highest similarity coefficient (94.9±1.8 %) regarding segmentation accuracy and the highest diagnostic accuracy (93.9±2.6 %) [8]. The above-mentioned automatic evaluation modules were not used in our study; the assessment was conducted by radiologist specialists based on the Pfirrmann criteria. Thus, the assessment of IVD status in clinical practice, whether automated or performed by a radiologist, follows the Pfirrmann criteria, based on the analysis of the degree of homogeneity of the IVD structure, its average intensity, contour characteristics, and height indicator.

Analysis of studies conducted by scientists examining the degree of degeneration of IVD shows that most of them used MRI data performed in the sagittal plane (over 75 %), while only 10% utilized both axial and sagittal planes. Regarding the MRI machines, 80 % of studies used machines with a magnetic field strength of 1.5 Tesla, and regardless of the machine, all researchers performed scans

of the vertebrae and IVD in T2-weighted imaging mode, with only a quarter additionally using T1-weighted images [4]. Similarly to the study by Iriondo C. et al. [15], our research employed simultaneous use of T1- and T2-SE, significantly improving segmentation accuracy and allowing for more reliable identification of the boundaries of the structures being studied.

Defining the boundaries of the structures under study is crucial, given that the Pfirrmann scale includes a height parameter for IVD. The height parameter is metric, making its assessment the most objective. In our study, we measured the height parameters (anterior, posterior, middle), as well as the transverse and sagittal dimensions. However, it should be noted that normative values for the height, sagittal, and transverse dimensions of IVD are absent. There are individual studies that provide linear dimensions of IVD, but these values exhibit significant variability. Using averaged linear dimensions has certain limitations related to the possibility of comparing them across different populations. Thus, the idea of individualizing normative IVD parameters, which is the goal of our study, is relevant and timely. Unlike the height parameter, our study introduces a new parameter - the sum of dimensions, which is an integral measure encompassing the height, sagittal, and transverse dimensions of the IVD.

Studying the possible causes of variability in linear IVD parameters shows that different measurement techniques are used, and age and sex differences within study groups are also noted. For example, Çetin T. et al. [3], who measured the heights of L4-L5 IVD in 219 women and 166 men aged 46.68±16.17 years, reported the following average values: ventrally 12.57 mm, centrally 11.92 mm, dorsally 7.79 mm, with an average of 10.88 mm. In our study, we also examined IVD height, but additionally measured the sagittal and transverse dimensions of IVD and studied not only L4-L5 but also L1-L4 IVDs. There was also a difference in the number of observations and the average age of the subjects (19.93±2.93 years in our study). In 2018, Bach K. et al. [1] (Florida, USA) performed computed tomography on 131 women aged 14-79 years. According to their study, the following IVD height parameters were defined: the average height of IVD LI-LII was 5.8±0.9 mm; IVD LII-LIII was 6.9±1.1 mm; IVD LIII-LIV was 7.6±1.2 mm; and for IVD LIV-LV, it was 8.5±1.6 mm. Unlike Bach K. et al.'s study [1], our research used MRI rather than CT for IVD assessment. Similarly to our study, Mirab S. M. H. and co-authors [22] conducted measurements of the height, sagittal, and transverse dimensions of IVD in the lumbar spine.

The parameters of the IVD are correlated with somatometric parameters, and the degree of degeneration correlates with disc height [22, 37], age [9], sex, and body weight. There are conflicting data regarding the correlation with the degree of fat tissue development [2, 17]. We studied the correlations between the linear parameters of IVD, but we also identified correlations between the sum of the IVD dimensions and the somato-disc coefficient with anthropometric parameters.

C. Gungor et al. [12] mathematically modeled the area of the IVD and the area of the spinal extensor muscles at corresponding levels based on somatometric data, such as the longitudinal, transverse, and circumference measurements of the head, trunk, and limbs. A modified model of this calculation was proposed by Turk Z. and Celan D. [33] in 2004, who included the square of the average value calculated from the diameters of the knee joint, elbow, and wrist bones in their model formula. R. Tang and colleagues [31] modeled the transverse cross-sectional area of the IVD from L3 to S1 by determining the bone component of body mass and applying the modified formula by Turk Z. In contrast to the aforementioned authors who modeled the transverse cross-sectional area of IVD, our study modeled the sum of the IVD dimensions.

Given the variability of the linear IVD parameters, the search for a mathematical solution to individualize normative IVD metrics, accounting for sex and individual somatometric data, becomes highly relevant.

Our work showed that the search for a functional mathematical model for the individualization of normative IVD parameters based on proportional (relative) measures is feasible. The inclusion of such calculation protocols into automated systems will enhance the accuracy of IVD characterization.

It is worth noting the limitations of this study, namely: the study included young women (ages 16-26), and no analysis of data from other age groups was conducted. The examinations were performed in the first half of the day in accordance with anthropometric measurement requirements, and data from other times of day were not considered. The morphometry of IVD was carried out without the involvement of automated data processing systems, using software for processing DICOM image formats by two specialists, with the consensus value being taken into account. The conclusion regarding the normality of IVD was based on a calculated parameter with an accuracy of approximately 90 %.

Conclusions

1. Assessment of IVD changes based on the analysis of the degree of homogeneity in IVD structure, its average intensity, and contour characteristics is subjective and feasible only with MRI. Therefore, it necessitates objectification by increasing the role of metric evaluation criteria such as IVD height, as well as our proposed integral index of IVD size (the arithmetic sum of IVD height, sagittal, and transverse dimensions).

2. The use of averaged IVD parameter values as normative criteria is justified but may lead to erroneous evaluations due to variability. Consequently, the search for individualized IVD normative values, based on proportionality laws and correlations with external body

parameters, including the application of novel indices like the sum of IVD dimensions, is optimal. Individualized metric parameters can be applied in computed tomography, where the evaluation used in MRI is not feasible.

3. Correlation analysis revealed a low relationship between partial dimensional parameters (height, sagittal, and transverse dimensions) and anthropometric characteristics. However, another index we proposed, the somatodiscal coefficient (the ratio of the body mass-to-height index to the sum of IVD dimensions), demonstrated a high degree of correlation with anthropometric parameters. Specifically, the share of significant correlations (r>0.3) between the somatodiscal coefficient and anthropometric parameters accounted for no less than 77.4 % of all correlations. Furthermore, medium and strong correlations between the somatodiscal coefficient and anthropometric parameters were noted, with a maximum correlation coefficient value of 0.868.

4. The high degree of correlation between the somatodiscal coefficient and anthropometric parameters justified its use in mathematical modeling via direct stepwise regression analysis. The resulting formula for calculating the somatodiscal coefficient, after algebraic transformation, allows for deriving a formula to calculate the linear integral index of the sum of IVD dimensions based on body length and weight.

5. An analysis of the results from visual assessment (using Pfirrmann criteria) and mathematical assessment (based on the difference between measured and mathematically predicted IVD size sums) showed an overall agreement in 91.2 % of cases for normal and pathologically altered IVDs. Cases of discrepancy between visual and mathematical assessments, identified in 8.8 % of the studied sample and attributed to possible under- or overdiagnosis in visual evaluation, require in-depth reanalysis of the IVD.

References

[1] Bach, K., Ford, J., Foley, R., Januszewski, J., Murtagh, R., Decker, S., & Uribe, J. S. (2019). Morphometric analysis of lumbar intervertebral disc height: an imaging study. *World Neurosurgery,* 124, e106-e118. doi: 10.1016/j.wneu.2018.12.014

[2] Canbek, U., Rosberg, D., Rosberg, H. E., Canbek, T. D., Akgün, U., & Comert, A. (2021). The effect of age, BMI, and bone mineral density on the various lumbar vertebral measurements in females. *Surgical and Radiologic Anatomy: SRA,* 43(1), 101-108. doi: 10.1007/s00276-020-02560-1

[3] Çetin, T., Kahraman, S., Kizilgöz, V., & Aydin, S. (2023). The Comparison between Herniated and Non-Herniated Disc Levels Regarding Intervertebral Disc Space Height and Disc Degeneration, A Magnetic Resonance Study. *Diagnostics* (Basel, Switzerland), 13(20), 3190. doi: 10.3390/diagnostics13203190

[4] Compte, R., Granville Smith, I., Isaac, A., Danckert, N., McSweeney, T., Liantis, P., & Williams, F. M. K. (2023). Are current machine learning applications comparable to radiologist classification of degenerate and herniated discs and Modic change? A systematic review and meta-analysis. *European Spine Journal: official publication of the European Spine Society, the European Spinal Deformity Society, and the European Section of the Cervical Spine Research Society,* 32(11), 3764-3787. doi: 10.1007/s00586-023-07718-0

[5] Coppock, J. A., Zimmer, N. E., Spritzer, C. E., Goode, A. P., & DeFrate, L. E. (2023). Automated segmentation and prediction of intervertebral disc morphology and uniaxial deformations from MRI. *Osteoarthritis and Cartilage Open,* 5(3), 100378. doi: 10.1016/j.ocarto.2023.100378

[6] Faur, C., Patrascu, J. M., Haragus, H., & Anglitoiu, B. (2019). Correlation between multifidus fatty atrophy and lumbar disc degeneration in low back pain. *BMC Musculoskeletal Disorders,* 20(1), 414. doi: 10.1186/s12891-019-2786-7

[7] Ge, Y., Chen, Y., Guo, C., Luo, H., Fu, F., Ji, W., … & Ruan, H. (2022). Pyroptosis and Intervertebral Disc Degeneration: Mechanistic Insights and Therapeutic Implications. *Journal of Inflammation Research,* 15, 5857-5871. doi: 10.2147/JIR.S382069

[8] Gong, H., Liu, J., Li, S., & Chen, B. (2021). Axial-SpineGAN: Simultaneous segmentation and diagnosis of multiple spinal structures on axial magnetic resonance imaging images. *Phys. Med. Biol.,* 66(11), 115014. doi: 10.1088/1361-6560/abfad9

[9] Grams, A. E., Rehwald, R., Bartsch, A., Honold, S., Freyschlag, C. F., Knoflach, M., … & Glodny, B. (2016). Correlation between degenerative spine disease and bone marrow density: a retrospective investigation. *BMC Medical Imaging,* 16, 17. doi: 10.1186/s12880-016-0123-2

[10] Griffith, J. F., Wang, Y.-X. J., Antonio, G. E., Choi, K. C., Yu, A., Ahuja, A. T., & Leung, P. C. (2007). Modified Pfirrmann Grading System for Lumbar Intervertebral Disc Degeneration. *Spine,* 32(24), E708-E712. doi: 10.1097/brs.0b013e31815a59a0

[11] Gunas I. V., Pinchuk S. V., & Lezhneva O. V. (2014). Відмінності комп'ютерно-томографічних розмірів поперекового відділу хребта на медіанно-сагітальних зрізах у здорових юнаків різних соматотипів [Difference of computed tomography sizes of lumbar spine on the mediansagittal slises in healthy young men of different somatotype]. *Світ медицини та біології=World of Medicine and Biology,* 4(47), 26-31.

[12] Gungor, C., Tang, R., Sesek, R. F., Davis, G. A., & Gallagher, S. (2019). Regression Models for the Erector Spinae Muscle Mass (ESMM) Cross-Sectional Area: Asymptomatic Populations. *Journal of Biomechanical Engineering,* 141(8), 081009. doi: 10.1115/1.4043558

[13] Han, Z., Wei, B., Mercado, A., Leung, S., & Li, S. (2018). Spine-GAN: Semantic segmentation of multiple spinal structures. *Med Image Anal,* 5023-5035. doi: 10.1016/j.media.2018.08.005

[14] Huang, J., Shen, H., Wu, J., Hu, X., Zhu, Z., Lv, X., … & Wang, Y. (2020). Spine Explorer: a deep learning based fully automated program for efficient and reliable quantifications of the vertebrae and discs on sagittal lumbar spine MR images. *The Spine Journal: Official Journal of the North American Spine Society*, 20(4), 590-599. doi: 10.1016/j.spinee.2019.11.010

[15] Iriondo, C., Pedoia, V., & Majumdar, S. (2020). Lumbar intervertebral disc characterization through quantitative MRI analysis: An automatic voxel-based relaxometry approach. *Magnetic Resonance in Medicine,* 84(3), 1376-1390. doi: 10.1002/mrm.28210

[16] Ito, S., Nakashima, H., Segi, N., Ouchida, J., Oda, M., Yamauchi, I. ... & Imagama, S. (2023). Automated Detection and Diagnosis

of Spinal Schwannomas and Meningiomas Using Deep Learning and Magnetic Resonance Imaging. *Journal of Clinical Medicine,* 12(15), 5075. doi: 10.3390/jcm12155075

[17] Kanbayti, I. H., Al-Buqami, A. S., Alsheikh, M. H., Al-Malki, S. M., Hadadi, I., Alahmadi, A. … & Ahmed, H. H. (2024). Lumbar Disc Degeneration Is Linked to Dorsal Subcutaneous Fat Thickness at the L1-L2 Intervertebral Disc Level Measured by MRI. *Tomography* (Ann Arbor Mich), 10(1), 159-168. doi: 10.3390/tomography10010012

[18] Kízígöz, V., & Uzuner, M. B. (2021). Influence of lumbar intervertebral disc height and geometry of the articular plateau surface on disc pathologies. *Ann. Clin Anal Med,* 12, 1325-1331. doi: 10.4328/ACAM.20731

[19] Koziy, T. P., & Vakulenko, M. S. (2018). Ефективність застосування пілатесу як засобу фізичної реабілітації при дегенеративно-дистрофічних змінах елементів поперекового хребетно-рухового сегменту [Effectiveness of Pilates as a Means of Physical Rehabilitation with Degenerative-Distrophic Changes of Elements of the Lumbar Spine-moving segment]. *Український журнал медицини, біології та спорту=Ukrainian Journal of Medicine, Biology and Sport,* 3, 2(11), 271-277.

[20] Liawrungrueang, W., Kim, P., Kotheeranurak, V., Jitpakdee, K., & Sarasombath, P. (2023). Automatic Detection, Classification, and Grading of Lumbar Intervertebral Disc Degeneration Using an Artificial Neural Network Model. *Diagnostics* (Basel, Switzerland), 13(4), 663. doi: 10.3390/diagnostics13040663

[21] Martens, F., Vajkoczy, P., Jadik, S., Hegewald, A., Stieber, J., & Hes, R. (2018). Patients at the Highest Risk for Reherniation Following Lumbar Discectomy in a Multicenter Randomized Controlled Trial. *JB & JS Open Access,* 3(2), e0037. doi: 10.2106/JBJS.OA.17.00037

[22] Mirab, S. M. H., Barbarestani, M., Tabatabaei, S. M., Shahsavari, S., & Zangi, M. B. (2018). Measuring Dimensions of Lumbar Intervertebral Discs in Normal Subjects. *ASJ*, 15(1), 3-8.

[23] Mwale, F., Iatridis, J. C., & Antoniou, J. (2008). Quantitative MRI as a diagnostic tool of intervertebral disc matrix composition and integrity. *European Spine Journal: official publication of the European Spine Society, the European Spinal Deformity Society, and the European Section of the Cervical Spine Research Society,* 17(4), 432-440. doi: 10.1007/s00586-008-0744-4

[24] Niemeyer, F., Galbusera, F., Tao, Y., Kienle, A., Beer, M., & Wilke, H. J. (2021). A Deep Learning Model for the Accurate and Reliable Classification of Disc Degeneration Based on MRI Data. *Investigative Radiology,* 56(2), 78-85. doi: 10.1097/RLI.0000000000000709

[25] Oh, C. H., & Yoon, S. H. (2017). Whole Spine Disc Degeneration Survey according to the Ages and Sex Using Pfirrmann Disc Degeneration Grades. *Korean Journal of Spine*, 14(4), 148-154. doi: 10.14245/kjs.2017.14.4.148

[26] Pan, Q., Zhang, K., He, L., Dong, Z., Zhang, L., Wu, X., … & Gao, Y. (2021). Automatically Diagnosing Disk Bulge and Disk Herniation With Lumbar Magnetic Resonance Images by Using Deep Convolutional Neural Networks: Method Development Study. *JMIR Medical Informatics*, 9(5), e14755. doi: 10.2196/14755

[27] Rim D. C. (2016). Quantitative Pfirrmann Disc Degeneration Grading System to Overcome the Limitation of Pfirrmann Disc Degeneration Grade. *Korean Journal of Spine,* 13(1), 1-8. doi: 10.14245/kjs.2016.13.1.1

[28] Santos, E. S., Bernardes, J. M., Vianna, L. S., Ruiz-Frutos, C., Gómez-Salgado, J., Alonso, M. S., … & Dias, A. (2023). The Impact of Low Back Pain on the Quality of Life of Children between 6 and 12 Years of Age. *Healthcare,* 11(7), 948. doi: 10.3390/healthcare11070948

[29] Sustersic, T., Rankovic, V., Milovanovic, V., Kovacevic, V., Rasulic, L., & Filipovic, N. (2022). A Deep Learning Model for Automatic Detection and Classification of Disc Herniation in Magnetic Resonance Images. *IEEE Journal of Biomedical and Health Informatics,* 26(12), 60360-6046. doi: 10.1109/JBHI.2022.3209585

[30] Tang, R., Gungor, C., Sesek, R. F., Foreman, K. B., Gallagher, S., & Davis, G. A. (2016). Morphometry of the lower lumbar intervertebral discs and endplates: comparative analyzes of new MRI data with previous findings. *Eur Spine J,* 25(12), 4116-4131. doi: 10.1007/s00586-016-4405-8

[31] Tang, R., Gungor, C., Sesek, R. F., Gallagher, S., Davis, G. A., & Foreman, K. B. (2019). Prediction models for the cross-sectional areas of lower lumbar intervertebral discs and vertebral endplates. *Int J Ind Ergon,* 72, 12-34. doi: 10.1016/j.ergon.2019.03.006

[32] Tong, N., Gou, S., Yang, Y., Liu, B., Bai, Y., Liu, J., & Ding, T. (2024). Fully Automatic Fine-Grained Grading of Lumbar Intervertebral Disc Degeneration Using Regional Feature Recalibration. *IEEE Journal of Biomedical and Health Informatics,* PP, 10.1109/JBHI.2024.3366780. Advance online publication. doi: 10.1109/JBHI.2024.3366780

[33] Turk, Z., & Celan, D. (2004). Importance of intervertebral disc size in low back pain. *Croat Med J,* 45(6), 734-739. PMID: 15578808

[34] Wu, A., March, L., Zheng, X., Huang, J., Wang, X., Zhao, J., … & Hoy, D. (2020). Global low back pain prevalence and years lived with disability from 1990 to 2017: estimates from the Global Burden of Disease Study 2017. *Ann Transl Med,* 8. doi: 10.21037/atm.2020.02.175

[35] Zahid-Al-Quadir, A., Zaman, M. M., Ahmed, S., Bhuiyan, M. R., Rahman, M. M., Patwary, I., … & Haq, S. A. (2020). Prevalence of musculoskeletal conditions and related disabilities in Bangladeshi adults: a cross-sectional national survey. *BMC Rheumatology,* 4(1), 69. doi: 10.1186/s41927-020-00169-w

[36] Zheng, H. D., Sun, Y. L., Kong, D. W., Yin, M. C., Chen, J., Lin, Y. P., … & Wang, Y. J. (2022). Deep learning-based high-accuracy quantitation for lumbar intervertebral disc degeneration from MRI. *Nature Communications,* 13(1), 841. doi: 10.1038/s41467-022-28387-5

[37] Zheng, J., & Shen, C. (2022). Quantitative Relationship between the Degree of Lumbar Disc Degeneration and Intervertebral Disc Height in Patients with Low Back Pain. *Contrast Media & Molecular Imaging,* 2022, 5960317. doi: 10.1155/2022/5960317

МОДЕЛЮВАННЯ ЛІНІЙНИХ ПАРАМЕТРІВ МІЖХРЕБЦЕВИХ ДИСКІВ ПОПЕРЕКОВОГО ВІДДІЛУ ХРЕБТА НА ОСНОВІ СОМАТОМЕТРИЧНИХ ПОКАЗНИКІВ

Данилевич В. П., Гумінський Ю. Й., Андрійчук В. М., Залевський Л. Л., Приходько С. О., Данилевич А. В.

Актуальність теми дослідження зумовлена значною поширеністю патології хребтового стовпа та стрімким розвитком діагностичних технологій, що спонукають до удосконалення критеріїв визначення змін структурних компонентів хребта, зокрема однієї із найуразливіших структур - міжхребцевих дисків. Використання суб'єктивних критеріїв оцінки стану міжхребцевих дисків при магнітно-резонасному чи комп'ютерно-томографічному досліженнях потребує пошуку більш

об'єктивних додаткових кількісних критеріїв визначення змін міжхребцевих дисків. Мета дослідження - створити оптимальну працездатну модель обчислення показника суми розмірів міжхребцевих дисків на основі зовнішніх параметрів тіла, котра може бути використана у медичній практиці, та довести її ефективність. Для досягнення поставленої мети юначкам та жінкам віком від 16 до 26 років, що є корінними жительками Вінниччини, провели магнітно-резонансну томографію поперекового відділу хребта. Основну групу становили 80 осіб, з яких 52 юначки були віком 16-20 років та 28 жінок віком 21-26 років; групу перевірки становили 65 юначок та жінок віком від 16 до 26 років. Всім обстеженим визначили показники довжини й маси тіла. Використовуючи дані, отримані при дослідженні основної групи, провели математичне моделювання суми розмірів міжхребцевих дисків поперекового відділу хребта. В основі моделювання лежав покроковий регресійний аналіз з використанням показників сомато-дискових коефіцієнтів окремих міжхребцевих дисків та антропометричних показників. В результаті моделювання отримали модель розрахунку показників сомато-дискового коефіцієнта на основі довжини та маси тіла. Подальше алгебраїчне перетворення сомато-дискового коефіцієнту дозволило отримати формулу розрахунку індивідуалізованих показників суми розмірів міжхребцевих дисків, що є інтегральним показником вертикального, сагітального та поперечного розмірів. Предиктивність отриманих моделей становить 85-91 %. При проведеному порівнянні фактичних показників суми розмірів, отриманих при вимірюванні міжхребцевих дисків в основній групі, з математично змодельованими показниками було визначено, що відхилення не перевищує ±10 %. Дана математична модель суми розмірів поперекових міжхребцевих дисків на основі соматометричних показників дозволяє визначити індивідуальне метричне значення нормального диску та об'єктивно виявити ранні зміни міжхребцевих дисків при його дегенерації. Так, при співставленні даних клінічної візуальної оцінки ступеня змін міжхребцевих дисків за критеріями Pfirrmann та математичної оцінки у групі перевірки збіг становить 91 %. У 9 % була виявлена розбіжність в оцінці, що потребує повторного аналізу для уточнення з метою запобігання гіпо- та гіпердіагностики оцінки змін міжхребцевих дисків. Таким чином, математичне моделювання слугує інструментом, направленим на розрахунок індивідуалізованих метричних показників норми, а запропоновані математичні моделі обчислення суми розмірів міжхребцевих дисків на основі маси та довжини тіла, є потужним доповненням до існуючих критеріїв оцінки міжхребцевих дисків.

Ключові слова: *міжхребцевий диск, сума розмірів, сомато-дисковий коефіцієнт, поперековий відділ хребта, моделювання, індивідуальна норма.*

Author's contribution

Danylevych V. P. - conceptualization, research, methodology and writing of the original project, data presentation, resources, software.
Guminskyi Yu. Y. - conceptualization, editing, administration, verification.
Andriichuk V. M. - editing, formal analysis and verification.
Zalevskyi L. L. - formal analysis and verification.
Prykhodko S. O. - formal analysis and verification.
Danylevych A. V. - research, editing, formal analysis and verification.

DOI: 10.31393/morphology-journal-2024-30(4)-03 Reports of Morphology, Vol. 30, №4, Pages 21-28

ISSN 1818-1295 eISSN 2616-6194

REPORTS OF MORPHOLOGY

Official Journal of the Scientific Society of Anatomists, Histologists, Embryologists and Topographic Anatomists of Ukraine

journal homepage: https://morphology-journal.com

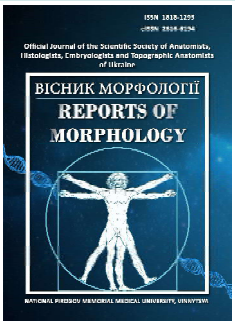

GLUT1 expression in patients with non-small cell lung cancer and its impact on survival

Vynnychenko O. I.[1], Moskalenko Yu. V.[2], Yazykov O. V.[2], Seleznov O. O.[3], Sulaieva O. M.[3], Moskalenko R. A.[2]

[1]Sumy Regional Clinical Oncology Center, Sumy, Ukraine;
[2]Sumy State University, Sumy, Ukraine;
[3]Kyiv Medical University, Medical Laboratory CSD, Kyiv, Ukraine.

ARTICLE INFO
Received: 13 February 2024
Accepted: 27 August 2024

UDC: 616.24-006.6-036.6:577.1

CORRESPONDING AUTHOR
e-mail: r.moskalenko@med.sumdu.edu.ua
Moskalenko R. A.

CONFLICT OF INTEREST
The authors have no conflicts of interest to declare.

FUNDING
This research has been performed with the financial support of grants of the external aid instrument of the European Union for the fulfillment of Ukraine's obligations in the Framework Program of the European Union for Scientific Research and Innovation "Horizon 2020" No. RN/ 11 - 2023 "The role of the DNA repair system in the pathogenesis and immunogenicity of lung cancer".

DATA SHARING
Data are available upon reasonable request to corresponding author.

GLUT1 is an essential glucose transporter, the expression of which increases in tumor cells, especially under conditions of hypoxia, and correlates with their active proliferation. This study aimed to investigate the relationship between GLUT1 expression and biological parameters and to evaluate the potential impact on survival in patients with radically treated non-small cell lung cancer (NSCLC). Forty-two patients who received radical treatment for NSCLC were involved in the study. Gender, age, smoking history, disease stage, and tumor histological type were considered when analyzing the data. GLUT1 antibodies were used to assess the degree of hypoxia. A semi-quantitative immunohistochemical score ranging from 0 to 12 was used for calculation. The chi2 and Student's t-test were used to compare categorical and parametric variables. The Cox proportional hazards model, the Kaplan-Meier method, and the Log-rank test were used to evaluate the effect of GLUT1 expression on survival. The results were considered statistically significant at $p<0.05$. A moderate correlation was found between GLUT1 expression and histological type of NSCLC ($r=0.432$, $p<0.0001$), sex ($r=0.336$, $p<0.0009$), and smoking ($r=0.325$, $p<0.0009$). GLUT1 overexpression was observed more in squamous cell carcinomas than in adenocarcinomas ($p=0.0001$). In patients with adenocarcinomas, the level of GLUT1 expression depended on age and T category. In patients with squamous cell carcinomas, GLUT1 expression was not associated with the studied clinicopathological characteristics. Patients with T1b-2a categories, without regional lymph node metastases, younger than 60, and non-smokers have better survival. Kaplan-Meier curves demonstrated no statistically significant differences in recurrence-free survival and overall survival between the patients with high and low GLUT1 (Log-rank $p=0.3284$ and Log-rank $p=0.7161$, respectively). In conclusion, GLUT1 overexpression is associated with squamous cell lung carcinomas. GLUT1 expression has no prognostic value and does not correlate with recurrence-free and overall survival in radically treated patients with NSCLC.

Keywords: *GLUT1, lung cancer, survival, adenocarcinoma.*

Introduction

At the beginning of the 20th century, Otto Warburg described a specific pattern of changes in the metabolism of tumors called the Warburg effect. Its essence is that even with sufficient oxygen concentration, malignant cells use glycolysis as the main pathway for adenosine triphosphate production. Unlike tumor cells, normal cells metabolize glucose by oxidative phosphorylation (OXPHOS) [25]. Hypoxia is the key factor determining tumor cells' metabolic reprogramming and shifting from OXPHOS to anaerobic glycolysis [26]. At the same time, tumor cells

demonstrate increased glucose utilization due to increased transport inside cells with glucose transporters (GLUT) involvement. Members of the glucose transporter family (GLUT1-14) are widely represented on the surface of most cells in the human body and are involved in maintaining cellular homeostasis. Among them, GLUT1 is considered an essential transporter, the expression of which increases in tumor cells, especially under conditions of hypoxia. It correlates with the acceleration of the proliferation of malignant cells [3].

Glucose metabolism is closely related to the state of immune cells in the tumor microenvironment. X. Lai et al. [18] established that an elevated glucose level weakens the primary effector functions of human CD4+ T cells. C. C. Yao et al. [28] demonstrated that reprogramming of glucose metabolism promotes antitumor immunity and effector function of CD8+ T cells.

GLUT1 may be a promising biomarker indicating the energy supply of the tumor and its aggressiveness [8]. In recent years, a topical issue has been the development of drugs that affect tumor metabolism, particularly energy consumption by tumor cells. More and more authors consider GLUT1 an attractive target for targeted therapy and are actively investigating the relationship with survival [20, 24]. L. Wu et al. [27] established that the deficiency of glucose-6-phosphate isomerase and GLUT1 leads to the activation of the antitumor effect of cytotoxic T cells. Blocking GLUT1 stimulates the transition from glycolysis to oxidative phosphorylation. As a result, there is hyperproduction of reactive oxygen species and death of tumor cells mediated by tumor necrosis factor alpha.

GLUT1 overexpression has been reported in a significant number of malignancies, including oral cancer [1], triple-negative breast cancer [21], gallbladder [9], liver [23], and non-small cell lung cancer (NSCLC) [30]. Previous studies have shown that depending on the stage of the disease [17], mutation burden, and histological variant [15], the prognostic role of GLUT1 in patients with NSCLC differs significantly. These factors identify a possible impact of GLUT1 expression on NSCLC aggressiveness and patient outcomes, but data on this issue are limited.

This study aimed to investigate the relationship between GLUT1 expression and biological parameters and assess the potential impact on survival in patients with radically treated NSCLC.

Materials and methods

Research design. The study involved 42 patients who received radical treatment for NSCLC at the Sumy Regional Clinical Oncology Center from 2015 to 2018. Inclusion criteria were age over 18 years, stages IA-IIIB of NSCLC, absence of severe cardiovascular and pulmonary pathology, and radical surgery in medical history ((bi)lobectomy or pneumonectomy). Exclusion criteria were comorbidities that could lead to the patient's death in the coming years, neoadjuvant chemotherapy or radiation therapy, and postoperative complications. In addition to surgical treatment, patients with IB-IIIB stages received adjuvant chemotherapy according to the histological variant of the primary tumor. Radiation therapy with a total dose of 30 Gray was performed for patients with category N2. Pathological stages were evaluated according to the 8th edition of the TNM tumor staging system (AJCC, 2017). Sex, age, smoking history, and histological type of tumor were also considered when analyzing the data.

Follow-up period. Thirty-six patients received adjuvant chemotherapy, and five patients received radiation therapy. After the radical treatment of NSCLC was completed, all patients moved to the follow-up phase. According to local practice, in the first two years after surgery, computed tomography scans were repeated every three months and every six months in the next three years. After a 5-year follow-up period, a chest X-ray was performed every year. In case of suspicion of disease recurrence, imaging examinations were performed unscheduled. Recurrence-free survival was considered the period from the surgery to the registration of the recurrence of the disease. Overall survival was considered the interval between the surgery and the patient's death. In general, the interval of the follow-up period was from 2 to 106 months. Data on the death of patients were obtained from the cancer registry of the Sumy Regional Clinical Oncology Center. The data collection end date was July 1, 2024.

The study was approved by the Local Ethics Committee of the Sumy Regional Clinical Oncology Center (protocol № 20, dated December 21, 2023). All alive patients signed an informed consent before the start of the study.

Histology and immunohistochemistry. Lung cancer tissue samples were fixed in a 10 % neutral formalin solution for 24 hours. The processing of biological material and production of paraffin blocks was carried out according to the generally accepted method. For immunohistochemical examination (IHC) of NSCLC tissues, serial sections with a thickness of 4 ?m were applied to SuperFrost slides (Thermo Scientific, Waltham, MA, USA). Deparaffinized sections were subjected to antigen unmasking by heat treatment in 0.1 M citrate buffer (pH 6.0) at 95-98 °C. The "In Vitro" detection system (Master-Diagnostica, Spain) was used to visualize IGH results. Antibodies to GLUT1 (polyclonal, Cell Marque, Rocklin, CA, USA) were used to assess the degree of hypoxia. A semi-quantitative immunohistochemical staining score (IHS) with a range from 0 to 12 was used to evaluate GLUT1 expression, where 0 points indicated the absence of immunoreactive cells, 1-4 points weak, 5-8 moderate, and 9-12 high expression of the biomarker). The IHS was calculated as the multiplication of the percentage of immunoreactive cells and the intensity of staining (0 - no staining, 1 - weak, 2 - moderate, 3 - strong). Less than 5 % of stained cells meant 0; 6-25 % - 1; 26-50 % - 2; 51-75 % - 3; $\geq$75 % - 4. As a positive control, we focused on erythrocytes [13].

Statistical analysis. Statistical analysis was performed

using Stata V.18.0 software (StataCorp, Texas, USA; https://www.stata.com; 2024). The normality of the distribution was determined by the Shapiro-Wilk test. Spearman's rank correlation coefficient was used to establish the relationship between GLUT1 expression level and clinicopathological characteristics. The significance of the difference between the two studied groups was assessed by the Student's t-test (for parametric variables). The Chi2 test was used to compare categorical variables. The Cox proportional hazards model was used to study the influence of clinicopathological characteristics on patients' recurrence-free and overall survival. The Kaplan-Meier method was used to compare survival depending on GLUT1 expression. The Log-rank test assessed the significance of the difference in survival in patients with low and high GLUT1. The results were considered statistically significant at $p<0.05$.

Results

Histology and immunohistochemistry. Adenocarcinoma tissue was characterized by the presence of atypical glandular structures that infiltrated the interstitial lung tissue. Tumor cells, which consist of glandular and pseudo-glandular structures, had signs of cellular atypia. Some tumors have a papillary structure and contain mucin. When adenocarcinoma tissue was stained with anti-GLUT1 antibodies, a focal membrane reaction was detected in tumor cells (Fig. 1 A-B).

Squamous cell carcinoma is represented by layers of atypical flat epithelium with pathological mitoses and cell polymorphism. Tumor cells and complexes are surrounded by fibrous tissue with lymphohistiocytic inflammatory infiltration. Staining of squamous cell carcinoma tissue with antibodies against GLUT1 showed the presence of a distinct membrane reaction in layers of tumor cells (Fig. 1 C, D).

Characteristics of the studied group of patients. Among the patients involved in the study, 22 had squamous cell carcinomas (52.4 %) and 20 - adenocarcinomas (47.6 %). The median age of patients in the studied cohort was 58.52±1.334 years. The median age of patients with

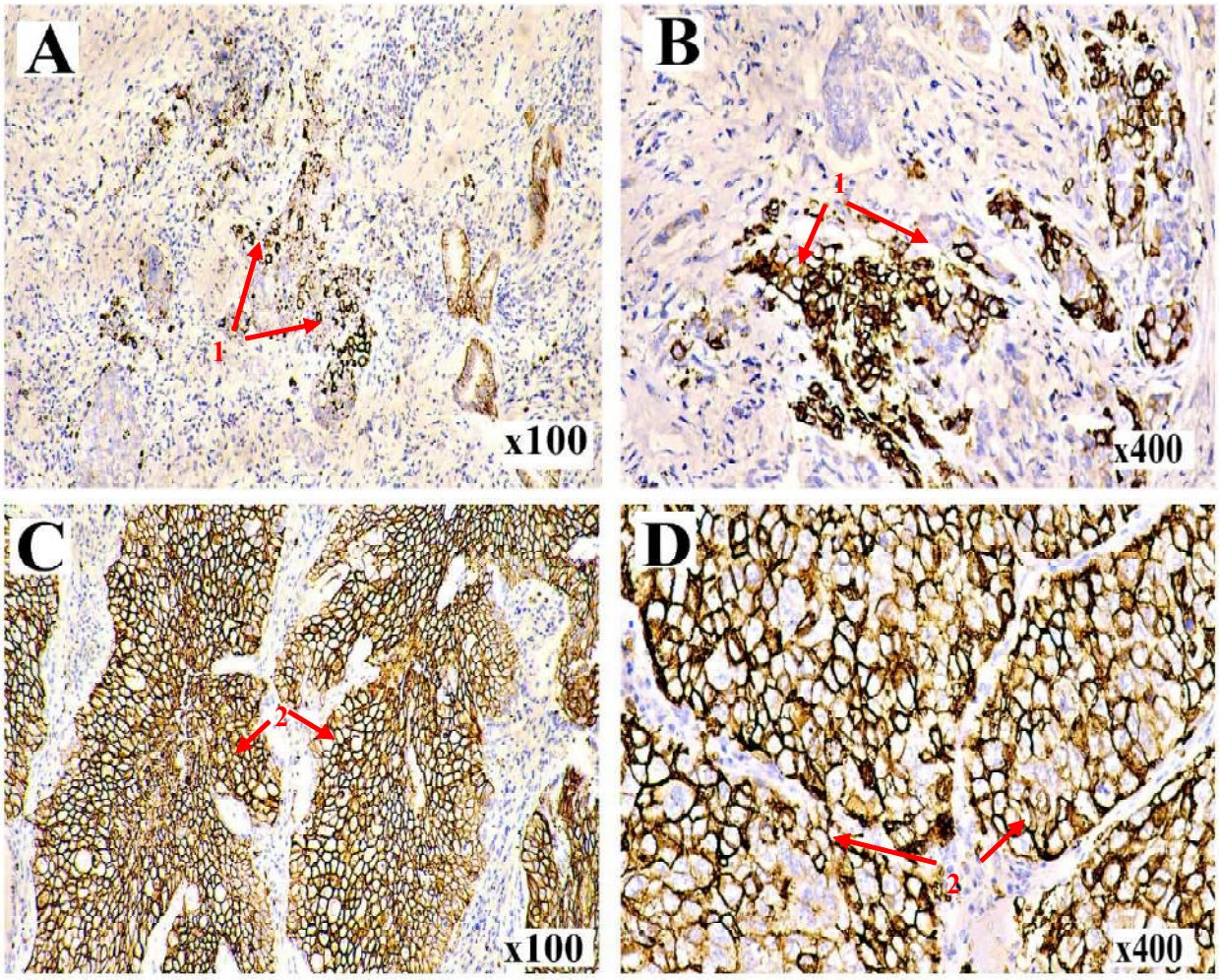

Fig. 1. Immunohistochemistry of NSCLC tissue with antibodies against GLUT1. A, B - adenocarcinoma, membrane staining (1), C, D - squamous cell carcinoma, membrane staining (2). Staining of nuclei with Mayer's hematoxylin. Magnification is indicated in each image's lower right corner.

adenocarcinoma is 59.53±1.861, and squamous cell carcinoma is 57.54±1.852. Among them, 34 patients were current or former smokers, and eight patients had no history of smoking.

According to GLUT1 expression, all patients were divided into 2 study groups: <9 IHS (low GLUT1) and ≥9 IHS (high GLUT1). A moderate correlation was found between GLUT1 expression and histological type of NSCLC (r=0.432, p<0.0001), sex (r=0.336, p<0.0009), and smoking (r=0.325, p<0.0009). The patients' other clinical and pathological characteristics did not demonstrate a statistically significant correlation with GLUT1. The results are presented in more detail in Table 1.

Table 1. Clinical and pathological characteristics of the studied cohort.

Baseline clinicopathological characteristics	Total (%) n=42	Low GLUT1 (%) n=29	High GLUT1 (%) n=13	r, p-value
Age, n (%): Median Range <60 ≥60	 58 29-75 22 (52.4) 20 (47.6)	 59 29-75 14 (48.3) 15 (51.7)	 58 40-69 8 (61.5) 5 (38.5)	 -0.123 (0.2647)
Sex, n (%): Female Male	 8 (19.0) 34 (81.0)	 8 (27.6) 21 (72.4)	 0 (0.0) 13 (100.0)	 0.336 (0.0009)
Stage, n (%): IA-IIA IIB-IIIB	 15 (35.7) 27 (64.3)	 10 (34.5) 19 (65.5)	 5 (38.5) 8 (61.5)	 -0,038 (0.7221)
Category T, n (%): T1b-2a T2b-4	 19 (45.2) 23 (54.8)	 11 (37.9) 18 (62.1)	 8 (61.5) 5 (38.5)	 -0.219 (0.0463)
Category N, n (%): N0 N1-2	 24 (57.1) 18 (42.9)	 16 (55.2) 13 (44.8)	 8 (61.5) 5 (38.5)	 -0,060 (0.5920)
Histology, n (%): Adenocarcinoma Squamous cell carcinoma	 20 (47.6) 22 (52.4)	 18 (62.1) 11 (37.9)	 2 (15.4) 11 (84.6)	 0.432 (0.0001)
Smoking status, n (%): Never smokers Current or former smokers	 8 (19.0) 34 (81.0)	 8 (27.6) 21 (72.4)	 0 (0.0) 13 (100.0)	 0.325 (0.0009)

Table 2. Association between GLUT1 expression in adenocarcinomas and squamous cell carcinomas and clinicopathological characteristics.

Baseline clinicopathological characteristics	Adenocarcinoma	p-value	Squamous cell carcinoma	p-value
Age: <60 ≥60	 3.837±1.686 0.291±0.247	 **0.0089**	 8.428±0.828/ 8.100±1.587	 0.2192
Sex: Female Male	 1.528±0.878 1.807±1.117	 0.1220	 2.601±0.321 8.580±0.744	 0.1480
Stage: IA-IIA IIB-IIIB	 1.762±1.384 1.675±0.954	 0.6670	 8.785±1.434 8.086±0.920	 0.5170
Category T: T1b-2a T2b-4	 3.171±1.983 0.923±0.502	 **0.0040**	 9.091±0.834 7.370±1.727	 1.0000
Category N: N0 N1-2	 1.307±0.855 2.457±1.599	 0.5070	 9.136±0.982 7.481±1.149	 0.0700
Smoking status: Never smokers Current or former smokers	 0.657±0.450 2.276±1.152	 0.1220	 2.611±0.102 8.815±0.742	 0.1480

Relationship between GLUT1 expression, NSCLC histology, and patients' clinicopathological characteristics. GLUT1 overexpression was observed more in squamous cell carcinomas than in adenocarcinomas (p=0.0001). Among patients with lung adenocarcinomas and squamous cell carcinomas, 10 % (2 of 20) and 50 % (11 of 22) of patients had high GLUT1, respectively. The average IHS of the studied cohort was 5.161±0.721. In patients with adenocarcinomas, the level of GLUT1 expression depended on age and T category. It is worth noting that GLUT1 expression in all patients with adenocarcinomas was low and did not reach the mean value of IHS for the studied cohort. However, higher GLUT1 expression was reported in patients younger than 60 and with categories T1b-2a. In patients with squamous cell carcinomas, GLUT1 expression was not associated with the studied clinicopathological characteristics (Table 2).

Relationship between GLUT1 expression and survival in patients with radically treated NSCLC. The median follow-up period was 57.92±4.23 months. The recurrence of the disease was registered in 19 patients. Nineteen patients died. In eighteen patients, death was related to lung cancer recurrence. One patient died of other causes. Cox regression analysis demonstrated that the T category, N category, and smoking impact recurrent-free survival. Patients with categories T1b-2a, without metastases in the lymph nodes, and non-smokers have better recurrence-free survival (Table 3).

Multivariable analysis showed that independent predictors of overall survival were category T, category N, age, and smoking status. Patients with categories T1b-2a, without lymph node metastases, younger than 60, and non-smokers have better overall survival (Table 4).

Kaplan-Meier curves showed a trend toward better recurrence-free survival in patients with high GLUT1. However, no statistically significant differences were found between the groups with high and low GLUT1 (Log-rank p=0.3284; Fig. 2).

Similar results were obtained during the analysis of overall survival. Patients with high GLUT1 tend to have a better prognosis. However, no statistically significant differences were found between the groups with high and low GLUT1 (Log-rank p=0.7161; Fig. 3).

Table 3. Multivariable analysis of the impact of clinical and pathological characteristics on recurrence-free survival.

Clinicopathological characteristic	Hazard ratio	95 % CI	p-value
Age (<60 versus ≥60)	2.23	0.89-5.56	0.0860
Sex (female versus male)	2.08	0.06-1.28	0.5710
Stage (IA-IIA versus IIB-IIIB)	0.29	0.6670	0.1050
Category T (T1b-2a versus T2b-4)	30.62	3.03-309.43	**0.0040**
Category N (N0 versus N1-2)	37.74	5.07-280.74	**0.0001**
Histology (adenocarcinoma versus squamous cell carcinoma)	2.70	0.86-8.42	0.0870
Smoking status (never smokers versus current or former smokers	11.18	1.12-111.13	**0.0390**
GLUT1 (low versus high)	1.96	0,44-8,64	0.3740

Table 4. Multivariable analysis of the impact of clinical and pathological characteristics on overall survival.

Clinicopathological characteristic	Hazard ratio	95 % CI	p-value
Age (<60 versus ≥60)	3.21	1.29-8.02	0.0120
Sex (female versus male)	2.22	0.08-58.22	0.6310
Stage (IA-IIA versus IIB-IIIB)	0.39	0.09-1.61	0.1960
Category T (T1b-2a versus T2b-4)	98.51	9.10-1065.6	**9.10-1065.6**
Category N (N0 versus N1-2)	29.85	3.93-226.33	3.93-226.33
Histology (adenocarcinoma versus squamous cell carcinoma)	3.16	0.89-11.16	0.0740
Smoking status (never smokers versus current or former smokers	28.96	1.43-584.99	**0.0280**
GLUT1 (low versus high)	2.79	0.67-11.66	0.1580

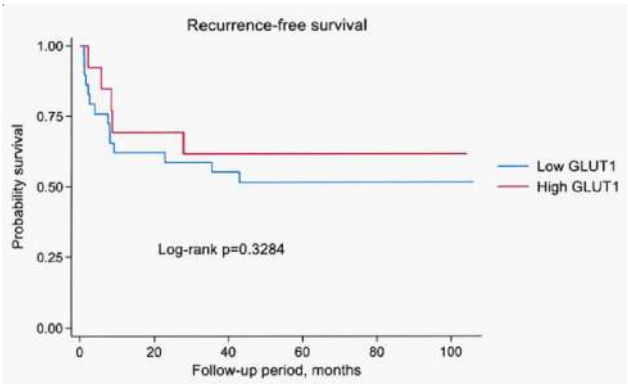

Fig. 2. Kaplan-Meier curves show recurrence-free survival of patients with low and high GLUT1 expression.

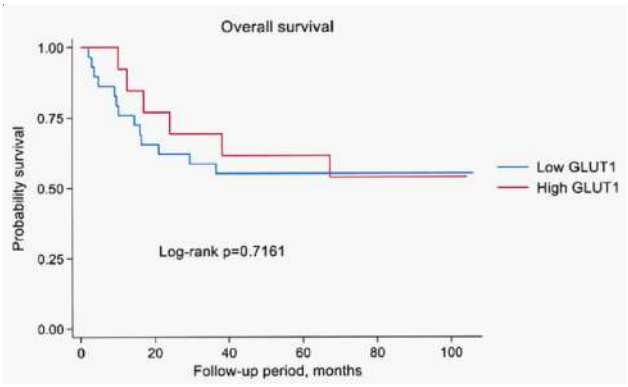

Fig. 3. Kaplan-Meier curves show patients' overall survival with low and high GLUT1 expression.

During the follow-up period, eight patients with adenocarcinoma and eleven patients with squamous cell carcinomas died. 7 of 8 patients with adenocarcinoma and 6 of 11 with squamous cell carcinoma had low GLUT1. Kaplan-Meier curves show a trend toward better overall survival in patients with low GLUT1 and adenocarcinoma. However, no statistically significant difference in the survival of patients was found (Log-rank p=0.8881; Fig. 4).

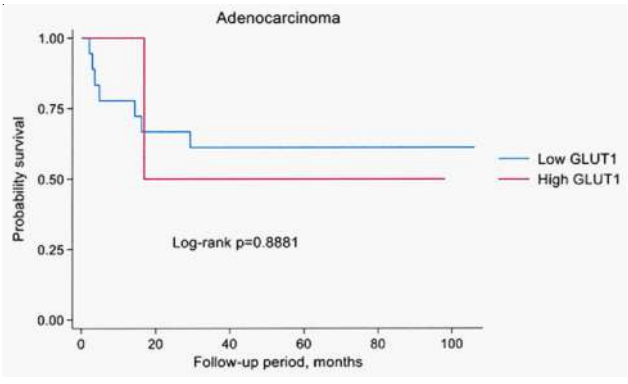

Fig. 4. Kaplan-Meier curves showing overall survival in patients with lung adenocarcinomas depending on GLUT1 expression.

For squamous cell carcinomas, there is a trend toward better survival in patients with high GLUT1, although there is also no significant difference between groups (Log-rank p=0.3160; Fig. 5).

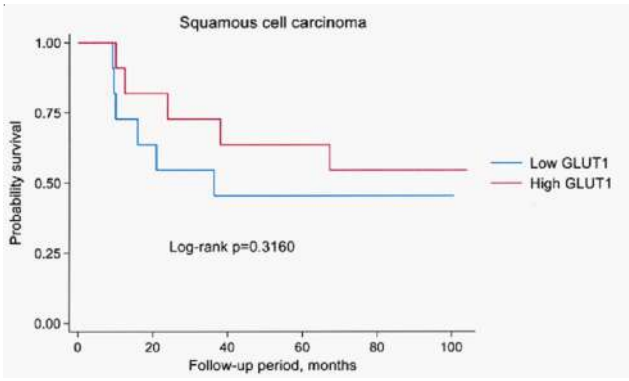

Fig. 5. Kaplan-Meier curves showing overall survival in patients with squamous cell carcinomas depending on GLUT1 expression.

Discussion

The current study found that GLUT1 expression correlates with NSCLC histology, sex, and smoking status. GLUT1 overexpression is significantly more common in squamous cell carcinomas than in adenocarcinomas. We have shown that GLUT1 expression does not impact recurrence-free and overall survival in patients with radically treated NSCLC.

Our results coincide with the findings of Tan Z. et al. [22], who, in their meta-analysis, found that GLUT1 overexpression is more associated with squamous cell carcinomas and correlates with gender. GLUT1 overexpression was correlated with poor survival in patients with lung adenocarcinomas. It is worth noting that most of the studies devoted to the impact of GLUT1 expression on survival were conducted on the Asian population [5, 11, 14]. At the same time, no statistically significant difference in patient survival was found in Caucasians [4]. The current study also found no correlation between GLUT1 expression and survival. This may be due to the ethnic characteristics and limitations of this study, such as the small sample size and heterogeneity of patients concerning histological diagnosis and tumor stage.

This study found a correlation between smoking and GLUT1 expression. Q. Zhang et al. [29] attributed this phenomenon to the stimulatory effect of nicotine on hypoxia-inducible factor-alpha (HIF-1ϐ), which closely enhances GLUT1 expression. It is believed that through the activation of acetylcholine receptors, nicotine causes metabolic reprogramming of cells and affects the redox balance in the tumor, changing the pH in NSCLC cells [16].

It is essential that, in addition to influencing the metabolism of tumor cells, GLUT1 and HIF1ϐ are also co-expressed in cells of the immune microenvironment, including in tumor-associated macrophages. HIF-1ϐ can induce macrophage polarization. Suppression of GLUT1 expression, on the contrary, can block this process. In addition, SLC2A1 (the gene encoding GLUT1) is negatively associated with other immune checkpoints, including PD-1, T cell receptor to Ig and ITIM domains (TIGIT), cytotoxic T lymphocyte-associated protein 3 (CTLA4) and LAG3, but

positively correlated with the level of CD44 expression [10].

The heterogeneity of GLUT1 expression in adenocarcinomas has both genetic and epigenetic determinants. S. K. Do et al. [7] showed that single-nucleotide variants significantly affect the overall survival of patients with squamous cell lung carcinomas but do not affect this indicator in adenocarcinomas. In addition, Contact C. et al. [6] found that lung adenocarcinoma is characterized by the presence of two glucose transporters, GLUT1 and GLUT3; therefore, when searching for predictive markers and vectors for the targeted action of new drugs, it is essential to take into account the expression of both glucose transporters. Y. Nakanishi et al. [19] also showed that GLUT4 can influence GLUT3 expression and survival in patients with NSCLC.

Given the expression of different GLUT types in NSCLC cells, it seems logical that regression analysis did not identify GLUT1 as an independent prognostic factor for recurrence-free and overall survival. However, it is promising to study the influence of GLUT1 gene expression and polymorphism on the effectiveness of chemotherapy, radiation therapy, and targeted therapy with tyrosine kinase inhibitors [2, 12].

Conclusions

1. GLUT1 overexpression is associated with squamous cell lung carcinomas. In patients with adenocarcinomas, the level of GLUT1 expression depended on age and T category, while GLUT1 expression in squamous cell carcinomas was not associated with the studied clinicopathological characteristics.

2. GLUT1 expression has no prognostic value and does not correlate with recurrence-free and overall survival in radically treated patients with NSCLC.

References

[1] Attur, S. K., Patel, A., & Attur, K. M. (2024). Study of expression of GLUT-1 in oral potentially malignant disorders and oral squamous cell carcinoma: An immuno-histochemical analysis. *Journal of Oral and Maxillofacial Pathology: JOMFP,* 28(1), 70-76. doi: 10.4103/jomfp.jomfp_474_23

[2] Bahremani, M., Rashtchizadeh, N., Sabzichi, M., Vatankhah, A. M., Danaiyan, S., Poursistany, H., … & Ghorbanihaghjo, A. (2023). Enhanced chemotherapeutic efficacy of docetaxel in human lung cancer cell line via GLUT1 inhibitor. *Journal of Biochemical and Molecular Toxicology,* 37(6), e23348. doi: 10.1002/jbt.23348

[3] Cao, S., Chen, Y., Ren, Y., Feng, Y., & Long, S. (2021). GLUT1 biological function and inhibition: research advances. *Future Medicinal Chemistry,* 13(14), 1227-1243. doi: 10.4155/fmc-2021-0071

[4] Chen, J., Yang, H., Teo, A. S. M., Amer, L. B., Sherbaf, F. G., Tan, C. Q., … & Zhai, W. (2020). Genomic landscape of lung adenocarcinoma in East Asians. *Nature Genetics,* 52(2), 177-186. doi: 10.1038/s41588-019-0569-6

[5] Chen, L., Zhang, L., He, H., Shao, F., Yu, Z., Gao, Y., & He, J. (2024). Ubiquitin-specific protease 54 regulates GLUT1-mediated aerobic glycolysis to inhibit lung adenocarcinoma progression by modifying p53 degradation. *Oncogene,* 43(26), 2025-2037. doi: 10.1038/s41388-024-03047-8

[6] Contat, C., Ancey, P. B., Zangger, N., Sabatino, S., Pascual, J., Escrig, S., … & Meylan, E. (2020). Combined deletion of Glut1 and Glut3 impairs lung adenocarcinoma growth. *eLife,* 9, e53618. doi: 10.7554/eLife.53618

[7] Do, S. K., Jeong, J. Y., Lee, S. Y., Choi, J. E., Hong, M. J., Kang, H. G., … & Park, J. Y. (2018). Glucose Transporter 1 Gene Variants Predict the Prognosis of Patients with Early-Stage Non-small Cell Lung Cancer. *Annals of Surgical Oncology,* 25(11), 3396-3403. doi: 10.1245/s10434-018-6677-1

[8] Du, D., Liu, C., Qin, M., Zhang, X., Xi, T., Yuan, S., Hao, H., & Xiong, J. (2022). Metabolic dysregulation and emerging therapeutical targets for hepatocellular carcinoma. *Acta Pharmaceutica Sinica B,* 12(2), 558-580. doi: 10.1016/j.apsb.2021.09.019

[9] Ferreira, E., Ferreira, D., Relvas-Santos, M., Freitas, R., Soares, J., Azevedo, R., … & Ferreira, J. A. (2024). Aberrantly Glycosylated GLUT1 as a Poor Prognosis Marker in Aggressive Bladder Cancer. *International Journal of Molecular Sciences,* 25(6), 3462. doi: 10.3390/ijms25063462

[10] Hao, B., Dong, H., Xiong, R., Song, C., Xu, C., Li, N., & Geng, Q. (2024). Identification of SLC2A1 as a predictive biomarker for survival and response to immunotherapy in lung squamous cell carcinoma. *Computers in Biology and Medicine,* 171, 108183. doi: 10.1016/j.compbiomed.2024.108183

[11] Ito, R., Yashiro, M., Tsukioka, T., Izumi, N., Komatsu, H., Inoue, H., … & Nishiyama, N. (2023). GLUT1 and PKM2 may be useful prognostic predictors in patients with non-small cell lung cancer following curative R0 resection. *Oncology Letters,* 25(3), 129. doi: 10.3892/ol.2023.13715

[12] Kang, M. K., Lee, S. Y., Choi, J. E., Baek, S. A., Do, S. K., Lee, J. E., … & Park, J. Y. (2021). Prognostic significance of genetic variants in GLUT1 in stage III non-small cell lung cancer treated with radiotherapy. *Thoracic Cancer,* 12(6), 874-879. doi: 10.1111/1759-7714.13851

[13] Kim, B. W., Cho, H., Chung, J. Y., Conway, C., Ylaya, K., Kim, J. H., & Hewitt, S. M. (2013). Prognostic assessment of hypoxia and metabolic markers in cervical cancer using automated digital image analysis of immunohistochemistry. *Journal of Translational Medicine,* 11, 185. doi: 10.1186/1479-5876-11-185

[14] Koh, Y. W., Lee, S. J., & Park, S. Y. (2017). Differential expression and prognostic significance of GLUT1 according to histologic type of non-small-cell lung cancer and its association with volume-dependent parameters. *Lung Cancer* (Amsterdam, Netherlands), 104, 31-37. doi: 10.1016/j.lungcan.2016.12.003

[15] Koike, Y., Aokage, K., Ikeda, K., Nakai, T., Tane, K., Miyoshi, T., … & Ishii, G. (2020). Machine learning-based histological classification that predicts recurrence of peripheral lung squamous cell carcinoma. *Lung Cancer* (Amsterdam, Netherlands), 147, 252-258. doi: 10.1016/j.lungcan.2020.07.011

[16] Kokeza, J., Strikic, A., Ogorevc, M., Kelam, N., Vukoja, M., Dilber, I., & Zekic, T. S. (2023). The Effect of GLUT1 and HIF-1α Expressions on Glucose Uptake and Patient Survival in Non-Small-Cell Lung Carcinoma. *International Journal of Molecular Sciences,* 24(13), 10575. doi: 10.3390/ijms241310575

[17] Kumari, A., Jha, A., Tiwari, A., Nath, N., Kumar, A., Nagini, S., & Mishra, R. (2023). Role and regulation of GLUT1/3 during oral cancer progression and therapy resistance. *Archives of Oral Biology,* 150, 105688. doi: 10.1016/j.archoralbio.2023.105688

[18] Lai, X., Liu, X., Cai, X., & Zou, F. (2022). Vitamin D

supplementation induces CatG-mediated CD4+ T cell inactivation and restores pancreatic β-cell function in mice with type 1 diabetes. *American Journal of Physiology. Endocrinology and Metabolism*, 322(1), E74-E84. doi: 10.1152/ajpendo.00066.2021

[19] Nakanishi, Y., Iwai, M., Hirotani, Y., Kato, R., Tanino, T., Nishimaki-Watanabe, H., … & Sasaki-Fukatsu, K. (2023). Correlations between class I glucose transporter expression patterns and clinical outcomes in non-small cell lung cancer. *Thoracic Cancer,* 14(27), 2761-2769. doi: 10.1111/1759-7714.15060

[20] Shriwas, P., Roberts, D., Li, Y., Wang, L., Qian, Y., Bergmeier, S., … & Chen, X. (2021). A small-molecule pan-class I glucose transporter inhibitor reduces cancer cell proliferation in vitro and tumor growth in vivo by targeting glucose-based metabolism. *Cancer & Metabolism*, 9(1), 14. doi: 10.1186/s40170-021-00248-7

[21] Szulc, A., & Wozniak, M. (2024). Targeting Pivotal Hallmarks of Cancer for Enhanced Therapeutic Strategies in Triple-Negative Breast Cancer Treatment-In Vitro, In Vivo and Clinical Trials Literature Review. *Cancers,* 16(8), 1483. doi: 10.3390/cancers16081483

[22] Tan, Z., Yang, C., Zhang, X., Zheng, P., & Shen, W. (2017). Expression of glucose transporter 1 and prognosis in non-small cell lung cancer: a pooled analysis of 1665 patients. *Oncotarget,* 8(37), 60954-60961. doi: 10.18632/oncotarget.17604

[23] Wang, B., & Pu, R. (2023). Association between glycolysis markers and prognosis of liver cancer: a systematic review and meta-analysis. *World Journal of Surgical Oncology,* 21(1), 390. doi: 10.1186/s12957-023-03275-4

[24] Wang, N., Zhang, S., Yuan, Y., Xu, H., Defossa, E., Matter, H., glucose transporters by exofacial inhibitors. *Nature communications,* 13(1), 2632. doi: 10.1038/s41467-022-30326-3

[25] Warburg, O. (1956). On the origin of cancer cells. *Science* (New York, N.Y.), 123(3191), 309-314. doi: 10.1126/science.123.3191.309

[26] Weljie, A. M., & Jirik, F. R. (2011). Hypoxia-induced metabolic shifts in cancer cells: moving beyond the Warburg effect. *The International Journal of Biochemistry & Cell Biology,* 43(7), 981-989. doi: 10.1016/j.biocel.2010.08.009

[27] Wu, L., Jin, Y., Zhao, X., Tang, K., Zhao, Y., Tong, L., … & Pan, D. (2023). Tumor aerobic glycolysis confers immune evasion through modulating sensitivity to T cell-mediated bystander killing via TNF-α. *Cell Metabolism,* 35(9), 1580-1596. doi: 10.1016/j.cmet.2023.07.001

[28] Yao, C. C., Sun, R. M., Yang, Y., Zhou, H. Y., Meng, Z. W., Chi, R., … & Wang, Y. (2023). Accumulation of branched-chain amino acids reprograms glucose metabolism in CD8+ T cells with enhanced effector function and anti-tumor response. *Cell Reports,* 42(3), 112186. doi: 10.1016/j.celrep.2023.112186

[29] Zhang, Q., Tang, X., Zhang, Z. F., Velikina, R., Shi, S., & Le, A. D. (2007). Nicotine induces hypoxia-inducible factor-1alpha expression in human lung cancer cells via nicotinic acetylcholine receptor-mediated signaling pathways. *Clinical Cancer Research: an Official Journal of the American Association for Cancer Research,* 13(16), 4686-4694. doi: 10.1158/1078-0432.CCR-06-2898

[30] Zhou, Z., Li, Y., Chen, S., Xie, Z., Du, Y., Liu, Y., … & Chen, G. (2024). GLUT1 promotes cell proliferation via binds and stabilizes phosphorylated EGFR in lung adenocarcinoma. *Cell Communication and Signaling: CCS*, 22(1), 303. doi: 10.1186/s12964-024-01678-8

ЕКСПРЕСІЯ GLUT1 У ПАЦІЄНТІВ З НЕДРІБНОКЛІТИННИМ РАКОМ ЛЕГЕНЬ ТА ЇЇ ВПЛИВ НА ВИЖИВАНІСТЬ

Винниченко О. І., Москаленко Ю. В., Язиков О. В., Селезньов О. О., Сулаєва О. М., Москаленко Р. А.

GLUT1 є ключовим транспортером глюкози, експресія котрого збільшується в пухлинних клітинах, особливо за умов гіпоксії, і корелює з прискоренням їх проліферації. Метою даного дослідження було вивчити зв`язок між експресією GLUT1 та біологічними параметрами та оцінити потенційний вплив на виживаність у пацієнтів з радикально пролікованим недрібноклітинним раком легень (НДКРЛ). Для проведення дослідження було залучено 42 пацієнта, котрі отримали радикальне лікування НДКРЛ. При аналізі даних враховували стать, вік, історію паління, стадію захворювання та гістологічний тип пухлини. Для оцінки ступеня гіпоксії застосовували антитіла до GLUT1. Для підрахунку використовували напівкількісну імуногістохімічну шкалу з діапазоном від 0 до 12. Chi2 тест та t-критерій Стьюдента використовували для порівняння категоріальних та параметричних змінних. Модель пропорційних ризиків Кокса, метод Каплана-Майєра та Log-rank тест застосовували для оцінювання впливу експресії GLUT1 на виживаність. Результати вважали статистично значущими при p<0,05. Кореляція середнього ступеня виявлена між експресією GLUT1 та гістологічним типом НДКРЛ (r=0,432, p<0,0001), статтю (r=0,336, p<0,0009) та палінням (r=0,325, p<0,0009). Гіперекспресію GLUT1 спостерігали здебільшого в плоскоклітинних карциномах, ніж в аденокарциномах (p=0,0001). У пацієнтів з аденокарциномами рівень експресії GLUT1 залежав від віку та категорії Т. У пацієнтів з плоскоклітинними карциномами експресія GLUT1 не була повязана з досліджуваними клініко-патологічними характеристиками. Кращу виживаність мали пацієнти з категоріями T1b-2a, без метастазів у регіонарних лімфатичних вузлах, віком молодше 60 років та ті, що не палили. Криві Каплана-Майєра продемонстрували відсутність статистично достовірних відмінностей у безрецидивній виживаності та загальній виживаності між групами з високим та низьким GLUT1 (Log-rank p=0,3284 та Log-rank p=0,7161 відповідно). Таким чином, гіперекспресія GLUT1 асоційована з плоскоклітинними карциномами легень. Експресія GLUT1 не має прогностичного значення та не корелює з безрецидивною та загальною виживаністю у радикально пролікованих пацієнтів з НДКРЛ.

Ключові слова: *GLUT1, рак легень, виживаність, аденокарцинома.*

Author's contribution

Vynnychenko O. I. – conceptualization, research, methodology and original project writing.
Moskalenko Yu. V. – data visualization, software.
Yazykov O. V. – data visualization, software.
Seleznov O. O. – validation.
Sulaieva O. M. – review writing and editing.
Moskalenko R. A. – review writing and editing, formal analysis, project administration, supervision.

DOI: 10.31393/morphology-journal-2024-30(4)-04 Reports of Morphology, Vol. 30, №4, Pages 29-43

ISSN 1818-1295 eISSN 2616-6194

REPORTS OF MORPHOLOGY

Official Journal of the Scientific Society of Anatomists, Histologists, Embryologists and Topographic Anatomists of Ukraine

journal homepage: https://morphology-journal.com

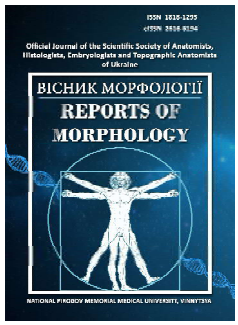

Modeling the parameters necessary for constructing the correct shape of the dental arch depending on the features of teleradiometric indicators using the Steiner or Tweed methods and computed tomography dimensions of teeth in Ukrainian young men and young women with physiological occlusion

Ryabov T. V., Shinkaruk-Dykovytska M. M., Pylypiuk O. Yu., Muntian O. V., Drachevska I. Yu., Rokunets I. L., Burdeina L. V.

National Pirogov Memorial Medical University, Vinnytsya, Ukraine

ARTICLE INFO

Received: 12 March 2024

Accepted: 3 September 2024

UDC: 616.314.26:616.714.1-053.81-73.75

CORRESPONDING AUTHOR

e-mail: dr.riabov1989@gmail.com

Ryabov T. V.

CONFLICT OF INTEREST

The authors have no conflicts of interest to declare.

FUNDING

Not applicable.

DATA SHARING

Data are available upon reasonable request to corresponding author.

The study of the parameters of the dental arch, taking into account teleradiometric indicators and tooth sizes, is important for planning orthodontic treatment, which contributes to achieving stable and functionally optimal results. The Steiner and Tweed methods, widely used to assess craniofacial proportions, allow identifying key anthropometric features that affect the shape of the dental arch. The additional use of computed tomography measurements provides high accuracy in analyzing tooth sizes, which is especially important for individualizing orthodontic approaches. The aim of the work is to build and analyze regression models of parameters necessary for constructing the correct shape of the dental arch in Ukrainian young men and young women with physiological occlusion, depending on the features of teleradiometric indicators according to the Steiner or Tweed methods and computed tomography sizes of the teeth. On standardly obtained teleradiograms and created in the 3D Slicer v5.4.0 software on teleradiograms with points marked on 3D objects (41 Ukrainian young men and 68 young women with physiological occlusion from the data bank of the Department of Pediatric Dentistry and the Scientific and Research Center of the National Pirogov Memorial Medical University, Vinnytsya), measurements according to the Steiner S. S. and Tweed C. H. methods were carried out in the OnyxCeph³™ application, version 3DPro, from Image Instruments GmbH, Germany. On computer tomograms for morphometric study of teeth and dental arches we used software applications i-Dixel One Volume Viewer (Ver.1.5.0) J Morita Mfg. Cor, and Planmeca Romexis Viewer (ver. 3.8.3.R 15.12.14) Planmeca OY. Regression models were built using the licensed package "Statistica 6.0". It was found that in young men, taking into account the Steiner method, all 18 possible reliable models with a coefficient of determination greater than 0.6 were built (R^2= from 0.611 to 0.911, p<0.001), and taking into account the Tweed method, 17 models (R^2= from 0.638 to 0.872, p<0.001); and young women only 5 reliable models with a coefficient of determination greater than 0.6 when taking into account the Steiner method (R^2= from 0.613 to 0.782, p<0.001) and only 4 reliable models when taking into account the Tweed method (R^2= from 0.619 to 0.745, p<0.001). When analyzing the frequency of occurrence in the regression equations of computed tomography sizes of teeth and teleradiometric indicators according to the Steiner or Tweed methods, it was established: in young men, the width of the crown part of the tooth in the mesio-distal and vestibulo-oral planes, the length of the tooth in the mesio-distal and vestibulo-oral planes and teleradiometric indicators are most often included in the models; and in young women: when taking into account the indicators according to the Steiner method - the width of the crown part of the tooth in the mesio-distal and vestibulo-oral plane and teleradiometric indicators; when taking into account the indicators according to the Tweed method - the width of the crown part of the tooth in the mesio-distal and vestibulo-oral plane, the length of the tooth in the mesio-distal and

vestibulo-oral planes, teleradiometric indicators and the length of the crown part of the tooth in the mesio-distal plane. When analyzing the frequency of occurrence in the regression equations of the corresponding teeth, it was found that in young men, the models that take into account the teleradiometric indicators according to the Steiner or Tweed methods most often include the upper and lower incisors, upper and lower premolars and upper canines; and in young women upper and lower incisors, upper and lower canines, lower premolars and upper first molars taking into account teleradiometric indicators according to the Steiner method, as well as upper and lower incisors and lower premolars taking into account teleradiometric indicators according to the Tweed method.

Keywords: *dentistry, teleradiometry according to the Steiner and Tweed methods, computed tomography dimensions of teeth and dental arches, regression analysis, Ukrainian young men and young women, physiological occlusion.*

Introduction

Modeling of dental arch parameters based on teleradiometric indicators and computed tomography measurements is an important aspect of modern orthodontics. In particular, the study of the dependence of the shape of the dental arch on anatomical and functional characteristics contributes to the development of individualized approaches to treatment. In this context, the use of Steiner and Tweed methods for the analysis of teleradiograms and cone-beam computed tomography data provides high accuracy in assessing the position of the teeth and jaws in space. The prevalence of dentition and occlusion anomalies is a significant factor determining the need for in-depth study of dental arch parameters. For example, a study in Turkey found that the frequency of anomalies such as macrodentia and microdentia is 13.2 %, and supernumerary teeth occur in 1.8 % of the population [6]. At the same time, in the French population, the frequency of anomalies reaches 27 %, with hypodontia being the most common disorder [8]. In a systematic review by Khalaf K. et al. [16], hypodontia had an average frequency of 6.4 %, with variations depending on the region and ethnic group [16]. A study of the prevalence of anomalies such as supernumerary teeth indicated that their frequency varied from 0.1 % to 3.8 %, depending on the population and diagnostic methods. In particular, a systematic review by Ata-Ali F. et al. [7] highlighted that these anomalies often lead to changes in the shape of the dental arch, especially in the anterior region. The presence of supernumerary teeth is also correlated with an increased risk of crowding of the dentition, which complicates the modeling process. A study by Herrera-Atoche J. R. et al. [14] in a Mexican population found that 19.5 % of the subjects had at least one dental anomaly. The most common were hypodontia and macrodontia, which in turn affect the width and symmetry of the dental arch.

Of particular interest are the parameters of the dental arch in individuals with normal occlusion, as they are the standard for orthodontic treatment. A study by Paranhos et al. found that the shape of the dental arch is closely related to the type of face: dolichocephalic individuals more often have a narrowed arch shape, while brachycephalic individuals have a wider one [22]. This confirms the importance of taking into account individual anthropometric characteristics when modeling the arch.

Data from Goncalves-Filho A. J. et al. [12] indicate that the presence of anomalies, such as fused teeth or root displacement, significantly affects the shape of the arch. For example, 3.1 % of patients with dental anomalies had pronounced arch asymmetry. In addition, a study by Shilpa G. et al. [27] showed that the frequency of anomalies in the temporary bite can reach 18.3 %, and these disorders often affect the parameters of the permanent bite.

The dependence of the arch shape on teleradiometric indicators has been widely studied in clinical studies. According to the results of Saghiri M. A. et al. [23], the arch shape largely depends on the ratio of the anterior-posterior and transverse parameters of the jaws, and indicators such as ANB are key in determining the harmony of the arch. At the same time, Muhamad A. H. et al. [20] indicate the stability of the dental arch curve in patients with a normal bite, with an average width of 33.4±1.5 mm in the frontal region.

The issue of modeling the shape of the dental arch also includes the study of the relationship with the parameters of the crowns. According to Lagana G. et al. [17], an increase in the width of the incisors by 1 mm can cause a change in the arch parameters by 0.8-1.1 mm. A systematic review conducted by Lombardo G. et al. [18] found that the prevalence of various forms of arch anomalies ranges from 11.6 % in children to 39.1 % in adults.

Thus, the analysis of the characteristics of the dental arch parameters in individuals with physiological occlusion is an important task for the development of optimal diagnostic and treatment algorithms.

The purpose of the study is to construct and analyze regression models of parameters necessary for constructing the correct shape of the dental arch in Ukrainian young men and young women with physiological occlusion, depending on the characteristics of teleradiometric indicators according to the Steiner or Tweed methods and computed tomography dimensions of the teeth.

Materials and methods

Primary computed tomography scans of 41 Ukrainian young men (aged 17 to 21) and 68 Ukrainian young women

(aged 16 to 20) with a physiological bite that was as close as possible to orthognathic were obtained from the data bank of the Department of Pediatric Dentistry and the Research Center of the National Pirogov Memorial Medical University, Vinnytsya. All teleradiography (using the Veraviewepocs 3D Morita dental cone-beam tomograph, Japan) and computed tomography (using the Planmeca ProMax 3D Mid dental cone-beam tomograph, Finland) studies were conducted on the basis of the principle of voluntary informed consent in the private dental clinic "Vinintermed" and in the "Planmeca 3D Maxillofacial Diagnostics Center". The Bioethics Committee of the National Pirogov Memorial Medical University, Vinnytsya (protocol No. 7 dated 8.11.2022) established that the conducted studies do not contradict the basic bioethical norms of the Declaration of Helsinki, the Council of Europe Convention on Human Rights and Biomedicine (1977), the relevant provisions of the WHO and the laws of Ukraine.

On standardly obtained teleradiograms and teleradiograms created in the 3D Slicer v5.4.0 software with points marked on 3D objects, measurements were performed using the method of Steiner S. S. [29] and Tweed C. H. [30] in the OnyxCeph³™ application, version 3DPro, from Image Instruments GmbH, Germany.

According to the Steiner method, the following angular and linear indicators were determined (Fig. 1, 2): **SNA_S angle** – characterizes the position of the anterior contour of the upper jaw in the sagittal plane (°); **SNB_S angle** – characterizes the position of the anterior contour of the chin, in the sagittal plane (°); **ANB_S angle** – characterizes the position of the lower jaw relative to the upper jaw in the sagittal plane (°); **SND angle** – characterizes the position of the center of the chin, in the sagittal plane (°); **SN-OcP angle** – characterizes the inclination of the occlusal plane relative to the anterior cranial base S-N (°); **SN-GoGn angle** – characterizes the inclination of the body of the lower jaw relative to the anterior cranial base S-N (°); **II angle (interincisor angle)** – characterizes the inclination of the upper and lower central incisors relative to each other (°); **Max1-NA angle** – characterizes the position of the upper central incisor to the N-A line (°); **angle Max1-SN** – characterizes the position of the central incisor to the anterior cranial base S-N (°); **angle Mand1-NB** – characterizes the position of the lower central incisor to the N-B line (°); **distance 1u-NA** – characterizes the position of the crown of the upper central incisor in the sagittal plane relative to the N-A line (mm); **distance 1l-NB** – characterizes the position of the crown of the lower central incisor in the sagittal plane relative to the N-B line (mm); **distance Pog-NB** – required to determine the Holdaway ratio (mm); **Holdaway Ratio** – the difference between the values of the 1l-NB and Pog-NB indicators, characterizes the position of the crown of the lower central incisor in the sagittal plane relative to the bone chin Pog (mm); **distance S-L** – characterizes the position of the anterior contour of the lower jaw (mm); **distance S-E** length of the posterior part of the base of the skull according to Steiner (mm).

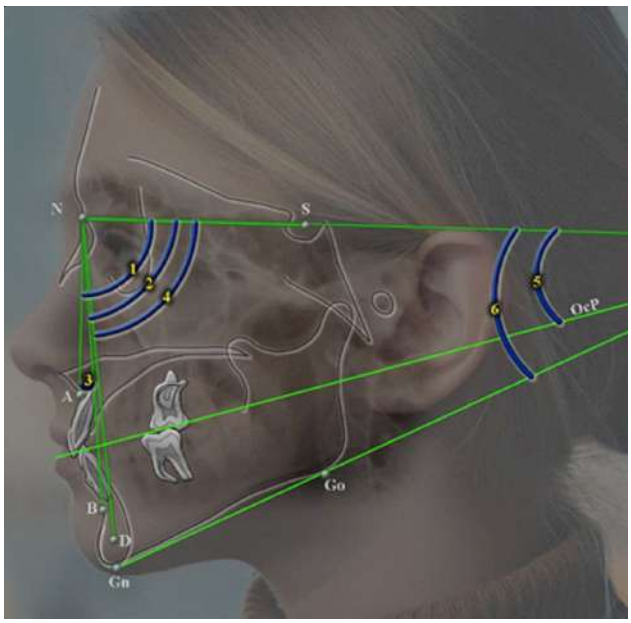

Fig. 1. Measurement according to the Steiner method. 1 – angle SNA_S, 2 – angle SNB_S, 3 – angle ANB_S, 4 – angle SND, 5 – angle SN-OcP, 6 – angle SN-GoGn.

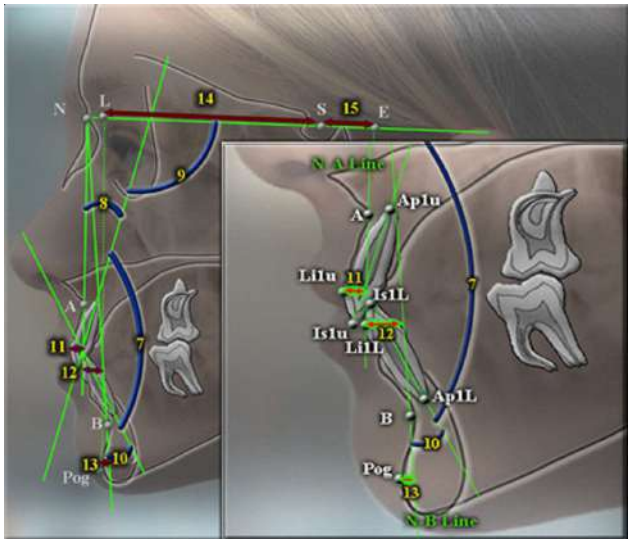

Fig. 2. Measurement according to the Steiner method. 7 – angle II, 8 – angle Max1-NA, 9 – angle Max1-SN, 10 – angle Mand1-NB, 11 – distance 1u-NA, 12 – distance 1l-NB, 13 – distance Pog-NB, 14 – distance S-L, 15 – distance S-E.

According to the Tweed method, the following angular and linear indicators were determined (Fig. 3-5): **IMPA angle** – the angle of the incisal plane of the lower jaw, formed by the central axis of the lower central incisor and the mandibular plane MP (°); **FMA angle** – the Frankfurt mandibular angle, formed by the mandibular plane and the Frankfurt plane FP (°); **FMIA angle** – the Frankfurt angle of the mandibular incisor, the central axis of the lower central

incisor and the Frankfurt plane FP (°); **SNA_T angle** – formed by the lines S-N and N-A (indicates the anterior-posterior location of the upper jaw to the base of the skull) (°); **SNB_T angle** – formed by the lines S-N and N-B (indicates the anterior-posterior location of the lower jaw to the base of the skull) (°); **angle ANB_T** – formed by lines A-N and N-B (indicates the angular inter-jaw relationship in the anterior-posterior direction; considered positive if point A is in front of line NB; if lines NA and NB overlap, the angle is 0°; if point A is behind line NB, the angle is considered negative) (°); **angle POr_OcP** – formed by the occlusal plane OclP

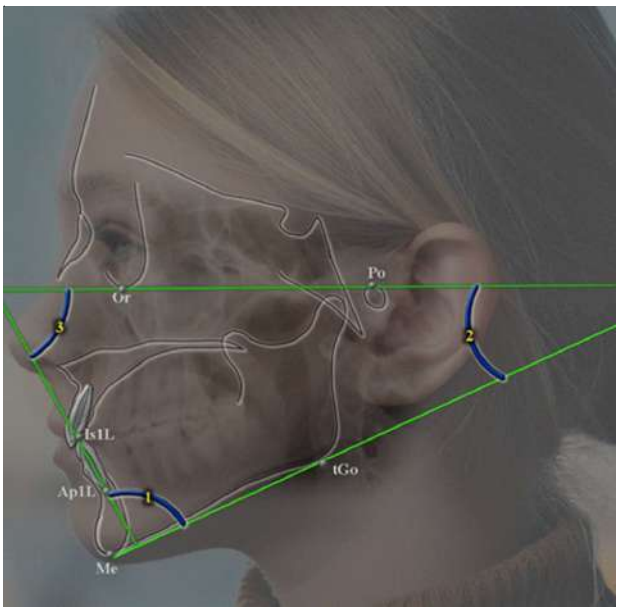

Fig. 3. Measurements according to the Tweed method. 1 – IMPA angle, 2 – FMA angle, 3 – FMIA angle.

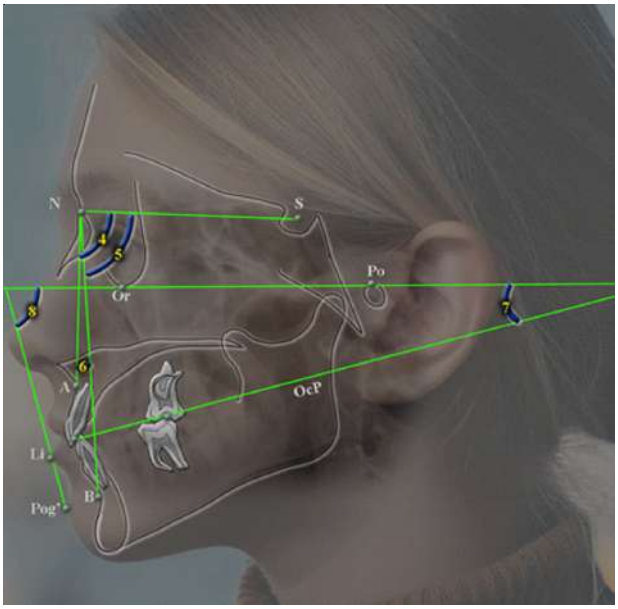

Fig. 4. Measurement according to the Tweed method. 4 – angle SNA_T, 5 – angle SNB_T, 6 – angle ANB_T, 7 – angle POr_OcP, 8 – angle Z.

and the Frankfurt plane FP (°); **angle Z** – the angle between the soft tissue profile, which is determined by the mandibular-labial line and the Frankfurt plane FP (°); **Wits index** – the distance between the projections of the corresponding points A and B on the occlusal plane OclP, indicates the linear inter-jaw relationship in the anterior-posterior direction (if the projection of point A is in front of the projection of point B, then the index takes a positive value; if the projection of point A is behind the projection of point B, then the index takes a negative value) (mm); **AFH distance** – the anterior height of the face (distance from the lowest point on the symphysis of the lower jaw and the plane of the base of the upper jaw SpP) (mm); **PFH distance** – the posterior height of the face (distance from point Ar to point tGo) (mm); **Ls1u_Ls distance** – the thickness of the upper lip (distance from point Ls1u to point Ls) (mm); **Pog_Pog' distance** – the thickness of the soft tissues of the chin (distance from point Pog to point Pog') (mm); **AFH_PFH ratio** – the ratio between the values of AFH and PFH.

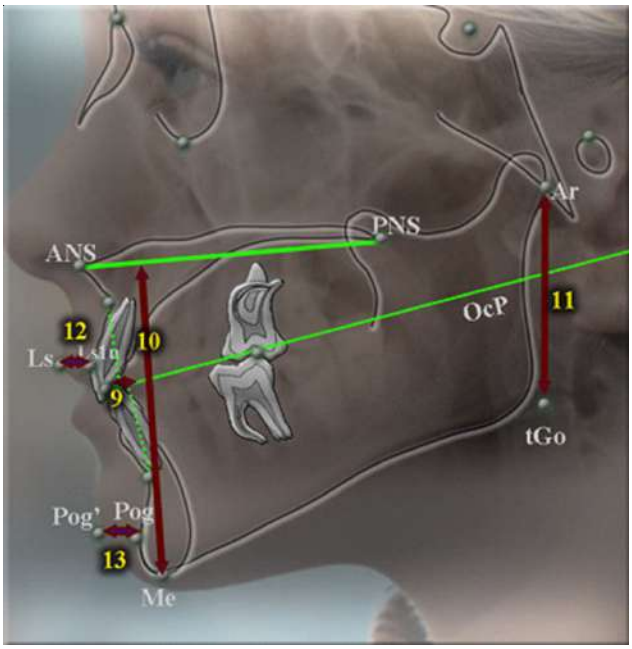

Fig. 5. Measurement according to the Tweed method. 9 – Wits index, 10 – AFH distance, 11 – PFH distance, 12 – Ls1u_Ls distance, 13 – Pog_Pog' distance.

To conduct a morphometric study of teeth and dental arches, we used the software applications i-Dixel One Volume Viewer (Ver.1.5.0) J Morita Mfg. Cor, and Planmeca Romexis Viewer (ver. 3.8.3.R 15.12.14) Planmeca OY.

For the frontal group of teeth, namely for the incisors and canines of the upper and lower jaws, the width of the coronal and cervical (width between the dentino-enamel boundaries) parts of the tooth and the length of the entire tooth in the coronal and sagittal planes (Fig. 6), as well as the length of the coronal and root parts relative to the cervical line in the corresponding planes (Fig. 7).

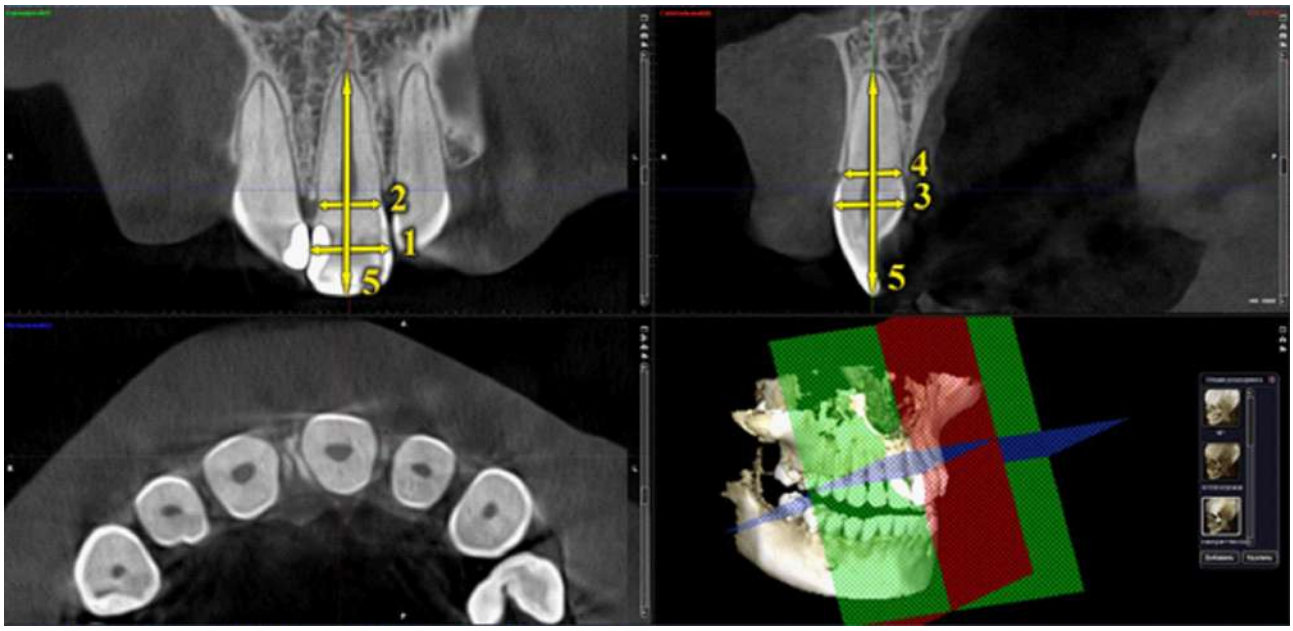

Fig. 6. Determination of metric characteristics of incisors and canines, upper and lower jaws (mm). 1 – width of the crown part of the tooth in the mesio-distal plane (MdK); 2 – width of the cervical part of the tooth in the mesio-distal plane (MdC); 3 – width of the crown part of the tooth in the vestibulo-oral plane (VoK); 4 – width of the cervical part of the tooth in the vestibulo-oral plane (VoC); 5 – length of the tooth (same) in the mesio-distal and vestibulo-oral planes (MdLD).

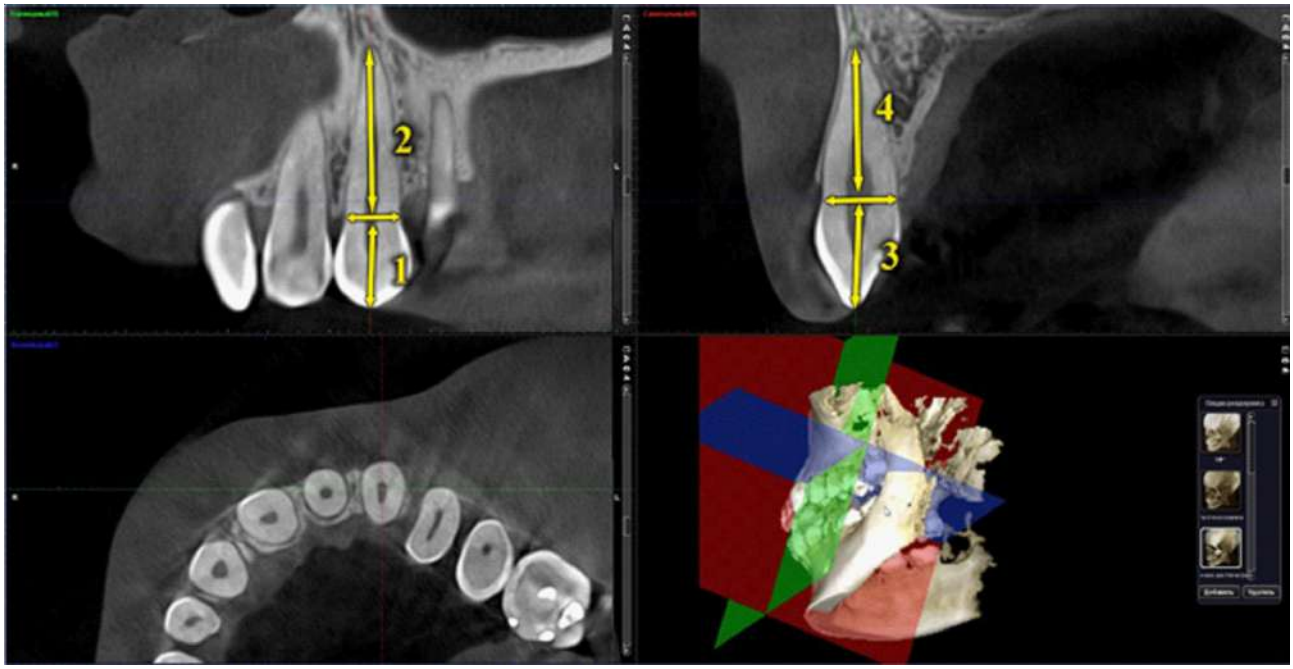

Fig. 7. Determination of metric characteristics of incisors and canines, upper and lower jaws (mm). 1 – length of the crown part of the tooth in the mesio-distal plane (MdLK); 2 – length of the root part of the tooth in the mesio-distal plane (MdLR); 3 – length of the crown part of the tooth in the vestibulo-oral plane (VoLK); 4 – length of the root part of the tooth in the vestibulo-oral plane (VoLR).

For the first and second premolars (Fig. 8) and the first molar (Fig. 9) of the upper and lower jaws, the width of the crown part in the mesio-distal and vestibulo-oral planes was determined. Additionally, for premolars, the length of the tooth was also determined, which was measured between the tops of the vestibular tubercle and the root. If the premolar has two roots, the top of the vestibular root was selected (see Fig. 8).

Since in previous studies conducted by Marchenko A. V. et al. [19], when comparing the computed tomography sizes

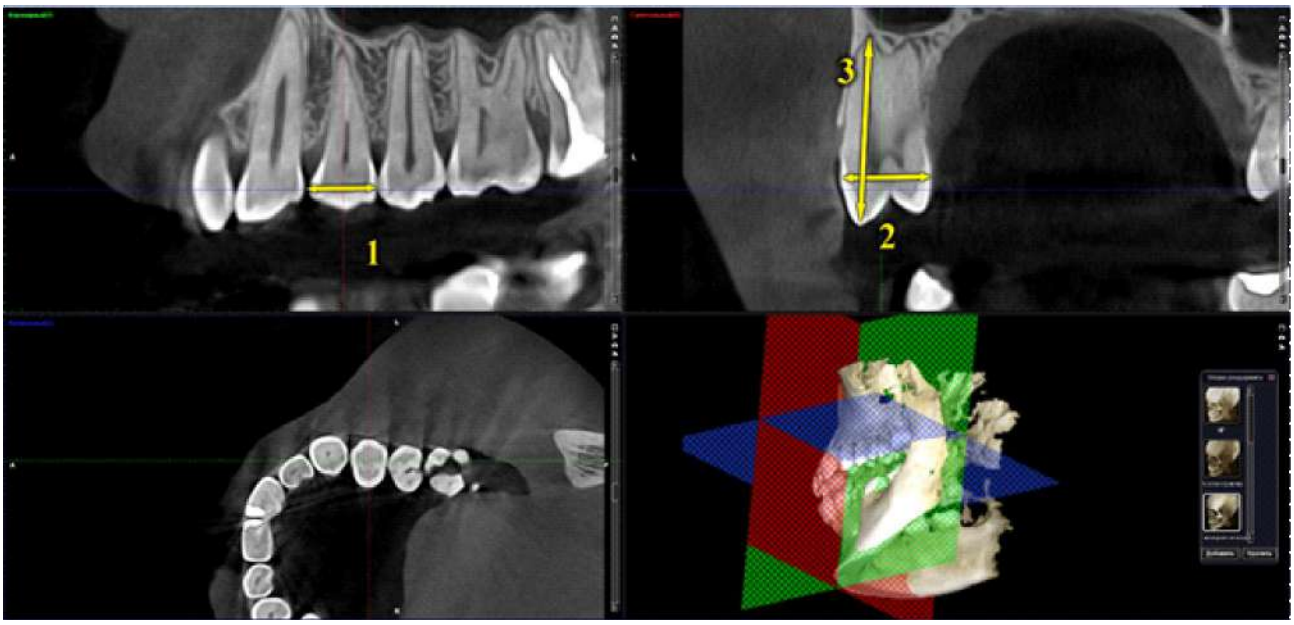

Fig. 8. Determination of metric characteristics of the premolars of the upper and lower jaws (mm). 1 – width of the crown part of the tooth in the mesio-distal plane (MdK); 2 – width of the crown part of the tooth in the vestibulo-oral plane (VoK); 3 – length of the tooth in the vestibulo-oral plane (MdLD).

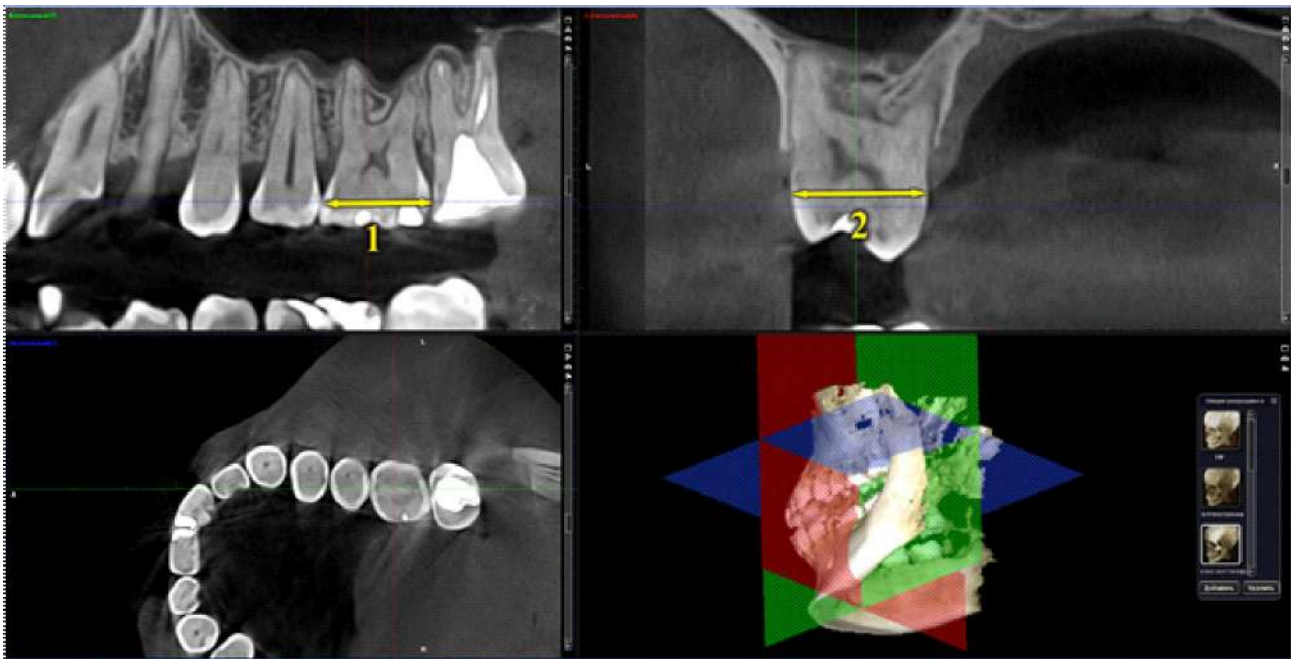

Fig. 9. Determination of metric characteristics of molars of the upper and lower jaws (mm). 1 – width of the crown part in the mesio-distal plane (MdK); 2 – width of the crown part in the vestibulo-oral plane (VoK).

of the same teeth on the right and left sides, no significant or trending differences were found, we used the average values of the corresponding teeth on the upper and lower jaws: 11 or 41 upper or lower central incisors, 12 or 42 upper or lower lateral incisors, 13 or 43 upper or lower canines, 14 or 44 upper or lower first premolars, 15 or 45 upper or lower second premolars, 16 or 46 upper or lower first molars.

To characterize the dental arches, we used indicators that in the transverse (axial) plane characterize the distance between the cusps of the crowns and the tops of the roots of the canines (Fig. 10) and the first molars (Fig. 11) of the upper and lower jaws, as well as the distance between the premolar and molar points according to Pon (Fig. 12); in the sagittal plane, the distance between the crowns of the central incisors and the lines connecting the canines, first

premolars and molars of the upper jaw (see Fig. 12); in the vertical (coronal) plane, the distances that characterize the position of the canines, first premolars and molars relative to the hard palate (Fig. 13).

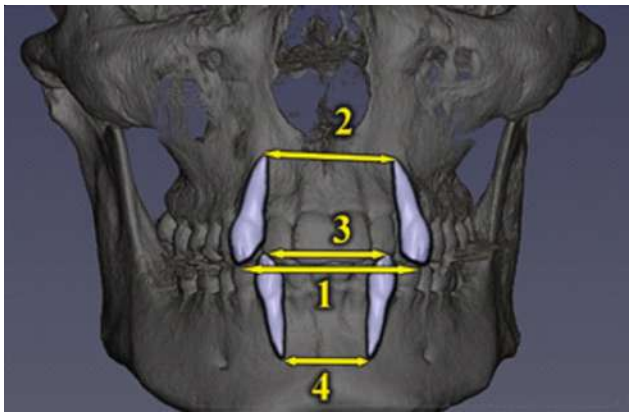

Fig. 10. Determination of the distance between the apical tubercles (1 – distance 13_23Bugr) and the root tips (2 – distance 13_23Apx) of the canines on the upper jaw and between the apical tubercles (3 – distance 33_43Bugr) and the root tips (4 – distance 33_43Apx) of the canines on the lower jaw (mm).

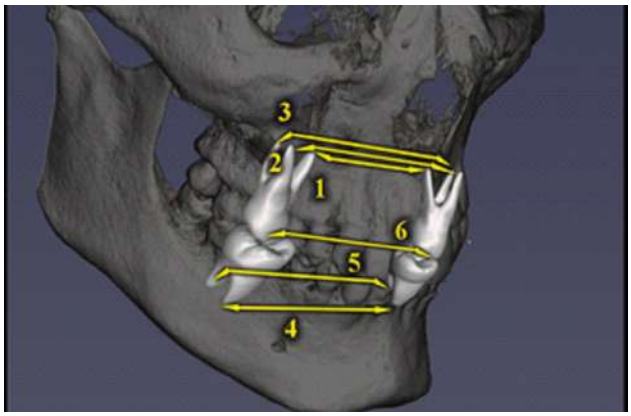

Fig. 11. Determination of the distances between the apices of the palatal (1 – distance mapex_6), medial vestibular (2 – distance napx_6) and distal vestibular roots (3 – distance dapx_6) and vestibular medial cusps (6 – distance VestBM) of the upper first molars and the distal (5 – distance dapx_46) and medial (4 – distance mapx_46) roots of the lower first molars (mm).

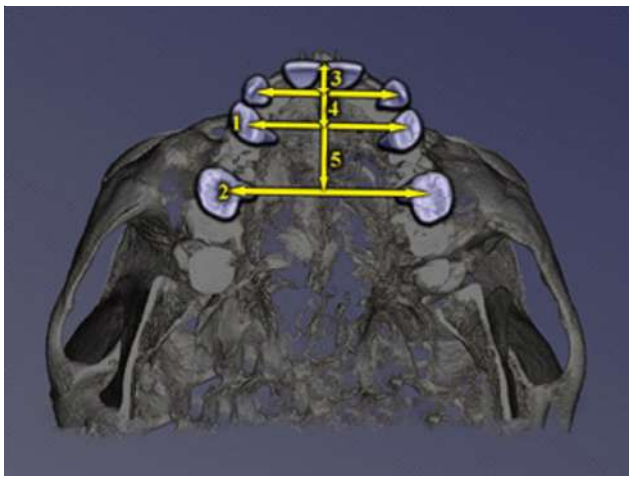

Fig. 12. Determination of the distances between the premolar (1 – distance PonPr) and molar (2 – distance PonM) points according to Pon, the distances between the crowns of the central incisors and the lines connecting the canines (3 – distance DL_C), the first premolars (4 – distance (DL_F) and molars (5 – distance DL_S) of the upper jaw (mm).

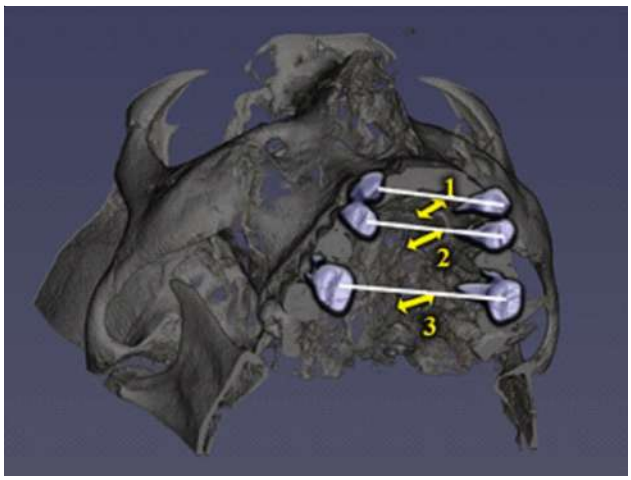

Fig. 13. Determination of distances characterizing the position of the intercanine (1– distance GL_1), premolar (2 – distance GL_2) and molar (3 – distance GL_3) lines relative to the hard palate (mm).

Using the stepwise regression analysis method in the licensed statistical package “Statistica 6.0”, the parameters necessary for constructing the correct shape of the dental arch were simulated depending on the features of teleradiometric indicators according to the Steiner or Tweed method and computed tomography dimensions of the teeth.

Results

In Ukrainian young men with physiological occlusion, reliable regression models (with the coefficient of determination of the regression polynomial $R^2>0.60$) of the sizes necessary for constructing the correct shape of the dental arch depending on the features of teleradiometric indicators according to the *Steiner method* and computed tomography sizes of the teeth have the form of the following linear equations:

distance DL_C (young men regardless of face type)= -10.55 + 1.235×MdK11 + 1.273×VoK41 - 0.394×VoLK41 + 0.339×VoLK13 + 0.115×S-E (R^2=0.880, $F_{(5.35)}$=23.94, p<0.001, Std.Error of estimate=0.683);

distance GL_1 (young men regardless of face type)= 32.39 - 0.283×Max1-NA + 2.244×MdK11 - 2.047×MdK46 - 1.232×MdLR12 + 2.111×VoK41 + 0.494×VoLK12 - 0.080×Il (R^2=0.864, $F_{(7.33)}$=13.90, p<0.001, Std.Error of estimate=1.343);

distance DL_F (young men regardless of face type)= -

9.925 + 1.390×MdK11 + 1.553×VoK45 - 0.304×VoLK42 - 1.001×VoK45 + 0.143×S-E + 1.637×MdK42 (R^2=0.911, $F_{(6.34)}$=27.63, p<0.001, Std.Error of estimate=0.689);

distance GL_2 (young men regardless of face type)= 10.86 - 0.251×Max1-NA + 1.224×MdLK12 - 1.193×MdLD45 + 2.141×VoK12 + 1.322×MdLK13 + 1.396×VoK14 - 2.004×MdK44 + 0.396×1I-NB (R^2=0.832, $F_{(8.32)}$=8.99, p<0.001, Std.Error of estimate=1.634);

distance PonPr (young men regardless of face type)= 5.701 + 1.366×MdK12 + 1.573×MdK15 - 0.478×MdLR12 + 2.217×MdK45 + 2.042×MdK41 - 0.319×MdLD14 (R^2=0.895, $F_{(6.34)}$=22.80, p<0.001, Std.Error of estimate=1.002);

distance DL_S (young men regardless of face type)= 0.843 + 1.493×MdK11 + 2.022×VoK15 + 0.979×VoK46 - 1.140×VoK45 + 0.163×S-E - 0.053×II + 0.197×MdLK43 (R^2=0.900, $F_{(7.33)}$=42.53, p<0.001, Std.Error of estimate=0.652);

distance GL_3 (young men regardless of face type)= 11.58 - 1.004×MdLD45 + 1.262×MdLD11 - 0.641×ANB_S - 0.567×MdLD41 + 3.090×MdK42 - 1.606×MdK16 + 1.343×VoK15 + 0.125×S-E (R^2=0.709, $F_{(8.32)}$=9.73, p<0.001, Std.Error of estimate=1.259);

distance PonM (young men regardless of face type)= 1.850 + 0.659×MdLD44 - 0.638×MdLD14 + 1.454×MdK15 + 2.664×MdK45 + 2.051×VoK43 + 2.196×MdK41 - 1.627×VoK42 (R^2=0.774, $F_{(7.33)}$=16.12, p<0.001, Std.Error of estimate=1.345);

distance 13_23Bugr (young men regardless of face type)= 7.992 + 2.502×MdK12 + 1.849×MdK13 - 0.487×VoLR12 - 0.913×VoK14 + 1.396×MdK41 + 1.171×MdC41 (R^2=0.764, $F_{(6.34)}$=18.34, p<0.001, Std.Error of estimate=1.058);

distance 13_23Apx (young men regardless of face type)= 42.43 + 1.853×MdC12 + 0.325×ANB_S - 1.672×VoK16 + 1.062×VoK45 - 1.600×VoC43 + 0.331×MdLK41 + 0.531×MdLD14 - 0.457×MdLD13 (R^2=0.611, $F_{(8.31)}$=6.08, p<0.001, Std.Error of estimate=1.600);

distance VestBM (young men regardless of face type)= 30.23 + 3.095×VoK15 + 1.197×MdLD44 - 0.595×MdLD42 - 0.819×MdLD45 + 0.805×MdLD11 - 1.273×MdK11 - 0.415×MdLR13 (R^2=0.786, $F_{(7.33)}$=17.28, p<0.001, Std.Error of estimate=1.348);

distance napx_6 (young men regardless of face type)= 31.79 + 3.799×MdC42 - 2.940×VoK16 + 3.934×MdK12 - 0.647×VoLR13 + 0.876×Pog-NB + 2.156×VoK13 - 1.387×MdK11 (R^2=0.731, $F_{(7.33)}$=12.80, p<0.001, Std.Error of estimate=1.824);

distance dapx_6 (young men regardless of face type)= -23.49 + 2.973×VoK15 + 3.030×MdK46 - 5.057×MdC13 + 1.121×VoLK13 + 2.296×MdK12 + 3.452×MdK15 + 2.377×VoC13 - 1.996×MdK16 (R^2=0.764, $F_{(8.32)}$=12.95, p<0.001, Std.Error of estimate=2.374);

distance mapex_6 (young men regardless of face type)= -18.54 + 3.609×MdK45 + 4.242×MdK15 + 2.438×MdK12 - 0.403×MdLR42 + 0.235×S-E + 3.481×MdC42 - 1.681×MdC13 (R^2=0.849, $F_{(7.33)}$=26.51, p<0.001, Std.Error of estimate=1.412);

distance 33_43Bugr (young men regardless of face type)= 1.121 + 1.479×MdK12 + 2.406×MdK42 - 0.343×MdLR11 + 0.380×MdLD43 - 0.227×VoLR13 (R^2=0.673, $F_{(5.35)}$=14.40, p<0.001, Std.Error of estimate=0.902);

distance 33_43Apx (young men regardless of face type)= 8.749 + 0.958×MdLD43 + 4.801×VoC12 - 3.475×VoK12 - 0.523×VoLR12 - 1.363×MdC11 + 3.167×VoK43 - 2.156×MdK15 - 1.760×VoC43 (R^2=0.709, $F_{(8.32)}$=9.74, p<0.001, Std.Error of estimate=1.400);

distance mapx_46 (young men regardless of face type)= 15.05 + 1.420×MdLK12 + 3.349×MdK45 + 2.606×VoK16 - 0.703×MdLD45 - 1.346×VoK46 + 1.219×MdC43 - 0.823×MdC11 (R^2=0.757, $F_{(7.32)}$=14.26, p<0.001, Std.Error of estimate=1.479);

distance dapx_46 (young men regardless of face type)= 17.74 + 5.132×MdK44 - 0.216×S-E + 0.429×VoLR13 - 2.885×VoK11 + 1.414×VoK16 - 0.172×Mand1-NB + 0.538×MdLR11 (R^2=0.689, $F_{(7.32)}$=10.14, p<0.001, Std.Error of estimate=1.746);

where, here and in the following equations, R^2 coefficient of determination; $F_{(!)}$=! critical $_{(!)}$ and obtained (!) Fisher's test value; p confidence level; Std.Error of estimate standard error of estimate.

In Ukrainian *young women* with physiological occlusion, reliable regression models (with the coefficient of determination of the regression polynomial R^2>0.60) of the sizes necessary for constructing the correct shape of the dental arch depending on the features of teleradiometric indicators according to the *Steiner method* and computed tomography sizes of the teeth have the form of the following linear equations:

distance DL_F (young women regardless of face type)= 6.836 + 0.747×MdK11 - 0.070×II + 1.276×MdK13 + 0.999×VoC11 - 0.549×VoK45 - 0.266×MdLK43 + 0.669×MdK43 (R^2=0.708, $F_{(7.60)}$=20.74, p<0.001, Std.Error of estimate=0.788);

distance GL_2 (young women regardless of face type)= 19.95 - 0.157×Max1-SN + 1.847×MdK46 - 1.493×VoLK43 + 1.023×VoLK41 + 1.627×VoK43 - 1.453×MdK16 - 1.720×VoK41 + 1.360×MdK45 (R^2=0.613, $F_{(8.59)}$=11.69, p<0.001, Std.Error of estimate=1.589);

distance DL_S (young women regardless of face type)= -3.048 + 1.461×MdK11 + 0.224×Holdaway Ratio + 1.170×MdK16 + 1.039×VoK11 + 0.251×MdLD11 - 0.196×MdLD15 (R^2=0.782, $F_{(6.61)}$=36.57, p<0.001, Std.Error of estimate=0.803);

distance mapx_46 (young women regardless of face type)= 8.581 + 0.234×SND - 0.075×MdC43 - 0.298×Holdaway Ratio + 1.091×MdK16 + 0.744×MdLK13 + 1.624×MdK41 - 0.887×VoK44 + 1.333×MdC13 (R^2=0.634, $F_{(8.53)}$=11.47, p<0.001, Std.Error of estimate=1.783);

distance dapx_46 (young women regardless of face type)= 9.425 + 0.670×MdLD45 - 0.439×Holdaway Ratio + 1.857×VoC12 + 0.277×SNB_S + 1.930×MdC12 -

1.028×VoLK13 (R^2=0.668, $F_{(6.55)}$=18.45, p<0.001, Std.Error of estimate=1.958).

Since, in young women, regardless of the type of face, in the constructed reliable models of *distances DL_C, GL_1, PonPr, GL_3, PonM, 13_23Bugr, 13_23Apx, VestBM, napx_6, dapx_6, mapex_6, 33_43Bugr and 33_43Apx*, the coefficient of determination of the regression equations is from 0.313 to 0.513, these models do not have important practical significance in dental practice.

In Ukrainian *young men* with physiological occlusion, reliable regression models (with the coefficient of determination of the regression polynomial R^2>0.60) of the sizes necessary for constructing the correct shape of the dental arch depending on the features of teleradiometric indicators according to the *Tweed method* and computed tomography sizes of the teeth have the form of the following linear equations:

distance DL_C (young men regardless of face type)= -6.910 + 1.098×MdK11 + 0.899×VoK41 - 0.417×VoLK41 + 0.237×VoLK13 + 0.100×Wits + 0.522×MdC11 (R^2=0.778, $F_{(6.34)}$=19.86, p<0.001, Std.Error of estimate=0.686);

distance GL_1 (young men regardless of face type)= 22.80 + 0.760×ANB_T - 0.653×VoLR12 + 1.085×VoC11 + 0.081×AFH - 1.606×MdK46 + 0.802×MdLK13 - 0.662×VoLK41 (R^2=0.694, $F_{(7.33)}$=10.68, p<0.001, Std.Error of estimate=1.476);

distance DL_F (young men regardless of face type)= -2.091 + 1.499×MdK11 + 1.231×VoK15 - 0.337×VoLK42 - 0.678×VoK45 + 1.189×VoC42 - 0.209×MdLR42 (R^2=0.794, $F_{(6.34)}$=21.79, p<0.001, Std.Error of estimate=0.759);

distance GL_2 (young men regardless of face type)= -4.788 + 0.281×POr_OcP + 2.384×MdK13 + 0.077×AFH - 0.584×MdLD41 + 2.200×VoK12 + 0.518×MdLK43 - 0.460×MdLD45 (R^2=0.638, $F_{(7.33)}$=8.33, p<0.001, Std.Error of estimate=1.743);

distance PonPr (young men regardless of face type)= 5.701 + 1.366×MdK12 + 1.573×MdK15 - 0.478×MdLR12 + 2.217×MdK45 + 2.042×MdK41 - 0.319×MdLD14 (R^2=0.801, $F_{(6.34)}$=22.80, p<0.001, Std.Error of estimate=1.002);

distance DL_S (young men regardless of face type)= 4.940 + 1.930×MdK11 + 1.724×VoK15 + 0.892×VoK46 - 0.080×FMIA - 0.759×VoK45 - 0.275×MdLR12 (R^2=0.872, $F_{(6.34)}$=38.76, p<0.001, Std.Error of estimate=0.726);

distance GL_3 (young men regardless of face type)= 7.243 + 0.79×AFH - 0.950×MdLD45 + 0.889×MdLD11 - 1.764×MdK16 + 3.160×MdK42 + 1.324×MdK13 - 0.271×ANB_T (R^2=0.715, $F_{(7.33)}$=11.82, p<0.001, Std.Error of estimate=1.227);

distance PonM (young men regardless of face type)= 1.850 + 0.659×MdLD44 - 0.638×MdLD14 + 1.454×MdK15 + 2.664×MdK45 + 2.051×VoK43 + 2.196×MdK41 - 1.627×VoK42 (R^2=0.774, $F_{(7.33)}$=16.12, p<0.001, Std.Error of estimate=1.345);

distance 13_23Bugr (young men regardless of face type)= 10.89 + 2.614×MdK12 + 2.102×MdK13 - 0.525×VoLR12 - 0.640×VoK14 + 1.393×MdK41 + 2.124×MdC41 - 1.432×VoC41 - 0.213×Ls1u_Ls (R^2=0.834, $F_{(8.32)}$=20.06, p<0.001, Std.Error of estimate=0.915);

distance VestBM (young men regardless of face type)= 23.72 + 2.982×VoK15 + 1.085×MdLD44 - 0.706×MdLD42 - 0.842×MdLD45 + 0.748×MdLD11 + 0.099×FMIA - 1.186×MdK11 (R^2=0.788, $F_{(7.33)}$=17.51, p<0.001, Std.Error of estimate=1.342);

distance napx_6 (young men regardless of face type)= 22.50 + 3.035×MdC42 - 4.144×VoK16 + 3.511×MdK12 - 0.686×VoLR13 + 0.924×MdLD45 - 1.123×VoLR11 + 3.222×MdK44 + 0.182×FMIA (R^2=0.798, $F_{(8.32)}$=15.76, p<0.001, Std.Error of estimate=1.606);

distance dapx_6 (young men regardless of face type)= -21.88 + 3.371×VoK15 + 2.222×MdK46 - 4.227×MdC13 + 1.151×VoLK13 + 2.578×MdK12 + 2.762×MdK15 (R^2=0.696, $F_{(6.34)}$=13.00, p<0.001, Std.Error of estimate=2.612);

distance mapex_6 (young men regardless of face type)= -11.23 + 3.492×MdK45 + 3.284×MdK15 + 2.133×MdK12 + 2.357×MdC41 - 0.645×MdLR42 + 0.486×MdLD44 - 0.572×MdLK13 (R^2=0.830, $F_{(7.33)}$=23.02, p<0.001, Std.Error of estimate=1.504);

distance 33_43Bugr (young men regardless of face type)= -2.284 + 1.418×MdK12 + 2.494×MdK42 - 0.349×MdLR11 + 0.450×MdLD43 - 0.281×VoLR13 + 0.265×MdLR42 + 0.032×AFH_PFH - 0.271×MdLR12 (R^2=0.760, $F_{(8.32)}$=12.65, p<0.001, Std.Error of estimate=0.808);

distance 33_43Apx (young men regardless of face type)= 24.62 + 0.800×MdLD43 - 0.411×Ls1u_Ls + 4.792×VoK43 - 3.023×VoC43 - 1.899×VoK42 - 0.406×MdLD45 - 1.881×MdK15 (R^2=0.737, $F_{(7.33)}$=13.23, p<0.001, Std.Error of estimate=1.308);

distance mapx_46 (young men regardless of face type)= 12.65 + 1.576×MdLK12 + 2.357×MdK45 + 2.845×VoK16 - 0.648×MdLD45 - 2.008×VoK46 - 0.099×PFH + 3.114×MdK42 (R^2=0.788, $F_{(7.32)}$=16.98, p<0.001, Std.Error of estimate=1.383);

distance dapx_46 (young men regardless of face type)= 19.97 + 4.741×MdK44 - 0.217×IMPA - 3.955×VoK11 + 0.396×MdLD13 + 2.057×MdK45 + 0.192×SNA_T + 1.030×VoK16 (R^2=0.733, $F_{(7.32)}$=12.57, p<0.001, Std.Error of estimate=1.618).

Since, in young men, regardless of the type of face, in the constructed reliable model of the *distance 13_23Apx*, the coefficient of determination of the regression equation is 0.529, this model does not have important practical significance in dental practice.

In Ukrainian *young women* with a physiological bite, reliable regression models (with a coefficient of determination of the regression polynomial R^2 >0.60) of the sizes necessary for constructing the correct shape of the dental arch depending on the features of teleradiometric indicators according to the *Tweed method* and computed tomography sizes of the teeth have the form of the following linear equations:

distance DL_C (young men regardless of face type)= -

6.910 + 1.098×MdK11 + 0.899×VoK41 - 0.417×VoLK41 + 0.237×VoLK13 + 0.100×Wits + 0.522×MdC11 (R^2=0.778, $F_{(6.34)}$=19.86, p<0.001, Std.Error of estimate=0.686);

distance GL_1 (young men regardless of face type)= 22.80 + 0.760×ANB_T - 0.653×VoLR12 + 1.085×VoC11 + 0.081×AFH - 1.606×MdK46 + 0.802×MdLK13 - 0.662×VoLK41 (R^2=0.694, $F_{(7.33)}$=10.68, p<0.001, Std.Error of estimate=1.476);

distance DL_F (young men regardless of face type)= -2.091 + 1.499×MdK11 + 1.231×VoK15 - 0.337×VoLK42 - 0.678×VoK45 + 1.189×VoC42 - 0.209×MdLR42 (R^2=0.794, $F_{(6.34)}$=21.79, p<0.001, Std.Error of estimate=0.759);

distance GL_2 (young men regardless of face type)= -4.788 + 0.281×POr_OcP + 2.384×MdK13 + 0.077×AFH - 0.584×MdLD41 + 2.200×VoK12 + 0.518×MdLK43 - 0.460×MdLD45 (R^2=0.638, $F_{(7.33)}$=8.33, p<0.001, Std.Error of estimate=1.743);

distance PonPr (young men regardless of face type)= 5.701 + 1.366×MdK12 + 1.573×MdK15 - 0.478×MdLR12 + 2.217×MdK45 + 2.042×MdK41 - 0.319×MdLD14 (R^2=0.801, $F_{(6.34)}$=22.80, p<0.001, Std.Error of estimate=1.002);

distance DL_S (young men regardless of face type)= 4.940 + 1.930×MdK11 + 1.724×VoK15 + 0.892×VoK46 - 0.080×FMIA - 0.759×VoK45 - 0.275×MdLR12 (R^2=0.872, $F_{(6.34)}$=38.76, p<0.001, Std.Error of estimate=0.726);

distance GL_3 (young men regardless of face type)= 7.243 + 0.79×AFH - 0.950×MdLD45 + 0.889×MdLD11 - 1.764×MdK16 + 3.160×MdK42 + 1.324×MdK13 - 0.271×ANB_T (R^2=0.715, $F_{(7.33)}$=11.82, p<0.001, Std.Error of estimate=1.227);

distance PonM (young men regardless of face type)= 1.850 + 0.659×MdLD44 - 0.638×MdLD14 + 1.454×MdK15 + 2.664×MdK45 + 2.051×VoK43 + 2.196×MdK41 - 1.627×VoK42 (R^2=0.774, $F_{(7.33)}$=16.12, p<0.001, Std.Error of estimate=1.345);

distance 13_23Bugr (young men regardless of face type)= 10.89 + 2.614×MdK12 + 2.102×MdK13 - 0.525×VoLR12 - 0.640×VoK14 + 1.393×MdK41 + 2.124×MdC41 - 1.432×VoC41 - 0.213×Ls1u_Ls (R^2=0.834, $F_{(8.32)}$=20.06, p<0.001, Std.Error of estimate=0.915);

distance VestBM (young men regardless of face type)= 23.72 + 2.982×VoK15 + 1.085×MdLD44 - 0.706×MdLD42 - 0.842×MdLD45 + 0.748×MdLD11 + 0.099×FMIA - 1.186×MdK11 (R^2=0.788, $F_{(7.33)}$=17.51, p<0.001, Std.Error of estimate=1.342);

distance napx_6 (young men regardless of face type)= 22.50 + 3.035×MdC42 - 4.144×VoK16 + 3.511×MdK12 - 0.686×VoLR13 + 0.924×MdLD45 - 1.123×VoLR11 + 3.222×MdK44 + 0.182×FMIA (R^2=0.798, $F_{(8.32)}$=15.76, p<0.001, Std.Error of estimate=1.606);

distance dapx_6 (young men regardless of face type)= -21.88 + 3.371×VoK15 + 2.222×MdK46 - 4.227×MdC13 + 1.151×VoLK13 + 2.578×MdK12 + 2.762×MdK15 (R^2=0.696, $F_{(6.34)}$=13.00, p<0.001, Std.Error of estimate=2.612);

distance mapex_6 (young men regardless of face type)= -11.23 + 3.492×MdK45 + 3.284×MdK15 + 2.133×MdK12 + 2.357×MdC41 - 0.645×MdLR42 + 0.486×MdLD44 - 0.572×MdLK13 (R^2=0.830, $F_{(7.33)}$=23.02, p<0.001, Std.Error of estimate=1.504);

distance 33_43Bugr (young men regardless of face type)= -2.284 + 1.418×MdK12 + 2.494×MdK42 - 0.349×MdLR11 + 0.450×MdLD43 - 0.281×VoLR13 + 0.265×MdLR42 + 0.032×AFH_PFH - 0.271×MdLR12 (R^2=0.760, $F_{(8.32)}$=12.65, p<0.001, Std.Error of estimate=0.808);

distance 33_43Apx (young men regardless of face type)= 24.62 + 0.800×MdLD43 - 0.411×Ls1u_Ls + 4.792×VoK43 - 3.023×VoC43 - 1.899×VoK42 - 0.406×MdLD45 - 1.881×MdK15 (R^2=0.737, $F_{(7.33)}$=13.23, p<0.001, Std.Error of estimate=1.308);

distance mapx_46 (young men regardless of face type)= 12.65 + 1.576×MdLK12 + 2.357×MdK45 + 2.845×VoK16 - 0.648×MdLD45 - 2.008×VoK46 - 0.099×PFH + 3.114×MdK42 (R^2=0.788, $F_{(7.32)}$=16.98, p<0.001, Std.Error of estimate=1.383);

distance dapx_46 (young men regardless of face type)= 19.97 + 4.741×MdK44 - 0.217×IMPA - 3.955×VoK11 + 0.396×MdLD13 + 2.057×MdK45 + 0.192×SNA_T + 1.030×VoK16 (R^2=0.733, $F_{(7.32)}$=12.57, p<0.001, Std.Error of estimate=1.618).

Since, in young men, regardless of the type of face, in the constructed reliable model of the *distance 13_23Apx*, the coefficient of determination of the regression equation is 0.529, this model does not have important practical significance in dental practice.

In Ukrainian *young women* with a physiological bite, reliable regression models (with a coefficient of determination of the regression polynomial R^2 >0.60) of the sizes necessary for constructing the correct shape of the dental arch depending on the features of teleradiometric indicators according to the *Tweed method* and computed tomography sizes of the teeth have the form of the following linear equations:

distance DL_F (young women regardless of face type)= -13.55 + 1.153×MdK11 + 0.069×IMPA + 0.900×VoC11 + 1.054×MdK13 - 0.346×VoK45 + 0.178×MdLD41 (R^2=0.653, $F_{(6.61)}$=19.14, p<0.001, Std.Error of estimate=0.851);

distance DL_S (young women regardless of face type)= -4.420 + 1.388×MdK11 + 1.076×MdK45 + 0.492×MdLD41 + 0.072×IMPA - 0.331×MdLD44 + 0.618×MdK16 (R^2=0.745, $F_{(6.61)}$=29.66, p<0.001, Std.Error of estimate=0.870);

distance mapx_46 (young women regardless of face type)= 8.346 + 1.500×MdK16 - 0.070×MdC43 + 0.220×Z + 1.333×MdLK13 - 1.551×VoK44 + 1.758×VoK43 - 0.229×MdLK41 (R^2=0.619, $F_{(7.54)}$=12.52, p<0.001, Std.Error of estimate=1.802);

distance dapx_46 (young women regardless of face type)= 0.885 + 0.302×Z + 0.477×VoLR42 + 2.351×MdC12 + 0.940×MdLD45 - 0.618×MdLR42 - 0.336×MdLR41 + 0.706×MdLK12 (R^2=0.719, $F_{(7.54)}$=19.70, p<0.001, Std.Error of estimate=1.820).

Since, in young women, regardless of face type, in the

constructed reliable models of *distances DL_C, GL_1, GL_2, PonPr, GL_3, PonM, 13_23Bugr, 13_23Apx, VestBM, napx_6, dapx_6, mapex_6, 33_43Bugr and 33_43Apx*, the value of the coefficient of determination of the regression equations is from 0.285 to 0.546, these models do not have important practical significance in dental practice.

Discussion

Thus, as a result of the regression analysis, *in young men* with physiological occlusion, all 18 possible reliable ($p<0.001$ in all cases) models of linear parameters of dental arches were constructed depending on the features of computed tomography sizes of teeth and teleradiometric indicators according to the *Steiner* method with a determination coefficient of more than 0.6 (R^2= from 0.611 to 0.911); as well as 17 reliable ($p<0.001$ in all cases) models depending on the features of computed tomography sizes of teeth and teleradiometric indicators according to the *Tweed* method with a determination coefficient of more than 0.6 (R^2= from 0.638 to 0.872).

As a result of the analysis of the frequency of occurrence in the regression equations of computed tomography tooth sizes and teleradiometric indicators according to the *Steiner* method or the *Tweed* method *in young men*, the following percentage of occurrence in the models of these indicators was established: taking into account teleradiometric indicators according to the *Steiner* method the width of the crown part of the tooth in the mesio-distal (27.64 %) and vestibulo-oral plane (19.51 %), the length of the tooth in the mesio-distal and vestibulo-oral planes (13.01 %), teleradiometric indicators according to the *Steiner* method (12.20 %), the width of the cervical part of the tooth in the mesio-distal (7.32 %) and vestibulo-oral plane (3.25 %), the length of the root part of the tooth in the mesio-distal (4.88 %) and vestibulo-oral plane (4.07 %) and the length of the crown part of the tooth in mesio-distal (4.07 %) and vestibulo-oral plane (4.07 %); taking into account teleradiometric indicators according to the *Tweed* method the width of the crown part of the tooth in the mesio-distal (29.06 %) and vestibulo-oral plane (16.24 %), the length of the tooth in the mesio-distal and vestibulo-oral planes (15.38 %), teleradiometric indicators according to the *Tweed* method (13.68 %), the length of the root part of the tooth in the mesio-distal (5.98 %) and vestibulo-oral plane (4.27 %), the length of the crown part of the tooth in the vestibulo-oral (4.27 %) and mesio-distal plane (3.42 %) and the width of the cervical part of the tooth in the mesio-distal (4.27 %) and vestibulo-oral plane (3.42 %).

As a result of the analysis of the frequency of occurrence in the regression equations of the corresponding teeth *in young men*, the following percentage of occurrence in the models of these indicators was established: taking into account teleradiometric indicators according to the *Steiner* method upper incisors (17.78 % of all independent variables, including 12.04 % central incisors and 15.74 % lateral incisors), lower incisors (15.74 % of all independent variables, including 8.33 % central incisors and 7.41 % lateral incisors), upper canines (12.04 %), lower canines (7.41 %), upper premolars (12.96 % of all independent variables, including 4.63 % first and 8.33 % second), lower premolars (14.81 % of all independent variables, including 3.70 % first and 11.11 % second), upper first molars (5.56 %), lower first molars (3.70 %); taking into account teleradiometric indicators according to the *Tweed* method upper incisors (23.76 % of all independent variables, including 10.89 % central incisors and 12.87 % lateral incisors), lower incisors (21.78 % of all independent variables, including 9.90 % central incisors and 11.88 % lateral incisors), upper canines (10.89 %), lower canines (5.94 %), upper premolars (11.88 % of all independent variables, including 2.97 % first and 8.91 % second), lower premolars (17.82 % of all independent variables, including 4.95 % first and 12.87 % second), upper first molars (3.96 %), lower first molars (3.96 %).

In *young women* with physiological occlusion, out of 18 possible, only 5 reliable ($p<0.001$ in all cases) models of linear parameters of dental arches were constructed depending on the features of computed tomography sizes of teeth and teleradiometric indicators according to the *Steiner* method with a coefficient of determination greater than 0.6 (R^2= from 0.613 to 0.782); and only 4 reliable ($p<0.001$ in all cases) models depending on the features of computed tomography sizes of teeth and teleradiometric indicators according to the *Tweed* method with a coefficient of determination greater than 0.6 (R^2= from 0.619 to 0.745).

As a result of the analysis of the frequency of occurrence in the regression equations of computed tomography tooth sizes and teleradiometric indicators according to the *Steiner* method or the *Tweed* method *in young women*, the following percentage of occurrence in the models of these indicators was established: taking into account teleradiometric indicators according to the *Steiner* method the width of the crown part of the tooth in the mesio-distal (28.57 %) and vestibulo-oral plane (14.28 %), teleradiometric indicators according to the *Steiner* method (20.00 %), tooth length in the mesio-distal and vestibulo-oral planes (8.57 %), the length of the crown part of the tooth in the vestibulo-oral (8.57 %) and mesio-distal plane (5.71 %) and the width of the cervical part of the tooth in the mesio-distal (8.57 %) and vestibulo-oral plane (5.71 %); taking into account the teleradiometric indicators according to the *Tweed* method - the width of the crown part of the tooth in the mesio-distal (23.08 %) and the vestibulo-oral plane (11.54 %), the length of the tooth in the mesio-distal and vestibulo-oral planes (15.38 %), teleradiometric indicators according to the *Tweed* method (15.38 %), the length of the crown part of the tooth in the mesio-distal plane (11.54 %), the width of the cervical part of the tooth in the mesio-distal (7.69 %) and the vestibulo-oral plane (3.85 %) and the length of the root part of the tooth in the mesio-distal (7.69 %) and the vestibulo-oral plane (3.85 %).

As a result of the analysis of the frequency of occurrence

in the regression equations of the corresponding teeth in *young women*, the following percentage of occurrence in the models of these indicators was established: taking into account teleradiometric indicators according to the *Steiner* method upper incisors (24.99 % of all independent variables, including 17.85 % central incisors and 7.14 % lateral incisors), lower incisors (10.71 % of all independent variables, including all central incisors), upper canines (14.29 %), lower canines (17.85 %), upper premolars (3.57 % of all independent variables, including all second incisors), lower premolars (14.28 % of all independent variables, including 3.57 % first and 10.71 % second incisors), upper first molars (10.71 %), lower first molars (3.57 %); taking into account teleradiometric indicators according to the *Tweed* method upper incisors (22.73 % of all independent variables, including 13.64 % central incisors and 9.09 % lateral incisors), lower incisors (27.27% of all independent variables, including 18.18 % central incisors and 9.09 % lateral incisors), upper canines (9.09 %), lower canines (9.09 %), lower premolars (22.73 % of all independent variables, including 9.09 % first and 13.64 % second), upper first molars (9.09 %).

The study of dental arch parameters and their relationship with teleradiometric indicators using the Steiner and Tweed methods, as well as measurements using cone-beam computed tomography, is important for creating prognostic models in orthodontics. Taking into account the parameters of the shape, length and width of the arch in combination with anatomical features allows improving approaches to diagnosis and treatment planning. M. K. Alam et al. [1] emphasize the influence of gender and age on the dimensions of the dental arch. Their study showed that the width of the dental arch in women is usually smaller than in men, with a difference of up to 2.4 mm in the frontal region. These results are consistent with the studies of Daoud R. et al. [9], which demonstrated that the length of the arch in girls is also smaller than in boys, with an average difference of 3.1 mm ($p<0.05$). At the same time, the data of Shahid M. K. et al. [2] confirmed that the relationship between tooth sizes in groups with different widths, lengths and perimeters of the arch showed consistent patterns. They noted that the increase in the perimeter of the arch was directly correlated with the increase in the size of the crowns in the anterior region (correlation coefficient 0.73; $p<0.05$).

The width and inclination of the molars are key parameters for assessing the shape of the dental arch. F. Albalawi et al. [3] showed that the correlation between the width of the arch and the inclination of the molars reaches 0.62, indicating a significant interdependence of these characteristics. Their findings complement the data of Alghamdi M. and Tashkandi N. [4], who found that a larger angle of the mandibular plane is associated with a smaller perimeter of the arch ($p<0.01$).

I. G. A. W. Ardani et al. [5] drew attention to the relationship between tooth sizes and arch shape in patients with physiological occlusion. Their data show that the correct ratio of the crowns of the upper and lower teeth has a positive effect on the harmony of the arch shape (correlation coefficient 0.75).

E. Salam et al. [24] work confirms that the width of the arch and the intercanine distance have a direct effect on its length. In particular, they note that each increase in the intercanine distance by 1 mm contributes to an increase in the length of the arch by 1.2 mm ($p<0.05$). Similar data are provided by Elhiny O. A. et al. [11], who showed that the ratio of the size of the teeth and the perimeter of the arch is an important prognostic factor for assessing possible occlusion pathologies.

H. Omar et al. [21] studies complement the understanding of the influence of the shape and size of the dental arch. They noted that in patients with a proportional arch shape, the ratio of the anterior and posterior widths is significantly correlated with indicators of functional occlusal load (correlation coefficient 0.67).

Of particular note is the study by Dmitriev M. et al. [10], who developed models for assessing the location of central incisors using the Steiner method. Their findings showed that in girls, the anterior location of the incisors is more often associated with a decrease in intermolar width, while in boys these indicators are more stable.

The results of the study by Hasegawa Y. et al. [13], where the dimensions of the dental arch in modern Mongolians and Japanese were compared, are interesting. They found that in Japanese patients, the arches have a greater width, which is associated with a greater length of teeth ($p<0.01$). Such ethnic differences are important for the creation of regional orthodontic standards, in particular for the Ukrainian population.

Regarding the relationship between crown dimensions and arch parameters, Shahid F. et al. [25, 26] determined that the crown size in the anterior region affects the shape of the arch. They found that the difference in crown width can change the arch perimeter by up to 4 mm. These findings are consistent with the study by Kato M. and Arai K. [15], who emphasized the importance of matching the basal arch shape to the coronal parameters in patients with mandibular crowding.

Regarding three-dimensional analysis of the dental arch, Somvasoontra S. et al. [28] drew attention to the relationship between the shape of the anterior part of the arch, the thickness of the alveolar bone and the sagittal position of the roots of the central incisors. In particular, they found that the incorrect position of the roots of the central incisors can lead to functional and aesthetic disorders in the future.

Thus, a comprehensive approach to dental arch analysis, combining teleradiometric indicators and cone-beam computed tomography, is an effective tool in predicting and correcting the shape of the dental arch. The obtained data can be used to create individualized orthodontic schemes that take into account the anatomical features of Ukrainian boys and girls with physiological occlusion.

Conclusion

1. In Ukrainian young men and young women with physiological occlusion without taking into account the type of face, as a result of the regression analysis, reliable ($p<0.001$ in all cases) models of linear parameters of dental arches were constructed depending on the computed tomography sizes of the teeth and the features of teleradiometric indicators according to the Steiner or Tweed methods with a coefficient of determination greater than 0.6 (in young men all 18 possible when taking into account the Steiner method, R^2= from 0.611 to 0.911 and 17 when taking into account the Tweed method, R^2= from 0.638 to 0.872; in young women only 5, when taking into account the Steiner method, R^2= from 0.613 to 0.782 and only 4 when taking into account the Tweed method, R^2= from 0.619 to 0.745).

2. When analyzing the frequency of occurrence in regression equations of computed tomography tooth sizes and teleradiometric indicators according to the Steiner or Tweed methods in young men, the models most often include the width of the crown part of the tooth in the mesio-distal (27.64 % and 29.06 %, respectively) and vestibulo-oral plane (19.51 % and 16.24 %, respectively), the length of the tooth in the mesio-distal and vestibulo-oral planes (13.01 % and 15.38 %, respectively) and teleradiometric indicators (12.20 % and 13.68 %, respectively). In young women, when taking into account the indicators according to the Steiner method - the width of the crown part of the tooth in the mesio-distal (28.57 %) and vestibulo-oral plane (14.28 %) and teleradiometric indicators (20.00 %); and when taking into account the indicators according to the Tweed method the width of the crown part of the tooth in the mesio-distal (23.08 %) and vestibulo-oral plane (11.54 %), the length of the tooth in the mesio-distal and vestibulo-oral planes (15.38 %), teleradiometric indicators (15.38 %) and the length of the crown part of the tooth in the mesio-distal plane (11.54 %).

3. When analyzing the frequency of occurrence in regression equations of the corresponding teeth in young men, the models that take into account teleradiometric indicators according to the Steiner or Tweed methods most often include: upper incisors (17.78 % and 23.76 %), lower incisors (15.74 % and 21.78 %), lower premolars (14.81 % and 17.82 %), upper premolars (12.96 % and 11.88 %) and upper canines (12.04 % and 10.89 %). In young women: when taking into account teleradiometric indicators according to the Steiner method upper incisors (24.99 %), lower canines (17.85 %), upper canines and lower premolars (14.28 % each), lower incisors and upper first molars (10.71 % each), and when taking into account teleradiometric indicators according to the Tweed method lower incisors (27.27 %), upper incisors and lower premolars (22.73 % each).

References

[1] Alam, M. K., Shahid, F., Purmal, K., Ahmad, B., & Khamis, M. F. (2014). Tooth size and dental arch dimension measurement through cone beam computed tomography: effect of age and gender. *Res J Recent Sci*, *3*, 85-94.

[2] Alam, M. K., Shahid, F., Purmal, K., Ahmad, B., & Khamis, M. F. (2014). Bolton tooth size ratio and its relation with arch widths, arch length and arch perimeter: A cone beam computed tomography (CBCT) study. *Acta Odontologica Scandinavica*, *72*(8), 1047-1053. doi: 10.3109/00016357.2014.946967

[3] Albalawi, F., Alwakeel, R., Alfuriji, S., Alqahtani, N. D., Barakeh, R. M., AlGhaihab, A., & Alsaeed, S. (2023). A Correlation Analysis between Arch Width and Molar Inclination Using Cone-Beam Computed Tomography Transverse Measurements: A Cross-Sectional Study. *Diagnostics*, *13*(11), 1875. doi: 10.3390/diagnostics13111875

[4] Alghamdi, M., & Tashkandi, N. (2022). Relationship between Dental Arch Parameters and Mandibular Plane Angle. *Journal of Advanced Medical and Dental Sciences Research*, *10*(5), 105-122. doi: 10.21276/jamdsr

[5] Ardani, I. G. A. W., Kannayyah, D., & Triwardhani, A. (2019). Correlation of maxillary and mandibular arch form and tooth size ratio in ethnic Javanese malocclusion patient. *Journal of International Oral Health*, *11*(2), 75-79. doi: 10.4103/jioh.jioh_8_19

[6] Aren, G., Güven, Y., Tolgay, C. G., Ozcan, Э., Bayar, Ц. F., Kose, T. E., ... & Ak, G. (2015). The prevalence of dental anomalies in a Turkish population. *Journal of Istanbul University Faculty of Dentistry*, *49*(3), 23-28. doi: 10.17096/jiufd.86392

[7] Ata-Ali, F., Ata-Ali, J., Pecarrocha-Oltra, D., & Pecarrocha-Diago, M. (2014). Prevalence, etiology, diagnosis, treatment and complications of supernumerary teeth. *Journal of clinical and experimental dentistry*, *6*(4), e414-e418. doi: 10.4317/jced.51499

[8] Baron, C., Houchmand-Cuny, M., Enkel, B., & Lopez-Cazaux, S. (2018). Prevalence of dental anomalies in French orthodontic patients: A retrospective study. *Archives de Pŭdiatrie*, *25*(7), 426-430. doi: 10.1016/j.arcped.2018.07.002

[9] Daoud, R., Bencze, M. A., Albu, C. C., Teodorescu, E., Dragomirescu, A. O., Vasilache, A., ... & Ionescu, E. (2021). Implications of permanent teeth dimensions and arch lengths on dental crowding during the mixed dentition period. *Applied Sciences*, *11*(17), 8004. doi: 10.3390/app11178004

[10] Dmitriev, M., Gunas, V., Polishchuk, S., Olkhova, I., & Kumar, A. (2020). Modeling of Central Incisors Position Indicators in boys and girls according to CC. Steiner method for Forensic Dental Identification. *Journal of Indian Academy of Forensic Medicine*, *42*(3), 155-160. doi: 10.5958/0974-0848.2020.00043.3

[11] Elhiny, O. A., Sharaf, R. F., Abou Elyazied, M., Radwan, E., & Salem, G. A. (2021). The relationship between tooth size, arch length and arch perimeter in Egyptians. *Bali Medical Journal, 10*(3), 1056-1060. doi: 10.15562/bmj.v10i3.2618

[12] Goncalves-Filho, A. J., Moda, L. B., Oliveira, R. P., Ribeiro, A. L. R., Pinheiro, J. J., & Alver-Junior, S. M. (2014). Prevalence of dental anomalies on panoramic radiographs in a population of the state of Parб, Brazil. *Indian Journal of Dental Research*, *25*(5), 648-652. doi: 10.4103/0970-9290.147115

[13] Hasegawa, Y., Amarsaikhan, B., Chinvipas, N., Tsukada, S. I., Terada, K., Uzuka, S., ... & Nakahara, S. (2014). Comparison

of mesiodistal tooth crown diameters and arch dimensions between modern Mongolians and Japanese. *Odontology*, *102*, 167-175. doi: 10.1007/s10266-013-0130-5

[14] Herrera-Atoche, J. R., Diaz-Morales, S., Colome-Ruiz, G., Escoffie-Ramirez, M., & Orellana, M. F. (2014). Prevalence of dental anomalies in a Mexican population. *Dentistry 3000*, *2*(1), a001. doi: 10.5195/d3000.2014.25

[15] Kato, M., & Arai, K. (2022). Relationship between dental and basal arch forms in mandibular anterior crowding. *American Journal of Orthodontics and Dentofacial Orthopedics*, *161*(1), 53-64. doi: 10.1016/j.ajodo.2020.06.046

[16] Khalaf, K., Miskelly, J., Voge, E., & Macfarlane, T. V. (2014). Prevalence of hypodontia and associated factors: a systematic review and meta-analysis. *Journal of orthodontics*, *41*(4), 299-316. doi: 10.1179/1465313314Y.0000000116

[17] Lagana, G., Venza, N., Borzabadi-Farahani, A., Fabi, F., Danesi, C., & Cozza, P. (2017). Dental anomalies: prevalence and associations between them in a large sample of non-orthodontic subjects, a cross-sectional study. *BMC oral health*, *17*, 62. doi: 10.1186/s12903-017-0352-y

[18] Lombardo, G., Vena, F., Negri, P., Pagano, S., Barilotti, C., Paglia, L., … & Cianetti, S. (2020). Worldwide prevalence of malocclusion in the different stages of dentition: A systematic review and meta-analysis. European journal of paediatric dentistry, 21, 115-122. doi: 10.23804/ejpd.2020.21.02.05

[19] Marchenko, A. V., Gunas, I. V., Petrushanko, T. O., Serebrennikova, O. A., & Trofimenko, Yu. Yu. (2017). Computer-tomographic characteristics of root length incisors and canines of the upper and lower jaws in boys and girls with different craniotypes and physiological bite. *Wiadomosci Lekarskie (Warsaw, Poland: 1960)*, *70*(3 pt 1), 499-502. PMID: 28711896

[20] Muhamad, A. H., Nezar, W., & Azzaldeen, A. (2015). The curve of dental arch in normal occlusion. *Open Science Journal of Clinical Medicine*, *3*(2), 47-54.

[21] Omar, H., Alhajrasi, M., Felemban, N., & Hassan, A. (2018). Dental arch dimensions, form and tooth size ratio among a Saudi sample. *Saudi medical journal*, *39*(1), 86-91. doi: 10.15537/smj.2018.1.21035

[22] Paranhos, L. R., Ramos, A. L., de Novaes Benedicto, E., Maltagliati, L. A., de Almeida Cardoso, M., & Capelozza Filho, L. (2014). Is there any association between facial type and mandibular dental arch form in subjects with normal occlusion? *Acta Scientiarum. Health Sciences*, *36*(1), 129-134. doi: 10.4025/actascihealthsci.v36i1.17668

[23] Saghiri, M. A., Eid, J., Tang, C. K., & Freag, P. (2021). Factors influencing different types of malocclusion and arch formA review. *Journal of Stomatology, Oral and Maxillofacial Surgery*, *122*(2), 185-191. doi: 10.1016/j.jormas.2020.07.002

[24] Salam, E., El-feky, H., & Khalifa, A. (2022). Assessment of arch length prediction based on CBCT measurements of inter-canine width in Egyptian population sample. *Egyptian Dental Journal*, *68*(1), 433-443. doi: 10.21608/edj.2021.101441.1831

[25] Shahid, F., Alam, M. K., & Khamis, M. F. (2015). Maxillary and mandibular anterior crown width/height ratio and its relation to various arch perimeters, arch length, and arch width groups. *European journal of dentistry*, *9*(04), 490-499. doi: 10.4103/1305-7456.172620

[26] Shahid, F., Alam, M. K., Khamis, M. F., Matsuda, S., Shoumura, M., & Osuga, N. (2015). Crown dimension in relation to arch perimeter, arch length and arch width in ideal occlusion: A digital Model Study. *Journal of Hard Tissue Biology*, *24*(3), 289-298. doi: 10.2485/jhtb.24.289

[27] Shilpa, G., Gokhale, N., Mallineni, S. K., & Nuvvula, S. (2017). Prevalence of dental anomalies in deciduous dentition and its association with succedaneous dentition: A cross-sectional study of 4180 South Indian children. *Journal of Indian Society of Pedodontics and Preventive Dentistry*, *35*(1), 56-62. doi: 10.4103/0970-4388.199228

[28] Somvasoontra, S., Tharanon, W., Serichetaphongse, P., & Pimkhaokham, A. (2022). Associations among the anterior maxillary dental arch form, alveolar bone thickness, and the sagittal root position of the maxillary central incisors in relation to immediate implant placement: A cone-beam computed tomography analysis. *Imaging Science in Dentistry*, *52*(2), 197-207. doi: 10.5624/isd.20210248

[29] Stomatologic, S. I. (2020). Worldwide prevalence of malocclusion in the different stages of dentition: A systematic review and meta-analysis. *European journal of paediatric dentistry*, *21*, 115-122. doi: 10.23804/ejpd.2020.21.02.05

[30] Tweed, C. H. (1954). The Frankfort-Mandibular Incisor Angle (FMIA) in Orthodontic Diagnosis, Treatment Planning and Prognosis. Angle Orthod, (3), 121-169. doi: 10.1043/0003-3219(1954)024<0121:TFIAFI>2.0.CO;2

МОДЕЛЮВАННЯ ПАРАМЕТРІВ НЕОБХІДНИХ ДЛЯ ПОБУДОВИ КОРЕКТНОЇ ФОРМИ ЗУБНОЇ ДУГИ В ЗАЛЕЖНОСТІ ВІД ОСОБЛИВОСТЕЙ ТЕЛЕРЕНТГЕНОМЕТРИЧНИХ ПОКАЗНИКІВ ЗА МЕТОДАМИ STEINER АБО TWEED І КОМП`ЮТЕРНО-ТОМОГРАФІЧНИХ РОЗМІРІВ ЗУБІВ В УКРАЇНСЬКИХ ЮНАКІВ І ДІВЧАТ ІЗ ФІЗІОЛОГІЧНИМ ПРИКУСОМ

Рябов Т. В., Шінкарук-Диковицька М. М., Пилипюк О. Ю., Мунтян О. В., Драчевська І Ю., Рокунець І. Л., Бурдейна Л. В.

Вивчення параметрів зубної дуги з урахуванням телерентгенометричних показників і розмірів зубів є важливим для планування ортодонтичного лікування, що сприяє досягненню стабільних і функціонально оптимальних результатів. Методи Steiner і Tweed, широко застосовувані для оцінки черепно-лицьових пропорцій, дозволяють виявити ключові антропометричні особливості, які впливають на форму зубної дуги. Додаткове використання комп`ютерно-томографічних вимірів забезпечує високу точність аналізу розмірів зубів, що особливо актуально для індивідуалізації ортодонтичних підходів. Мета роботи – в українських юнаків і дівчат із фізіологічним прикусом побудувати та провести аналіз регресійних моделей параметрів необхідних для побудови коректної форми зубної дуги в залежності від особливостей телерентгенометричних показників за методами Steiner або Tweed і комп`ютерно-томографічних розмірів зубів. На отриманих стандартним шляхом телерентгенограмах і створених в програмному забезпеченні 3D Slicer v5.4.0 телерентгенограмах з маркованими на 3D об`єктах точками (41 українських юнаків і 68 дівчат із фізіологічним прикусом із банку даних кафедри стоматології дитячого віку та науково-дослідного центру Вінницького національного медичного університету ім. М. І. Пирогова), вимірювання за методами Steiner С. С. і Tweed С. Н. проводилося в застосунку OnyxCeph³™, версії 3DPro, компанії Image Instruments GmbH, Німеччина. На комп`ютерних томограмах для проведення морфометричного дослідження зубів та зубних дуг нами використовувалися програмні застосунки i-Dixel One Volume Viewer (Ver.1.5.0) J Morita Mfg. Cor та Planmeca Romexis Viewer (ver. 3.8.3.R 15.12.14) Planmeca OY. Регресійні моделі побудовані за допомогою ліцензійного пакету «Statistica 6.0». Встановлено, що в юнаків при урахуванні методу Steiner побудовані усі 18 можливих достовірних моделей із коефіцієнтом

детермінації більшим 0,6 (R^2= від 0,611 до 0,911, p<0,001), а при урахуванні методу Tweed 17 моделей (R^2= від 0,638 до 0,872, p<0,001); а у дівчат лише 5 достовірних моделей із коефіцієнтом детермінації більшим 0,6 при урахуванні методу Steiner (R^2= від 0,613 до 0,782, p<0,001) і лише 4 достовірних моделі при урахуванні методу Tweed (R^2= від 0,619 до 0,745, p<0,001). При аналізі частоти входження до регресійних рівнянь комп`ютерно-томографічних розмірів зубів і телерентгенометричних показників за методами Steiner або Tweed встановлено: в юнаків найбільш часто до моделей входять ширина коронкової частини зуба у мезіо-дистальній і вестибуло-оральній площині, довжина зуба у мезіо-дистальній та вестибуло-оральній площинах і телерентгенометричні показники; а у дівчат: при урахуванні показників за методом Steiner ширина коронкової частини зуба у мезіо-дистальній і вестибуло-оральній площині та телерентгенометричні показники; при урахуванні показників за методом Tweed ширина коронкової частини зуба у мезіо-дистальній і вестибуло-оральній площині, довжина зуба у мезіо-дистальній та вестибуло-оральній площинах, телерентгенометричні показники та довжина коронкової частини зуба у мезіо-дистальній площині. При аналізі частоти входження до регресійних рівнянь відповідних зубів встановлено, що в юнаків до моделей, які враховують телерентгенометричні показники за методами Steiner або Tweed, найбільш часто входять верхні й нижні різці, верхні й нижні малі кутні зуби та верхні ікла; а у дівчат верхні й нижні різці, верхні й нижні ікла, нижні малі кутні зуби та верхні перші великі кутні зуби при урахуванні телерентгенометричних показників за методом Steiner, а також верхні й нижні різці та нижні малі кутні зуби при урахуванні телерентгенометричних показників за методом Tweed.

***Ключові слова**: стоматологія, телерентгенометрія за методами Steiner і Tweed, комп`ютерно-томографічні розміри зубів і зубних дуг, регресійний аналіз, українськи юнаки та дівчата, фізіологічний прикус.*

Author's contribution

Ryabov T. V. – research, methodology and writing of the original draft, formal analysis, validation.
Shinkaruk-Dykovytska M. M. – conceptualization, supervision.
Pylypiuk O. Yu. – data visualization.
Muntian O. V. – review writing and editing.
Drachevska I. Yu. – review writing and editing.
Rokunets I. L. – software.
Burdeina L. V. – review writing and editing.

DOI: 10.31393/morphology-journal-2024-30(4)-05 Reports of Morphology, Vol. 30, №4, Pages 44-51

ISSN 1818-1295 eISSN 2616-6194

REPORTS OF MORPHOLOGY

Official Journal of the Scientific Society of Anatomists, Histologists, Embryologists and Topographic Anatomists of Ukraine

journal homepage: https://morphology-journal.com

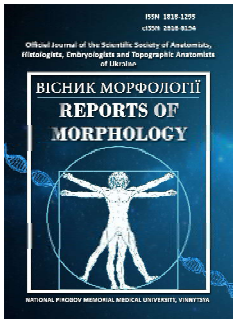

Morphological features of white adipose tissue in rats with different levels of energy metabolism in visceral obesity

Yanko R. V., Safonov S. L., Levashov M. I.

Bogomoletz Institute of Physiology of the NAS of Ukraine, Kyiv, Ukraine

ARTICLE INFO

Received: 4 March 2024

Accepted: 10 September 2024

UDC: 616.382.1+616.-56.52:577.121

CORRESPONDING AUTHOR

e-mail: biolag@ukr.net Yanko R. V.

CONFLICT OF INTEREST

The authors have no conflicts of interest to declare.

FUNDING

Not applicable.

DATA SHARING

Data are available upon reasonable request to corresponding author.

Histomorphological changes of visceral white adipose tissue in obesity as a function of the level of energy metabolism in the body have not been sufficiently studied. The aim of this study was to investigate and compare the structural changes of visceral white adipose tissue in rats with different metabolic levels and severe visceral obesity. The study was carried out on male Wistar rats aged 3 months at the start of the experiment. Control animals received standard diet. Experimental rats were fed a high calorie diet for 12 weeks. At the end of the experiment, rats from both the control and experimental groups were divided into low and high level of energy metabolism depending on the intensity of total oxygen consumption. Histological preparations of visceral white adipose tissue were prepared according to the standard method. Histomorphometry was performed on digital images using the "Image J 1.34p" computer program. Biochemical methods were used to determine the concentration of triglycerides, lipids and cholesterol in blood serum. The method of multifrequency bioimpedance was used to assess the biophysical properties of visceral white adipose tissue. The data obtained were processed by methods of variational statistics using one-way analysis of variance. It was shown that long-term use of a high-calorie diet led to the development of visceral obesity, which was manifested by a significant increase in the weight of visceral fat and an increase in the concentration of indicators of lipid metabolism in blood serum. It was found that a high-calorie diet altered the morphological structure of the rats visceral white adipose tissue, leading to adipocyte hypertrophy, reduced blood volume and increased the amount of connective tissue in it. The bioelectrical properties of the visceral white adipose tissue changed, as evidenced by an increase in its electrical impedance and a decrease in its frequency dispersion coefficient. The intensity of structural, biochemical and biophysical changes in the visceral white adipose tissue was more pronounced in rats with low level of energy metabolism and depended on the degree of obesity. The results obtained are important for practical medicine in the development of new effective methods for the prevention and treatment of obesity in patients according to level of energy metabolism.

***Keywords**: white adipose tissue, obesity, energy metabolism, rats.*

Introduction

Obesity is one of the most serious problems facing modern society and medicine, and its prevalence is constantly increasing [7, 15]. Of course, hereditary factors can play a role in the development of obesity, but one of the main causes of this "epidemiological" growth of the disease is excessive calorie intake and a sedentary lifestyle [3, 4]. Visceral obesity is closely linked to the development of a number of diseases such as: type 2 diabetes, hypertension, dyslipidaemia, apnoea, gout, fatty hepatosis, reproductive and endocrine disorders, depression and the incidence of some cancers [1, 26, 30].

Previously, it was thought that the main role of visceral white adipose tissue was to delay the supply of energy in the form of triglycerides and its secretion in the form of free fatty acids, depending on the needs of the body [14, 17]. Currently, the concept of the biological role of visceral white adipose tissue has changed. Adipocytes of visceral white adipose tissue are synthesised by a number of active molecules: leptin, resistin, adiponectin, steroids, etc [9, 25]. Therefore, visceral white adipose tissue is a complex hormone-active organ that plays an important role in the regulation of energy balance and homeostasis of the whole organism [5].

It is known that the development of visceral obesity is associated with characteristic morphological changes in

the visceral white adipose tissue. The size of the adipocytes increases [18]. Their shape is often misshapen. Hypertrophied cells can reach a diameter of 200 мм. The fat content of adipocytes increases, the intercellular spaces decrease, the intercellular walls become thinner, some of them rupture with the formation of fat cysts. In the vessels of the microcirculatory bed, blood circulation is disturbed, signs of hypoxia, adiponecrosis, lymphocytic-macrophage infiltration develop, with subsequent manifestations of inflammatory reactions and fibrosis [12].

It is thought that the basal level of energy metabolism is increased in obesity, but may be decreased under certain conditions, contributing to the increased deposition of visceral fat in the body. However, histomorphological changes in visceral white adipose tissue in obesity as a function of the level of energy metabolism in the body have not been fully investigated. The question of the mechanisms linking the peculiarities of the morphofunctional state of visceral white adipose tissue with the state of energy metabolism and their role in the pathogenesis of visceral obesity also remains open and requires further study. This may be of practical interest in the development of new effective methods of prevention and treatment of visceral obesity in people with different level of metabolism.

The aim of this study was to investigate and compare the structural changes of visceral white adipose tissue in rats with different metabolic levels and severe visceral obesity.

Material and methods

Rats. The study was conducted on 24 male rats of the Wistar line, which were subjected to an experiment at the age of 3 months. The animals were obtained from the vivarium of the Bogomoletz Institute of Physiology of the NAS of Ukraine. The rats were divided into 2 groups (12 animals each): I control, in which rats received a normal diet; II experimental, in which rats received a high calorie diet (HCD).

The rats were maintained at 20 °C and 40-60 % humidity with a 12-hour light/dark cycle. Animals were housed individually in cages with mesh partitions. All protocols were approved by the Biomedical Ethics Committee for the Care and Use of Animals of the Bogomoletz Institute of Physiology of the NAS of Ukraine (protocol № 5, dated 31.11.2019). Rats were sacrificed by decapitation under isoflurane anaesthesia in accordance with the European Convention for the Protection of Vertebrate Animals (Strasbourg, 1986).

Modeling of visceral obesity. Visceral obesity was modelled by placing the rats on diets containing excess fat (45 %) and carbohydrates (31 %) for 12 weeks. Each rat received 6 g of specially prepared granular feed (70 % of standard compound feed with the addition of 30 % pork lard); 6.8 g of pork fat; 3.6 g of white bread crumbs; 3.6 g of sunflower seeds, providing 116 kcal. The experimental animals were given food *ad libitum*, with the fullness of the food being checked daily. One day later, the experimental rats were given a 10 % solution of fructose instead of water. The rat in the control group ate 20 g of standard feed daily, with a caloric content of 66 kcal, and had free access to water. At the end of the experiment, the visceral fat (by mechanical removal from the peritoneal cavity) and the gravimetric method were differentiated by gravity.

Distribution of rats by the level of oxygen consumption. Rats in both the control and experimental groups were divided into low and high energy metabolism groups according to the intensity of oxygen consumption. Rats in which oxygen consumption was below average were considered to be in the low level of energy metabolism group, and those in which it was above average were considered to be in the high level of energy metabolism group. Oxygen consumption in rats was determined on an empty stomach in a closed gas exchange system. The oxygen consumption value was calculated in ml per kg of body weight per 1 hour and adjusted to standard physical conditions (STPD): dry gas at 0 °C and 760 mmHg.

Histomorphological analysis of white adipose tissue. For histomorphological studies, visceral white adipose tissue samples were randomly selected and histological preparations were made according to the standard method: fixed in Bouin's fluid, dehydrated in alcohols of increasing concentration. The samples obtained were embedded in paraffin. Paraffin sections of 6 мм thickness were made on a sliding microtome. The sections were stained according to the Van Gieson method [21]. Using a digital camera ("Levenhuk", USA), the microtissues were photographed on a microscope "Nikon Eclipse E100" (Japan). Morphometry was performed using the "ImageJ 1.34p" computer program.

The relative areas of parenchyma, connective tissue and blood vessels were determined on visceral white adipose tissue micropreparations, the mean diameter and cross-sectional area of adipocytes, the area of adipocyte nuclei, and the density of adipocytes per unit area were measured. The size (diameter) of the adipocytes was divided into 3 types: AI diameter <50 мм, AII diameter 50-100 мм, AIII diameter >100 мм. 100 adipocytes were counted on different sections. The number of adipocytes of each type was expressed as a percentage of the total number of cells. The stromal-parenchymal index (the ratio of the relative area of vessels and connective tissue to the area of parenchyma) and the trophic index (the ratio of the relative area of vessels to the area of parenchyma) was measured [6, 16]. Histomorphometric analysis of the visceral white adipose tissue was performed on 10 microphotographs from each rat at a magnification of Ч200.

Evaluation of lipids in blood serum. The concentration of lipids and cholesterol in rat blood serum was determined by the colorimetric-enzymatic method using standard reagent kits ("Filisit-Diagnostika", Ukraine) on a biochemical analyser ("Sinnowa", China).

Bioimpedance analysis of white adipose tissue. The method of multifrequency bioimpedance measurement was used to assess the bioelectrical properties of visceral white adipose tissue [8, 11, 24]. Bioimpedance measurement of freshly removed visceral white adipose tissue specimens was performed *ex tempore* on the

"Quad Tech 1920 LCR-meter" (USA) in the parallel equivalent circuit mode of the instrument. The absolute values of the electrical parameters were determined at frequencies of 1000 Hz 1 MHz. Measurements were made using 2 flat silver electrodes with an area of 25 mm^2. The impedance values obtained at the maximum (10^4 Hz) and minimum (10^6 Hz) polarisation frequencies of the object were used for the analysis. On the basis of the results obtained, the impedance dispersion coefficient was calculated as the ratio of its values measured at low and high frequencies ($DZ=Z_{10}^4/Z_{10}^6$).

Statistical analysis. The data obtained were processed by the methods of variational statistics using the software "Statistica 6.0 for Windows" (StatSoft, USA) and "Excel 2010" (Microsoft, USA). Data are presented as mean (M) ± standard deviation (SD) with normal distribution. Groups were analysed by one-way analysis of variance followed by Bonferroni t-tests for multiple comparisons. Differences were considered significant at $p<0.05$.

Results

It was found that the limits of average individual variation in VO_2 in the control group were 1761 ml/kg/h. An increase in oxygen consumption by 75 % to 3079 ml/kg/h was observed when the animals were on high calorie diet. Keeping rats on high calorie diet for 12 weeks resulted in the development of visceral obesity, which was manifested by a significant increase in visceral fat weight by 151 % and visceral obesity index (ratio of fat weight to body weight) by 107 % compared to controls. In experimental rats with high level of energy metabolism, the weight of visceral fat was 35 % lower ($p<0.05$) than in animals with low level of energy metabolism.

Histological analysis showed that visceral white adipose tissue in both control and experimental rats was composed of parenchymal and connective tissue components. The parenchyma is represented by fat cells adipocytes. The adipocytes appeared optically empty with a narrow cytoplasmic border under the cytolemma. In the thickened part of the cytoplasmic rim, a flattened nucleus was observed, which had shifted to the edge of the cell (due to a large fat droplet). The adipocytes were quite close together. The shape and size of the adipocytes varied between groups. For example, in control animals the cells were mostly oval and elongated, whereas in rats with visceral obesity they were often irregular in shape and large in size. In both control and experimental rats, the connective tissue component of visceral white adipose tissue was represented by microcirculatory vessels, lymphatic capillaries, nerve fibres and connective tissue fibres. Layers of loose connective tissue divided the parenchyma into lobes (Fig. 1).

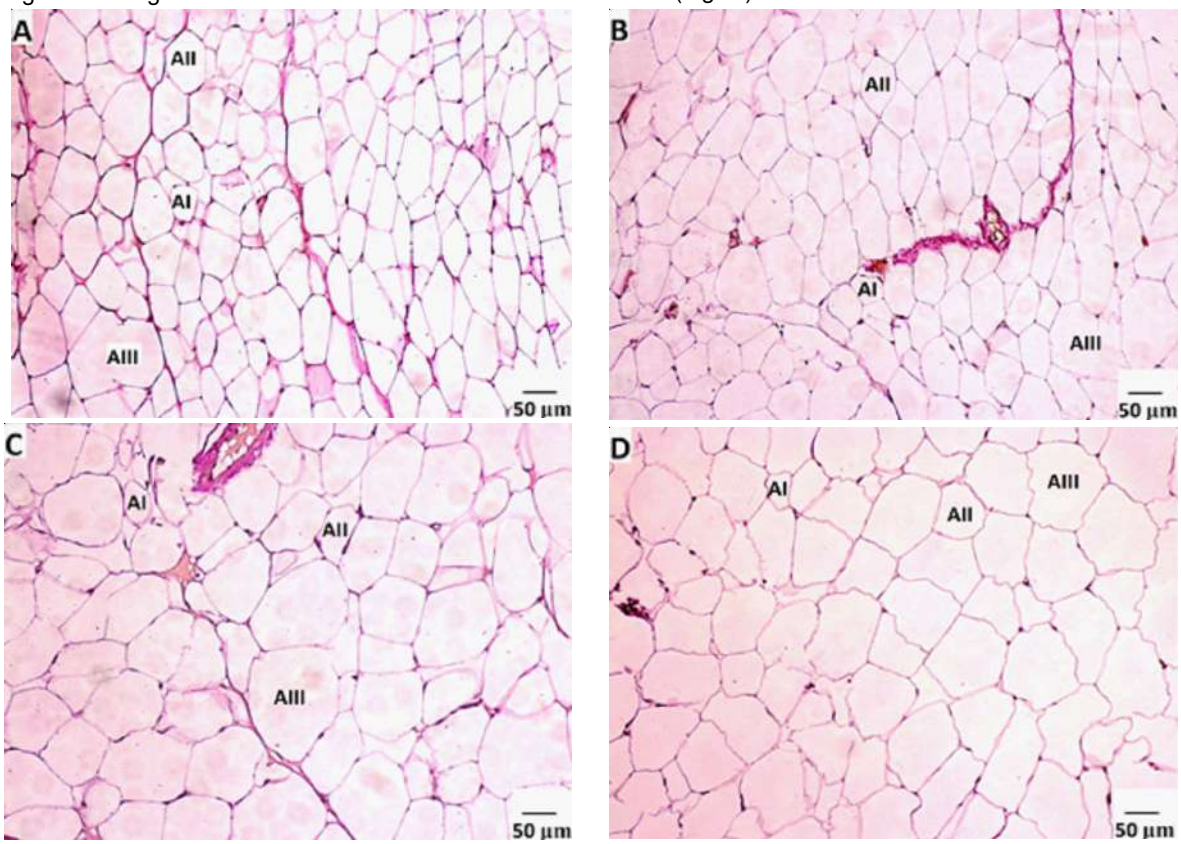

Fig. 1. Microphotography of the visceral white fat of the control rat (A – low level of metabolism, B – high level of metabolism) and a rat with visceral obesity (C – low level of metabolism, D – high level of metabolism). AI – diameter <50 µm, AII – diameter 50-100 µm, AIII – diameter >100 µm. Staining by the Van Gieson. ×200.

The effect of high calorie diet altered the morphological structure of rat visceral white adipose tissue, leading to hypertrophy of adipocytes, decreased blood saturation of adipose tissue and increased amount of connective tissue in it. The structural changes were most pronounced in experimental rats with low level of energy metabolism (see Fig. 1).

In the visceral white adipose tissue of low level of energy metabolism rats exposed to high calorie diet, more significant structural changes were found than in high level of energy metabolism experimental animals compared to controls. The diameter and cross-sectional area of the adipocytes in the low level of energy metabolism rats were 25 % and 72 % larger ($p<0.05$), respectively, and the thickness of the cell walls 19 % smaller than in the controls. At the same time, the density of adipocyte arrangement per unit area was 39 % lower ($p<0.05$) (Table 1). In experimental animals with low level of energy metabolism, the number of adipocytes of type AI (<50 мм) was 24 % lower ($p<0.05$) and the number of AII (50-100 мм) and AIII (>100 мм) cells was 50 % and 529 % higher ($p<0.05$), respectively, than in control animals with corresponding level of energy metabolism (Fig. 2). The relative area of connective tissue was also greater by 19 % ($p<0.05$; see Table 1).

Table 1. Histomorphometric indicators of white adipose tissue (M±SD, n=6).

Indicators	Control		Obesity	
	Low levels of consumption O_2	High levels of consumption O_2	Low levels of consumption O_2	High levels of consumption O_2
Adipocyte diameter,μm	48.72±2.33	53.73±3.50	60.76±3.02^	55.54±3.20
Adipocyte area, $μm^2$	2369±170	2692±179	4065±198^	2823±152*
Adipocyte nucleus area, $μm^2$	19.02±3.29	16.54±1.93	19.34±2.78	18.93±2.34
Adipocyte placement density, pcs/mm^2	330.4±23.1	258.3±22.1*	202.9±25.2^	268.0±26.5*
The thickness of the adipocytes walls, μm	1.530±0.201	1.751±0.110	1.243±0.151	1.741±0.133*
Relative area, % parenchyma connective tissue vessels	 90.31±3.48 5.310±0.702 4.412±1.101	 91.80±3.60 4.012±0.645 4.201±0.836	 89.31±2.65 6.311±0.502 4.414±0.919	 91.80±3.43 4.502±0.501* 3.721±0.950
Connective tissue-parenchyma index	0.111±0.075	0.089±0.015	0.121±0.062	0.089±0.063
Trophic index	0.049±0.098	0.046±0.098	0.049±0.075	0.041±0.059

Note: here and in the table 2: *$p<0.05$ significant compared to rats with low metabolism of the respective group; ^$p<0.05$ significant compared to control rats with the corresponding level of metabolism.

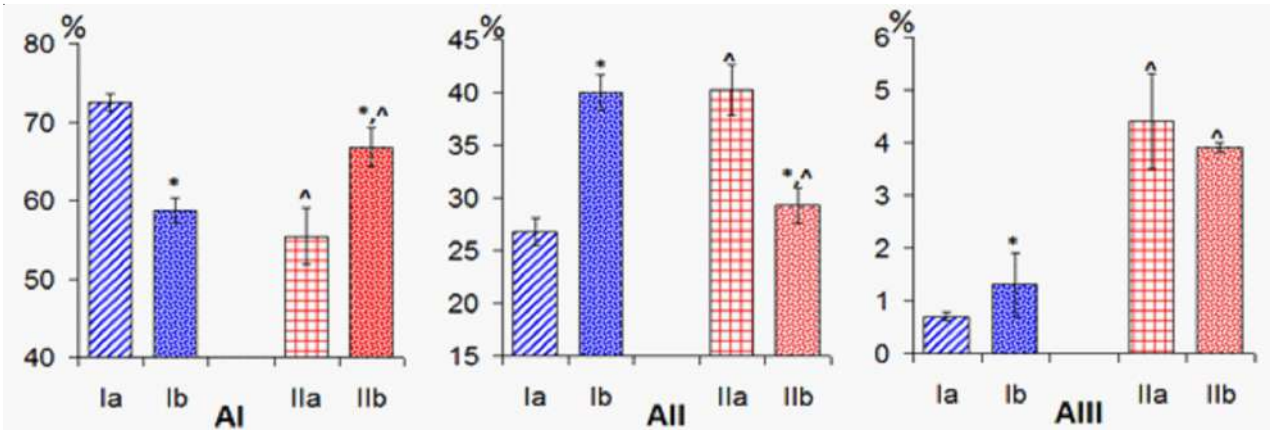

Fig. 2. Distribution of adipocytes by size: AI – diameter <50 μm, AII – diameter 50-100 μm, AIII – diameter >100 μm. The number of cells of each type is represented as a percentage of the total number of adipocytes: Ia i Ib – control rats with low and high levels of oxygen consumption; IIa i IIb – rats with low and high levels of oxygen consumption that were in a high-calorie diet. *$p<0.05$ significant compared to rats with low metabolism of the respective group; ^$p<0.05$ significant compared to control rats with the corresponding level of metabolism.

A 14 % higher number of AI-type adipocytes ($p<0.05$), a 27 % lower number of AII cells ($p<0.05$) and a 200 % higher number of AIII cells ($p<0.05$) were observed in the visceral white adipose tissue of experimental animals with high level of energy metabolism compared to control animals with the corresponding level of energy metabolism (see Fig. 2). Other morphometric indicators remained close to control values (see Table 1).

Comparison of the histomorphometric indicators obtained between rats with different level of energy metabolism after exposure to high-calorie diet revealed certain differences in the structure of visceral white adipose tissue. In experimental rats with high level of energy metabolism, the cross-sectional area of adipocytes was significantly smaller by 31 % ($p<0.05$) than in experimental animals with low level of energy metabolism. At the same time, the density of adipocyte placement per unit area was 32 % higher ($p<0.05$) (see Table 1). In experimental animals with high level of energy metabolism, a significantly higher number of adipocytes of type AI was observed by 21 % ($p<0.05$), a lower number of AII cells by 27 % ($p<0.05$) and AIII cells by 11 % than in experimental animals with low level of energy metabolism (see Fig. 2). In the visceral white adipose tissue of rats with high level of energy metabolism, the relative area of connective tissue and the stromal-parenchymal index were smaller by 29 % ($p<0.05$) and 26 %, respectively. Relative vascular area and trophic index were also 16 % and 18 % lower, respectively, in these animals compared to rats with low level of energy metabolism. In rats with high level of energy metabolism, adipocyte wall thickness was significantly greater by 40 % (see Table 1). Therefore, visceral obesity was much more pronounced in rats with low level of energy metabolism than in animals with high metabolism.

The morphological data are confirmed by biochemical indicators of lipid metabolism in blood serum. In rats with low level of energy metabolism, the concentrations of lipids, triglycerides and cholesterol were increased by 51 % ($p<0.05$), 84 % ($p<0.05$) and 14 %, respectively, compared to controls. In animals with high level of energy metabolism, the concentration of lipids was significantly higher by 40 % and triglycerides by 72 % compared to controls. When comparing relevant biochemical indicators between rats with different level of energy metabolism after exposure to high-calorie diet, it was found that in experimental animals with high level of energy metabolism, the concentration of lipids and triglycerides was 19 and 16 % lower, respectively ($p<0.05$), compared to rats with low metabolism (Table 2).

Bioimpedance studies showed that the value of electrical impedance was significantly higher in rats with visceral obesity than in control rats, both at a frequency of 10^4 Hz and at a frequency of 10^6 Hz. At the same time, impedance changes were more pronounced in rats with low level of energy metabolism than in rats with high level of energy metabolism. The impedance-frequency variance ratio was also most significantly reduced in diet-obese rats with low level of energy metabolism. This was apparently due to differences in fat accumulation in the adipocytes of the visceral white adipose tissue of experimental rats with different level of energy metabolism (Fig. 3).

Table 2. Histomorphometric indicators of white adipose tissue (M±SD, n=6).

Indicators	Control		Obesity	
	Low levels of consumption O_2	High levels of consumption O_2	Low levels of consumption O_2	High levels of consumption O_2
Lipids, mmol/l	2.811±0.280	2.455±0.211	4.253±0.209^	3.433±0.230*^
Triglycerides, mg/dl	97.12±6.87	87.51±5.21	179.1±7.2^	150.2±8.5*^
Cholesterol, mmol/l	1.971±0.114	1.921±0.116	2.242±0.131	2.162±0.151

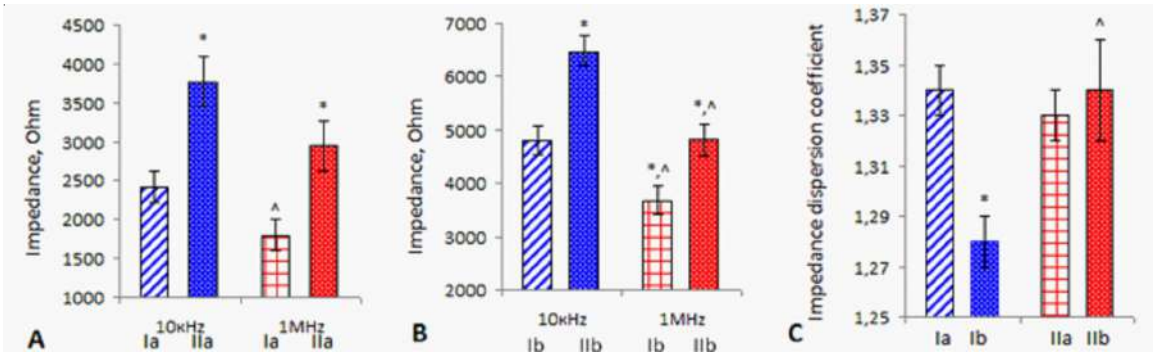

Fig. 3. Impedance of the visceral white adipose tissue of rats with low (**A**) and high (**B**) level of energy metabolism at a frequency of 10 kHz and 1 MHz: Ia – control, IIa – experimental rats with low level of oxygen consumption; Ib – control, IIb – experimental rats with high level of oxygen consumption. Visceral white adipose tissue impedance dispersion coefficient (**C**): Ia – control, Ib – experimental rats with low level of oxygen consumption; IIa – control, IIb – experimental rats with high level of oxygen consumption. *$p<0.05$ – significant compared to rats with low metabolism of the respective group; ^$p<0.05$ – significant compared to control rats with the corresponding level of metabolism.

Discussion

The development of visceral obesity is closely linked to the state of energy metabolism in the body. The level of oxygen consumption reflects the state of metabolic processes and the amount of energy used by the body [19, 23]. We have found that obesity increases oxygen consumption in rats. And the animals' stay in the high calorie diet leads to the development of visceral obesity. This is evidenced by a significant increase in the weight of visceral white adipose tissue, the concentration of lipids, triglycerides and cholesterol in the blood serum of experimental rats. There was a restructuring of the visceral white adipose tissue structure, indicating a hypertrophic type of obesity. Thus, the adipocytes increased in size due to the accumulation of fat in them. In some places, cracks were observed in their thinned walls. Blood saturation of adipose tissue decreased and the amount of connective tissue in it increased, which indicates inhibition of oxygen transport to parenchymal elements, deterioration of conditions for metabolic processes. At the same time, the most pronounced changes in the structure of visceral white adipose tissue with visceral obesity were observed in rats with low level of energy metabolism.

A similar regularity was observed in the analysis of the results of research on the bioelectrical properties of visceral white adipose tissue. It was found that the development of visceral obesity was accompanied not only by quantitative but also by qualitative changes in visceral white adipose tissue, especially in rats with low level of energy metabolism. Further studies are needed to fully understand the mechanisms of the relationship between the level of oxygen consumption, visceral obesity and the state of visceral white adipose tissue.

It is known from the literature that an increase in the weight of visceral white adipose tissue can occur in two ways through hypertrophy or hyperplasia of the adipocytes. In hypertrophy, there is an increase in the size of the adipocytes due to the accumulation of triglycerides in them [13, 22]. In hyperplasia, there is not only an increase in the size of the adipocytes themselves, but also an increase in their number due to differentiation from precursor cells [10]. For a long time it was thought that the number of adipocytes in the visceral white adipose tissue of the adult body was constant and that fat accumulation was due to hypertrophy of pre-existing cells [27]. In recent years, it has been found that a hyperplastic type of obesity can also occur under the influence of certain factors. It is thought that individual adipocytes increase in size until the total mass of adipose tissue in the body does not exceed 30 kg. After that, the number of adipocytes begins to increase [20]. The transition to the hyperplastic type of fat is due to the limited growth capacity of individual adipocytes (normally cells can accumulate a maximum of 1 мм of fat). With excessive accumulation of fat (10 times more than normal) adipocytes acquire the ability to share [2]. Adipocytes hyperplasia leads to the appearance of small cells that are more sensitive to insulin and have a high capacity to store fat [28, 29].

The results obtained are not only of theoretical importance, but also of interest for practical medicine in the development of new effective methods of prevention and treatment of obesity in patients depending on their level of energy metabolism. In the future, we plan to investigate the mechanisms of the relationship between the level of oxygen consumption, obesity and the state of white adipose tissue.

Conclusions

1. Exposure to a high calorie diet for 12 weeks leads to the development of visceral obesity and the appearance of histomorphological changes in white adipose tissue indicative of a hypertrophic type of obesity.

2. The intensity of structural, biochemical and biophysical changes in visceral white adipose tissue is more pronounced in rats with a low level of energy metabolism and depends on the degree of obesity.

References

[1] Aparecida, S. E., Vaseghi, G., de Carvalho Santos, A. S., Kliemann, N., Masoudkabir, F., Noll, M., ... & de Oliveira, C. (2020). Visceral obesity and its shared role in cancer and cardiovascular disease: A scoping review of the pathophysiology and pharmacological treatments. *Int J Mol Sci*, *23*, 9042. doi: 10.3390/ijms21239042

[2] Arner, P., & Rydén, M. (2022). Human white adipose tissue: A highly dynamic metabolic organ. *J Intern Med*, *291*(5), 611-621. doi: 10.1111/joim.13435

[3] Black, M. H., Watanabe, R. M., Trigo, E., Takayanagi, M., Lawrence, J. M., Buchanan, T. A., & Xiang, A. H. (2013). High-fat diet is associated with obesity-mediated insulin resistance and в-cell dysfunction in Mexican Americans. *J Nutr*, *143*(4), 479-485. doi: 10.3945/jn.112.170449

[4] Camacho, S., & Ruppel, A. (2017). Is the calorie concept a real solution to the obesity epidemic? *Glob Health Action*, *10*(1), 1289650. doi: 10.1080/16549716.2017

[5] Cinti, F., & Cinti, S. (2022). The endocrine adipose organ: A system playing a central role in COVID-19. *Cells*, *11*(13), 2109. doi: 10.3390/cells11132109

[6] Costa, S. S., Blotta, R. M., Meurer, L., & Edelweiss, M. I. (2011). Adipocyte morphometric evaluation and angiogenesis in the omentum transposed to the breast: a preliminary study. *Clinics (Sao Paulo)*, *66*(2), 307-312. doi: 10.1590/s1807-59322011000200021

[7] Fruh, S. M. (2017). Obesity: risk factors, complications, and strategies for sustainable long-term weight management. *J Am Assoc Nurse Pract*, *29*(S1), S3-S14. doi: 10.1002/2327-6924.12510

[8] Hanna, D. J., Jamieson, S. T., Lee, C. S., Pluskota, C. A., Bressler, N. J., Benotti, P. N., ... & Still, C. D. (2021). Bioelectrical impedance analysis in managing sarcopenic obesity in NAFLD. *Obes Sci Pract*, *7*(5), 629-645. doi: 10.1002/osp4.509

[9] Harris, R. B. (2014). Direct and indirect effects of leptin on

adipocyte metabolism. *Biochim Biophys Acta*, *1842*(3), 414-423. doi: 10.1016/j.bbadis.2013.05.009
[10] Horwitz, A., & Birk, R. (2023). Adipose tissue hyperplasia and hypertrophy in common and syndromic obesity-the case of BBS obesity. Nutrients, 15(15), 3445. doi: 10.3390/nu15153445
[11] Khalil, S. F., Mohktar, M. S., & Ibrahim F. (2014). The theory and fundamentals of bioimpedance analysis in clinical status monitoring and diagnosis of diseases. Sensors (Basel), 14(6), 10895-10928. doi: 10.3390/s140610895
[12] Liu, F., He, J., Wang, H., Zhu, D., & Bi, Y. (2020). Adipose morphology: a critical factor in regulation of human metabolic diseases and adipose tissue dysfunction. Obes Surg, 30(12), 5086-5100. doi: 10.1007/s11695-020-04983-6
[13] Longo, M., Zatterale, F., Naderi, J., Parrillo, L., Formisano, P., Raciti, G. A., ... & Miele, C. (2019). Adipose tissue dysfunction as determinant of obesity-associated metabolic complications. Int J Mol Sci, 20(9), 2358. doi: 10.3390/ijms20092358
[14] Luo, L., & Liu, M. (2016). Adipose tissue in control of metabolism. J Endocrinol, 231(3), R77-R99. doi: 10.1530/JOE-16-0211
[15] Malik, V. S., Willet, W. C., & Hu, F. B. (2020). Nearly a decade on – trends, risk factors and policy implications in global obesity. Nat Rev Endocrinol, 16, 615-616. doi: 10.1038/s41574-020-00411-y
[16] Miljkovic, D., Drijaca, J., Loverenski, A., & Gajic, M. (2022). A comprehensive morphometric study of visceral and subcutaneous adipose tissue depots in mice, hamsters and rats. Int J Morphol, 40(5), 1219-27. doi: 10.4067/S0717-95022022000501219
[17] Mittal, B. (2019). Subcutaneous adipose tissue & visceral adipose tissue. Indian J Med Res, 149(5), 571-573. doi: 10.4103/ijmr.IJMR_1910_18
[18] Muir, L. A., Neeley, C. K., Meyer, K. A., Baker, N. A., Brosius, A. M., Washabaugh, A. R., ... & O'Rourke, R. W. (2016). Adipose tissue fibrosis, hypertrophy, and hyperplasia: Correlations with diabetes in human obesity. Obesity (Silver Spring), 24(3), 597-605. doi: 10.1002/oby.21377
[19] Ozugur, S., Kunz, L. & Straka, H. (2020). Relationship between oxygen consumption and neuronal activity in a defined neural circuit. BMC Biol, (18), 76. doi: 10.1186/s12915-020-00811-6
[20] Palacios-Marin, I., Serra, D., Jimenez-Chillaron, J., Herrero, L., & Todorcevic, M. (2023). Adipose tissue dynamics: cellular and lipid turnover in health and disease. Nutrients, 15(18), 3968. doi: 10.3390/nu15183968
[21] Rehfeld, A., Nylander, M., & Karnov, K. (2017). Histological Methods. In: Compendium of Histology. Springer, Cham, 11-24.
[22] Sakers, A., De Siqueira, M. K., Seale, P., & Villanueva, C. J. (2022). Adipose-tissue plasticity in health and disease. Cell, 185(3), 419-446. doi: 10.1016/j.cell.2021.12.016
[23] Salin, K., Auer, S. K., Rey, B., Selman, C., & Metcalfe, N. B. (2015). Variation in the link between oxygen consumption and ATP production, and its relevance for animal performance. Proc Biol Sci, 282(1812), 20151028. doi: 10.1098/rspb.2015.1028
[24] Shchelykalina, S. P., Nikolaev, D. V., Kolesnikov, V. A., Korostylev, K. A., & Starunova, O. A. (2021). Technology of two-dimensional bioimpedance analysis of the human body composition. Journal of Electrical Bioimpedance, 12(1), 17-25. doi: 10.2478/joeb-2021-0004
[25] Silva Rosa, S. C., Liu, M., & Sweeney, G. (2021). Adiponectin synthesis, secretion and extravasation from circulation to interstitial space. Physiology (Bethesda), 36(3), 134-149. doi: 10.1152/physiol.00031.2020
[26] Silveira, E. A., Kliemann, N., Noll, M., Sarrafzadegan, N., & de Oliveira, C. (2021). Visceral obesity and incident cancer and cardiovascular disease: An integrative review of the epidemiological evidence. Obes Rev, 22(1), e13088. doi: 10.1111/obr.13088
[27] Spalding, K. L., Arner, E., Westermark, P. O., Bernard, S., Buchholz, B. A., Bergmann, O., ... & Arner, P. (2008). Dynamics of fat cell turnover in humans. Nature, 453, 783-87. doi: 10.1038/nature06902
[28] Strissel, K. J., Stancheva, Z., Miyoshi, H., Perfield, J. W., DeFuria, J., Jick, Z., ... & Obin, M. S. (2007). Adipocyte death, adipose tissue remodeling, and obesity complications. Diabetes, 56, 2910-2918. doi: 10.2337/db07-0767
[29] Trudel, G., Uhthoff, H. K., Wong, K., Dupuis, J., & Laneuville, O. (2019). Adipocyte hyperplasia: the primary mechanism of supraspinatus intramuscular fat accumulation after a complete rotator cuff tendon tear: a study in the rabbit. Adipocyte, 8(1), 144-153. doi: 10.1080/21623945.2019.1609201
[30] White, U. (2023). Adipose tissue expansion in obesity, health, and disease. Front Cell Dev Biol, (11), 1188844. doi: 10.3389/fcell.2023.1188844

МОРФОЛОГІЧНІ ОСОБЛИВОСТІ БІЛОЇ ЖИРОВОЇ ТКАНИНИ У ЩУРІВ З РІЗНИМ РІВНЕМ ЕНЕРГЕТИЧНОГО МЕТАБОЛІЗМУ ПРИ ВІСЦЕРАЛЬНОМУ ОЖИРІННІ

Янко Р. В., Сафонов С. Л., Левашов М. І.

Гістоморфологічні зміни вісцеральної білої жирової тканини при ожирінні в залежності від рівня енергетичного метаболізму в організмі вивчені недостатньо. Метою роботи було дослідити та порівняти структурні зміни вісцеральної білої жирової тканини у щурів з різним метаболізмом та вираженим вісцеральним ожирінням. Дослідження проведено на щурах-самцях лінії Вістар, вік яких на початку експерименту становив 3 міс. Контрольні тварини отримували стандартний раціон харчування. Дослідні щури впродовж 12 тижнів знаходилися на висококалорійному раціоні. Наприкінці експерименту щурів як контрольної, так і дослідної групи, в залежності від інтенсивності загального споживання кисню, розподілили на групи з низьким і високим рівнем енергетичного метаболізму. З вісцеральної білої жирової тканини виготовляли гістологічні препарати за стандартною методикою. Гістоморфометрію здійснювали на цифрових зображеннях за допомогою комп`ютерної програми «Image J 1.34p». Біохімічними методами в сироватці крові визначали концентрацію тригліцеридів, ліпідів та холестерину. Для оцінки біофізичних властивостей вісцеральної білої жирової тканини використовували метод багаточастотної біоімпедансометрії. Отримані дані обробляли методами варіаційної статистики з використанням одностороннього дисперсійного аналізу. Показано, що тривале вживання висококалорійного раціону призводило до розвитку вісцерального ожиріння, котре проявлялося у суттєвому збільшенні маси вісцерального жиру та концентрації показників ліпідного обміну в сироватці крові. Виявлено, що висококалорійний раціон змінював морфологічну структуру вісцеральної білої жирової тканини щурів, а саме призводив до гіпертрофії адипоцитів, зменшував кровонаповненість та збільшував в ній кількість сполучної тканини. Змінювалися біоелектричні властивості вісцеральної білої жирової тканини, про що

свідчило збільшення її електричного імпедансу та зменшення коефіцієнта частотної дисперсії. Таким чином, встановлено, що вплив висококалорійного раціону впродовж 12 тижнів призвів до розвитку вісцерального ожиріння та появи гістоморфологічних змін у білій жировій тканині. Інтенсивність структурних, біохімічних та біофізичних змін у вісцеральній білій жировій тканині більш виражена у щурів з низьким рівнем енергетичного метаболізму і залежить від ступеня ожиріння. Отримані результати мають значення для практичної медицини у розробці нових ефективних методів профілактики та лікування ожиріння у пацієнтів, в залежності від рівня енергетичного метаболізму.
***Ключові слова**: біла жирова тканина, ожиріння, енергетичний метаболізм, щури.*

Author's contribution

Yanko R. V. – research, methodology, data visualization, software, writing an original article.
Safonov S. L. – research, methodology, data visualization, resources.
Levashov M. I. – conceptualization, supervision, formal analysis and verification, editing, project administration.

DOI: 10.31393/morphology-journal-2024-30(4)-06 Reports of Morphology, Vol. 30, №4, Pages 52-57

ISSN 1818-1295 eISSN 2616-6194

REPORTS OF MORPHOLOGY

Official Journal of the Scientific Society of Anatomists, Histologists, Embryologists and Topographic Anatomists of Ukraine

journal homepage: https://morphology-journal.com

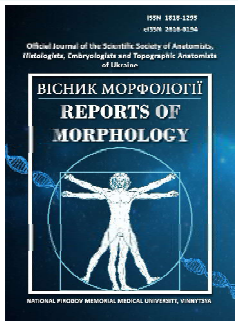

Histological organization of the spleen of rats under conditions of acute intoxication with viper venom Vipera berus berus

Maievskyi O. Ye.[1], Bobr A. M.[2], Gunas I. V.[2], Tkach G. F.[3], Maslii V. P.[2], Kyrychenko I. M.[2], Ihnatishchev M. R.[4]

[1]Educational and Scientific Center "Institute of Biology and Medicine", Taras Shevchenko National University of Kyiv, Kyiv, Ukraine
[2]National Pirogov Memorial Medical University, Vinnytsya, Ukraine
[3]National University of Life and Environmental Sciences of Ukraine, Kyiv, Ukraine
[4]Bogomolets National Medical University,Kyiv, Ukraine

ARTICLE INFO
Received: 20 March 2024
Accepted: 13 September 2024

UDC: 61:612.1:615.9.616.1:616-099

CORRESPONDING AUTHOR
e-mail: maevsklyalex8@gmail.com
Maievskyi O. Ye.

CONFLICT OF INTEREST
The authors have no conflicts of interest to declare.

FUNDING
Not applicable.

DATA SHARING
Data are available upon reasonable request to corresponding author.

The immune system plays an important role in the body's response to numerous environmental factors, including snake venom toxins. The composition of snake venom and the specifics of its effect on the human body are quite diverse. The predominance of one or another component of the toxin becomes decisive for the appearance of complications or even death. The study aims to study the peculiarities of the histological organization of the spleen of rats under conditions of acute intoxication with Vipera berus berus viper venom. Experimental studies were carried out on white, non-linear male rats. The animals were conditionally divided into a control and an experimental group of 10 individuals. Experimental rats were injected intraperitoneally with a semi-lethal dose (LD_{50}) (1.576 mg/g^{-1}) of Vipera berus berus venom in a physiological solution. Animals of the control group were injected intraperitoneally with only a physiological solution. Rats were removed from the experiment 24 hours after exposure to the poison and anaesthetized by cervical dislocation. Spleen samples were taken for microscopic examination. Fixation of the material and preparation of paraffin blocks were carried out according to generally accepted methods. Histological preparations of the spleen were stained with hematoxylin and eosin. Histological preparations were studied using an SEO SCAN light microscope. Acute intoxication with Vipera berus berus viper venom was associated with disorganization of the white pulp of the spleen of experimental animals, which manifested itself in the form of a loss of clarity and orderliness of the placement of its structural elements, poor visualization of the marginal zone of lymphoid nodules. An increase in the number of lymphoblasts characterized the germinal centres. Areas of spleen tissue destruction and hemorrhage were noted in the red pulp of the organ. The presence of foci of lymphocyte apoptosis, thickening of trabeculae, stasis and sludge of erythrocytes in the lumen of trabecular veins was also observed. Thus, under the influence of Vipera berus berus venom, disorganization of the white pulp is observed at the structural level of the rat spleen, and areas of organ destruction, lymphocyte apoptosis, and connective tissue proliferation are noted in the red pulp.

Keywords: *anatomy, histology, spleen, lymphoid nodules, lymphocytes, rats, vipers, poison.*

Introduction

The spleen is one of the most reactive organs, and it shows a rapid response to the action of damaging factors during the early stages of their impact. According to numerous experimental studies, it is essential to develop specific immunological reactions since multiple cell populations ensure the constancy of the body's internal environment [13, 23, 24]. To date, there is convincing evidence that the spleen can maintain the body's resistance in response to the action of physical and chemical environmental factors. However, under conditions of their chronic influence, the reserves of the immune status of the organ suffer significantly. They are depleted due to impaired morphology and functions of critical structural elements. In this regard, among today's scientific studies, more and more studies are focused on studying the pathophysiological pathways of spleen

damage under the influence of adverse factors of various genesis [3, 29, 32, 33].

Snakes use their venom to neutralise prey and to deter or weaken predators [2, 19]. The realisation of these goals is possible because toxins cause the development of muscle paralysis (by blocking the transmission of nerve impulses), cause changes in the functioning of the cardiovascular system, or cause pronounced local lesions at the site of bites [7, 18,]. Among all venomous animals, snakes attract special attention from humanity [11, 16, 17]. On the one hand, such interest is because cases of poisoning by their toxins are prevalent and are among the unsolved health problems worldwide, as they cause numerous fatal consequences [9, 22, 26]. According to WHO estimates, between 81,000 and 138,000 people die from snakebites each year, and another 400,000 victims suffer severe complications or even disability [30].

The immune system is essential in the body's response to numerous environmental factors, including snake venom toxins. The composition of the venom and the features of its effect on the human body are pretty diverse. The predominance of one or another component of the toxin becomes decisive for complications or even death [10, 14]. Despite sufficiently thorough and large-scale studies by scientists worldwide, individual components of snake toxins, the features of their action and the pathogenesis of damage to internal organs have not yet been established. In particular, the mechanisms of spleen damage under these conditions have not been fully revealed, and information about the features of morphological changes in organs at the light-optical and submicroscopic levels has not been provided. In addition, data on the effect of V. berus berus viper toxins on the structure and function of the immune system are currently absent. Therefore, research on this issue with the aim of early diagnosis, prevention of complications, and opportunities to improve treatment methods is an urgent task.

The study aims to investigate the features of the histological organization of the spleen of rats under acute intoxication with the viper Vipera berus berus venom.

Materials and methods

The experimental study was conducted with special care and attention to the condition of the animals. The rats underwent a thorough 7-days acclimatization in a particular Taras Shevchenko National University of Kyiv animal facility. This was followed by transfer to laboratory conditions with strict adherence to temperature and light regimes [12]. During this period, the rats received standard food and water ad libitum. The experiment was conducted per the Recommendations of the National Institute of Health for the Care and Use of Laboratory Animals and the European Council Directive of November 24, 1986, on the Care and Use of Laboratory Animals (86/609/EEC). The study was approved and confirmed by the Bioethics Commission of the Institute of Biology and Medicine of the Taras Shevchenko National University of Kyiv (protocol No. 2, dated August 19, 2021). The venom of Vipera berus berus used in our study was obtained from the V. N. Karazin Kharkiv National University. The lyophilized native venom was carefully stored at -20 °C and dissolved in saline immediately before the experiment, ensuring our study's highest scientific accuracy and reliability.

The animals were divided into two groups of 10 individuals: control and experimental. In saline, experimental rats were intraperitoneally injected with a semi-lethal dose (LD_{50}) (1.576 mg/g^{-1}) of Vipera berus berus venom. Animals in the control group were intraperitoneally injected with saline only. Rats were removed from the experiment 24 hours after exposure to the venom and euthanized by cervical dislocation.

Spleen samples were taken from previously weighed animals of all groups for microscopic examination. The pieces were fixed in 10 % formalin solution, and the duration of exposure did not exceed 1-2 days. The applied fixative solution prevents the process of autolysis and stabilises cells and tissues for further processing and use in staining procedures. Then, the pieces were dehydrated in alcohols with increasing concentration and embedded in paraffin blocks. Histological preparations of the spleen were stained with hematoxylin and eosin [4, 18]. Histological preparations were examined on an SEO SCAN light microscope and photo-documented using a Vision CCD camera with an image output system from histological preparations.

Results

Modelling acute intoxication with the viper Vipera berus berus venom was associated with the development of histological changes in the spleen of experimental rats. Microscopic examination of the organ revealed disorganization of the white pulp structure. In particular, lymphoid nodules had indistinct contours; their marginal zone was almost not differentiated. In addition, enlarged germinative centres with a significant number of lymphoblasts were visualised, distinguished by large sizes, hypochromic nuclei and pale cytoplasm. Mature B-lymphocytes in the reactive centres of lymphoid nodules were significantly less than lymphoblasts. A moderate number of T-lymphocytes and macrophages characterized periarterial zones of lymphoid nodules. Small light and dark lymphocytes were mainly noted. The lumens of the central arteries were rounded, and their walls were somewhat thickened, mainly due to the middle and adventitious membranes. The endothelial lining of the central arteries' intima mainly was continuous, with loosening of the endothelial layer observed in some places (Fig. 1).

In the spleen's red pulp, under the administration of Vipera berus berus venom to rats, numerous erythrocytes, platelets, lymphocytes, plasma cells and macrophages were detected. In some areas of the red pulp, foci of the destruction of the spleen tissue and haemorrhage were

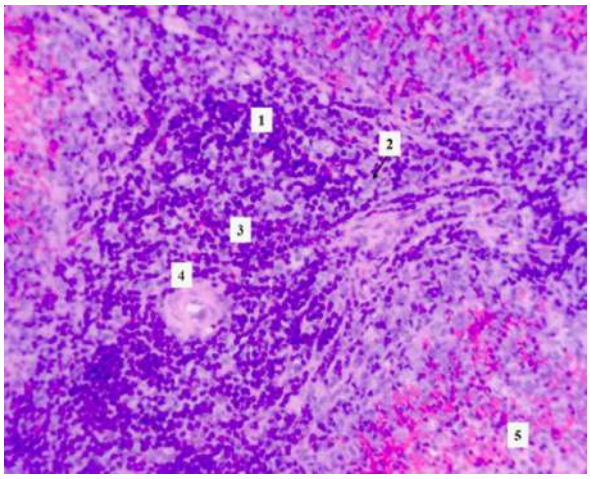

Fig. 1. Morphological changes in the spleen of rats exposed to the viper Vipera berus berus venom. Lymphoid nodule (1), lymphoblasts (2), marginal zone (3), central artery (4), red pulp (5). Staining with hematoxylin and eosin. ×400.

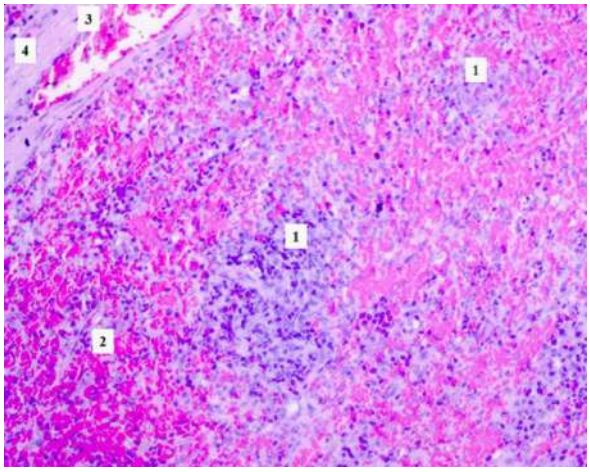

Fig. 2. Histological structure of the spleen of rats under the influence of the viper Vipera berus berus venom. Lymphoid nodules (1), the red pulp (2), the lumen of the trabecular vein (3) and splenic trabeculae (4). Staining with hematoxylin and eosin. ×400.

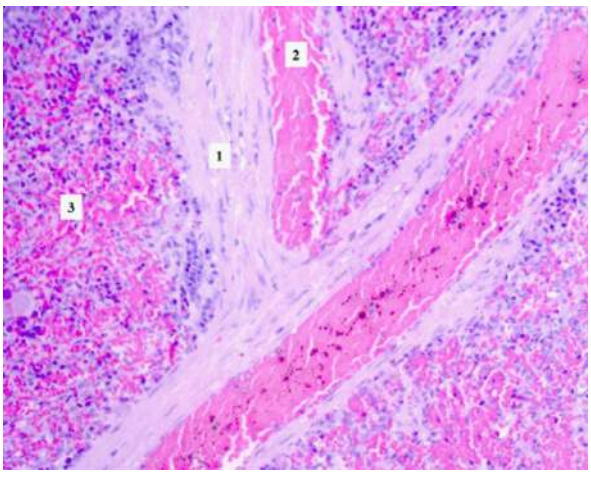

Fig. 3. Photo-optical changes in the structure of the spleen of rats under the influence of the venom of the viper Vipera berus berus. Splenic trabeculae (1), trabecular vein (2), red pulp (3). Staining with hematoxylin and eosin. ×400.

observed. Lymphocytes in the red pulp had a rounded shape. Their nuclei were hyperchromic; the cytoplasm occupied a small part of the cell, and sometimes, it was not visualized or was concentrated paranuclearly in the form of a rim. Plasma cells of the spleen had a rounded or slightly elongated shape. Their nuclei were shifted to the cell poles and were hyperchromic. In the red pulp, numerous macrophages were large and had processes. The nuclei of these cells occupied an eccentric position. The cytoplasm was sometimes illuminated, swollen, and contained remnants of phagocytised material. It should be noted that areas of lymphocyte apoptosis were observed during histological examination of the spleen of rats injected with the venom of the viper Vipera berus berus. The trabeculae of the spleen under these conditions were thickened. The smooth myocytes had elongated nuclei in their composition. The spaces between the muscle fibres were dilated, and the fibres were swollen. The trabecular veins had precise contours. Stasis and sludge of erythrocytes and adhesion of erythrocytes to the walls of the veins were detected in their lumen (Fig. 2, 3).

Discussion

The immune system plays an essential role in the body's response to numerous environmental factors that affect the ordinary course of physiological processes. An immune response accompanies any changes in homeostasis. According to the literature, the latter is also induced in the case of bites of poisonous animals, including snakes. It has been established that their toxins can activate the type II immune response; however, as recent studies have shown, the features of the pathogenesis of the interaction of this body system and viper venom are much more complex [8, 21]. Given the wide variety of enzymes and non-enzymatic components in its composition, it is unsurprising that the consequence is developing a pronounced inflammatory process. Its mechanisms are still being studied. However, the main participants are PLA2 and SVMP [15]. The high activity of PLA2 in snake venom maintains a significant concentration of arachidonic acid and associated cytokines [5]. Also, the effect of toxins triggers the production of IL-6, TNF-6, IL-1, chemokines, and lipid mediators, creating conditions for the activation and migration of leukocytes. Lipid mediators (prostaglandins, leukotrienes, thromboxanes) accompany the inflammatory process, manifesting various pathological effects (oedema, pain). It is a proven fact that snake toxins can activate endogenous PLA2. The latter affect ryanodine receptors, activate protein kinase C, release Ca^{2+}, and, thus, form a persistent humoral immune response.

Studies by Kou J. Q. [20] and Wang S. Z. [29] have shown that viper venom exerts a pronounced effect on cellular and humoral immune responses. Toxins obtained from the Naja naja atra species in mice with normal immunity increased the activity of NK cells and the proliferation of B lymphocytes. Also, in this group of animals, they suppressed the delayed-

type hypersensitivity reaction caused by dinitrofluorobenzene and inhibited the proliferation of T lymphocytes stimulated by concavalin A. In mice with moderately expressed immunodeficiency states, administering the venom of this species of viper caused an increase in the levels of Ig G and Ig M and the restoration of germinal centres in the spleen. In addition, in spleen cells examined by flow cytometry, a selective increase in Th1, Th2, IFN-r, and IL-4 levels and a decrease in IL-17 were observed.

According to scientific sources, PLA2 from snake venom activates inflammasomes. The latter are multiprotein complexes located in the cytoplasm of immune cells. They can recognise and respond to infectious agents, damage, etc. One of the most studied is the NLRP3 inflammasome (nucleotide oligomeric domain, leucine-rich protein). In the case of the interaction of PLA2, in which the catalytic domain contains lysine (at position 49) instead of aspartate and is characteristic of the venom of the snake Bothrops jararacussu, with cell membranes, NLRP3 is activated, which causes the formation of the inflammasome complex. Activated NLRP3 promotes the interaction procaspase-1 with ASC (apoptosis-associated cytosolic adaptor protein). This process leads to the formation of caspase-1, the release of IL-1β and the initiation of apoptosis [6].

Snake venoms are capable of modulating the immune system, particularly at the level of cytokine production. Venom components of some members of the Elapidae family have been shown to exhibit anti-arthritic and anti-inflammatory activity in rats, primarily through a reduction in serum levels of the pro-inflammatory cytokines IL-1β, IL-17, and TNF-α. At the same time, intraperitoneal injection of Bothrops atrox and Bothrops erythromelas venoms into mice resulted in an inflammatory response characterised by an increase in multiple serum and spleen cytokines, such as TNF-α, IL-6, IL-10, IL-12p70, and IFN-γ [25].

The crude venom of Montivipera bornmuelleri has antimicrobial activity against gram-positive and gram-negative bacteria, with the most significant effect on Staphylococcus aureus and Morganella morganii, as well as against the fungus Candida albicans [1]. This species of snake has been found to contain toxic compounds that affect components of the immune system of the spleen of mice. T. Yacoub et al. [31] investigated the effect of intraperitoneal injection of multiple doses of Montivipera bornmuelleri venom on the levels of various cytokines (TNF-α, IFN-γ, IL-4, IL-10, IL-1β and IL-17) in the spleen tissue of BALB/c mice, which helped further to evaluate the potential use of the venom in immunotherapy. The study showed that Montivipera bornmuelleri venom can significantly modulate the immune system towards a pro-inflammatory Th1/Th17 response rather than an anti-inflammatory Th2/Treg response. This shift is likely mediated and maintained by an increase in the production of pro-inflammatory cytokines – IL-1β, TNF-α and IFN-γ and by the suppression of the anti-inflammatory cytokine IL-10 on the other hand, which is regulated by the ability of the venom to induce the production of IL-4. These results, together with the finding that Montivipera bornmuelleri venom is selectively cytotoxic to human keratinocyte cancer cell lines (low-grade II4) compared to the non-tumor HaCaT cell line, demonstrate that this venom is valuable in the field of immunotherapy [27, 28].

Conclusions

1. Acute intoxication with the venom of the viper Vipera berus berus leads to disorganization of the white pulp of the spleen of experimental animals, which manifests itself in a loss of clarity and orderliness in the placement of its structural elements and poor visualization of the marginal zone of lymphoid nodules. An increase in the number of lymphoblasts characterizes germinative centres.

2. In the organ's red pulp, areas of destruction of the spleen tissue and haemorrhages are noted. There are also foci of lymphocyte apoptosis, thickening of trabeculae, stasis, and erythrocyte sludge in the lumens of the trabecular veins.

References

[1] Accary, C., Hraoui-Bloquet, S., Hamze, M., Mallem, Y., El Omar, F., Sabatier, J. M., … Fajloun, Z. (2018). Protein content analysis and antimicrobial activity of the crude venom of Montivipera bornmuelleri; a viper from Lebanon. *Infect Disord Drug Targets*, *18*(1), 49-55. doi: 10.2174/1871526514666140522114754

[2] Almeida, J. R., Resende, L. M., Watanabe, R. K., Carregari, V. C., Huancahuire-Vega, S., da S Caldeira, C. A., … Da Silva, S. L. (2017). Snake venom peptides and low mass proteins: Molecular tools and therapeutic agents. *Curr Med Chem*, *4*(30), 3254-3282. doi: 10.2174/0929867323666161028155611

[3] Avilova, O., Shyian, D., Marakushin, D., Erokhina, V., & Gargin, V. (2018). Ultrastructural changes in the organs of the immune system under the influence of xenobiotics. *Georgian Med News*, (279), 132-137. PMID: 30035735

[4] Bagriy, M. M., Dibrova, V. A., Popadynets, O. G., & Hryschuk, M. I. (2016). *Методики морфологічних досліджень* [*Methods of morphological research*]. Вінниця: Нова книга=Vinnytsia: New Book.

[5] Boda, F., Banfai, K., Garai, K., Curticapean, A., Berta, L., Sipos, E., … Kvell, K. (2018). Effect of vipera ammodytes ammodytes snake venom on the human cytokine network. *Toxins (Basel)*, *10*(7), 259. doi: 10.3390/toxins10070259

[6] Boeno, C. N., Paloschi, M. V., Lopes, J. A., Pires, W. L., Setúbal, S. D. S., Evangelista, J. R., … Zuliani, J. P. (2019). Inflammasome activation induced by a snake venom Lys49-phospholipase A_2 homologue. *Toxins (Basel)*, *12*(1), 22. doi: 10.3390/toxins12010022

[7] Bolon, I., Durso, A. M., Mesa, S. B., Ray, N., Alcoba, G., Chappuis, F., … Ruiz de Castaneda, R. (2020). Identifying the snake: first scoping review on practices of communities and

healthcare providers confronted with snakebite across the world. *PLoS One*, *15*(3), e0229989. doi: 10.1371/journal.pone.0229989

[8] Burin, S. M., Menaldo, D. L., Sampaio, S. V., Frantz, F. G., & Castro, F. A. (2018). An overview of the immune modulating effects of enzymatic toxins from snake venoms. *Int J Biol Macromol*, (109), 664-671. doi: 10.1016/j.ijbiomac.2017.12.101.

[9] Casewell, N. R., Jackson, T. N. W., Laustsen, A. H., & Sunagar, K. (2020). Causes and consequences of snake venom variation. *Trends Pharmacol Sci*, *41*(8), 570-581. doi: 10.1016/j.tips.2020.05.006

[10] Chan, Y. S., Cheung, R. C. F., Xia, L., Wong, J. H., Ng, T. B., & Chan, W. Y. (2016). Snake venom toxins: toxicity and medicinal applications. *Appl Microbiol Biotechnol*, *100*(14), 6165-6181. doi: 10.1007/s00253-016-7610-9

[11] Di Nicola, M. R., Pontara, A., Kass, G. E. N., Kramer, N. I., Avella, I., Pampena, R., … Paolino, G. (2021). Vipers of major clinical relevance in Europe: Taxonomy, venom composition, toxicology and clinical management of human bites. *Toxicology*, (453), 152724. doi: 10.1016/j.tox.2021.152724

[12] Dobrelia, N. V., Boitsova, L. V. & Danova, I. V. (2015). Правова база для проведення етичної експертизи доклінічних досліджень лікарських засобів з використанням лабораторних тварин [Legal basis for ethical examination of preclinical studies of drugs using laboratory animals]. *Фармакологія та лікарська токсикологія=Pharmacology and drug toxicology*, (2), 95-100.

[13] Feriani, D. J., Sousa, A. S., Delbin, M. A., Ruberti, O. M., Crestani, C. C., & Rodrigues, B. (2021). Spleen tissue changes after restraint stress: effects of aerobic exercise training. *Stress*, *24*(5), 572-583. doi: 10.1080/10253890.2021.1895112

[14] Frangieh, J., Rima, M., Fajloun, Z., Henrion, D., Sabatier, J. M., Legros, C., … Mattei, C. (2021). Snake Venom Components: Tools and cures to target cardiovascular diseases. *Molecules*, *26*(8), 2223. doi: 10.3390/molecules26082223

[15] Giannotti, K. C., Leiguez, E., Carvalho, A. E. Z., Nascimento, N. G., Matsubara, M. H., Fortes-Dias, C. L., … Teixeira, C. (2017). A snake venom group IIA PLA_2 with immunomodulatory activity induces formation of lipid droplets containing 15-d-PGJ_2 in macrophages. *Sci Rep*, *7*(1), 4098. doi: 10.1038/s41598-017-04498-8

[16] Gutiérrez, J. M., Calvete, J. J., Habib, A. G., Harrison, R. A., Williams, D. J., & Warrell, D. A. (2017). Snakebite envenoming. *Nat Rev Dis Primers*, (3), 17063. doi: 10.1038/nrdp.2017.63

[17] Herzig, V., Cristofori-Armstrong, B., Israel, M. R., Nixon, S. A., Vetter, I., & King, G. F. (2020). Animal toxins natures evolutionary-refined toolkit for basic research and drug discovery. *Biochem Pharmacol*, (181), 114096. doi: 10.1016/j.bcp.2020.114096

[18] Horalskyi, L. P., Khomych, V. T., & Kononskyi, O. I. (2011). *Основи гістологічної техніки і морфофункціональні методи досліджень у нормі та при патології* [*Fundamentals of histological technique and morphofunctional research methods in normal and pathology*]. Житомир, Полісся=Zhytomyr: Polissya.

[19] Kalita, B., Patra, A., Das, A., & Mukherjee, A. K. (2018). Proteomic analysis and immune-profiling of Eastern India Russells Viper (Daboia russelii) venom: correlation between RVV composition and clinical manifestations post RV bite. *J Proteome Res*, *17*(8), 2819-2833. doi: 10.1021/acs.jproteome.8b00291

[20] Kou, J. Q., Han, R., Xu, Y. L., Ding, X. L., Wang, S. Z., Chen, C. X., … Qin, Z. H. (2014). Differential effects of Naja naja atra venom on immune activity. *Evid Based Complement Alternat Med*, *2014*, 287631. doi: 10.1155/2014/287631

[21] Lisnychuk, N., Soroka, Y., Andrijchuk, I., Nebesna, Z., & Volkov, K. (2018). Histological changes in spleen under conditions of toxic carcinogenesis. *Georgian Med News*, (280-281), 160-164. PMID: 30204117

[22] Liu, J., Wang, H. W., Zhao, W. P., Li, X. T., Lin, L., & Zhou, B. H. (2019). Induction of pathological changes and impaired expression of cytokines in developing female rat spleen after chronic excess fluoride exposure. *Toxicol Ind Health*, *35*(1), 43-52. doi: 10.1177/0748233718809773

[23] Malina, T., Krecsák, L., Westerström, A., Szemán-Nagy, G., Gyémánt, G., M-Hamvas, M., … Vasas, G. (2017). Individual variability of venom from the European adder (Vipera berus berus) from one locality in Eastern Hungary. *Toxicon*, (135), 59-70. doi: 10.1016/j.toxicon.2017.06.004

[24] Minghui, R., Malecela, M. N., Cooke, E., & Abela-Ridder, B. (2019). WHO's snakebite envenoming strategy for prevention and control. *Lancet Glob Health*, *7*(7), 837-838. doi: 10.1016/S2214-109X(19)30225-6

[25] Moreira, V., Dos-Santos, M. C., Nascimento, N. G., Borges da Silva, H., Fernandes, C. M., D'Império Lima, M. R., & Teixeira, C. (2019). Local inflammatory events induced by Bothrops atrox snake venom and the release of distinct classes of inflammatory mediators. *Toxicon*, *60*(1), 12-20. doi: 10.1016/j.toxicon.2019.03.004.

[26] Paolino, G., Di Nicola, M. R., Pontara, A., Didona, D., Moliterni, E., Mercuri, S. R., … Pampena, R. (2020). Vipera snakebite in Europe: a systematic review of a neglected disease. *J Eur Acad Dermatol Venereol*, *34*(10), 2247-2260. doi: 10.1111/jdv.16722

[27] Rima, M., Accary, C., Haddad, K., Sadek, R., Hraoui-Bloquet, S., Desfontis, J. C., & Fajloun, Z. (2013). Identification of L-amino acid oxidase (Mb-LAAO) with antibacterial activity in the venom of Montivipera bornmuelleri, a viper from Lebanon. *Infect Disord Drug Targets*, *13*(5), 337-43. doi: 10.2174/18715265130514040312233 4

[28] Sawan S, Yaacoub T, Hraoui-Bloquet S, Sadek R, Hleihel W, Fajloun Z, & Karam M. (2017). Montivipera bornmuelleri venom selectively exhibits high cytotoxic effects on keratinocytes cancer cell lines. *Exp Toxicol Pathol*, *69*(4), 173-178. doi: 10.1016/j.etp.2017.01.001

[29] Wang, S. Z., & Qin, Z. H. (2018). Anti-Inflammatory and immune regulatory actions of Naja naja atra venom. *Toxins (Basel)*, *10*(3), 100. doi: 10.3390/toxins10030100

[30] Williams, H. F., Layfield, H. J., Vallance, T., Patel, K., Bicknell, A. B., Trim, S. A., … Vaiyapuri, S. (2019). The urgent need to develop novel strategies for the diagnosis and treatment of snakebites. *Toxins (Basel)*, *11*(6), 363. doi: 10.3390/toxins11060363

[31] Yacoub, T., Rima, M., Sadek, R., Hleihel, W., Fajloun, Z., & Karam, M. (2018). Montivipera bornmuelleri venom has immunomodulatory effects mainly up-regulating pro-inflammatory cytokines in the spleens of mice. *Toxicol Rep*, (5), 318-323. doi: 10.1016/j.toxrep.2018.02.011

[32] Zanetti, G., Duregotti, E., Locatelli, C. A., Giampreti, A., Lonati, D., Rossetto, O., … Pirazzini, M. (2018). Variability in venom composition of European viper subspecies limits the cross-

effectiveness of antivenoms. *Sci Rep*, *8*(1), 9818. doi: 10.1038/s41598-018-28135-0

[33] Zinenko, O., Tovstukha, I., & Korniyenko, Y. (2020). PLA_2 Inhibitor Varespladib as an Alternative to the Antivenom Treatment for Bites from Nikolsky's Viper Vipera berus nikolskii. *Toxins (Basel)*, *12*(6), 356. doi: 10.3390/toxins12060356

ГІСТОЛОГІЧНА ОРГАНІЗАЦІЯ СЕЛЕЗІНКИ ЩУРІВ ЗА УМОВ ГОСТРОЇ ІНТОКСИКАЦІЇ ОТРУТОЮ ГАДЮК VIPERA BERUS BERUS

Маєвський О. Є., Бобр А. М., Гунас І. В., Ткач Г. Ф., Маслій В. П., Кириченко І. М., Ігнатіщев М. Р.

Імунна система відіграє важливу роль в реакції організму на чисельні фактори середовища, в тому числі токсинів зміїних отрут. Склад отрути змій та особливості її впливу на організм людини є досить різноманітними. Переважання того, чи іншого компоненту токсину стає визначальним для появи ускладнень чи навіть смерті. Метою дослідження є вивчення особливостей гістологічної організації селезінки щурів за умов гострої інтоксикації отрутою гадюк Vipera berus berus. Експериментальні дослідження проводили на білих нелінійних щурах самцях. Тварин умовно розподіляли на дві групи – контрольну і дослідну по 10 особин в кожній. Дослідним щурам внутрішньоочеревинно вводили напівлетальну дозу (LD_{50}) (1,576 мг/г$^{-1}$) отрути Vipera berus berus на фізіологічному розчині. Тваринам контрольної групи внутрішньоочеревинно вводили лише фізіологічний розчин. Виводили щурів з експерименту через 24 години після впливу отрути, знеживлюючи шляхом цервікальної дислокації. Для мікроскопічного дослідження забирали зразки селезінки. Фіксацію матеріалу та приготування парафінових блоків проводили за загальноприйнятими методиками. Забарвлення гістологічних препаратів селезінки здійснювали гематоксиліном та еозином. Гістологічні препарати вивчали за допомогою світлового мікроскопа SEO SCAN. Гостра інтоксикація отрутою гадюк Vipera berus berus асоціювалась з дезорганізацією білої пульпи селезінки дослідних тварин, що проявлялась у вигляді втрати чіткості та впорядкованості розміщення її структурних елементів, поганою візуалізацією крайової зони лімфоїдних вузликів. Гермінативні центри характеризувались зростанням чисельності лімфобластів. В червоній пульпі органу відмічали ділянки деструкції тканини селезінки, геморагії. Спостерігали також наявність вогнищ апоптозу лімфоцитів, потовщення трабекул, стази і сладжі еритроцитів в просвітах трабекулярних вен. Таким чином, під впливом дії отрути Vipera berus berus на структурному рівні селезінки щурів спостерігається дезорганізація білої пульпи, а в червоній пульпі відмічаються ділянки деструкції органу, апоптоз лімфоцитів та розростання сполучної тканини.

Ключові слова: *анатомія, гістологія, селезінка, лімфоїдні вузлики, лімфоцити, щури, гадюки, отрута.*

Author's contribution

Maievskyi O. Ye. – research, review writing and editing.
Bobr A. M. – conceptualisation, research, and writing of the original draft.
Gunas I. V. – project administration.
Tkach G. F. – methodology.
Maslii V. P. – validation.
Kyrychenko I. M. – formal analysis.
Ihnatishchev M. R. – software, resources.

DOI: 10.31393/morphology-journal-2024-30(4)-07 Reports of Morphology, Vol. 30, №4, Pages 58-66

ISSN 1818-1295 eISSN 2616-6194

REPORTS OF MORPHOLOGY

Official Journal of the Scientific Society of Anatomists, Histologists, Embryologists and Topographic Anatomists of Ukraine

journal homepage: https://morphology-journal.com

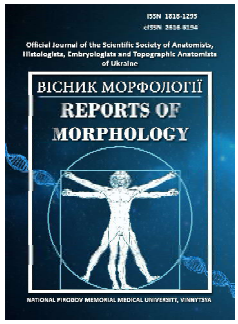

Histo-morphometric evaluation of post-augmentation bone tissue of the human mandible

Oshurko A. P.[1], Oliinyk I. Yu.[2], Maystruk M. V.[1], Sukhliak V. V.[1], Tsurkan M. M.[2], Ruskovoloshyn D. V.[2]

[1]State Establishment "Lugansk State Medical University", Rivne, Ukraine
[2]HEI Bukovinian State Medical University Of The Ministry Of Health Of Ukraine, Chernivtsi, Ukraine

ARTICLE INFO
Received: 27 February 2024
Accepted: 18 September 2024

UDC: 616.314.22.018.4-089.844-044.954-071.3

CORRESPONDING AUTHOR
e-mail: olijnyk1961@gmail.com
Oliinyk I. Yu.

CONFLICT OF INTEREST
The authors have no conflicts of interest to declare.

FUNDING
Not applicable.

DATA SHARING
Data are available upon reasonable request to corresponding author.

The clinical challenge of today is to restore the biological structure of atrophied bone tissue by combining methods of complex clinical rehabilitation, that is, intraosseous implantation and augmentation, in its interimplant sites. The aim of the study was to perform a histo-morphometric assessment of post-augmentation bone tissue using a combined technique of controlled autocellular transplantation with the use of bone allograft filler on edentulous distal segments of the human mandible with varying degrees and forms of atrophy. Trepanbiopsy specimens were used as the study material, after microtomy processing of which histological slides were prepared, followed by the accelerated May-Grunwald staining-fixation technique (Sigma-Aldrich, St. Louis, USA). For the histomorphometric study, stained histological specimens of post-augmentation bone tissue were imaged with an optical microscope camera (Leica DMLB, Germany). The analysis was performed using the Fiji information software, with the formation of reconstructed mosaic digital micrographs for further histomorphometry. The results of the evaluation of controlled bone tissue formation (post-augmentation), which are the key tasks, novelty, and justification of modern and effective methods of rehabilitation of patients with acquired forms of atrophy in the edentulous distal segments of the human mandible, are illustrated by microphotographs and presented in detail in this paper by the percentage of the quality of cross-linking of the cortical layer. The ratio of the newly formed cortical layer of bone tissue to the total area of the post-augmentation tissue study was 61.30 %, with a lateral form of atrophy (according to J. Cawood and R. Howell: class IV), in the post-augmentation period 4 months. The histo-morphometric assessment of the qualitatively formed cortical bone in the post-augmentation period of six months is 92.80 % of the total postoperative area. Therefore, it is biased to evaluate the quality of the formed bone in the mandible within the generally accepted average period of four months, although paraclinical densitometry shows positive values.

Keywords: *bone atrophy, morphometry, augmentation, mandible, human.*

Introduction

The edentulous mandible in human postnatal ontogeny is increasingly becoming an object of modern research. It acquires characteristics that depend on the strength and time of exposure to polyetiological factors, control of remodeling processes, and mineralization (maturation), that is, on the course of metabolic processes that lead to pathophysiological and morphological changes [18, 20, 22, 25].

An important indicator for assessing the controlled formation of bone (post-augmentation) tissue as a result of its directed regeneration [2, 26] is the quality of cross-linking of the cortical layer with the reproduction of histomorphological architectonics [14, 16, 31]. After all, the cortical layer is the hardest tissue of the mandible, which serves as a protective mechanical and permanent isolation barrier. The loss of its density in localized sites indicates the activity of remodeling processes, or the manifestation of pathological inflammatory-destructive or dystrophic processes as a result of metabolic disorders, etc [5, 12, 13]. Understanding these mechanisms and mastering the skills of densitometric assessment is a reliable basis for clinical diagnosis and planning of surgical operations. At the same time, the paraclinical differentiation between remodeling processes [4, 24] and inflammatory and destructive changes during radiographic densitometry is difficult. Therefore, most clinicians decide to postpone the

previously drawn up plan for the full rehabilitation of edentulous patients until the above manifestations "fade" or regress, which will result from the general functional state of the human body, acquiring new qualitative and quantitative characteristics of bone tissue [11, 15].

Another gap in research is the lack of accurate data describing the processes of bone tissue restoration, depending on the method of directed regeneration in a combination of bone replacement materials of biological and artificial origin with automeso concentrate or other biological and artificial activators [21, 27, 28].

The priority tasks in the study of post-augmentation bone tissue were aimed at studying: the acquired morphological, histological (overview) architectonics (general structure); activity (severity) of remodeling (physiologically replacement) processes of bone tissue; assessment of the qualitative characteristics of the newly formed cortical and trabecular layers of bone tissue over time.

That is why both the researcher and the clinician faced a twofold problem in choosing reliable diagnostic methods, or focusing on the results of the studies [6, 29, 32], as well as the data we have obtained below.

At first glance, bone grafting has long been used in maxillofacial surgery, demonstrating its priority on atrophied edentulous segments of the lower/upper jaws, affecting topographic changes in the canal(s) of the lower jaw [1, 7, 17], the position of the teeth of the upper jaws to their sinuses, and changes in bone density of even adjacent morphological structures.

The use of bone autografts or their substitutes faces certain difficulties in timely clinical support, due to the lack of a national "donor bone bank", which forces the use of existing fractional stocks in urgent cases, not always for their intended purpose. To achieve good integration of bone grafts and simplify the procedures for the formation and reproduction of the biological structure of bone, we have mastered the combined technique of controlled autocellular transplantation (Endoret - PRGF, Spain) with the development of our results, which are detailed in this paper.

The aim of the work was to perform a histo-morphometric assessment of post-augmentation bone tissue using a combined technique of controlled autocellular transplantation with the use of bone allograft filler on edentulous distal segments of the human mandible with varying degrees and forms of atrophy.

Materials and methods.

An equally important stage is the collection of newly formed bone tissue using standard rotating protocol trepanation osteotomes (BTIs) in the defined sites of the human mandible and for analytical comparison in two sites of the right and left upper jaws in the projection of the first and second large molar teeth (Table 1).

For proper fixation of the biopsy material, a buffered neutral 10 % formalin solution was used. It was prepared in the ratio: 9 parts of phosphate buffer with pH 7.2-7.4 and 1 part of formalin (formalin 10 ml, tap water 90 ml, NaH_2PO_4 0.4 g, Na_2HPO_4 0.65 g). In this way, a fixing effect was achieved and cross-links were formed between proteins and nucleic acids (NAs): protein-protein, protein-NAs, and NAs-NAs.

It is clear that at a high concentration gradient, diffusion processes will occur rapidly and can damage or deform the post-augmentation bone material under study. That is why, for dehydration, the samples were not placed directly in pure ethyl alcohol, but a set of alcohol solutions with a gradual increase in concentration was used: 70 °, 80 °, 90 °, and 96 °, each for 2 (two) hours.

The samples were then transferred to molten pure paraffin. To do this, paraffin wax in a porcelain cup was placed in a thermostat in advance (several days before pouring) at a temperature 2-3 °C higher than the melting point of paraffin wax (56 °C), poured into laboratory block molds, into which the samples were transferred. Double portions of paraffin wax were used to better rid them of organic solvent residues.

After microtomic processing and preparation of

Table 1. Histo-morphometric analysis of post-augmentation bone tissue of the lower (A, B, C, D, E, F) and upper (H, I) human jaws.

No. of marking	AS, μm^2	Post-augmentation period, months	AF, μm^2	AS/AF ratio, %
A	1560879649	4	956660353	61.30
B	3512170701	4	1505813540	42.90
C	3364192514	6	3123476138	92.80
D	3830031835	6	1881446888	49.10
E	2231635550	6	1173544.816	52.60
F	1693794773	10	1377650262	81.30
H	3071512894	8.0	1840123131	59.90
I	3027724997	8.0	1633063262	53.90

Notes: AS – the area of bone tissue under study; AF – the area of well-formed bone tissue.

histological specimens, we used the accelerated May-Grunwald staining-fixation technique (TU U 20.5-20650786-004:2012) to meet the outlined objectives.

Before staining, a working solution of the May-Grunwald stain-fixative was prepared by diluting it with neutral water in a ratio of 1:2 to 1:5. Neutral water was prepared according to the instructions as follows:

1) dissolve 9.50 g of anhydrous sodium phosphate in 900 mL of distilled water. Bring the water level to 1000 ml and mix well (solution A);

2) dissolve 9.07 g of potassium phosphoric acid monosubstituted in 900 mL of distilled water. Bring the water level to 1000 ml and mix well (solution B);

3) pour 63 mL of solution A and 37 mL of solution B into a 1000 mL volumetric cylinder and bring to 1000 mL with distilled water. The pH of the resulting neutral water was determined using a pH meter. The pH value was 7.0±0.2.

Undiluted May-Grunwald stain-fixative (Sigma-Aldrich, St. Louis, USA) was applied to unfixed sections to cover the entire section. After 3 minutes, the fixative dye was washed off with neutral water and then stained with a diluted working solution of the fixative dye for 10-15 minutes. Then they were washed with neutral water, air-dried, and examined under an optical microscope (Leica DMLB, Germany).

For histo-morphometric studies, stained histological specimens of post-augmentation bone tissue were photographed with an optical microscope camera (Leica DMLB, Germany). The analysis was carried out using the information software "Fiji", with the formation of reconstructive mosaic digital micrographs (Fig. 1) for further histo-, morphometry, the results of which are presented in Table 1.

Informed Consents provided and signed by patients regarding their participation in research in compliance with the main provisions of the GDPR (1996), the Council of Europe Convention on Human Rights and Biomedicine (04.04. 1997), the Declaration of Helsinki of the World Medical Association for the Ethical Principles of Scientific Medical Research Involving Human Subjects (1964-2013), Order of the Ministry of Health of Ukraine No. 690 of 23.09.2009, No. 616 of 03.08.2012 and approved by the decision of the Commission on Biomedical Ethics of Bukovinian State Medical University (Protocol No. 2 of 21.10.2021).

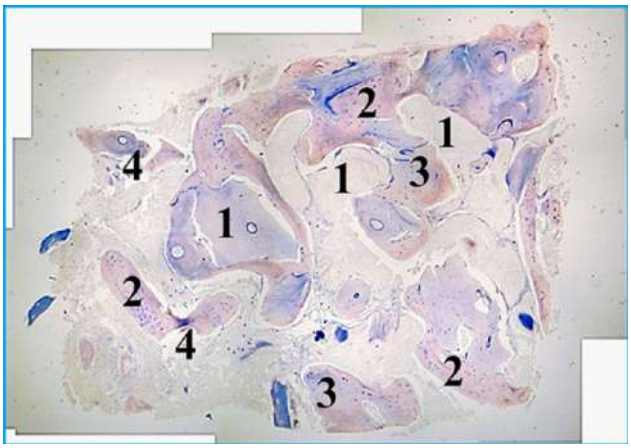

Fig. 1. Post-augmentation biopsy material of the distal edentulous segment of the mandible above the implant in the projection of the first large molar tooth of the mandible on the left side. 1 – sites of a well-formed cortical layer; 2 – sites of active bone remodeling; 3 – sites at the stage of completion of cortical formation; 4 – sites of cortical prolapse (flexion), and granulation replacement. Staining: according to May-Grunwald (Sigma-Aldrich, St. Louis, USA). Microphotograph by the method of programmatic (mosaic) reconstruction. Zoom: ×320.

The work is a fragment of the initiative research work of the Department of Histology, Cytology and Embryology of Bukovinian State Medical University "Structural and functional features of tissues and organs in ontogenesis, patterns of variant, constitutional, gender, age and comparative human morphology", state registration number 0121U110121.

Results

Our research aspiration was to evaluate the quality of the newly formed cortical layer of post-augmentation bone tissue, which was performed using the technique of controlled autocellular transplantation (Endoret PRGF, Spain) with the use of bone allograft (Human-Corticalis, Germany).

The most challenging task of today is to restore the biological structure of atrophied bone tissue by combining methods of complex clinical rehabilitation, that is, intraosseous implantation and augmentation, in its interimplant sites. The first iatrogenic obstacle is a significant loss of intraosseous trophic nutrition of the site. The second is blocking the main canal, which provides not only nutrition but also innervation and drainage function of this segment of bone tissue. Therefore, it is not an objective decision to assess the quality of the formed bone within the generally accepted average period of 4 months, although paraclinical densitometry determines positive values. Our clinical rationale for maintaining the density of post-augmentation bone tissue even at the stages of remodeling is based on the quality of allogeneic homograft and its dispersion (grinding, size, shape). The ratio of the newly formed cortical layer of bone tissue to the total area of the post-augmentation tissue study was 61.30 % (Fig. 2, see Table 1).

The deficit of cortical cross-linking over the implant, which is placed using the subcortical implantation technique, occurs due to a violation of histomorphological reconstruction at the stages of its osseointegration, which is limited by an artificial temporary block (plug). In this case, time only works to reverse the process cortical deproficit (Fig. 3). These conditions reduce the coefficient of the newly formed cortical bone layer from the total area of the post-augmentation tissue study to 42.90% (see Table 1).

Partial decortication and stability of the bone augmentation, in the lateral form of atrophy with adequate body height and cellular part of the mandible, even with insufficient bone width, contributes to a positive prognostic result (Fig. 4).

Taking into account the volume of surgical interventions performed and the increase in the planned width of the operative toothless distal segment of the mandible,

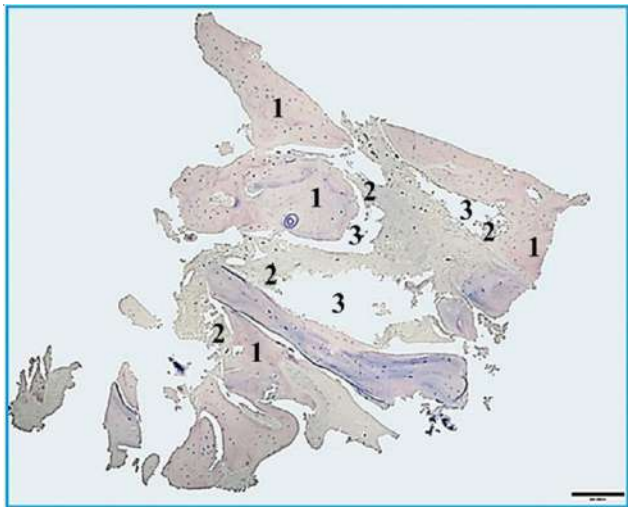

Fig. 2. A – post-augmentation biopsy material of the distal edentulous segment between the implants in the projection of the first and second large molar teeth of the lower jaw on the left, from the buccal side. Clinical diagnosis: Lateral atrophy (according to J. Cawood and R. Howell: class IV – the ridge of the mandible in the form of a knife blade, adequate height, and insufficient bone width). The post-augmentation period is 4 months. 1 – sites of a well-formed cortical layer; 2 – sites of active bone remodeling; 3 – sites of cortical prolapse (flexion), and granulation replacement. Coloring: according to May-Grunwald-Gimza (MGG). Microphotograph. Zoom: ×320.

extending the post-augmentation period to six months, we achieved 92.80% of the well-formed cortical bone area (see Fig. 4, table 1).

The use of combined techniques in the treatment of a pronounced horizontal form of atrophy on edentulous distal segments, even after ensuring full stability of the augmentation, does not provide confidence in the restoration of the predicted volume of both the height and width of the body and the cellular part of the mandible. Accordingly, the expectations for the histological and morphological quality of the newly formed cortical layer, even if the clinical observation of the post-augmentation period is prolonged, are unjustified (Fig. 5).

The coefficient of the ratio of the newly formed cortical layer of bone tissue to the total area of the post-augmentation tissue study, after treatment of the horizontal form of atrophy class V flat ridge, was only 49.10 % (see Fig. 5, table 1).

The study of a similar form of atrophy in the same post-augmentation period as described above, over the implant in the projection of 3.6 tooth, showed better results, where the quality of cortical cross-linking was 52.60 % (Fig. 6, see Table 1).

This pattern is because the bone tissue under study was taken from the site on the border of the functioning dentition. Accordingly, the quality of trophic support is higher, which contributed to the formation of the cortical layer.

The study of bone tissue after the conservation of the post-extraction socket of the tooth without an implant,

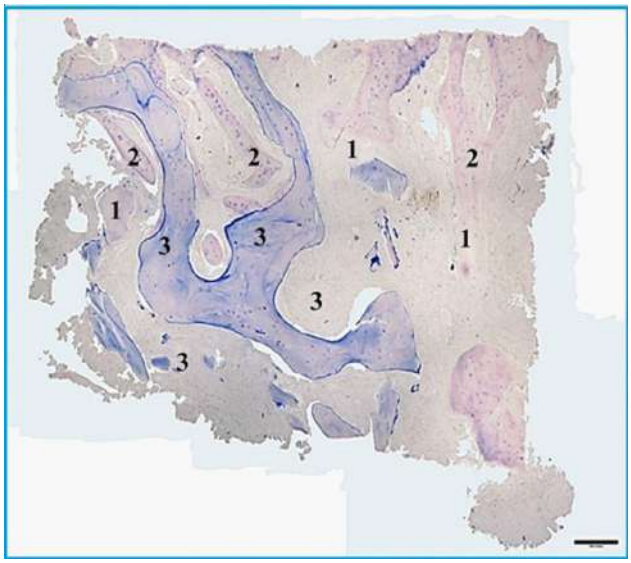

Fig. 3. B – post-augmentation biopsy material of the distal edentulous segment of the mandible above the implant in the projection of the first large molar tooth on the right side. Horizontal form of atrophy (according to J. Cawood and R. Howell: class VI – depression of the ridge, loss of bone tissue of the body of the mandible). The post-augmentation period is 4 months. 1 – sites of a well-formed cortical layer; 2 – sites of active bone remodeling; 3 – sites at the stage of completion of cortical formation. Coloring: according to May-Grunwald-Gimza (MGG). Microphotograph. Zoom: ×320.

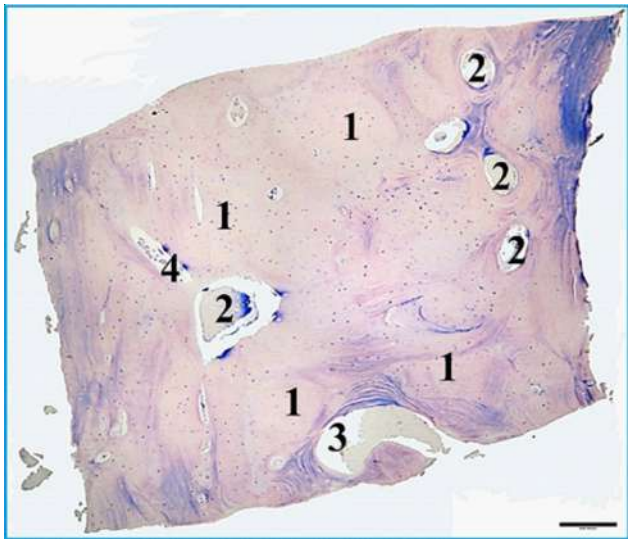

Fig. 4. C – post-augmentation biopsy material of the distal edentulous segment between the implants on the buccal side of the mandible of the first and second large molar teeth on the right side, with a lateral form of atrophy (according to J. Cawood and R. Howell: class IV – the ridge of the mandible in the form of a knife blade, adequate height, and insufficient bone width). The post-augmentation period is 6 months. 1 – sites at the stage of completion of cortical formation; 2 – sites of active apositional bone growth; 3 – site of cortical prolapse (flexion); 4 – site of active replacement (displacement) of granulation germination. Coloring: according to May-Grunwald-Gimza (MGG). Microphotograph. Zoom: ×320.

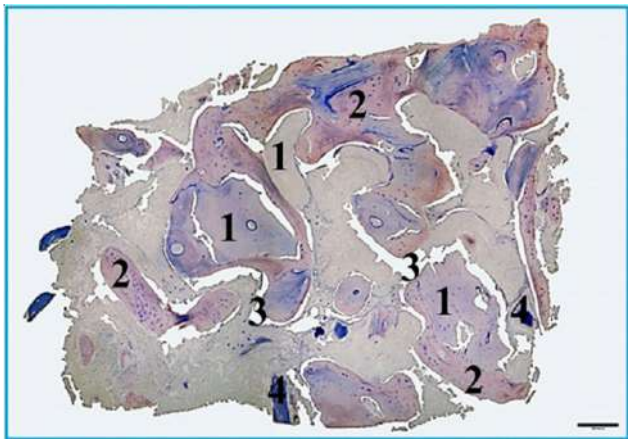

Fig. 5. D – post-augmentation biopsy material of the distal edentulous segment of the mandible above the implant in the projection of the second large molar tooth on the left side, with a horizontal form of atrophy (according to J. Cawood and R. Howell: class V – flat ridge of the mandible, insufficient height and width of the bone). The post-augmentation period is 6 months. 1 – sites of well-formed cortical layer; 2 – sites at the stage of completion of cortical formation; 3 – site of cortical prolapse (flexion); 4 – sites with oxidative inclusions from the implant cover. Coloring: according to May-Grunwald-Gimza (MGG). Microphotograph. Zoom: ×320.

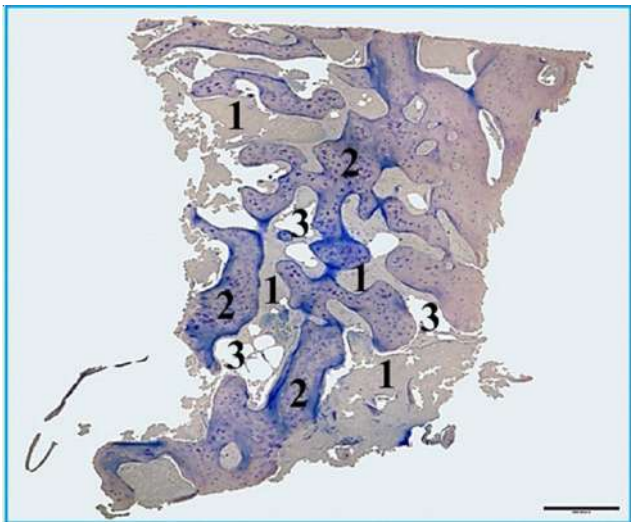

Fig. 6. E – post-augmentation biopsy material of the distal edentulous segment of the mandible above the implant in the projection of the first large molar tooth on the left side, with a horizontal form of atrophy (according to J. Cawood and R. Howell: class V – flat ridge of the mandible, insufficient height and width of the bone). The post-augmentation period is 6 months. 1 – sites of a well-formed cortical layer; 2 – sites of active bone remodeling; 3 – site of cortical prolapse (flexion). Coloring: according to May-Grunwald-Gimza (MGG). Microphotograph. Zoom: ×320.

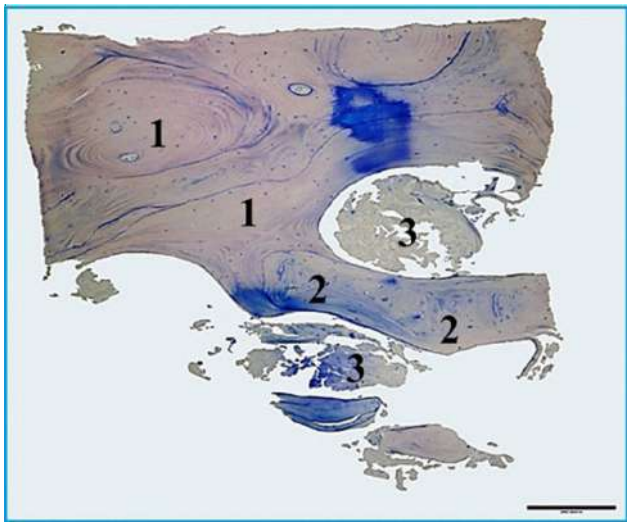

Fig. 7. F – biopsy material after the physiological process of bone tissue regeneration of the mandible, during the conservation of the socket of the first large molar on the right side using the Endoret PRGF technique (without bone replacement materials). The post-augmentation period is 10 months. 1 – sites of well-formed cortical layer; 2 – inter-root septum; 3 – site of active bone remodeling. Coloring: according to May-Grunwald-Gimza (MGG). Microphotograph. Zoom: ×320.

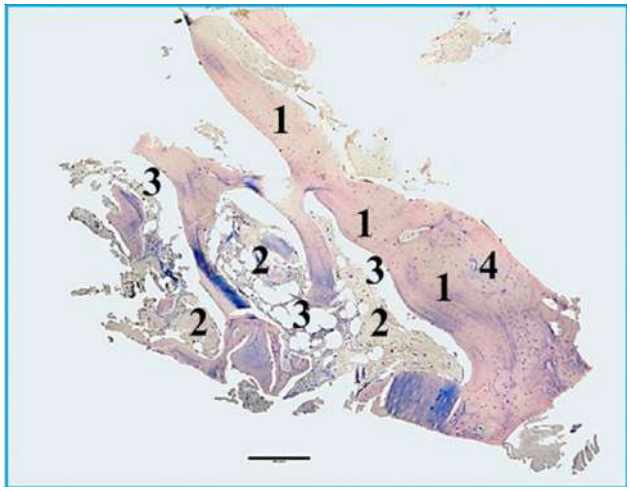

Fig. 8. H – post-augmentation biopsy material was taken from the distal edentulous segment of the upper jaw above the implant in the projection of the second large molar tooth of the upper jaw on the left side, with a mixed form of atrophy. The post-augmentation period is 8 months. 1 – sites of well-formed cortical layer; 2 – site of active bone remodeling; 3 – site of cortical prolapse (flexion); 4 – sites at the stage of completion of cortical formation. Coloring: according to May-Grunwald-Gimza (MGG). Microphotograph. Zoom: ×320.

according to the Endoret - PRGF method, without the use of bone replacement fillers (Fig. 7), under the conditions of the physiological regeneration process, provided a high result of cortical cross-linking by 81.30 % (see Table. 1).

Preservation of the interdental septum and adequate early sealing of the socket using obturation blocks of automesoconcentrate make it impossible to prevent the early development of bone atrophy of the edentulous segment of the jaw.

To compare the results, we studied the post-augmentation biopsy material from the distal edentulous segments of the left (Fig. 8) and right (Fig. 9) sides of the

upper jaw above the implants placed using the subcortical implantation technique. The ratio of the area of cortical cross-linking of the newly formed bone tissue to the total area of the study was: in the projection of 1.7 tooth 53.90 % and the projection of 2.7 tooth 59.90 % in the post-augmentation period of 8 months (see Table. 1).

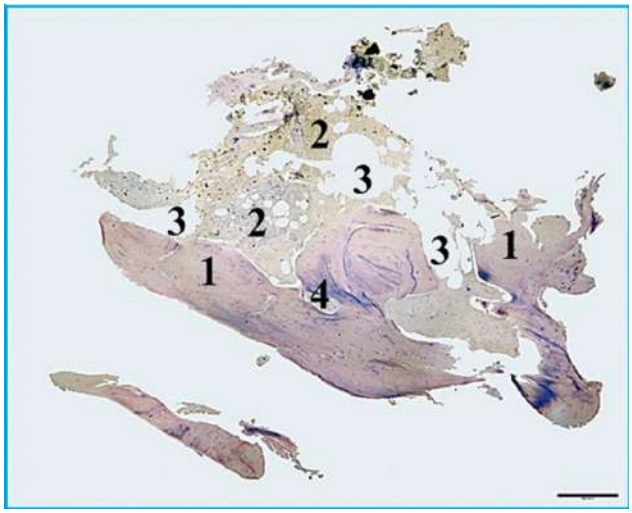

Fig. 9. I – post-augmentation biopsy material of the distal edentulous segment of the upper jaw above the implant in the projection of the first large molar tooth of the upper jaw on the right side, with a mixed form of atrophy. The post-augmentation period is 8 months. 1 – sites of well-formed cortical layer; 2 – site of active bone remodeling; 3 – site of cortical prolapse (flexion); 4 – sites of active apositional bone growth. Coloring: according to May-Grunwald-Gimza (MGG). Microphotograph. Zoom: ×320.

It is clear that the upper jaws, in particular the distal segments, are characterized by lower densitometric parameters and are easily subject to pathomorphological processes of fibrous replacement as a result of epithelial growth due to the loss of the membrane barrier caused by their excessive blood supply in general and in the postoperative period.

Discussion

Traditionally, the quality of bone and tissue repair is usually evaluated in the upper jaw within 4-6 months, and in the lower jaw within 3-4 months.

Scientists Kutsevliak V. F. and Liubchenko O. V. in their work [19] also conducted a layer-by-layer histomorphological assessment of directed bone tissue regeneration (DBTR). They determined the zonation of the regenerate structure on histotopograms with a division into surface and deep zones. The results of DBTR on day 42 are described: in the structure of the regenerate, 1 % of the hematoma remnants, 55 % cell-fiber tissue, 12 % osteoid, and 32 % newly formed bone trabeculae. Thus, the structure of the regenerate was dominated by cell-fiber tissue, well vascularized, with almost no leukocyte infiltration, and the osteogenesis zones occupied the deeper parts of the defect. On the 90th day, histotopograms showed that, according to morphometric data, cell-fiber tissue accounted for only 8 % of the regenerate structure, and a network of osteoid and newly formed bone trabeculae accounted for 92 %, with 9 % of them being large-looped. In the peripheral sites of the bone trabeculae network, the formation of neoplasms of the cortical layer was detected, which occupied 7 %. In other words, the area of cortical cross-linking (reparative osteogenesis) of the mandibular defects at the end of the third month was only 7 %.

Usually, both clinicians and researchers want to keep all tissue regeneration processes under close control to increase the effectiveness of osteotropic drugs on bone regeneration [3, 8, 9, 10, 30]. The researchers contributed to the study of the processes of regeneration of the cellular process of the jaws of experimental animals, on the processes of local resorption, under the influence of osteotropic drugs. A month after the experiment began, complete regeneration of bone plates was noted on almost all the damaged bone tissue, and only in some places narrow bands or islets of cartilage remained. The authors do not describe the quality of cortical layer formation, which makes it impossible to compare the results obtained, but it does open a proper discussion about the concentration and active ingredient of osteotropic drugs.

The results of the original study of ultrastructural changes in bone tissue and periosteum after gunshot and non-gunshot injury to the jaws in rats in the experiment [23] are available, which are presented only on day 7, with proper detail and conclusions, in particular, after gunshot injury, the periosteum shows signs of productive inflammation with connective tissue edema, with the accumulation of a large number of cells of histiogenic origin and with the localization of capillaries between them and the activation of osteoblasts. The bone is being actively restored.

Developing the discussion on the impact of autologous grafts, which are obvious and important for tissue engineering, on the quality of bone formation, the authors give an example of the use of autologous pulp progenitor cells derived from milk or permanent teeth [35], which is a promising source for engineering not only dental tissues. These cells are easy to isolate, easy to propagate in vitro, and ethically unobjectionable, making them an attractive model system for a variety of research applications. At the same time, the lack of universally recognized markers remains a serious problem in the isolation of such stem cells, and there is no standardized method for their isolation or purification. Such an interpretation limits clinical implementation, indicates low ergonomics of the technique, and does not provide confidence in the control of DBG, respectively, and in the final result.

We agree with the conclusions of the authors [34], who described the use of allogeneic bone implants saturated with mesenchymal stem cells (MSCs). Injections of allogeneic MSCs together with allograft immediately after bone injury, regardless of age, caused signs of slowed

bone formation and excessive connective tissue formation, so the combination of allogeneic MSCs with an allogeneic bone implant is inappropriate to use fresh.

We understand that autografts have better biological characteristics, but their scope and application are limited, primarily due to the somatic pathologies of the donor-recipient.

P. R. Verma et al. in their paper [33] provide projects for regional problem solving, which, in our opinion, is a favorable national solution. After all, the need for a skeleton arising from growing clinical demands is compensated by the use of different origin (auto-, allo-, xeno-) grafts and reduces the quality of the biological basis of the body's bone.

Thus, the objective, structured assessment according to clinical protocols presented in our study is a one-step combination of rehabilitation techniques for patients with bone tissue atrophy caused by the loss of the masticatory group of teeth and complicated by the topographic and anatomical features of the mandibular canal(s), which is a reliable and evidence-based clinical basis for the preparation of a treatment plan and a proper prognosis of preservation of the functional state, including the morphological characteristics of the newly formed bone tissue.

Conclusions

1. Complete bone and tissue repair of the cortical layer of the human mandible is not completed within the generally interpreted time frame of 3-4 months of the post-augmentation period.

2. Post-augmentation bone tissue formed by the technique of controlled autocellular transplantation using bone allograft filler on edentulous distal segments of the human mandible of various degrees and forms of their atrophy, according to histo-morphometric assessment, is 92.80 % of the qualitatively formed cortical bone area within the post-augmentation period of 6 months.

3. The process of regeneration of the bone tissue of the human mandible, under conditions of preservation of the post-extraction socket of the tooth, using the Endoret PRGF technique (without bone replacement materials), ensures the formation of the cortical layer in the postoperative period within 10 months by 81.30 %.

References

[1] Ahmed, A. A., Ahmed, R. M., Jamleh, A., & Spagnuolo, G. (2021). Morphometric Analysis of the Mandibular Canal, Anterior Loop,and Mental Foramen: A Cone-Beam Computed TomographyEvaluation. In *J Environ Res*, *18*(7), 3365. doi: 10.3390/ijerph18073365

[2] Andia, I., Perez-Valle, A., Del Amo, C., & Maffulli, N. (2020). Freeze-Drying of Platelet-Rich Plasma: The Quest for Standardization. *Int J Mol Sci*, *21*(18), 6904. doi: 10.3390/ijms21186904

[3] Anitua, E., Allende, M., & Alkhraisat, M. H. (2022). Unravelling Alveolar Bone Regeneration Ability of Platelet-Rich Plasma: A Systematic Review with Meta-Analysis. *Bioengineering*, *9*(10), 506. doi: 10.3390/bioengineering9100506

[4] Anitua, E., Fuente, M. D. L., Troya, M., Zalduendo, M., & Alkhraisat, M. H. (2022). Autologous Platelet Rich Plasma (PRGF) Preserves Genomic Stability of Gingival Fibroblasts and Alveolar Osteoblasts after Long-Term Cell Culture. *Dentistry Journal*, *10*(9), 173. doi: 10.3390/dj10090173

[5] Baldwin, P., Li, D. J., Auston, D. A., Mir, H. S., Yoon, R. S., & Koval, K. J. (2019). Autograft, allograft, and bone graft substitutes: clinical evidence and indications for use in the setting of orthopaedic trauma surgery. *Journal of Orthopaedic Trauma*, *33*(4), 203-213. doi: 10.1097/BOT.0000000000001420

[6] Bambuliak, A., Kuzniak, N., Lopushniak, L., Dmytrenko, R., & Boichuk, O. (2021). Використання остеопластичних матеріалів для заповнення кісткових дефектів щелеп після проведеного хірургічного лікування пацієнтів груп дослідження [Use of osteoplastic materials to restore bone defects following the surgical treatment]. *Актуальні проблеми сучасної медицини: Вісник Української медичної стоматологічної академії=Actual Problems of the Modern Medicine: Bulletin of Ukrainian Medical Stomatological Academy*, *21*(4), 98-107. doi: 10.31718/2077-1096.21.4.98

[7] Borghesi, A., & Bondioni, M. P. (2021). Unilateral triple mandibularcanal with double mandibular foramen: cone-beam computedtomography findings of an unexpected anatomical variant. *Folia Morphol (Warsz)*, *80*(2), 471-475. doi: 10.5603/FM.a2020.0057

[8] Caponio, V. C. A., Baca-González, L., González-Serrano, J., Torres. J., & Lypez-Pintor, R. M. (2023). Effect of the use of platelet concentrates on new bone formation in alveolar ridge preservation: a systematic review, meta-analysis, and trial sequential analysis. *Clin Oral Investi*, *27*(8), 4131-4146. doi: 10.1007/s00784-023-05126-8

[9] Dienha, O. V., Tsevukh, L. B., Mirchuk, B. M., Konovalov, M. F., Novikova, Zh. O., Tarasenko, I. Y., & Yudina, O. O. (2024). Morphologic assessment of the effectiveness of osteotropic preparations on bone tissue regeneration in experimental animals. *World of medicine and biology*, *1*(87), 197-201. doi: 10.26724/2079-8334-2024-1-87-197-201

[10] DuVal, M., & Alkhraisat, M. H. (2023). Adjunctive Plasma Rich in Growth Factors in the Treatment of Osteomyelitis and Large Odontogenic Cysts Prior to Successful Implant Rehabilitation: Case Report. *Dent J (Basel)*, *11*(8), 184. doi: 10.3390/dj11080184

[11] Frenea-Robin, M., & Marchalot, J. (2022). Basic Principles and Recent Advances in Magnetic Cell Separation. *Magnetochemistry*, 8(1), 11. doi: 10.3390/magnetochemistry8010011

[12] Gautam, D., Arora, N., Gupta, S., George, J., & Malhotra, R. (2021). Megaprosthesis Versus allograft prosthesis composite for the management of massive skeletal defects: a meta-analysis of com-parative studies. *Current reviews in Musculoskeletal Medicine*, *14*(3), 255-270. doi: 10.1007/s12178-021-09707-6

[13] Gharedaghi, M., Peivandi, M. T., Mazloomi, M., Shoorin, H. R., Hasani, M., Seyf, P., & Khazaee, F. (2016). Evaluation of clinical

results and complications of structural allograft reconstruction after bone tumor surgery. *Arch Bone Joint Surgery*, *4*(3), 236-242. PMID: 27517069

[14] Golovina, Y., Malyk, R., Karpinsky, M., & Karpinska, O. (2022). Дослідження рентгенологічної кісткової щільності у пацієнтів з кістковими пухлинами у разі застосування сегментарних кісткових алоімплантатів [Examination of X-ray bone density in patients with bone tumors using segmental bone aloimplants]. *Травма=Trauma, 23*(1), 43-50. doi: 10.22141/1608-1706.1.23.2022.881

[15] Hefzollesan, S. M., Mammadov, F. Y., Arkhmamadova, G. M., & Mammadov, R. M. (2022). Experimental substantiation for applying actovegin in combination with osteoplastic materials in mandibular bone tissue regeneration. *Actual Problems of the Modern Medicine: Bulletin of Ukrainian Medical Stomatological Academy*, *22*(2), 86-91. doi: 10.31718/2077-1096.22.2.86

[16] Huang, Z., He, D., & Li, H. W. (2020). A fluorometric assay of thrombin using magnetic nanoparticles and enzyme-free hybridization chain reaction. *Mikrochim Acta*, *187*(5), 295. doi: 10.1007/s00604-020-04279-7

[17] Iwanaga, J., Takeshita, Y., Matsushita, Y., Hur, M. S., Ibaragi, S., & Tubbs, R. S. (2022). What are the retromolar and bifid/trifid mandibular canals as seen on cone-beam computed tomography? Revisiting classic gross anatomy of the inferior alveolar nerve and correcting terminology. *Surg Radiol Anat*, *44*(1), 147-156. doi: 10.1007/s00276-021-02862-y

[18] Kulynych, M., & Savytska, I. (2021). Регенерація кістки при ліквідації дефекту альвеолярного відростка верхньої щелепи у щурів з аутотрансплататами різного походження та ступеня його наповнення [Bone regeneration during elimination of the upper jaw alveolar process defect in rats with autotransplants of different origin and degree of its filling]. *Вісник стоматології=Stomatological Bulletin*, *112*(3), 2-10. doi: 10.35220/2078-8916-2020-37-3-2-10

[19] Kutsevlyak, V. F., & Lyubchenko, O. V. (2024). Особливості репаративного остеогенезу дірчастих дефектів нижньої щелепи із застосуванням стовбурових клітин жирової тканини на колапановій підложці в експериментальних тварин [Peculiarities of reparative osteogenesis of mandibular perforation defects using adipose tissue stem cells on collagenous scaffold in experimental animals]. *Харківський стоматологічний журнал=Kharkiv Dental Journal*, *1*(1), 13-19. doi: 10.26565/3083 -5607-2024-1-02

[20] Latimer, J. M., Maekawa, S., Yao, Y., Wu, D. T., Chen, M., & Giannobile, W. V. (2021). Regenerative Medicine Technologies to Treat Dental, Oral, and Craniofacial Defects. *Front. Bioeng. Biotechnol*, *9*, 704048. doi: 10.3389/fbioe.2021.704048

[21] Lie, S. A. N., Claessen, R. M. M. A., Leung, C. A. W., Merten, H. A., & Kessler, P. A. W. H. (2022). Non-grafted versus grafted sinus lift procedures for implantation in the atrophic maxilla: a systematic review and meta-analysis of randomized controlled trials. *Int J Oral Maxillofac Surg*, *51*(1), 122-132. doi: 10.1016/j.ijom.2021.03.016

[22] Malanchuk, V. A., Grigorovsky, V. V., & Huseynov, A. N. (2020). Гістологічні зміни і кореляційні залежності морфологічних показників ураження та репарації у кісткових уламків при уламкових переломах нижньої щелепи [Histological changes and correlation of morphological indices of injury and repair in bone splints in comminuted mandibular fractures]. *Вісник стоматології=Stomatological Bulletin*, *113*(4), 63-72. doi: 10.35220/2078-8916-2020-38-4-63-72

[23] Pedchenko, D. M., Guljuk, A. G., Molchaniuk, N. I., & Logai, V. A. (2024). Ультраструктурні зміни кісткової тканини та окістя після вогнепального та невогнепального пошкодження щелеп у щурів в експерименті [Ultrastructural changes in bone tissue and periosteum after gunshot and non-gunshot jaw injuries in rats in the experiment]. *Вісник стоматології=Stomatological Bulletin*, *127*(2), 40-46. doi: 10.35220/2078-8916-2024-52-2.7

[24] Prots, G. (2021). Біохімічні маркери кісткового ремоделювання в прогнозуванні результатів дентальної імплантації [The impact of biological markers of bone remodeling in prognostication of the results of dental implantation]. *Терапевтика=Therapeutics*, *2*(1), 22-26. doi: 10.31793/2709-7404.2021.2-1.22

[25] Raeissadat, S. A., Ghazi Hosseini, P., Bahrami, M. H., Salman Roghani, R., Fathi, M., Gharooee Ahangar, A., & Darvish, M. (2021). The comparison effects of intra-articular injection of Platelet Rich Plasma (PRP), Plasma Rich in Growth Factor (PRGF), Hyaluronic Acid (HA), and ozone in knee osteoarthritis; a one year randomized clinical trial. *BMC Musculoskelet Disord*, *22*(1), 134. doi: 10.1186/s12891-021-04017-x

[26] Rybak, V. A., Kopchak, A. V., Pavlychuk, T. O., & Shnaider, S. A. (2018). Клініко-рентгенологічні особливості ремоделювання аутологічних кісткових трансплантатів та ксеногенних кістково-заміщуючих матеріалів у пацієнтів з дефектами кісток лицевого черепу при застосуванні плазми збагаченої факторами росту [Clinical and radiological features of autologous and xenogeneic bone grafts remodeling in patients with facial bone defects treated with the use of plasma rich in growth factors]. *Вісник стоматології=Stomatological Bulletin*, *3*, 65-75.

[27] Seo, S. J., & Kim, Y. G. (2020). In-situ analysis of the hydration ability of bone graft material using a synchrotron radiation X-ray micro-CT. *Journal of Applied Biomaterials & Functional Materials, 18*, 2280800020963476. doi: 10.1177/2280800020963476

[28] Shpachynskyi, O., Kiss, T., Helyes, & Kopchak, A. (2024). Maxillary Bone Microstructure After Lateral Sinus Flour Augmentation with Deproteinized Bovine Bone Material in Severe Alveolar Bone Atrophy: Comparative Micro-CT Study. *J Maxillofac Oral Surg*, Corpus ID: 268013466. doi: 10.1007/s12663-024-02113-8

[29] Solakoglu, Ц., Heydecke, G., Amiri, N., & Anitua, E. (2020). The use of plasma rich in growth factors (PRGF) in guided tissue regeneration and guided bone regeneration. A review of histological, immunohistochemical, histomorphometrical, radiological and clinical results in humans. *Ann Anat*, *231*, 151528. doi: 10.1016/j.aanat.2020.151528

[30] Stumbras, A., Januzis, G., Gervickas, A., Kubilius, R., & Juodzbalys, G. (2020). Randomized and Controlled Clinical Trial of Bone Healing After Alveolar Ridge Preservation Using Xenografts and Allografts Versus Plasma Rich in Growth Factors. *J Oral Implantol*, *46*(5), 515-525. doi: 10.1563/aaid-joi-D-19-00179

[31] Tripathi, H., Peng, H., Donahue, R., Chelvarajan, L., Gottipati, A., Levitan, B., … & Berron, B. J. (2020). Isolation Methods for Human CD34 Subsets Using Fluorescent and Magnetic Activated Cell Sorting: An In Vivo Comparative Study. *Stem Cell Rev Rep*, *16*, 413-423. doi: 10.1007/s12015-019-09939-7

[32] Valico-Cultelli, V., Varela-Lypez, У., & González-Cantalapiedra, A. (2021). Does PRGF Work? A Prospective Clinical Study in Dogs with A Novel Polylactic Acid Scaffold Injected with PRGF Using the Modified Maquet Technique. *Animals (Basel)*, *11*(8),

2404. doi: 10.3390/ani11082404
[33] Verma, P. R., Anjankar, A., & Singh, P. V. (2022). Need, Strategies and Requirements in the Medical System for Bone Banks: A Review Article. *Cureus*, *14*(9), e28785. doi: 10.7759/cureus.28785
[34] Vorontsov, P. M., Korzh, M. O., Leontieva, F. S., & Tuliakov, V. O. (2023). Біохімічні показники сироватки крові щурів різного віку після заповнення дефекту в метафізі стегнової кістки алогенними кістковими імплантатами, насиченими мезенхімальними стовбуровими клітинами [Serum biochemical indicators in rats of different ages after replacing femoral metaphysis defects with allogeneic bone implants saturated with mesenchymal stem cells]. *Запорізький медичний журнал=Zaporizhzhia Medical Journal*, *25*(5), 421-427. doi: 10.14739/2310-1210.2023.5.274774
[35] Yildirim, S. (2024). *Isolation, Cryopreservation, and Differentiation Methods of DPSC*. In: Dental Pulp Derived Mesenchymal Stromal Cells. Springer, New York, NY. doi: 10.1007/978-1-0716-4244-3_7

ГІСТО-МОРФОМЕТРИЧНА ОЦІНКА ПОСТАУГМЕНТАЦІЙНОЇ КІСТКОВОЇ ТКАНИНИ НИЖНЬОЇ ЩЕЛЕПИ ЛЮДИНИ

Ошурко А. П., Олійник І. Ю., Майструк М. В., Сухляк В. В., Цуркан М. М., Русоволошин Д. В.

Клінічним викликом сьогодення є відновлення біологічної структури атрофованої кісткової тканини, під час поєднання методів комплексної клінічної реабілітації, тобто, внутрішньо-кісткової імплантації та аугментації, на її міжімплантаційних ділянках. Мета дослідження – гісто-морфометрична оцінка постаугментаційної кісткової тканини за комбінованою методикою керованої аутоклітинної трансплантації з використанням кісткового аллонаповнювача, на беззубих дистальних сегментах нижньої щелепи людини з різним ступенем та формами їх атрофії. Як матеріал дослідження в роботі використано трепанбіопсійні зразки, після мікротомічної обробки яких проведено підготовку гістологічних скелець, з подальшим застосуванням прискореної методики забарвлення-фіксації зрізів за Май-Грюнвальдом (Sigma-Aldrich, Сент-Луїс, США). Для гістоморфометричного дослідження забарвлені гістологічні препарати постаугментаційної кісткової тканини знімали камерою оптичного мікроскопа (Leica DMLB, Німеччина). Аналіз проведений за допомогою інформаційного програмного забезпечення «Fiji», з формуванням реконструкційних мозаїчних цифрових мікрофотографій для подальшої гістоморфометрії. Результати оцінки керованого формування кісткової (постаугментаційної) тканини, що є ключовими завданнями, новизною та обґрунтуванням сучасних й ефективних методик реабілітації пацієнтів із набутими формами атрофії на беззубих дистальних сегментах нижньої щелепи людини, ілюстровані мікрофотографіями та деталізовано подаються в даній роботі за відсотковим співвідношенням якості зшивання кортикального шару. Коефіцієнт співвідношення новоутвореного кортикального шару кісткової тканини до загальної площі дослідження постаугментаційної тканини склав 61,30 %, при латеральній формі атрофії (за J. Cawood та R. Howell: клас IV), у постаугментаційний період 4 місяці. Гісто-морфометрична оцінка якісно сформованої кортикальної кістки у терміни постаугментаційного періоду шість місяців складає 92,80 % від загальної постопераційної площі. Тому, проводити оцінку якості сформованої кістки на нижній щелепі, у загально прийнятому усередненому терміні чотирьох місяців, є необ`єктивним рішенням, хоч параклінічна денситометрія визначає позитивні значення.

Ключові слова: *атрофія кісткової тканини, морфометрія, аугментація, нижня щелепа, людина.*

Author's contribution

Oshurko A. P. – work concept and design, data collection and analysis, writing the article, critical review.
Oliinyk I. Yu. – work concept and design, writing the article, final approval of the article.
Maystruk M. V. – writing the article, critical review, final approval of the article.
Sukhliak V. V. – writing the article, critical review, final approval of the article.
Tsurkan M. M. – writing the article, critical review, final approval of the article.
Ruskovoloshyn D. V. – writing the article, critical review, final approval of the article.

DOI: 10.31393/morphology-journal-2024-30(4)-08 Reports of Morphology, Vol. 30, №4, Pages 67-73

ISSN 1818-1295 eISSN 2616-6194

REPORTS OF MORPHOLOGY

Official Journal of the Scientific Society of Anatomists, Histologists, Embryologists and Topographic Anatomists of Ukraine

journal homepage: https://morphology-journal.com

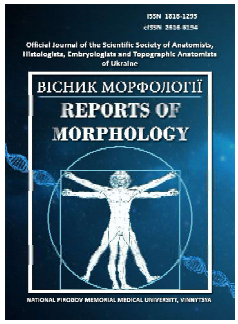

Modeling, based on discriminant analysis, the possibility of occurrence and features of the course of multiple sclerosis in Ukrainian women depending on the features of the structure and sizes of the body

Gunas M. M., Moskovko G. S., Nazarova M. S., Kyrychenko Yu. V., Prokopenko S. V., Ruban M.M.
National Pirogov Memorial Medical University, Vinnytsya, Ukraine

ARTICLE INFO
Received: 13 March 2024
Accepted: 23 September 2024

UDC: 616.832:572.087

CORRESPONDING AUTHOR
e-mail: Neuronchik.gunas@gmail.com
Gunas M. M.

CONFLICT OF INTEREST
The authors have no conflicts of interest to declare.

FUNDING
Not applicable.

DATA SHARING
Data are available upon reasonable request to corresponding author.

Considering the existence of different ways of the course of multiple sclerosis, the disability caused by this disease, modern medicine needs the creation of new, easy-to-use and cheap methods to solve this issue. Promising in this case may be the use of clinical anthropometry, which is already successfully used to predict the forms of development and severity of various diseases of various human organ systems. The objective of the study was to construct and analyze discriminant models predicting the likelihood and characteristics of multiple sclerosis progression in young Ukrainian women, based on anthropometric and somatotypological parameters. A clinical-laboratory and anthropo-somatotypological examination was conducted on 59 young Ukrainian women diagnosed with multiple sclerosis. Disability levels were assessed using the Expanded Disability Status Scale. The control group consisted of primary anthropometric and somatotypological data from 101 healthy Ukrainian women of the same age group (sourced from the database of the Scientific and Research Center of the National Pirogov Memorial Medical University, Vinnytsya). Discriminant models predicting the occurrence and progression of multiple sclerosis based on body anthropo-somatotypological parameters were constructed using the licensed "Statistica 6.0" software. The analysis revealed significant discrimination between healthy individuals and the general multiple sclerosis patient group, as evidenced by the discriminant equations (Wilks' Lambda=0.052, p<0.001). Key contributors to the discrimination models for distinguishing healthy women from those with multiple sclerosis included pelvic dimensions (37.50 %, contributing the most), body circumferences and head dimensions (25.0 % each), and the transverse lower thoracic diameter of the torso (12.5 %). Further analysis differentiated women with multiple sclerosis based on the severity of their symptoms mild, moderate, or moderately severe also demonstrated statistically significant differentiation (Wilks' Lambda=0.349, p<0.001). The most influential factors for mild, moderate, or moderately severe patients groups in these models were distal epiphyseal widths of long tubular bones in the extremities (33.33 %, contributing the most), pelvic conjugate diameter, maximum head length, the ectomorphic component of somatotype according to Heath-Carter, and the skeletal mass component according to Matiegka (each contributing 16.67 %). These findings underscore the importance of anthropometric and somatotypological parameters in predicting multiple sclerosis occurrence and progression severity in young Ukrainian women.

***Keywords**: nervous diseases, multiple sclerosis, anthropo-somatotypological body parameters, discriminant models, practically healthy and sick women.*

Introduction

Multiple sclerosis (MS) is a chronic, autoimmune, inflammatory and degenerative disease of the central nervous system, characterized by the destruction of the myelin sheath of neurons, the formation of sclerotic plaques and progressive damage to the nervous tissue. The disease is one of the leading causes of disability in

young people in the world, as it most often affects people aged 20-40, a period of greatest social, professional and family activity. The pathology arises as a result of an autoimmune process in which the immune system attacks the myelin covering axons, causing nerve conduction disorders and causing numerous neurological symptoms. The symptoms of MS vary from moderate impairment of motor functions to severe disability, including loss of control over the limbs, impaired vision, speech, cognitive function and psychoemotional state, which significantly affects the quality of life of patients and their ability to social integration [6, 20].

MS has a wide geographical distribution, and the incidence of the disease varies depending on climatic, ethnic and socio-economic factors. In countries with a temperate climate, the incidence is much higher. For example, in Europe, the prevalence of MS ranges from 100 to 200 cases per 100,000 population, while in South Asia it is much lower 0.5-10 cases per 100,000 population [9, 12]. At the same time, in the Middle East and North Africa, the prevalence varies from 10 to 100 cases per 100,000 people, which confirms the influence of regional and genetic factors on the incidence of the disease [12]. Studies conducted in the United Kingdom demonstrate a steady increase in incidence, which may be associated with both improved diagnostic capabilities and an increase in the life expectancy of patients [16].

MS is classified into several forms depending on the course of the disease. The most common form is the relapsing-remitting form, which accounts for up to 80 % of new cases and is characterized by alternating periods of exacerbation and remission. The primary-progressive form, which occurs in 10-15 % of patients, is characterized by a gradual progression of symptoms from the very beginning without pronounced remissions. The secondary-progressive form occurs in most patients over time against the background of a relapsing-remitting course and indicates a deterioration in functional status. Benign MS is defined as a form with minimal symptoms and a low level of disability even many years after diagnosis [17, 24].

The pathogenesis of the disease involves a complex interaction of genetic and environmental factors. The main triggers are Epstein-Barr virus infection, vitamin D deficiency, smoking, and disruption of the intestinal microbiota. Patients with MS exhibit chronic inflammation, which activates a cascade of processes leading to demyelination, neuronal degeneration, and the formation of sclerotic plaques [17]. These processes underlie many of the clinical manifestations of MS, including pain, coordination disorders, limb weakness, visual impairment, and cognitive impairment. Pain, as one of the main symptoms, is reported in 50-75 % of patients, significantly affecting their quality of life [8]. Cognitive impairments, such as decreased attention, memory, and processing speed, are a serious problem, especially for young patients, as they complicate their professional activities and social adaptation [13].

MS not only leads to serious disability, but also represents a significant economic burden on the health care system. In Europe, the average cost of treating a patient per year ranges from €22,000 to €57,500 depending on the severity of the disease, with the main costs related to treatment, rehabilitation and disability [18]. High-cost disease modifiers, such as interferons and monoclonal antibodies, are important in reducing disease activity, but they impose an additional financial burden on patients and the healthcare system [20]. The psychosocial impact of MS is also significant. According to meta-analyses, depression and anxiety disorders are observed in 30-50 % of patients, which complicates treatment and reduces their quality of life [23].

Thus, MS remains a complex multifactorial pathology with serious medical, social and economic consequences [30]. Therefore, the development of methods to predict the course and risk of MS is a priority area for research.

The purpose of the study construction and analysis of discriminant models of the possibility of occurrence and features of the course of multiple sclerosis in young Ukrainian women depending on the features of anthropo-somatotypological body parameters.

Material and methods

In 59 young Ukrainian women (aged 25-44 according to the WHO age classification, 2015) diagnosed with multiple sclerosis, a clinical-laboratory and anthropological examination was conducted based on the Bunak V. V. schemes as modified by Shaparenko P. P. [26], somatotypological assessment using the Heath-Carter method [4], determination of body composition components using the formulas of Matiegka J. [19], and assessment of muscle mass components according to the formulas of the American Institute of Nutrition [27]. This research was performed at the Department of Nervous Diseases of the National Pirogov Memorial Medical University, Vinnytsya, and the medical center “Salutem” (Vinnytsya). Committee on Bioethics of National Pirogov Memorial Medical University, Vinnytsya (protocol № 10 from 10.12.2021) found that the studies do not contradict the basic bioethical standards of the Declaration of Helsinki, the Council of Europe Convention on Human Rights and Biomedicine (1977), the relevant WHO regulations and laws of Ukraine.

The diagnosis of multiple sclerosis was established according to the 2017 McDonald criteria [29]. The degree of disability was assessed using the Expanded Disability Status Scale (EDSS). The group of patients with mild impairments (EDSS 2.0-3.0) included 26 women; those with moderate impairments (EDSS 3.5-4.5) comprised 24 women; and the group with moderately severe impairments (EDSS 5.0-6.5) consisted of 9 women.

As the control group, primary anthropo-somatotypological parameters of 101 practically healthy young Ukrainian women of the same age group were taken from the database of the Research Center at the National

Pirogov Memorial Medical University, Vinnytsya.

Discriminant models of the likelihood of occurrence and characteristics of multiple sclerosis progression depending on the body structure and size features of Ukrainian women were developed using the licensed software package “Statistica 6.0.”

Results

It has been established that when dividing Ukrainian women into practically healthy and the general group of those with multiple sclerosis, considering anthropometric, somatotypological parameters, and body composition indicators, the classification matrix encompasses 100 % of cases. The discriminant variables distinguishing practically healthy women from those with multiple sclerosis are the conjugate diameter (CONJ), forearm circumference in the lower part (OBPR2), intercristal distance (CRIS), lower thoracic transverse diameter of the trunk (PNG), interspinous distance (SPIN), sagittal arc of the head (SAG_DUG), calf circumference in the lower part (OBG2), and the maximum width of the head (B_SH_GL). Among these parameters, the conjugate diameter and intercristal distance of the pelvis contribute most significantly to the discrimination. The combination of all identified anthropometric variables demonstrates pronounced discrimination (Wilks’ Lambda statistic=0.052; p<0.001) between practically healthy women and the general group of those with multiple sclerosis.

The classification indicators (Df) identified in our study enable categorizing the obtained measurements as “typical” for either the group of practically healthy women or those with multiple sclerosis. Below, the determination of the Df value is presented in the form of equations, where a Df value close to 351.5 indicates belonging to the group of practically healthy Ukrainian women, while a Df value near 296.7 corresponds to Ukrainian women with multiple sclerosis:

– Df (*for practically healthy women*)= CONJ×3.827 + OBPR2×1.473 + CRIS×1.692 + PNG×1.016 + SPIN×0.569 + SAG_DUG×13.01 - OBG2×0.366 + B_SH_GL×9.332 - 351.5;
– Df (*for the general group of women with multiple sclerosis*)= -CONJ×0.046 + OBPR2×3.198 + CRIS×0.029 + PNG×2.521 + SPIN×1.398 + SAG_DUG×11.09 + OBG2×1.126 + B_SH_GL×7.276 - 296.7;

where (here and in the following), pelvic dimensions in cm; girth dimensions of the body in cm; transverse dimensions of the torso in cm; head dimensions in cm.

As can be seen from Table 1, the calculated χ^2 criterion with the removal of consecutive roots confirms the statistical significance of both discriminant functions.

When Ukrainian women were categorized into those with multiple sclerosis with mild (EDSS 2.0-3.0), moderate (EDSS 3.5-4.5), and moderately severe (EDSS 5.0-6.5) impairments, considering anthropometric, somatotypological parameters, and body composition indicators, the classification matrix accounted for 76.92 % of cases with EDSS 2.0-3.0, 79.17 % of cases with EDSS 3.5-4.5, and 55.56 % of cases with EDSS 5.0-6.5. Overall, the classification matrix covered 74.58 % of cases. The discriminant variables distinguishing women with mild, moderate, and moderately severe impairments were the width of the distal epiphysis of the forearm (EPPR), the width of the distal epiphysis of the upper arm (EPPL), the conjugate diameter (CONJ), the maximum length of the head (B_DL_GL), the ectomorphic component of the somatotype according to Heath-Carter (LX), and the bone component of body mass according to Matiegka (OM). Among these parameters, the widths of the distal epiphyses of the forearm and upper arm contributed the most to the discrimination. The combination of all identified anthropometric and somatotypological variables demonstrated moderate discrimination (Wilks’ Lambda statistic=0.349; p<0.001) among Ukrainian women with multiple sclerosis and varying degrees of impairments.

The determination of the Df value is presented below in the form of equations, where belonging to the group of Ukrainian women with multiple sclerosis and mild impairments is possible with a Df value close to 762.5; to the group with moderate impairments at a Df value close to 760.0; and to the group with moderately severe impairments at a Df value close to 794.3:

– Df (*for women with multiple sclerosis with mild impairments*)= -EPPR×46.50 + EPPL×180.9 - CONJ×1.908 + B_DL_GL×50.05 + LX×18.67 - OM×39.14 - 762.5;
– Df (*for women with multiple sclerosis with moderate impairments*)= -EPPR×37.53 + EPPL×179.0 - CONJ×1.560 + B_DL_GL×48.34 + LX×18.55 - OM×40.70 - 760.0;
– Df (*for women with multiple sclerosis with moderate to severe impairments*)= -EPPR×54.62 + EPPL×197.2 - CONJ×2.611 + B_DL_GL×50.25 + LX×19.78 - OM×42.05 - 794.3;

where, the width of the distal epiphyses of the long tubular bones of the limbs in cm; the components of the

Table 1. Report of step-by-step analysis with the inclusion of the χ^2 criterion for practically healthy and multiple sclerosis patients Ukrainian women taking into account anthropo-somatotypological body parameters.

	Eigen-value	Canonicl R	Wilks' Lambda	Chi-Sqr.	df	p-level
0	18.35	0.974	0.052	0.052	8	0.052

Notes: here and in the following table, Eigenvalue root value for each discriminant function; Canonicl R – canonical R value for different roots; Wilks` Lambda – Wilks` Lambda statistic; Chi-Sqr. – standard χ^2 test of consecutive roots; Df number of degrees of freedom; p-level p-level associated with the corresponding χ^2.

somatotype in points; the indicators of the component composition of body weight in kg.

As can be seen from Table 2, the calculated χ^2 criterion with the removal of consecutive roots confirms the statistical significance of all discriminant functions.

Table 2. Report of a step-by-step analysis with the inclusion of the χ^2 criterion for Ukrainian women with multiple sclerosis with mild, moderate, and moderately severe disorders, taking into account anthropo-somatotypological body parameters.

	Eigen-value	Canonicl R	Wilks' Lambda	Chi-Sqr.	df	p-level
0	1.011	0.709	0.349	56.37	12	0.0000
1	0.426	0.547	0.701	19.00	5	0.0019

Notes: here and in the following table, Eigenvalue root value for each discriminant function; Canonicl R – canonical R value for different roots; Wilks` Lambda – Wilks` Lambda statistic; Chi-Sqr. – standard χ^2 test of consecutive roots; Df number of degrees of freedom; p-level p-level associated with the corresponding χ^2.

Discussion

Thus, in the classification of Ukrainian women into practically healthy and the general group of those with multiple sclerosis, the analysis of the obtained discriminant equations revealed statistically significant ($p<0.001$) and pronounced discrimination (Wilks' Lambda=0.052) based on the derived classification indicators (Df). The models distinguishing practically healthy women from the general group of those with multiple sclerosis include pelvic dimensions (37.50 %), body circumferences (25.00 %), head dimensions (25.00 %), and the transverse lower thoracic diameter of the torso (12.50 %). The greatest contribution to the discrimination between practically healthy women and the general group of those with multiple sclerosis was made by the conjugate diameter and the intercristal distance.

In the classification of Ukrainian women with multiple sclerosis into groups with mild, moderate, and moderately severe impairments, the analysis of the obtained discriminant equations revealed statistically significant ($p<0.001$) moderate discrimination (Wilks' Lambda=0.349) based on the derived classification indicators (Df). The models distinguishing women with mild, moderate, and moderately severe impairments included the widths of the distal epiphyses of long tubular bones of the limbs (33.33 %), the conjugate diameter, the maximum head length, the ectomorphic component of the somatotype according to Heath-Carter, and the bone component of body mass according to Matiegka (each at 16.67 %). The greatest contribution to the discrimination among women with mild, moderate, and moderately severe impairments was made by the widths of the distal epiphyses of the forearm and upper arm.

The substantially higher percentage of pelvic, torso, and head dimensions included in the discriminant models distinguishing healthy women from the general group of those with multiple sclerosis (75.00 % of all variables) and the percentage of the widths of distal epiphyses of long tubular bones of the limbs, pelvic dimensions, head dimensions, the ectomorphic component of the somatotype, and the bone component of body mass included in the discriminant models distinguishing women with mild, moderate, and moderately severe impairments (100 % of all variables), which according to the literature are highly genetically determined indicators [10], suggest a predominant genetic predisposition to both the development and progression of this multifactorial disease.

The relationship between multiple MS and anthropometric parameters is a complex and multifaceted issue that is at the center of current research. Anthropometric parameters, such as body mass index (BMI), fat distribution, and physical activity levels, have been shown to have a significant impact on the risk of developing MS, the course of the disease, and its clinical outcomes. One of the most important factors determining the relationship between MS and anthropometric parameters is BMI. A high BMI before the manifestation of MS can significantly increase the risk of developing this disease. In a large cohort study conducted by Cortese M. et al. [7], it was found that an increased BMI in adolescence is associated with a higher probability of MS in adulthood (relative risk is 2.0 for obese individuals compared with normal weight). Similar results were obtained in the study by Guerrero-Garcна J. D. J. et al. [11], where it was found that obesity contributes to systemic inflammation and increased levels of pro-inflammatory cytokines, which can activate autoimmune processes characteristic of MS.

On the other hand, excess weight also affects the course of the disease. A study by Stampanoni Bassi M. et al. [28] demonstrated that obesity enhances central inflammation and increases the risk of disability progression. High BMI was correlated with more severe clinical manifestations of MS, including a higher number of relapses and accelerated progression of the secondary progressive form of the disease. Similarly, Castro K. et al. [5] demonstrated that obesity modulates metabolic pathways, in particular through changes in ceramide metabolism, which may affect DNA methylation and the course of the disease.

The level of physical activity is also an important factor that can modify the risk of developing MS. According to a study by Sääksjärvi K. et al. [25], regular physical activity is associated with a reduced risk of MS, which is also supported by the study by Cortese M. et al. [7]. The authors emphasize that an active lifestyle can reduce systemic inflammation and improve immune regulation, which are key mechanisms of protection against autoimmune diseases.

The role of genetic and epigenetic factors in the association between anthropometry and MS remains an

important question. The work of Olsson T. et al. [22] emphasizes that genetic predisposition to obesity can interact with environmental factors, such as diet and physical activity, to influence the risk of MS. For example, the study of Amato M. P. et al. [1] suggested that vitamin D deficiency, characteristic of individuals with high BMI, may be a key mediator in the pathogenesis of MS.

In addition, some anthropometric changes may be secondary to MS. The study of Vikdahl M. et al. [31] reported a significant increase in central obesity in patients with early-stage MS, which may be a consequence of the disease-induced decrease in physical activity. Similarly, McKay K. A. et al. [21] noted that weight changes may be the result of both systemic inflammation and the side effects of glucocorticosteroids, which are often used to treat MS flare-ups.

The use of predictive models to examine the relationship between anthropometry and MS progression has also become an important area of research. As Brown F. S. et al. [3] noted, incorporating BMI and other anthropometric measures into predictive models can more accurately predict the risk of disability and relapse in patients with MS. F. B. Briggs et al. [2] noted that such approaches may contribute to the individualization of therapeutic strategies aimed at weight control and improving the physical condition of patients.

Overall, current evidence supports the important role of anthropometric factors in the pathogenesis, clinical course, and prognosis of MS [14, 15]. Future studies should focus on unraveling the precise mechanisms of these relationships, which will allow for improved preventive and therapeutic strategies for patients with MS.

Conclusions

1. Based on the specific anthropo-somatotypological body parameters, reliable discriminant models have been developed that allow for high-probability prediction of the risk of developing multiple sclerosis in young Ukrainian women (the classification matrix covers 100 % of cases, Wilks' Lambda=0.052; p<0.001) and moderate-probability assessment of disease progression characteristics (the classification matrix covers 74.58 % of cases, Wilks' Lambda=0.349; p<0.001).

2. The constructed models distinguishing practically healthy women from those with multiple sclerosis most frequently include pelvic dimensions (37.50 %), while the models differentiating women with mild, moderate, and moderately severe impairments due to multiple sclerosis most commonly incorporate the widths of the distal epiphyses of long tubular bones of the limbs (33.33 %).

References

[1] Amato, M. P., Derfuss, T., Hemmer, B., Liblau, R., Montalban, X., Soelberg Sшrensen, P., ... & 2016 ECTRIMS Focused Workshop Group. (2018). Environmental modifiable risk factors for multiple sclerosis: Report from the 2016 ECTRIMS focused workshop. *Multiple Sclerosis Journal*, *24*(5), 590-603. doi: 10.1177/1352458516686847

[2] Briggs, F. B., Thompson, N. R., & Conway, D. S. (2019). Prognostic factors of disability in relapsing remitting multiple sclerosis. *Multiple sclerosis and related disorders*, *30*, 9-16. doi: 10.1016/j.msard.2019.01.045

[3] Brown, F. S., Glasmacher, S. A., Kearns, P. K., MacDougall, N., Hunt, D., Connick, P., & Chandran, S. (2020). Systematic review of prediction models in relapsing remitting multiple sclerosis. *PLoS One*, *15*(5), e0233575. doi: 10.1371/journal.pone.0233575

[4] Carter, J. L., & Heath, B. H. (1990). *Somatotyping development and applications*. Cambridge University Press.

[5] Castro, K., Ntranos, A., Amatruda, M., Petracca, M., Kosa, P., Chen, E. Y., ... & Casaccia, P. (2019). Body Mass Index in Multiple Sclerosis modulates ceramide-induced DNA methylation and disease course. *EBioMedicine*, *43*, 392-410. doi: 10.1016/j.ebiom.2019.03.087

[6] Ciampi, E., Uribe-San-Martin, R., Soler, B., Molnar, K., Reyes, D., Keller, K., & Carcamo, C. (2020). Prevalence of comorbidities in Multiple Sclerosis and impact on physical disability according to disease phenotypes. *Multiple Sclerosis and Related Disorders*, *46*, 102565. doi: 10.1016/j.msard.2020.102565

[7] Cortese, M., Riise, T., Bjørnevik, K., Myhr, K. M., & Multiple Sclerosis Conscript Service Database Study Group. (2018). Body size and physical exercise, and the risk of multiple sclerosis. *Multiple Sclerosis Journal*, *24*(3), 270-278. doi: 10.1177/1352458517699289

[8] Drulovic, J., Basic-Kes, V., Grgic, S., Vojinovic, S., Dincic, E., Toncev, G., ... & Pekmezovic, T. (2015). The prevalence of pain in adults with multiple sclerosis: a multicenter cross-sectional survey. *Pain medicine*, *16*(8), 1597-1602. doi: 10.1111/pme.12731

[9] Eskandarieh, S., Heydarpour, P., Minagar, A., Pourmand, S., & Sahraian, M. A. (2016). Multiple sclerosis epidemiology in east Asia, south east Asia and south Asia: a systematic review. *Neuroepidemiology*, *46*(3), 209-221. doi: 10.1159/000444019

[10] Fedonyuk, Ya. I., & Dubinin, S. I. (2010). *Медична біологія, анатомія, фізіологія та патологія людини. Навчальний посібник* [*Medical Biology, Anatomy, Physiology and Human Pathology. Textbook*]. Вінниця НОВА КНИГА=Vinnytsia NOVA KNYGA.

[11] Guerrero-Garcна, J. D. J., Carrera-Quintanar, L., Lypez-Roa, R. I., Márquez-Aguirre, A. L., Rojas-Mayorquín, A. E., & Ortuño-Sahagún, D. (2016). Multiple sclerosis and obesity: possible roles of adipokines. *Mediators of inflammation*, *2016*(1), 4036232. doi: 10.1155/2016/4036232

[12] Heydarpour, P., Khoshkish, S., Abtahi, S., Moradi-Lakeh, M., & Sahraian, M. A. (2015). Multiple sclerosis epidemiology in Middle East and North Africa: a systematic review and meta-analysis. *Neuroepidemiology*, *44*(4), 232-244. doi: 10.1159/000431042

[13] Howard, J., Trevick, S., & Younger, D. S. (2016). Epidemiology of multiple sclerosis. *Neurologic clinics*, *34*(4), 919-939. doi: 10.1016/j.ncl.2016.06.016

[14] Huitema, M. J., & Schenk, G. J. (2018). Insights into the mechanisms that may clarify obesity as a risk factor for multiple sclerosis. *Current neurology and neuroscience reports*, *18*, 18. doi: 10.1007/s11910-018-0827-5

[15] Jacobs, B. M., Belete, D., Bestwick, J., Blauwendraat, C.,

Bandres-Ciga, S., Heilbron, K., ... & Noyce, A. J. (2020). Parkinsons disease determinants, prediction and geneenvironment interactions in the UK Biobank. *Journal of Neurology, Neurosurgery & Psychiatry, 91*(10), 1046-1054. doi: 10.1136/jnnp-2020-323646

[16] Jick, S. S., Li, L., Falcone, G. J., Vassilev, Z. P., & Wallander, M. A. (2015). Epidemiology of multiple sclerosis: results from a large observational study in the UK. *Journal of neurology*, *262*, 2033-2041. doi: 10.1007/s00415-015-7796-2

[17] Klineova, S., & Lublin, F. D. (2018). Clinical course of multiple sclerosis. *Cold Spring Harbor perspectives in medicine*, *8*(9), a028928. doi: 10.1101/cshperspect.a028928

[18] Kobelt, G., Thompson, A., Berg, J., Gannedahl, M., Eriksson, J., MSCOI Study Group, & European Multiple Sclerosis Platform. (2017). New insights into the burden and costs of multiple sclerosis in Europe. *Multiple Sclerosis Journal*, *23*(8), 1123-1136. doi: 10.1177/1352458517694432

[19] Matiegka, J. (1921). The testing of physical efficiency. *Am. J. Phys. Antropol*, *2*(3), 25-38. doi: 10.1002/ajpa.1330040302

[20] McGinley, M. P., Goldschmidt, C. H., & Rae-Grant, A. D. (2021). Diagnosis and treatment of multiple sclerosis: a review. *Jama*, *325*(8), 765-779. doi: 10.1001/jama.2020.26858

[21] McKay, K. A., Jahanfar, S., Duggan, T., Tkachuk, S., & Tremlett, H. (2017). Factors associated with onset, relapses or progression in multiple sclerosis: a systematic review. *Neurotoxicology*, *61*, 189-212. doi: 10.1016/j.neuro.2016.03.020

[22] Olsson, T., Barcellos, L. F., & Alfredsson, L. (2017). Interactions between genetic, lifestyle and environmental risk factors for multiple sclerosis. *Nature Reviews Neurology*, *13*(1), 25-36. doi: 10.1038/nrneurol.2016.187

[23] Peres, D. S., Rodrigues, P., Viero, F. T., Frare, J. M., Kudsi, S. Q., Meira, G. M., & Trevisan, G. (2022). Prevalence of depression and anxiety in the different clinical forms of multiple sclerosis and associations with disability: A systematic review and meta-analysis. *Brain, behavior, & immunity-health*, *24*, 100484. doi: 10.1016/j.bbih.2022.100484

[24] Reynders, T., D'haeseleer, M., De Keyser, J., Nagels, G., & D'hooghe, M. B. (2017). Definition, prevalence and predictive factors of benign multiple sclerosis. *Eneurologicalsci*, *7*, 37-43. doi: 10.1016/j.ensci.2017.05.002

[25] Sääksjärvi, K., Knekt, P., Männistö, S., Lyytinen, J., Jääskeläinen, T., Kanerva, N., & Heliövaara, M. (2014). Reduced risk of Parkinsons disease associated with lower body mass index and heavy leisure-time physical activity. *European journal of epidemiology*, *29*, 285-292. doi: 10.1007/s10654-014-9887-2

[26] Shaparenko, P. P. (2000). *Антропометрія* [*Anthropometry*]. Вінниця: ВДМУ ім. М. І. Пирогова= Vinnytsia: VDMU im. M. I. Pyrogova.

[27] Shephard, R. J. (2005). *Body composition in biological anthropology*. Cambridge University Press, Cambridge, UK; New York.

[28] Stampanoni Bassi, M., Iezzi, E., Buttari, F., Gilio, L., Simonelli, I., Carbone, F., ... & Matarese, G. (2020). Obesity worsens central inflammation and disability in multiple sclerosis. *Multiple Sclerosis Journal*, *26*(10), 1237-1246. doi: 10.1177/1352458519853473

[29] Thompson, A. J., Banwell, B. L., Barkhof, F., Carroll, W. M., Coetzee, T., Comi, G., ... & Cohen, J. A. (2018). Diagnosis of multiple sclerosis: 2017 revisions of the McDonald criteria. *The Lancet Neurology*, *17*(2), 162-173. doi: 10.1016/S1474-4422(17)30470-2

[30] Vaughn, C. B., Jakimovski, D., Kavak, K. S., Ramanathan, M., Benedict, R. H., Zivadinov, R., & Weinstock-Guttman, B. (2019). Epidemiology and treatment of multiple sclerosis in elderly populations. *Nature Reviews Neurology*, *15*(6), 329-342. doi: 10.1038/s41582-019-0183-3

[31] Vikdahl, M., Carlsson, M., Linder, J., Forsgren, L., & Heglin, L. (2014). Weight gain and increased central obesity in the early phase of Parkinson's disease. *Clinical nutrition*, *33*(6), 1132-1139. doi: 10.1016/j.clnu.2013.12.012

МОДЕЛЮВАННЯ, НА ОСНОВІ ДИСКРИМІНАНТНОГО АНАЛІЗУ, МОЖЛИВОСТІ ВИНИКНЕННЯ ТА ОСОБЛИВОСТЕЙ ПЕРЕБІГУ МНОЖИННОГО СКЛЕРОЗУ В УКРАЇНСЬКИХ ЖІНОК У ЗАЛЕЖНОСТІ ВІД ОСОБЛИВОСТЕЙ БУДОВИ ТА РОЗМІРІВ ТІЛА

Гунас М. М., Московко Г. С., Назарова М. С., Кириченко Ю. В., Прокопенко С. В., Рубан М. М.

Зважаючи на існування різних шляхів перебігу множинного склерозу, інвалідизацію, що викликає дане захворювання, сучасна медицина потребує створення нових, простих у застосуванні і дешевих методик для вирішення даного питання. Перспективним у даному випадку може бути застосування клінічної антропометрії, що вже успішно застосовується для передбачення форм розвитку та тяжкості різноманітних захворювань різних систем органів людини. Мета дослідження – побудова та аналіз дискримінантних моделей можливості виникнення та особливостей перебігу множинного склерозу в українських жінок молодого віку в залежності від особливостей антропо-соматотипологічних параметрів тіла. Проведено клініко-лабораторне та антропо-соматотипологічне обстеження 59 українських жінок молодого віку, хворих на множинний склероз. Оцінка ступеня інвалідизації проводилася за допомогою шкали Expanded Disability Status Scale. В якості контрольної групи використані первинні антропо-соматотипологічні показники 101 практично здорової української жінки аналогічної вікової групи (взяті з банку даних науково-дослідного центру Вінницького національного медичного університету ім. М. І. Пирогова). Дискримінантні моделі можливості виникнення та особливостей перебігу множинного склерозу в залежності від антропо-соматотипологічних параметрів тіла побудовані в ліцензійному пакеті «Statistica 6.0». Встановлено, що при розподілі українських жінок на практично здорових та загальну групу хворих на множинний склероз, при аналізі отриманих дискримінантних рівнянь можлива достовірна виражена дискримінація (Wilks' Lambda=0,052, p<0,001) отриманих показників класифікації. До складу моделей між практично здоровими та загальною групою хворих на множинний склероз жінок входять розміри таза (37,50 %, вносять найбільший внесок у дискримінацію), обхватні розміри тіла та розміри голови (по 25,0 %), а також поперечний нижньогрудний діаметр тулуба (12,5 %). При розподілі українських жінок на хворих на множинний склероз з легкими, помірними та помірно-тяжкими порушеннями, при аналізі отриманих дискримінантних рівнянь також можлива достовірна середня дискримінація (Wilks' Lambda=0,349, p<0,001) отриманих показників класифікації. До складу моделей між хворими на множинний склероз із легкими, помірними та помірно-тяжкими порушеннями жінками входять ширина дистальних епіфізів довгих трубчастих кісток кінцівок (33,33 %, вносять найбільший внесок у дискримінацію), зрвнішня кон`югата, найбільша довжина голови, ектоморфний компонент соматотипу за Хіт-Картер та кістковий

компонент маси тіла за Матейко (по 16,67 %). Ці дані підкреслюють важливість антропометричних і соматотипологічних параметрів у прогнозуванні виникнення та тяжкості прогресування розсіяного склерозу у молодих українських жінок.
***Ключові слова**: нервові захворювання, множинний склероз, антропо-соматотипологічні параметри тіла, дискримінантні моделі, практично здорові та хворі жінки.*

Author's contribution

Gunas M. M. – conceptualization, formal analysis and validation, research, review writing and editing, methodology and writing of the original draft.
Moskovko G. S. – project administration, supervision, review writing and editing.
Nazarova M. S. – data visualization, review writing and editing.
Kyrychenko Yu. V. – software, review writing and editing.
Prokopenko S. V. – resources, review writing and editing.
Ruban M. M. – resources, review writing and editing.

DOI: 10.31393/morphology-journal-2024-30(4)-09 Reports of Morphology, Vol. 30, №4, Pages 74-81

ISSN 1818-1295 eISSN 2616-6194

REPORTS OF MORPHOLOGY

Official Journal of the Scientific Society of Anatomists, Histologists, Embryologists and Topographic Anatomists of Ukraine

journal homepage: https://morphology-journal.com

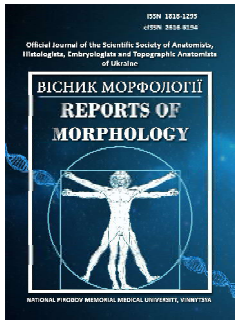

Ultrastructure of adrenal glands endocrinocytes after thermal skin injury under conditions of correction with cryo-lyophilized xenograft skin substrate

Kulbitska V. V., Ohinska N. V., Slabyy O. B., Lisnychuk N. Ye., Trach Rosolovska S. V., Nebesnyi O. R., Nebesna Z. M.

I. Horbachevsky Ternopil National Medical University, Ternopil, Ukraine

ARTICLE INFO

Received: 5 March 2024

Accepted: 26 September 2024

UDC: 616.45-091.8:616.5-001.17-06]-085.36

CORRESPONDING AUTHOR

e-mail: kulbitska@tdmu.edu.ua

Kulbitska V. V.

CONFLICT OF INTEREST

The authors have no conflicts of interest to declare.

FUNDING

Not applicable.

DATA SHARING

Data are available upon reasonable request to corresponding author.

According to WHO studies, burn injuries are one of the most common injuries in the world, and their number has increased significantly due to the military actions in Ukraine. The adrenal glands, which regulates metabolism and participates in the body's defense reactions, is sensitive to burn injuries, which leads to morphological changes in the organ. The aim of the study was to investigate the ultrastructural changes in endocrinocytes of the adrenal glands after experimental thermal skin injury under conditions of correction with cryo-lyophilized xenograft skin substrate. A second-degree burn was modeled by applying heated copper plates to the skin of the back of laboratory male rats, which accounted for 18-20 % of the body surface. For electron microscopic analysis on days 7th, 14th, and 21st of the experiment, pieces of the adrenal glands were taken. They were fixed in a glutaraldehyde solution, post-fixed in osmium tetraoxide, and processed according to standard procedures. Ultrathin sections were contrasted with uranyl acetate and lead citrate, and submicroscopic changes were studied using a PEM-125K electron microscope. On the 7th day after the burn with correction (using a cryo-lyophilized xenograft skin substrate), moderate changes in the ultrastructure of the nuclei and organelles of the endocrinocytes were found. Mitochondrial hyperplasia, changes in the shape of the nuclei and the presence of small clumps of heterochromatin in the karyoplasm were observed. On the 14th day, under the conditions of correction, there were signs of restoration of the cell ultrastructure, in particular, the structure of the nucleus and the membrane of the zona glomerulosa cells was restored, ribosomes and hypertrophied mitochondria with an electronically bright matrix appeared, as well as numerous lipid droplets. After 21 days, the ultrastructure of the cells of the zona glomerulosa was restored, and lipid droplets were evenly distributed in the cytoplasm. In the zona reticularis and adrenal medulla, changes in the submicroscopic organization of endocrinocytes were insignificant. We observed a uniform distribution of secretory granules in the cytoplasm of chromaffinocytes, mitochondrial recovery and unchanged ultrastructural organization of the organelles of the synthetic apparatus. Thus, the results of the study confirmed that the cryo-lyophilized xenograft skin substrate effectively promotes the restoration of the ultrastructure of adrenal endocrinocytes, reducing the degree of damage to cytoplasmic membranes, organelles of the synthetic apparatus of cells, endocrinocyte nuclei, especially activating the regeneration processes in the late stages after thermal skin injury.

Key words: *adrenal glands, endocrinocytes, ultrastructural changes, thermal injury, crushed substrate of lyophilized xenodermograft.*

Introduction

A retrospective analysis of burn injuries of various genesis according to the WHO and the International Society of Burn Injuries showed that it is estimated that about 11 million cases of this type of injury occur annually worldwide and it is a significant public health problem at the global level [14]. In Ukraine, several tens of thousands of cases of burn injuries are registered annually. Due to military actions on the territory of Ukraine, the number of burn injuries

caused by explosions and fires has increased significantly [25, 28].

Burn injury causes a powerful cascading stress reaction. In response to significant tissue loss and stress, the body enters a hypermetabolic state, when energy expenditure increases dramatically [2, 10, 12, 20]. This is manifested by an acceleration of metabolism, catabolism of proteins, fats, and carbohydrates, which leads to exhaustion. Stress activates systemic inflammation, which is accompanied by the release of cytokines and inflammatory mediators. This can lead to a systemic inflammatory response, which is a risk factor for the development of multiple organ failure [1, 7, 19].

The activation of a chain reaction in the body to a stressor plays a key role. It is known that the adrenal gland as an organ of the endocrine system, produces a number of hormones, regulates metabolism, takes an active part in the formation of protective and adaptive reactions of the body, it is sensitive to this factor and as a result, the structural components of the organ undergo significant morphological changes [3, 9, 17].

Burn wound healing remains a challenging public health problem worldwide due to the lack of effective and accurate therapy [4, 16, 18, 21]. An effective means of temporary closure of the burn wounds surface is the use of a crushed cryo-lyophilized xenograft skin substrate [15]. The use of this corrective factor prevents the progressive intoxication of the body from the lesion site, reduces the loss of water, proteins and micronutrients from the site of injury, promotes skin recovery after a burn wound by inhibiting oxidative stress of tissues, activates the processes of epithelialization and neoangiogenesis during wound healing, which promotes faster recovery of the skin and has a positive effect on the morphological and functional state of the organs of the affected organism [6].

The aim of the study is to investigate ultrastructural changes in endocrinocytes of the adrenal cortex and medulla after simulated thermal skin injury using lyophilized xenodermografts.

Material and methods

The work is a part of the research topic of the Department of Histology and Embryology of the Ivan Horbachevsky Ternopil National Medical University Ministry of Health of Ukraine “Features of structural reorganization of the nervous, digestive, endocrine systems, hematopoietic and immune organs under conditions of thermal injury and the use of corrective factors” (state registration number 0120U104152).

The experiment was performed on 48 adult white male rats divided into the following experimental groups: I – intact animals; II – animals with a second degree of skin burn degree; III – animals with thermal skin trauma, which underwent early necrectomy with subsequent application of a cryolyophilized xenograft skin substrate.

Animals were kept in vivarium conditions on an ad libitum basic diet. All animal experiments used in this study complied with generally accepted international standards and were approved by the Bioethics Committee of the Ivan Horbachevsky Ternopil National Medical University Ministry of Health of Ukraine (Protocol No. 74 of September 01, 2023). All animal manipulations were carried out in accordance with the requirements of the European Convention for the Protection of Vertebrate Animals Used for Experimental and Other Scientific Purposes (Strasbourg, 1986) [8].

Burn injury was modeled under thiopental-sodium anesthesia using copper plates heated in boiled water to a temperature of 97-100 °C, which were applied for 15 seconds to the epilated skin of the animals’ backs. The total area of the burn lesions was 18-20 % of the body surface, corresponding to third-degree burns. Early necrectomy of the damaged skin areas was performed one day after the injury, and the wounds were covered with a crushed cryo-lyophilized xenograft skin substrate.

Animals were withdrawn from the experiment on days 7, 14, and 21. For electron microscopic analysis, the organ pieces were fixed in a 2.5 % glutaraldehyde solution based on Millonigs phosphate buffer and postfixed in a 1 % osmium tetraoxide solution in phosphate buffer. Further processing was performed according to the standard method [11]. Ultrathin sections were made on an Ultrotome LKB 4801A ultramicrotome and contrasted using the Reynolds method. Submicroscopic changes of the organ were studied using an electron microscope PEM-125K.

Results

Submicroscopic examination of the adrenal gland after 7 days under conditions of modeled burn injury and with the use of a cryo-lyophilized xenograft skin substrate as a corrective drug revealed destruction of the components of the nuclei and cytoplasm of corticocytes, epi- and norepinephrocytes. It was determined that the hyaloplasm of endocrinocytes of the zona glomerulosa contained volumetric mitochondria with indistinct cristae, the characteristic feature of which was the presence of tubular and tubular-vesicular cristae. Fragmentation of cristae and a matrix of mild osmiophilia were observed in some mitochondria. The endoplasmic reticulum was formed by short and partially dilated tubules and vesicles. The Golgi complex was formed by clear cisternae, vesicles and microbubbles. A moderate number of lipid inclusions were detected in the cytoplasm of cells containing heterogeneous contents. The cell nuclei were rounded, containing shallow invaginations of karyolemma, the perinuclear space was partially expanded, but the nuclear pores were numerous and well expressed. The karyoplasm included electron-light euchromatin, and small loci of marginal heterochromatin which were peripherally located. As a manifestation of the onset of regenerative processes, binuclear corticocytes appeared in this period of the experiment.

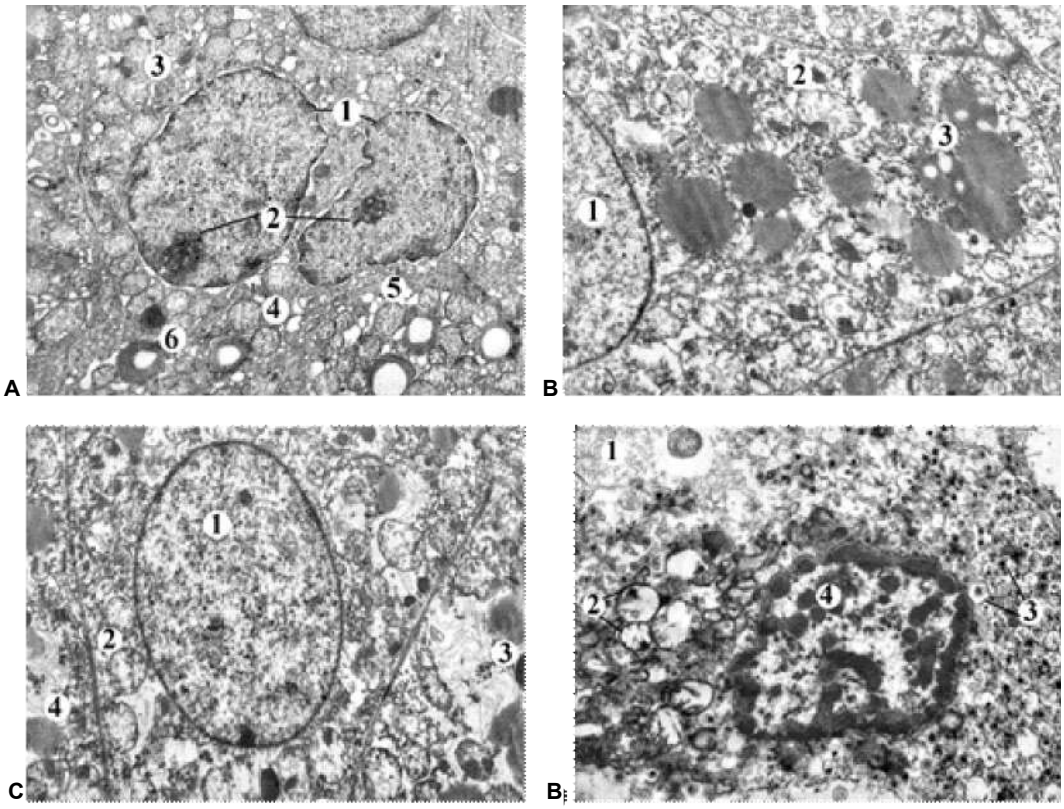

Fig. 1. Ultrastructural changes in endocrinocytes of the adrenal cortex and medulla on day 7 after modeled burn injury and correction. **A** – binuclear endocrinocyte of the zona glomerulosa: 1 – nuclei, 2 – small osmiophilic nucleoli, 3 – endocrinocyte hyaloplasm, 4 – partially destructed mitochondria, 5 – dilated tubules and vesicles of the endoplasmic reticulum, 6 – lipid inclusions. × 9 000; **B** – corticocytes of the zona fasciculata: 1 – endocrinocyte nucleus, 2 – electron-light mitochondria, 3 – lipid inclusions with resorption zones. ×15 000; **C** – corticocytes of the zona reticularis: 1 – oval nucleus of corticocyte, 2 – partially fragmented mitochondria, 3 – formation of myelin-like bodies, 4 – deformed lipid inclusions. ×12 000; **D** norepinephrocyte of adrenal medulla: 1 – electron-lucent hyaloplasmic loci, 2 – vacuolated mitochondria with lysed cristae, 3 – secretory granules, 4 – irregularly shaped nucleus with heterochromatin clumps. ×12 000.

Submicroscopically, it was found that the spongiocytes of the zona fasciculata had distinct cell membranes. The endocrinocyte hyaloplasm included a significant number of vesicular mitochondria, primary osmiophilic lysosomes, distinct ribosomes and polysome rosettes. The lipid inclusions were characterized by an electron-illuminated structure, some of which were voluminous, and in some areas there were signs of their resorption. The endoplasmic reticulum was formed by short tubules and vacuoles. The dictyosomes of the Golgi complex were arranged paranuclearly, their cisternae and vesicles were dilated. Characteristic, concentric clusters of endoplasmic reticulum tubules were observed, which was a manifestation of functional tension of endocrinocytes. Corticocytes contained rounded-oval nuclei with a smooth karyolemma, the karyoplasm contained mainly active euchromatin. Two-nucleated spongiocytes of the zona fasciculata, “dark” cells with intensely osmiophilic cytoplasm and karyoplasm were often detected. Such cells contained numerous tubules and endoplasmic reticulum vacuoles with paranuclear localization. Mitochondria were also numerous, partially deformed, with an electron-dense matrix. “Light” endocrinocytes were found singly, with the presence of lipid droplets. Liposomes were often connected to lysosomes, indicating the immediate lysis of lipid inclusions, and myelin-like bodies were also observed (Fig. 1B).

Submicroscopic examination of the endocrinocytes of the zona reticularis revealed that the tubules and vacuoles of the endoplasmic reticulum were well structured. Single lipid inclusions were characteristic of endocrinocytes in this zone, myelin-like bodies were also detected. The nuclei of endocrinocytes had clearly defined nuclear membranes with well-defined nuclear pores and contained nucleoli. Functionally active euchromatin prevailed in the karyoplasm, and heterochromatin clumps were marginally localized. Mitochondrial hyperplasia was detected in the cytoplasm of the zona reticularis cells. In this zone, there were “dark” endocrinocytes and rarely single cells with electron-light cytoplasm and karyoplasm (Fig. 1C).

The endocrinocytes of the adrenal medulla were characterized by electron-dense nuclei, round-oval, irregular in shape, with invaginations of karyolemma. Heterochromatin prevailed in the karyoplasm, which accumulated in clumps. The tubules and vacuoles of the endoplasmic reticulum were partially dilated, and the

cisternae of the Golgi complex were single. The mitochondria were destructured according to the vacuolar type, with reduction of cristae. A characteristic feature of the chromaffinocytes of 3rd group of animals undergoing correction was a high content of secretory inclusions throughout the cytoplasm, especially in cells located near sinusoidal capillaries. The integrity of the cell plasma membrane was preserved. The cytoplasm of most epinephrocytes contained large secretory granules, although small granules with uneven osmiophilic content were also observed (Fig. 1D).

The electron microscopic study of the adrenal glands 14 days after the simulated burn injury and with the use of the corrective cryo-lyophilized xenograft skin substrate drug showed regenerative processes in endocrinocytes.

In the cells of the zona glomerulosa, the nuclei were round-oval in shape, with a predominance of euchromatin, heterochromatin clumps were marginally present. The karyolemma was clearly contoured, nuclear pores were clearly defined, and large nucleoli were found in the karyoplasm. Some organelles were destructed. Near the nucleus, partially thickened tubules of the endoplasmic reticulum were visible, many ribosomes were detected, and the cisternae and vacuoles of the Golgi complex were moderately vacuolized. Mitochondria in most cells were hypertrophied, their matrix was of low electron density, and cristae were partially fragmented. Lipid inclusions were evenly distributed throughout the cytoplasm, showed no signs of resorption, and sometimes formed groups (Fig. 2A).

At this stage of the experiment, spongiocytes with clearly defined rounded nuclei were observed in the zona fasciculata. Euchromatin predominated in the karyoplasm, 1-2 nucleoli and small osmiophilic clusters of heterochromatin were visible, which were located mainly peripherally. The karyolemma was clear, formed minor indentations and contained well-defined nuclear pores. binucleated endocrinocytes were often detected. The organelles were without marked destruction, although occasionally slightly dilated tubules of the endoplasmic reticulum and cisternae of the Golgi apparatus were observed. Lysosomes were rare. Mitochondria were round, with an electron-light matrix and slightly lysed cristae. The saturation of ribosomes and polysomes in the cytoplasm was high. Lipid droplets varied in size and electron content, some of them had a central light zone (Fig. 2B).

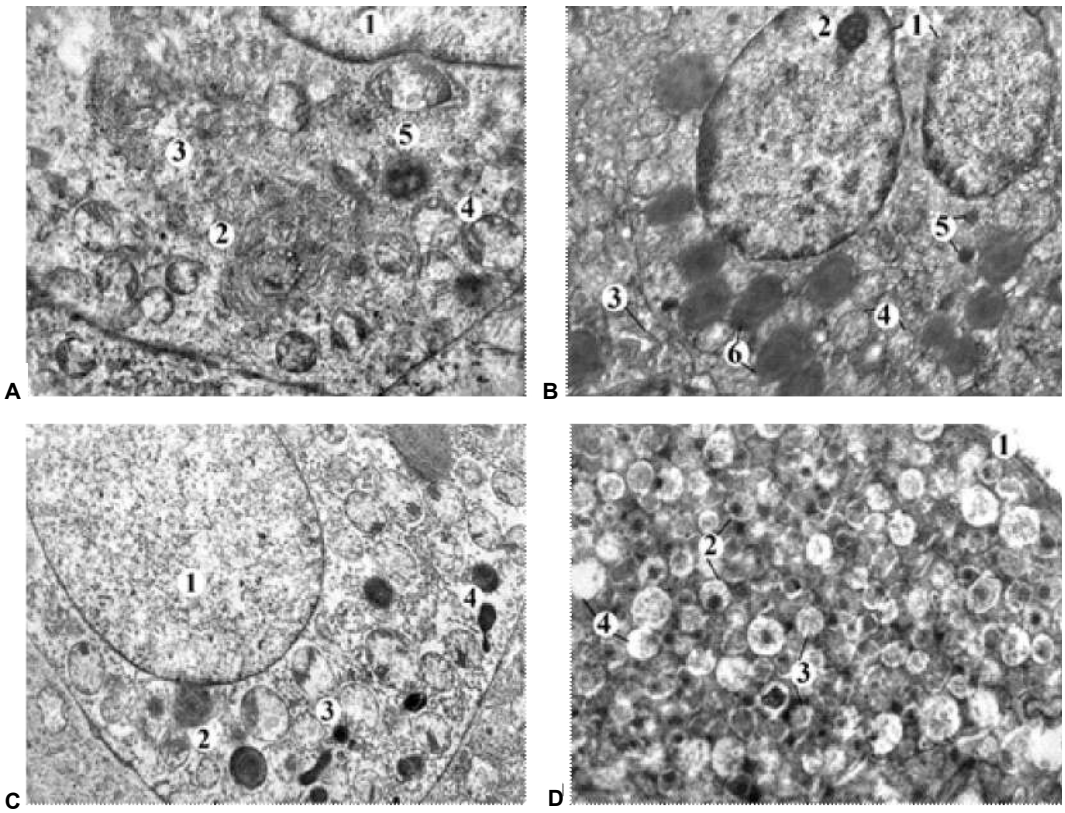

Fig. 2. Ultrastructural changes in endocrinocytes of the adrenal cortex and medulla on day 14 after modeled burn injury and under conditions of correction. **A** – endocrinocyte of the zona glomerulosa: 1 – nucleus, 2 – Golgi apparatus, 3 – destructed cytoplasm, 4 – partially deformed mitochondria, 5 – lipid inclusions. ×15 000; **B** – corticocytes of the zona fasciculata: 1 – nuclei, 2 – osmiophilic nucleolus, 3 – endoplasmic reticulum tubules, 4 – mitochondria, 5 – lysosomes, 6 – lipid inclusions. ×10 000; **C** – endocrinocyte of the zona reticularis: 1 – nucleus, 2 – lipid inclusions, 3 – mitochondria, 4 – lysosomes. ×15 000; **D** – epinephrocyte of the adrenal medulla: 1 – epinephrocyte plasma membrane, 2 – secretory granules with electron-dense content, 3 – granules with low electron density content, 4 – granules with reduced electron density. ×27 000.

In the zona reticularis, the endocrinocytes were rounded and oval in shape, the cytoplasm of some of them showed signs of vacuolization. The nuclei were mostly centralized. The karyoplasm contained euchromatin, and small clumps of heterochromatin which were located mainly marginally. The tubules of the endoplasmic reticulum and the cisternae of the Golgi apparatus were moderately thickened in some cells. Mitochondria were oval with single lysed cristae and low osmiophilicity. Lipid granules were also rarely found in the hyaloplasm (Fig. 2C).

In the adrenal medulla at this stage of the experiment, epi- and norepinephrocytes were ultrastructurally determined, which contained numerous secretory granules with different osmiophilic content. The bulk of the granules were those with low or moderate osmiophilicity. Euchromatin dominated in the cell nuclei, while small clumps of heterochromatin were mainly located under the karyolemma. In the nuclei, 1-2 small nucleoli were clearly defined. The karyolemma was clear, and the perinuclear space was slightly enlarged in some places. The tubules of the endoplasmic reticulum were rarely dilated and indistinct. The Golgi complex was formed by partially deformed cisternae, vacuoles and microbubbles. The mitochondria had clear membrane cristae with moderate osmiophilia of the matrix, although there were individual mitochondria with light matrix and fragmented cristae (Fig. 2D).

Electron microscopic examination of the adrenal gland after 21 days of the experiment showed that corticocytes, epi- and norepinephrocytes actively underwent regenerative processes and restoration of their submicroscopic state compared to the group of animals that did not undergo correction of thermal injury. The nuclei of corticocytes of the zona glomerulosa were quite voluminous, rounded, with a smooth karyolemma and clearly defined nuclear pores. Euchromatin dominated in the karyoplasm, and nucleoli with granular and fibrillar components were detected. Well-structured Golgi cisternae, vesicles, and tubules of the endoplasmic reticulum were found in the cytoplasm. The mitochondria contained a matrix of low osmiophilicity and contoured cristae, although some mitochondria showed signs of fragmentation. Lipid inclusions of different sizes, were numerous, and some of them had resorption zones (Fig. 3A).

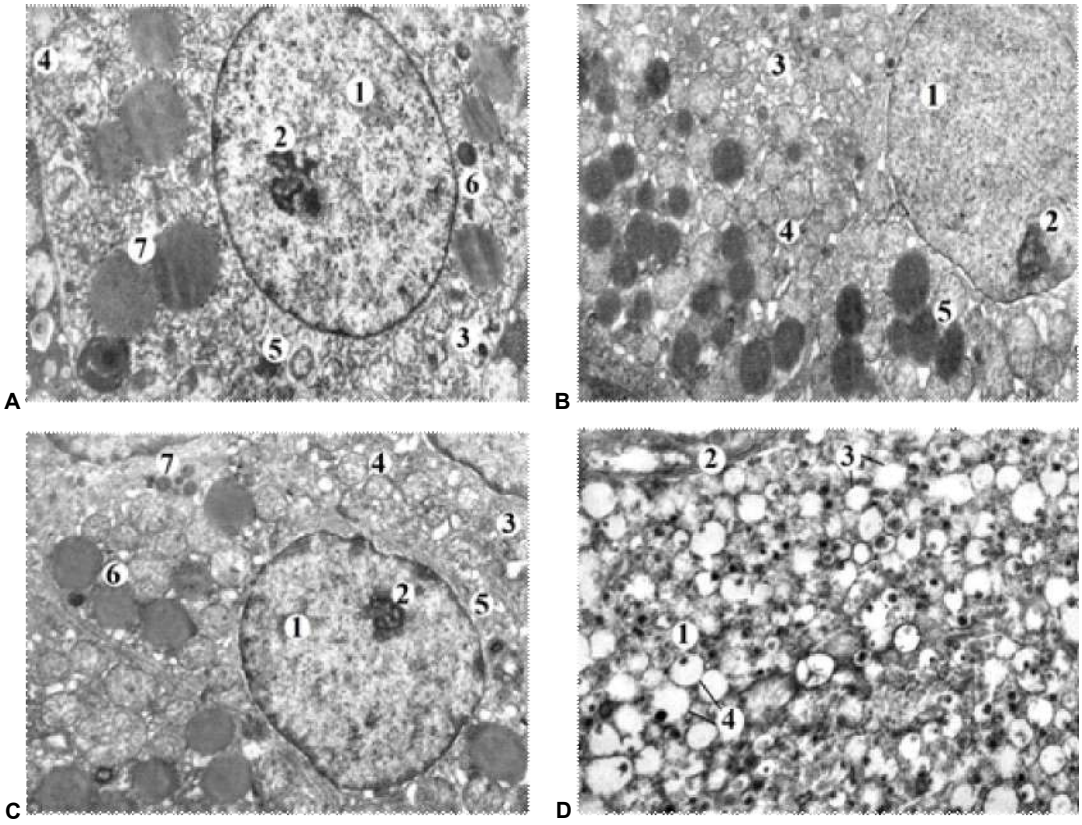

Fig. 3. Ultrastructural changes in endocrinocytes of the adrenal gland cortex and medulla on day 21 after experimental thermal injury and under conditions of correction. **A** – endocrinocyte of the zona glomerulosa: 1 – cell nucleus, 2 – osmiophilic nucleolus, 3 – cytoplasm, 4 – small mitochondria, 5 – pronounced tubules and vacuoles of the endoplasmic reticulum, 6 – osmiophilic lysosome, 7 – lipid droplets. ×12 000; **B** – corticocytes of the zona fasciculata: 1 – nucleus, 2 – small nucleolus, 3 – numerous tubules of the endoplasmic reticulum, 4 – multiple mitochondria, 5 – osmiophilic lipid droplets. ×15 000; **C** – endocrinocytes of the zona reticularis: 1 – small nucleus, 2 – nucleolus, 3 – cell cytoplasm, 4 – numerous mitochondria, 5 – pronounced endoplasmic reticulum tubules, 6 – lipid inclusions, 7 – osmiophilic lysosomes. ×12 000; **D** – norepinephrocyte of the adrenal medulla: 1 – cell cytoplasm, 2 – plasma membrane, 3 – granules without electron-dense content, 4 – secretory granules with small, eccentrically located osmiophilic content. ×25 000.

The corticocytes of the zona fasciculata contained bulky nuclei, euchromatin predominated in the karyoplasm, and electron-dense nucleoli were eccentrically arranged. The karyolemma was slightly deformed, the perinuclear space was uniform, with numerous nuclear pores. In the cytoplasm, there were partially dilated tubules and vacuoles of the endoplasmic reticulum, well-distributed cisternae, vesicles, and microbubbles of the Golgi complex. The mitochondria were numerous, without pronounced cristae fragmentation, and had a matrix of low electron density. Lipid droplets were numerous and of various shapes and sizes (Fig. 3B).

At this stage of the study, the oval nuclei of the zona reticularis corticocytes had clearly defined membranes. Distinct nucleoli were detected in the nuclei, the karyoplasm contained mainly euchromatin, and heterochromatin was located in thin band along the clear karyolemma. In the cytoplasm, well-developed tubules of the endoplasmic reticulum and well-structured cisternae, vesicles of the Golgi complex were observed. Mitochondria had distinct cristae, and their matrix was of low osmiophilicity. Numerous ribosomes were observed. Lipid inclusions in the cytoplasm of the cells were few (Fig. 3C).

Electron microscopic examination of the adrenal medulla of the organ showed that single empty granules and granules with moderate osmiophilicity were observed in epinephrocytes and norepinephrocytes. The endocrinocytes were characterized by the presence of whole organelles in the hyaloplasm. The cell nuclei were rounded, the karyolemma formed shallow invaginations, and the nuclear pores were clearly defined. Euchromatin dominated in the karyoplasm, and small clusters of heterochromatin were found marginally (Fig. 3D).

Discussion

The adrenal gland, as organ of the endocrine system that responds sensitively to stress, plays an important role in the development of the body's adaptive mechanisms under the influence of various exogenous and endogenous stress factors [22, 29]. Our studies of adrenal endocrinocytes after simulated thermal skin injury and under conditions of application of a corrective factor using a cryo-lyophilized xenograft skin substrate showed that at the initial stages of the experiment, increased functional activity of the gland was observed, which is typical for the general adaptation syndrome caused by acute stress.

Similar changes were observed during exposure to cold stress with the use of stress protectors, where stabilization of the endocrinocyte structure was noted at the late stages of the experiment [5]. In the adrenal gland, the restoration of the submicroscopic organization of membranous and nonmembranous organelles of the synthetic and energy apparatus of endocrinocytes was noted. The dynamics of changes in the ultrastructure reached its peak on day 21 of the experiment. The karyolemma of endocrinocyte nuclei was clearly contoured, shallow invaginations were noted in some areas. The perinuclear space in the vast majority was characterized by minor dilatations. The karyoplasm was electronically bright, heterochromatin was marginally located.

Other studies that examined the effects of heavy metal salts, acute peritonitis, hypergravity, experimental diabetes mellitus, and their correction by various means also showed similar dynamics of changes [13, 24, 26]. Since the adrenal gland is a target for toxic substances, intoxication is a typical consequence of stress [23]. Corrective factors in the late stages of the experiment showed a stress-protective effect, reducing the signs of depletion of the general adaptation syndrome. The degree of recovery depended on the duration of the experiment, the effect of the correction, the ability of cells to regenerate, the concentration of hormones in the blood, and the residual toxic effects of stress factors.

Our data are more closely identified with the rate of changes in other organs in thermal skin damage and the subsequent stage of application of the cryo-lyophilized xenograft skin substrate. In the early stages of the experiment, the authors [27] observed a violation of the cell ultrastructure in the cells of organs both in animals with burns and cryo-lyophilized xenograft skin substrate and in those who did not undergo correction of thermal injury. Already at the early stages of the study, we could see a better preservation of the submicroscopic organization of nuclei, membranous and nonmembranous organelles of endocrinocytes and the first manifestations of their recovery process. The euchromatin nuclei of endocrine cells were round in shape, and the karyolemma often formed depressions. In the cytoplasm, fewer destructive changes in organelles and structures performing secretory and resorption functions were recorded compared to the group of animals without the use of the corrective factor. In the paranuclear zone, hypertrophy of the Golgi complex cisternae was observed, the tubular system of the rough endoplasmic reticulum was hypertrophied, and their length was increased. The hypertrophied mitochondria contained partially damaged cristae and light osmiophilic matrix. In the paranuclear region of the cells, organelles were better preserved than in animals without correction. The nuclei were oval in shape and had a clearly defined karyolemma. In the late stages of the experiment, the rounded nuclei of the cells were hypertrophied, the membranes of the karyolemma contained distinct, numerous nuclear pores, which indicated increased functional activity of the organ. Euchromatin predominated in the karyoplasm, and nucleoli were also present. Mitochondrial hyperplasia was observed in the cytoplasm, with partially damaged cristae in the matrix. Most of the membranous organelles retained their integrity, although in some cells the expansion of endoplasmic reticulum tubules, as well as cisternae and vacuoles of the Golgi complex was observed. In contrast to the second group of animals, single primary and secondary lysosomes were detected in the apical pole of the cells.

Such positive dynamics of organ recovery at the submicroscopic level was also observed in our studies in

the modeling of thermal injury and under the conditions of using a cryo-lyophilized xenograft skin substrate.

In further studies, it is planned to find out the effect of other corrective factors on the structural reorganization of adrenal endocrinocytes in severe thermal injury.

Conclusions

1. The results of electron microscopic studies of the adrenal gland of animals on day 7 after the application of thermal skin trauma with subsequent correction with a cryo-lyophilized xenograft skin substrate established the effectiveness of the protective effect of the substrate in burns on the ultrastructure of endocrinocytes in the cortex and medulla of the organ, It prevented the occurrence of deep changes, reduced the degree of damage to cytoplasmic membranes, organelles of the synthetic apparatus of cells, endocrinocyte nuclei and activated regenerative processes in them.

2. The regenerative effect of the cryo-lyophilized xenograft skin substrate was manifested in the late period after the burn (on the 14th and especially on the 21st day of the study) and it was characterized by the restoration of the ultrastructure of corticocytes of the adrenal cortex and chromaffinocytes of the medulla, the restoration of their nuclei and cytoplasmic components.

References

[1] Ahmad, A., Herndon, D. N., & Szabo, C. (2019). Oxandrolone protects against the development of multiorgan failure, modulates the systemic inflammatory response and promotes wound healing during burn injury. *Burns*, *45*(3), 671-681. doi: 10.1016/j.burns.2018.10.006

[2] Bali, A., & Jaggi, A. S. (2015). Preclinical experimental stress studies: Protocols, assessment and comparison. *European journal of pharmacology*, *746*, 282-292. doi: 10.1016/j.ejphar.2014.10.017

[3] Berger, I., Werdermann, M., Bornstein, S. R., & Steenblock, C. (2019). The adrenal gland in stress adaptation on a cellular level. *The journal of Steroid Biochemistry and Molecular Biology*, *190*, 198-206. doi: 10.1016/j.jsbmb.2019.04.006

[4] Bittner, E. A., Shank, E., Woodson, L., & Martyn, J. J. (2015). Acute and perioperative care of the burn-injured patient. *Anesthesiology*, *122*(2), 448-464. doi: 10.1097/ALN.0000000000000559

[5] Bondarev, Ye. V., Shtrygol, S. Yu., & Laryanovskaya, Yu. B. (2018). Стреспротекторна дія препаратів глюкозаміну та ацетилсаліцилової кислоти за умов гострої загальної холодової травми [Stress-protective effect of glucosamine preparations and acetylsalicylic acid in acute general cold injury]. *Фармакологія та лікарська токсикологія=Pharmacology and Drug Toxicology,* (6), 34-43.

[6] Chen, X., Feng, X., Xie, J., Ruan, S., Lin, Y., Lin, Z., … & Zhang, F. (2013). Application of acellular dermal xenografts in full-thickness skin burns. *Experimental and therapeutic medicine*, *6*(1), 194-198. doi: 10.3892/etm.2013.1114

[7] Comish, P. B., Carlson, D., Kang, R., & Tang, D. (2020). Damage-associated molecular patterns and the systemic immune consequences of severe thermal injury. *The journal of immunology*, *205*(5), 1189-1197. doi: 10.4049/jimmunol.2000439

[8] de l'Europe, C. (1986*). European Convention for the protection of vertebrate animals used for experimental and other scientific purposes/Convention européenne sur la protection des animaux vertŭbrŭs utilisŭs a des fins expŭrimentales ou a d'autres fins scientifiques: [Strasbourg, 18.III.1986]*. Conseil de l'Europe Section des publications.

[9] Di Lorenzo, M., Barra, T., Rosati, L., Valiante, S., Capaldo, A., De Falco, M., & Laforgia, V. (2020). Adrenal gland response to endocrine disrupting chemicals in fishes, amphibians and reptiles: a comparative overview. *General and comparative endocrinology*, *297*, 113550. doi: 10.1016/j.ygcen.2020.113550

[10] Evers, L. H., Bhavsar, D., & Mailänder, P. (2010). The biology of burn injury. *Experimental Dermatology*, *19*(9), 777-783. doi: 10.1111/j.1600-0625.2010.01105.x

[11] Horalskyi, L. P., Khomych, V. T., & Kononskyi, O. I. (2005). *Основи гістологічної техніки та морфофункціональних методів дослідження в нормі та при патології* [*Fundamentals of histological technique and morphofunctionalmethods of research in normal and pathology*]. Державний агроекологічний університет. Житомир: Полісся=State Agroecological University. Zhytomyr: Polissya.

[12] Hew, J., Parungao, R., Shi, H., Tsai, K., Kim, S., Ma, D. … & Wang, Y. (2020). Mouse models in burns research: Characterisation of the hypermetabolic response to burn injury. *Burns*, *46*(3), 663-674. doi: 10.1016/j.burns.2019.09.014

[13] Hryntsova, N. B., Romaniyk, A. M., & Bumeister, V. I. (2019). Морфологічні перебудови кіркової речовини наднирників щурів за умов довготривалого впливу солей важких металів та негормональної корекції [Morphological rearrangements of the rats adrenal cortex under conditions of prolonged exposure to heavy metal salts and non-hormonal correction]. *Морфологія=Morphologia*, *13*(3), 26-31. doi: 10.26641/1997-9665.2019.3.26-31

[14] Jeschke, M. G., van Baar, M. E., Choudhry, M. A., Chung, K. K., Gibran, N. S., & Logsetty, S. (2020). Burn injury. *Nature reviews. Disease primers*, *6*(1), 11. doi: 10.1038/s41572-020-0145-5

[15] Kalsi, R., Messner, F., & Brandacher, G. (2020). Skin xenotransplantation: technological advances and future directions. *Current Opinion in Organ Transplantation*, *25*(5), 464-476. doi: 10.1097/mot.0000000000000798

[16] Kearney, L., Francis, E. C., & Clover, A. J. (2018). New technologies in global burn care a review of recent advances. *International Journal of Burns and Trauma*, *8*(4), 77-87. PMID: 30245912

[17] Manukhina, E. B., Tseilikman, V. E., Tseilikman, O. B., Komelkova, M. V., Kondashevskaya, M. V., Goryacheva, A. V., … & Downey, H. F. (2018). Intermittent hypoxia improves behavioral and adrenal gland dysfunction induced by posttraumatic stress disorder in rats. *Journal of Applied Physiology*, *125*(3), 931-937. doi: 10.1152/japplphysiol.01123.2017

[18] Nahaichuk, V. I., Khimich, S. D., Zheliba, M. D., Zhuchenko, O. P., Povoroznyk, A. M., Prysiazhniuk, M. B., & Chornopyshchuk, R. M. (2017). Сучасні технології лікування хворих з критичними та надкритичними опіками [Modern technologies of treatment of patients with critical and supravithic burns]. *Вісник Вінницького національного медичного університету=Bulletin of Vinnytsia National Medical University*, *2*(21), 428-433.

[19] Nielson, C. B., Duethman, N. C., Howard, J. M., Moncure, M., & Wood, J. G. (2017). Burns: Pathophysiology of Systemic

Complications and Current Management. *Journal of Burn Care & Research: Official Publication of the American Burn Association*, *38*(1), e469-e481. doi: 10.1097/BCR.0000000000000355

[20] Ogura, A., Tsurumi, A., Que, Y. A., Almpani, M., Zheng, H., Tompkins, R. G., … & Rahme, L. G. (2019). Associations between clinical characteristics and the development of multiple organ failure after severe burns in adult patients. *Burns: journal of the International Society for Burn Injuries*, *45*(8), 1775-1782. doi: 10.1016/j.burns.2019.02

[21] Palmieri T. L. (2021). Transfusion and Infections in the Burn Patient. *Surgical infections*, *22*(1), 49-53. doi: 10.1089/sur.2020.160

[22] Porter, C., Tompkins, R. G., Finnerty, C. C., Sidossis, L. S., Suman, O. E., & Herndon, D. N. (2016). The metabolic stress response to burn trauma: current understanding and therapies. *Lancet*, *388*(10052), 1417-1426. doi: 10.1016/S0140-6736(16)31469-6

[23] Roshangar, L., Soleimani Rad, J., Kheirjou, R., Reza Ranjkesh, M., & Ferdowsi Khosroshahi, A. (2019). Skin burns: Review of molecular mechanisms and therapeutic approaches. *Wounds*, *31*(12), 308-315. doi: 10.1038/s41572-020-0145-5

[24] Skotarenko, T. A., & Shepitko, K. V. (2016). Reaction of the adrenal cortex in acute aseptic peritonitis and its correction by the introduction of cryopreserved placenta [Реакція кіркової речовини надниркових при гострому асептичному перитоніті та його корекції введенням кріоконсервованої плаценти]. *The world of Medicine and Biology=Світ медицини та біології*, *1*, 156-159

[25] Tejiram, S., Romanowski, K. S., & Palmieri, T. L. (2019). Initial management of severe burn injury. *Current opinion in critical care*, *25*(6), 647-652. doi: 10.1097/mcc.0000000000000662

[26] Tkachuk, Yu. L. (2016). Морфологічна характеристика судин гемомікроциркуляторного русла кори надниркових залоз при цукровому діабеті та його корекції [Morphological characteristics of microvascular bed in adrenal cortex under diabetes mellitus and under its correction]. *Актуальні проблеми сучасної медицини=Actual Problems of the Modern Medicine, 16*(1), 245-248.

[27] Viter, V. S., & Volkov, K. S. (2014). Ultrastructural state of muscular tunic of the heart after experimental thermal injury in applying lyophilized xenografts. *Nauka i Studia*, *8*(118), 107-111.

[28] Young, A. W., Dewey, W. S., & King, B. T. (2018). Rehabilitation of Burn Injuries. *Physical Medicine and Rehabilitation Clinics of North America*, *30*(1), 111-132. doi: 10.1016/j.pmr.2018.08.004

[29] Zhang, Q.-H., Hao, J.-W., Xiao-Jing, J., Guang-Lei, L., Zhou, M., & Yao, Y.-M. (2019). Long-lasting neurobehavioral alterations in burn-injured mice resembling post-traumatic stress disorder in humans. *Experimental Neurology*, *323,* 113084. doi: 10.1016/j.expneurol.2019.113084

УЛЬТРАСТРУКТУРА ЕНДОКРИНОЦИТІВ НАДНИРКОВИХ ЗАЛОЗ ПІСЛЯ ТЕРМІЧНОЇ ТРАВМИ ШКІРИ ЗА УМОВ КОРЕКЦІЇ ПОДРІБНЕНИМ ЛІОФІЛІЗОВАНИМ КСЕНОСУБСТРАТОМ

Кульбіцька В. В., Огінська Н. В., Слабий О. Б., Лісничук Н. Є., Трач Росоловська С. В., Небесний О. Р., Небесна З. М.

Опікові травми, як зазначено в дослідженнях ВООЗ, є одними з найпоширеніших уражень в світі, а через військові дії в Україні їх кількість значно зросла. Надниркові залози, які регулюють обмін речовин і беруть участь у захисних реакціях організму, є чутливими до опікових травм, що призводить до морфологічних змін в органі. Метою дослідження було вивчити ультраструктурні зміни ендокриноцитів досліджуваних залоз після змодельованого опіку шкіри за умов корекції ліофілізованими ксенодермотрансплантатами. Опік IIб ступеня моделювали шляхом накладання нагрітих мідних пластин на шкіру спини лабораторних самців-щурів, що становило 18-20 % поверхні тіла. Для електронно-мікроскопічного аналізу на 7, 14 і 21 добу експерименту вилучали шматочки надниркових залоз. Їх фіксували в розчині глютаральдегіду, постфіксували в тетраоксиді осмію та обробляли за стандартною методикою. Ультратонкі зрізи контрастували за методом Рейнольдса та вивчали із використанням електронного мікроскопа ПЕМ-125К. На 7 добу після опіку з корекцією (використали подрібнений субстрат ліофілізованої ксеношкіри) було виявлено помірні зміни ультраструктури ядер та органел ендокриноцитів залози. Спостерігалася гіперплазія мітохондрій, зміна форми ядер та наявність дрібних грудочок гетерохроматину в каріоплазмі. На 14 добу за умов корекції відзначали ознаки відновлення ультраструктури клітин, зокрема в клубочковій зоні відновлювалася структура ядра, мембрани каріолеми, зявлялися рибосоми та гіпертрофовані мітохондрії з електронно світлим матриксом, а також чисельні ліпідні краплі. Після 21 доби ультраструктура клітин клубочкової зони відновлювалася, ліпідні краплі рівномірно розподілялися в цитоплазмі. У сітчастій зоні та мозковій речовині зміни субмікроскопічної організації ендокриноцитів були незначними. Спостерігали рівномірний розподіл секреторних гранул в цитоплазмі хромафіноцитів, відновлення мітохондрій та незмінену ультраструктурну організацію органел синтетичного апарату. Отже, результати дослідження підтвердили, що подрібнений субстрат ліофілізованої ксеношкіри ефективно сприяє відновленню ультраструктури ендокриноцитів надниркових залоз, зменшуючи ступінь ушкодження цитоплазматичних мембран, органел синтетичного апарату клітин, ядер ендокриноцитів, особливо активізуючи процеси регенерації в пізні терміни після термічної травми шкіри.

Ключові слова: *надниркові залози, ендокриноцити, ультраструктурні зміни, термічна травма, подрібнений субстрат ліофілізованої ксеношкіри.*

Author's contribution

Kulbitska V. V. – conceptualization, visualization, investigation, methodology, writing original draft.

Ohinska N. V. – conceptualization, formal analysis, validation, investigation, methodology, writing original draft, funding acquisition, software, supervision.

Slabyy O. B. – formal analysis, validation, investigation, project administration, supervision.

Lisnychuk N. Ye. – conceptualization, formal analysis, validation, investigation, project administration, methodology, writing original draft, supervision.

Trach Rosolovska S. V. – formal analysis, validation, investigation, project administration, funding acquisition, software, supervision.

Nebesnyi O. R. – conceptualization, investigation, funding acquisition, software.

Nebesna Z. M. – conceptualization, formal analysis, validation, investigation, project administration, writing review & editing, methodology, writing original draft, supervision.

DOI: 10.31393/morphology-journal-2024-30(4)-10 Reports of Morphology, Vol. 30, №4, Pages 82-92

ISSN 1818-1295 eISSN 2616-6194

REPORTS OF MORPHOLOGY

Official Journal of the Scientific Society of Anatomists, Histologists, Embryologists and Topographic Anatomists of Ukraine

journal homepage: https://morphology-journal.com

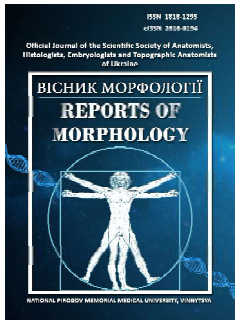

Impact of gamma-aminobutyric acid receptors modulators on renal and liver functional, molecular and histological characteristics in white male mice

Al-Azzawie A. F.[1], Ajeel M. A.[2], Al-Bayti A. A. H.[3]

[1]Department of Biology, College of Science, Tikrit University, Tikrit, Iraq
[2]Department of Clinical Laboratory Science, College of Pharmacy, Mosul University, Mosul, Iraq
[3]College of Health and Medical Techniques, Northern Technical University, Kirkuk, Iraq

ARTICLE INFO
Received: 27 February 2024
Accepted: 30 September 2024

UDC:
615.9:616.61:616.36:591.4:599.323.4

CORRESPONDING AUTHOR
e-mail: ayoub00ali00@gmail.com
AL-Bayti A. A. H

CONFLICT OF INTEREST
The authors have no conflicts of interest to declare.

FUNDING
Not applicable.

DATA SHARING
Data are available upon reasonable request to corresponding author.

The gamma-aminobutyric acid (GABA) receptors are considered the main receptors that inhibit neurotransmitters in the mammalian brain, and they have been proven to exist in non-neuronal cells. The study's purpose is to determine the impact of GABA modulation on renal and liver functions and molecular and histological characteristics using different doses of lorazepam. Lorazepam, one of the benzodiazepine drugs known for its modulatory effect on GABA receptors, has been used as a modulator to determine the impact of GABA modulation on renal and liver functions and molecular and histological characteristics in 30 albino male mice, out of which 21 were divided into 3 groups. Each group were treated with different dose of lorazepam (1 mg/kg, 2 mg/kg and 3 mg/kg body weight respectively). The rest 9 of animals were considered as a control group. Histological and functional parameters were studied in kidney and liver functional states to evaluate the impact of GAPA modulation using lorazepam. Total genomic DNA was extracted from liver, brain, kidney and blood and random amplification polymorphic DNA (RAPD) technique were used to detect the molecular impact of GABA modulation on the genomic DNA. The data were analyzed using SPSS Version 20.0 (SPSS Inc.), with means and standard deviations (SD) calculated for quantitative variables, and ANOVA applied for comparing group means. Functional parameters (blood urea, creatinine, GOT, GPT, GGT) and histopathological examination showed a significant change in treated groups compared to the control group. In both the liver and kidneys of mice, with increasing doses of lorazepam, there was an increase in the severity of congestive phenomena in blood vessels with the appearance of hemorrhages, signs of inflammation, and cell degeneration and necrosis. The molecular investigation indicated substantial changes in RAPD profiles of treated groups, with normal bands disappearing and novel bands appearing in contrast to the control group. The RAPD profiles of the treated and control samples revealed 432 bands, with 109 as control bands, 167 (loss of normal bands and emergence of novel bands) as polymorphic bands, and 156 as homomorphic bands. It is concluded that GABA modulation by lorazepam increases the functional and histopathological alterations, producing variations in the genomic DNA.

Keywords: *GABA modulation, molecular features, Lorazepam, molecular impact, functional characteristics.*

Introduction

The gamma-aminobutyric acid (GABA) receptors play a significant role in inhibiting neurotransmitter activity in the mammalian brain. The isoforms of their structure include five homologous subunits and a central channel that selectively allows the passage of chloride ions. This channel is regulated by GABA receptors. The exact number of isoforms of these receptors is currently unknown. However, they are positioned in the postsynaptic membrane and are responsible for mediating neuronal inhibition within milliseconds. On the other hand, the isoforms located in the extra synaptic membrane react to ambient GABA and provide long-term inhibition [14]. Several study

declared that GABA receptors can be found in other cells, like the pancreases the endocrine cells [27], liver cells [29], alveolar cells [31] and surfaces lining cells of the intestine [10]. Earlier researches have illustrated that rat and hepatocytes of human express vast amounts of GABAs [34] and $GABA_AR$ subunits [17]. It has been declared that $GABA_AR$ involve para and autocrine mechanisms of signal transmission in the livers different cells types. Moreover, Dgalactosamine which is a hepatic toxin alters the hepatocytes $GABA_AR$ expression and activate the GABA signals that protects the liver because of the Dgalactosamine insult [34]. Another reports have demonstrated that heavy ethanol intake elevates GABA concentration in human plasma which prevent liver cells cytotoxicity induced by ethanol in vitro by an unknown mechanism(s) [36]. It has been shown that nonsynaptic GABA receptor activation in glial fibrillary acidic protein (GFAP)-expressing cells limits their cell cycle progression [15]. Furthermore, the stimulation of $GABA_A$ receptors enhances the increment of cell volume and the accumulation of stem cells in the S phase, as a result, there will be a rapid cell proliferation decrement [26]. The benzodiazepines, a group of popular drugs, considers a first example of exogenous modulators of GABA [14, 32]. Benzodiazepines bind to GAB_AA receptor in a specific site where they enhance hyperpolarization of the cell membrane mediated by chloride channel. Classical benzodiazepines like lorazepam consider as allosteric upregulator module of that respond to GABA. Benzodiazepines high affinity bind with their recognition site on the GABA receptor which induce a conformational alteration in the receptor and eventually lower the GABA concentrations [12]. Y. S. Oghli and colleagues [25] stated in a study that benzodiazepines increase the regulatory circuits excitability in cortex of human motors. In another study benzodiazepine significantly reduce brief delay in the afferent inhibition of the cerebral motor cortex in human [9]. Due to the molecular methods used to diagnosis different disease [19, 24] so this study aimed to determine the influence of GAPA modulation on some functional, molecular and histological characteristic in albino mice.

The study's purpose is to determine the impact of GABA modulation on renal and liver functions and molecular and histological characteristics using different doses of lorazepam.

Materials and methods

This study was conducted in male adult mice (Mus Musculus). Department of Biology, Collage of Science, Tikrit University. Experiments on GABA modulation was performed using lorazepam, one of the benzodiazepines widely known for modulating GABA [9, 12, 20]. The present study was conducted on 30 adult albino male mice weighing between 25-30 gm, of which 21 were divided into three groups. The animals were kept at temperature and light-controlled quarters with free access to water and standard chow.

In this treatment, group 1 received lorazepam at a dose of 1 mg/kg once daily for each mouse, while in group 2 and group 3 they were administered at doses of 2 mg/kg and a dose of lorazepam (3 mg/kg) respectively. Oral drug doses were given for 2 weeks. Control group was mice that were given the same volume of normal saline instead.

Histological sections were taken to investigate the influence of GABA modulation with lorazepam on liver and kidney tissues. After some weeks, the mice were anaesthetized and killed. Blood specimens in EDTA tubes were obtained from each mouse in order to measure liver function and take a DNA sample for extraction. The liver and kidney were fixed in 10 % formal saline solution. Paraffin blocks were made and sections cut at 5 μm. The tissue sections were stained with hematoxylin and eosin for histopathological examination [6].

The effect on hepatic function state of GABA modulation was assessed by means of several physiological parameters of which blood urea and serum creatinine as reflectors kidney functional states; while tests for glutamate-pyruvic transaminase activity (GPT) or glutamate-oxaloacetic transaminase function (GOT) or g-Glutamyl enzyme levels show what liver condition is like. Biochemical tests were performed with a biochemistry auto analyzer SK3002B machine according to the manufacturer's instructions.

RAPD-PCR analysis of the impact of GABA modulation on the genomic DNA was also made. RAPD-PCR technique for was utilized using ten arbitrary primers (Operon Tech., Inc) [4, 37], as revealed in Table 1.

Table 1. Primers sequences for RAPDgene amplification**.**

No.	Primer	Sequence 5 to 3	No.	Primer	Sequence 5 to 3
1	OP A-6	GGTGCCTGAC	6	OP B-21	GGACCGTTAC
2	OP A-1	CAGCGCCTTC	7	OP D-3	GTGGCCGTCA
3	OP C-9	TGGAGCGGTG	8	OP D-18	GACAGCCAAC
4	OP C-16	CAGACTCCAG	9	OP E-3	CCACATGCAC
5	OP B-15	TCCGGTCTGG	10	OP E-11	GAGTGTCAGG

DNA extracted from the liver, brain and kidney was in accordance with method of the Pearce and Stillring [7]. Meanwhile, blood samples for extraction should be processed by the Harrison-Thompson protocol [16]. Nucleic acid was electricially separated in agarose and stained with red Asve. Testing genomic DNA quality, meanwhile, involves measuring absorbance not only at wavel engths from 260 to 280 nm, but also running an. Then product size was checked by agarose gel electrophoresis. The system adopted to amplify DNA was the milling mix (Mt) which includes 15 мl of Mt, a Pico mole of primer, 150 ng of DNA template and H_2O to make up

volume then mixed well with top off at a final volume of 25 мl. Scaling up from M-MLV, the 10ЧRT-PCR Buffer included 80 mm Tris-HCl pH 8.4, 10 mm $MgCl_2$, 20 mm DTT, 8 picomole olig (DT) 16.0 picomole dNTP(Mix), total volume 20 мL. This was done by vortex spin for 10-15 s then stored at 20°C. In a final volume of 20 мl containing 10 мl of PCR master mix, 10 мl of primer (50 pmol/мL) and 100 ng DNA template, use an Biometra thermocycler an initial denaturation (4 min at 94°C) followed. Bands resulting from the RS-PCR were observed with a Haaker H-4000 (BHD company) in standard U.V. gel documentation log system using the 100 bp DNA ladder as the standard (Bioloabs) [30]. The same PCR technique is employed in different articles of medicine [2, 18].

The data were coded and arranged in the form of tables so that integers could be automatically processed using SPSS Version 20.0 (SPSS Inc). For quantitative data, the mean and standard deviation (SD) were computed. ANOVA was used to compare means of multiple groups. A p-value less than both 0.05 and 0.001 was considered significant. There were good clear reproducible amplification bands as highlighted by the clearly defined figures in the table show. In contrast disappearance and/or appearance of bands was scored as a great change in RAPD profiles compared with those from untreated control The polymorphism calculation was made as described in Gene 9 GTS was calculated by this formula: GTS=(1-a/n)×100; where (a) is the number of polymorphic bands detected in each treated sample and (n) is the total number of bands detected in control [1, 25].

Results

Physiological and Biochemical parameters: According to Table 2, GPT, GGT and s.creatinine were significantly increased in all treatment groups compared with the control group. Whereas GOT and b. urea had no significant changes compared to untreated controls.

Histopathological examination. The lesions of liver sections in the treated showed that immune cell infiltration became sounder, congestion became much more serious and was found in almost all of the mice. Group 1 had hemorrhage, congestion significantly greater than other groups and dead cells (Fig. 1). In group 2 its effect on bone

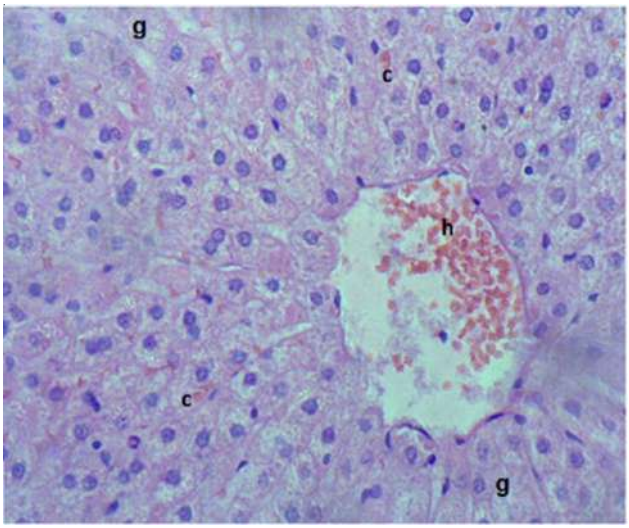

Fig. 1. A section of liver from G1 group showing congestion (c) and hemorrhage (h) and cell ghost (g). HE staining. ×400.

marrow was to produce central vein congestion, the infiltration of immune cells and degenerated hepatocytes (Fig. 2). But in case 3 mentioned above, these changes greatly intensify: here are severe hemorrhages and sinusoidal doublearization can be seen (Fig. 3). The pathological changes in treated kidney sections showed congestion, tubular necrosis and a cast in certain lobules' lumen, group 1 (Fig. 4). In group 2 congestion of central was the theme, (Fig.6) as well as tubular necrosis in which live cells die off en masse right before one's eyes. Then, necrotic debrites are present at local facture sites in the tubuli lumen (Fig. 5). And then in case 3, there was pronounced overall congestion, cellular as well as tubular necrosis and a bitrowed debrites at local construction points (Fig. 6)

Table 2. Physiological parameters of liver and kidney.

Groups	No.	Mean±SD				
		GOT	GPT	GGT	B. urea	S. creatinine
Control	9	33.24±3.51	0.1946	36.26±6.74	22.02±8.21 a	0.801±0.13
G1	7	34.51±1.92	42.74±1.71	56.02±2.84	26.74±2.62 a	1.844±0.037
G2	7	36.26±1.71	37.51±1.28	50.51±3.68	31.51±18.44	1.863±0.363
G3	7	37.24±2.97	38.26±4.98	52.52±1.28	40.26±10.72	1.884±0.086
p value		0.1946	0.0161*	0.001**	40.26±10.72	0.0001**

Note: M±SD – mean±standard deviation; No. – number of animals in each group; * – significant at pd≤0.05; ** – significantly at pd≤0.01.

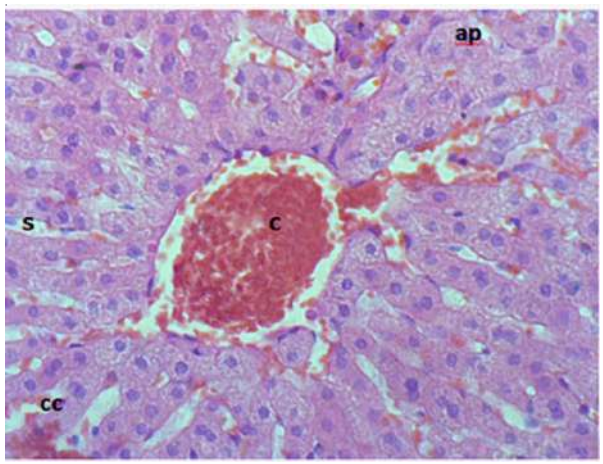

Fig. 2. A section of mouse liver from G2 group showing congestion (C), and sinusoidal dilatation (s), congestion (cc) with apoptotic cells (ap). HE staining. ×400.

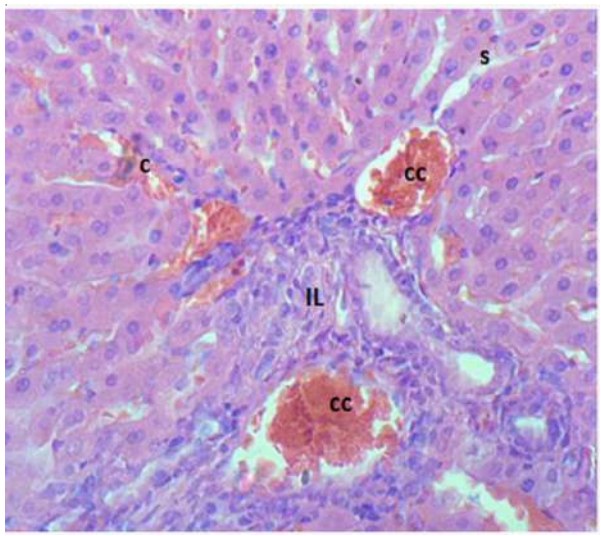

Fig. 3. A section of mouse liver from G3 group showing congestion (cc) and sinusoidal dilatation (s), infiltration (IN), degenerated cells, and congestion in sinusoids (c). HE staining. ×400.

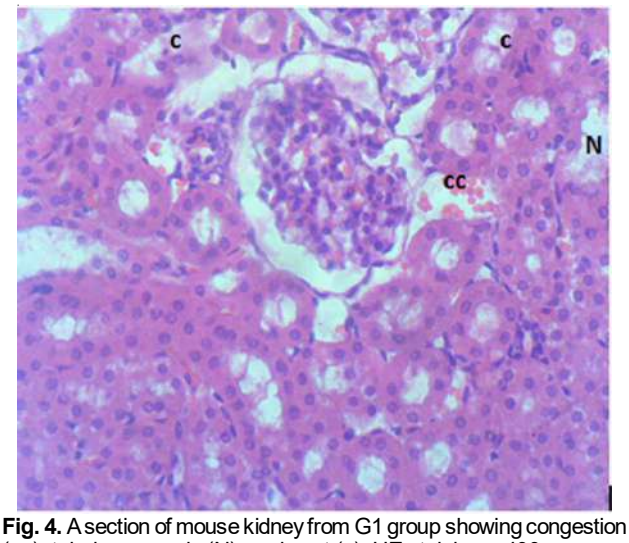

Fig. 4. A section of mouse kidney from G1 group showing congestion (cc), tubular necrosis (N), and cast (c). HE staining. ×400

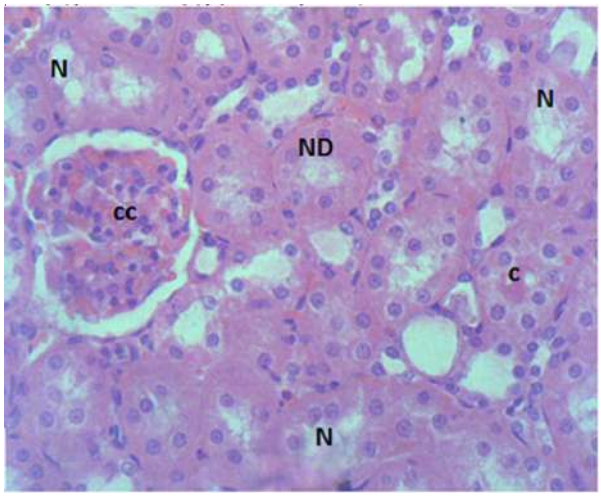

Fig. 5. A section of mouse kidney from G2 group showing congestion (cc), tubular necrosis (N), necrotic in the tubuli lumen (ND) and cast (c). HE staining. ×400.

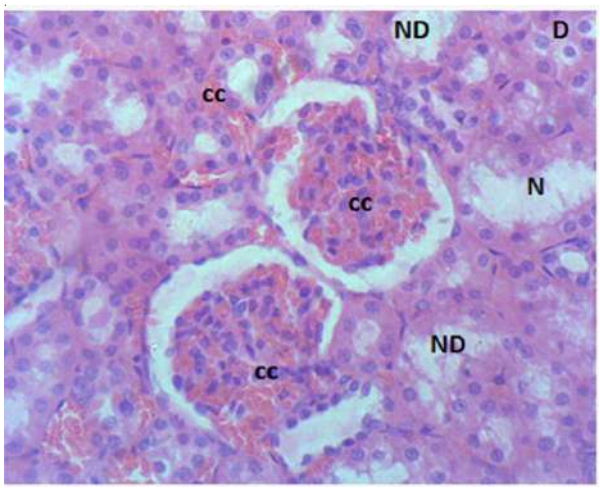

Fig. 6. A section of mouse kidney from G3 group showing marked congestion (cc), cellular necrosis (N), necrotic in the tubule lumen (ND) and degenerated cells (D). HE staining. ×400.

Molecular analysis: First contribute was a random amplification of polymorphic DNA (RAPD-PCR) to study the gene modifications induced by GABA modulation and Lorazepam drugs at different concentration levels (1, 2 or 3 mg/kg) on male albino mice tissues (DNA from liver, kidney, brain and blood are with M behind them to denote mice). Overall, ten oligonucleotide primers were themselves used for screening DNA from both treated and untreated organisms. Three (OP D-18, OP E-3 and OP E-11) of the occupied primers could not come through with DNA. The remaining seven primers (OP A-1, OP A-6, OP B-15, OP B-21, OP C-9, OP C-16 and OP D-3) could produce 432 bands of visible nature. No matter what the primers produced homormorphic as well as polymorphic bands which were 100-1500 bp. The bands were made with different sizes and tended to separate and rearrange (Fig. 7).

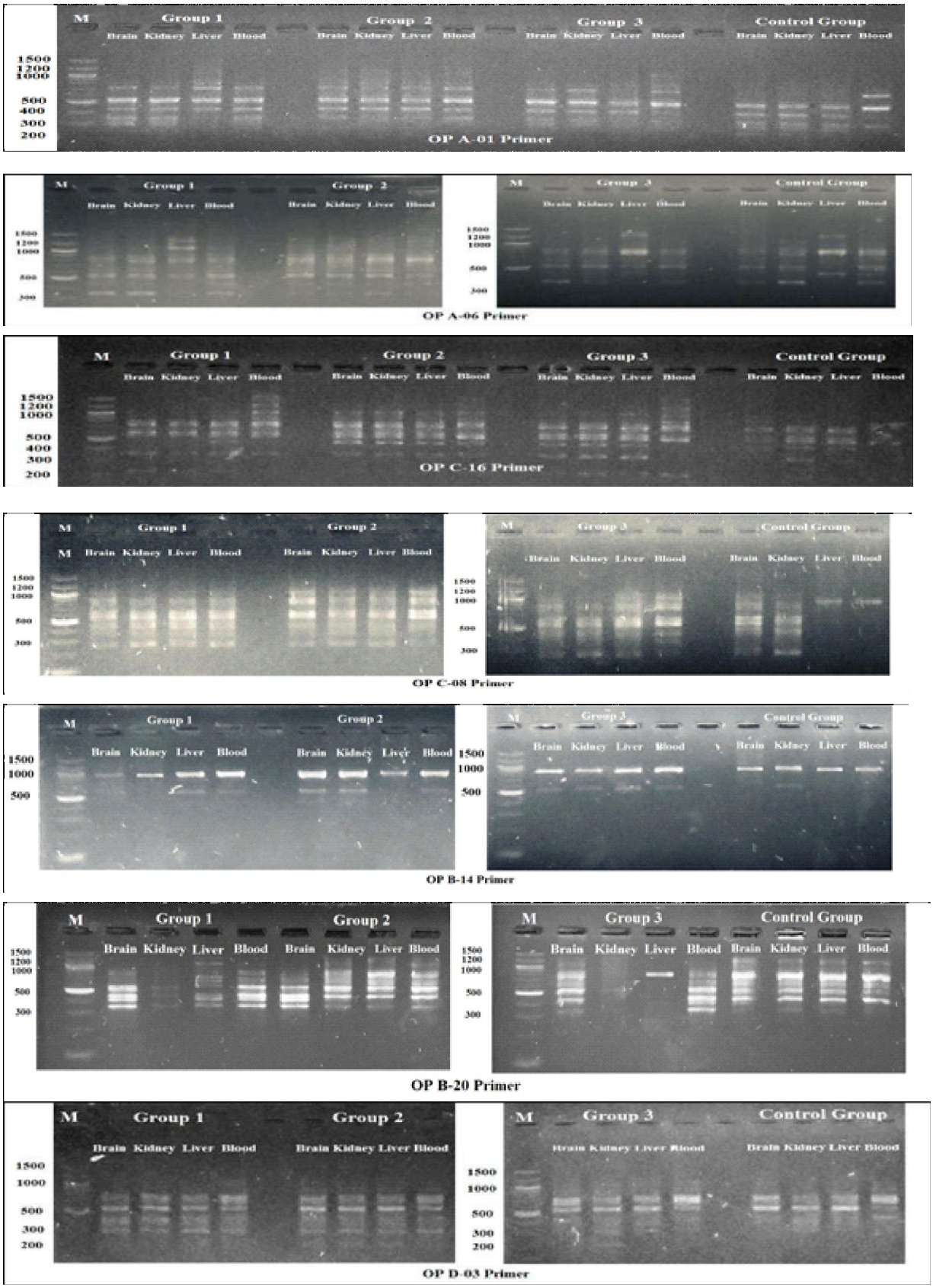

Fig. 7. Shows 1.5 % gel electrophoresis of RAPD-PCR profiles of genomic DNA (Brain, Kidney, Liver and Blood) of the study animals.

Table 3. The number of amplified, polymorphic, control and aberrance or absence bands and polymorphism percentage of (Brain, Kidney, Liver and Blood) samples of male albino mice (Mus Musculus) treated with different Lorazepam concentrations.

Primer	G 1		G 2		G 3		Polymorphic bands	Control bands	Total amplified bands
	a	d	a	d	A	d			
OP A-6	7	2	7	4	4	2	26	14	60
OP A-1	8	5	8	5	6	5	37	14	58
OP C-9	8	2	8	2	5	0	25	15	65
OP C-16	11	5	9	2	7	1	35	23	89
OP B-15	2	1	3	1	4	1	12	6	26
OP D-3	4	0	4	1	1	1	11	14	54
OP B-21	1	4	1	4	2	9	21	23	80
Total	41	19	40	19	29	19	167	109	432
a + b	60		59		48				
Polymorphism %	55.04		54.13		44.03				
∑Polymorphism %	51.06								

Notes: Group 1 1 mg/kg; Group 2 2 mg/kg; Group 3 3 mg/kg; a appearance of new bands; d loss of normal bands. (G1=Group1, G2=Group2, G3=Group3).

Impact of GABA modulation by lorazepam on RAPD-PCR pattern. The differences found in the profiles of DNA fragments amplified by RAPD using primers from treated animals versus those of controls are almost entirely dependent upon which of the primer was used. The DNA profiles generated from the seven primers displayed variations between treated and control cells, with marked changes in the DNA fragments amplified. Absence of a normal band and/or the appearance of a new band are conspicuous differences lorazepam treatment has brought about in RAPD patterns. Tables 3, 4, 6 and Fig. 7 give an all-inclusive view of RAPD profiles for all treatments of lorazepam, providing that between them the seven primers included several polymorphic bands and what the polymorphic ratio was for each treated rat.

The results of tables 3, 4, 5, 6 and 7 show that all treatments are different for total zoom bands lost and gained; in addition to the difference between treatments of the same sample interpret as samples among all. The seven primers (used) in total produced 432 banding patterns of RAPD profiles for this study samples, 109 were monomorphic as control bands, 167 polymorphic (loss of target and gain of new) and the others were homomorphic bands which were equivalent to 156. RAPD analysis indicated that the highest number of polymorphic bands was observed at 1 and 2 mg/ kg for Lorazepam with 60 and 59 bands respectively, a number of appearing new bands were 41 and 40 respective, while a losing normal band was estimated 19 for both treated. In presence of RAPD polymorphisms (indicated by the presence or absence of the same set of amplified bands as in control RAPD profile), gain and/or loss of the amplified bands respect to control. Where the greatest value of genetic polymorphic percent (55.04 %) was at 1 mg/kg treatment that differed significantly with the lowest percent, it was detected for 3 mg/kg treatment (44.03 %). A rate of genetic polymorphism (55.04 %) was observed at Lorazepam concentration (1mg/ kg). However, this level of genetic polymorphism was minimized to (44.03 %) in the treated group (3 mg/kg). OP A-01 have produced maximum number of polymorphic bands (37) whereas the minimum with OP D-03 primer band is 11.

Table 4. The total number of bands, bands polymorphism and polymorphic percent of all treatments of and of polymorphic bands of RAPD-PCR profiles of (Brain, Kidney, Liver and Blood) samples of male albino mice (Mus Musculus) treated with different Lorazepam concentrations.

Sample	Total amplifie-d bands	Total amplified bands	∑ Polymorphic % of treatments	∑ Polymorphic % of all polymorphic bands
Liver	106	47	52.22	44.33
Kidney	118	32	38.09	27.11
Blood	88	34	59.65	38.63
Brain	120	54	56.25	45.00
Total or Average	432	167	51.55	38.76

Summary of changes in RAPD-PCR data of brain, kidney, liver and blood samples treated with Lorazepam are tabulated in Table 4. The highest number of altered bands was for the comparison of brain sample with the lowest number is from blood sample (Table 4). The maximum number of polymorphic bands were obtained in blood sample and minimum in kidney sample. The blood samples provided the highest polymorphic percentage, and this was the most homogeneous group as well (Table 3). As seen above, it would appear that the blood sample has been much more affected by Lorazepam than those in the kidney sample.

Nucleic acid stability: The fragments retrieved from the RAPD-PCR polymorphism of brain, liver kidney, and blood samples for each diagnosed tested specimens in addition to a control were used for the calculation of genomic template stability (GTS %). Qualitative indicator: GTS % were evaluated for the primers and treatment; Table 5 and Figure 8. Values decreased gradually obviously according to Lorazepam concentration.

Table 5. Genomic template stability (GTS %) of brain, kidney, liver and blood samples of the male albino mice (Mus Musculus) exposed to different Lorazepam concentrations.

GST % of Brain Samples									
Primers	Control		G1		G2		G3		Average of GTS %
	Total	(%)	a/d	(%)	a/d	(%)	a/d	(%)	
OP A-6	4	100	2/0	50.00	3/1	0	1/1	50.00	33.33
OP A-1	4	100	2/2	0	2/2	0	2/2	0	0
OP C-9	4	100	2/1	25.00	2/1	25.00	1/0	75.00	41.67
OP C-16	8	100	5/2	12.50	3/1	50.00	1/0	87.50	50.00
OP B-15	2	100	0/1	50.00	1/1	0	1/1	0	16.67
OP D-3	4	100	2/0	50.00	2/0	50.00	0/0	100	66.67
OP B-21	4	100	0/2	66.67	1/1	50.00	1/0	100	63.89
Total or Average	32	100	21	55.36	22	25.00	11	36.31	38.89
∑GTS %			38.89						

GST % of Kidney Samples									
Primers	Control		G1		G2		G3		Average of GTS %
	Total	(%)	a/d	(%)	a/d	(%)	a/d	(%)	
OP A-6	3	100	2/1	100	1/1	33.33	1/0	66.67	66.67
OP A-1	4	100	2/1	25.00	2/1	25.00	2/1	25.00	25.00
OP C-9	4	100	1/1	50.00	1/1	50.00	0/0	100	66.67
OP C-16	6	100	½	50.00	1/0	83.33	1/0	83.33	72.22
OP B-15	1	100	0/0	100	1/0	0	1/0	0	33.33
OP B-21	6	100	0/1	83.33	0/0	100	0/3	50.00	77.78
OP D-3	4	100	0/0	66.67	0/1	66.67	1/0	100	77.78
Total &Average	28	100	12	67.86	10	51.19	10	60.71	59.92
∑GTS %			59.92						

GST % of Liver Samples									
Primers	Control		G1		G2		G3		Average of GTS %
	Total	(%)	a/d	(%)	a/d	(%)	a/d	(%)	
OP A-6	3	100	1/1	33.33	1/1	33.33	2/1	0	22.22
OP A-1	3	100	2/1	0	1/1	0	1/1	33.33	11.11
OP C-9	6	100	4/0	33.33	4/0	33.33	3/0	33.33	11.11
OP C-16	7	100	3/1	42.86	3/1	42.86	3/1	42.86	42.86
OP B-15	2	100	1/0	50.00	0/0	100	1/0	50.00	66.67
OP D-3	3	100	1/0	66.67	1/0	66.67	0/0	100	77.78
OP B-21	6	100	0/0	100	0/0	100	0/0	16.67	72.22
Total &Average	30	100	15	46.60	14	53.74	18	39.46	46.60
∑GTS %			46.60						

GST % of Blood Samples									
Primers	Control		G1		G2		G3		Average of GTS %
	Total	(%)	a/d	(%)	a/d	(%)	a/d	(%)	
OP A-6	4	100	2/0	50.00	2/1	75.00	0/0	100	75.00
OP A-1	3	100	2/1	0	2/1	0	1/1	33.33	11.11
OP C-9	1	100	1/0	0	1/0	0	1/0	0	0
OP C-16	2	100	2/0	0	2/0	0	2/0	0	0
OP B-14	1	100	1/0	0	1/0	0	1/0	0	0
OP D-3	3	100	1/0	66.67	1/0	66.67	0/1	66.67	66.67
OP B-21	5	100	1/1	60.00	1/1	60.00	1/1	60.00	60.00
Total &Average	19	100	12	25.24	13	28.81	9	37.14	30.40
∑GTS %			30.40						

Notes: Group 1 1 mg/kg; Group 2 2 mg/kg; Group 3 3 mg/kg; a appearance of new bands; d lack of normal bands. (G1=Group1, G2=Group2, G3=Group3).

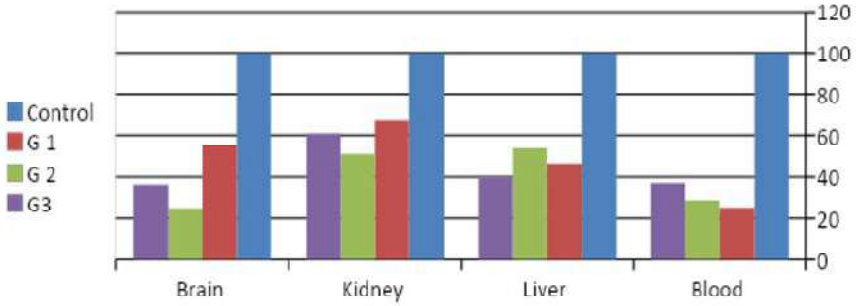

Fig. 8. Changes of percentage genomic template stability (GTS %) of the studied organs (G1=Group1, G2=Group2, G3=Group3).

Following Lorazepam exposure at different concentrations of Lorazepam were dose-dependent turnover [downward from high to low quantities for the green modulating status (GTS)], altered in comparison with control. These results indicate that GTS was really impacted by Lorazepam and also any amounts of Lorazepam getting to the treated samples will have been enough to create a hyperproliferation inside genomic DNA. The lowest values of GST % was found in the brain sample (25 %) treated with concentration (2 mg/kg) and blood sample (25.24 %) treated with concentration (1 mg/kg), while in the Kidney samples, higher GTS values were obtained [c(1 mg/kg)=67.86 % and c(2 mg/kg)=60.71] that might have less sensitivity for Lorazepam as shown in table 5 and figure 8.

Average of (GTS %) of all samples and treatment is presented in table 6. Reduced GTS percentage in those untreated Specimens. Especially blood and brain were the most sensitive tissues to which GTS values decreased to 30.40 % and 38.89 % respectively for all treatments as comparing to kidney and liver where lesser sensitiveness was demonstrated, that is, GTS values 59.92 % and 46.60 % respectively (see Table 6). The second concentration gave the least tensile strength with GTS of 39.68 % depending on severity of the treatment used as compared to that obtained from the first concentration which produced highest GTS (48.76 %).

Table 6. Average of genomic template stability (GTS %) of brain, kidney, liver and blood samples of the male albino mice (Mus Musculus) exposed to different Lorazepam concentrations.

Sample Type	GST %				
	Control	G1	G2	G3	Average
Liver	100	46.60	53.74	39.46	46.60
Kidney	100	67.86	51.19	60.71	59.92
Blood	100	25.24	28.81	37.14	30.40
Brain	100	55.36	25.00	36.31	38.89
Average	**100**	**48.76**	**39.68**	**43.40**	-

Notes: (G1=Group1, G2=Group2, G3=Group3).

Discussion

This is the first study that used three techniques at three levels physiological, histological and molecular (RAPD-PCR technique) to detect effects of GABA modulation using lorazepam drug at different concentrations (1 ml/kg, 2 ml/kg and 3 ml/kg). SGPT was significantly increased while no significant difference in SGOT levels in comparison to control cells, this may be due to the absence of the protective effect of GABA signaling path way especially in the liver, wang et al revealed that intrahepatic GABAergic system activation prevent liver cells toxic damage [22]. The loss of GABA protective pathway may increase the oxidative damage of tissue in the liver as a result of the repeated lorazepam ingestion and the effects of its deleterious metabolites such as desmethyldiazepam. The increase in this enzyme action is profoundly returns to the enzyme leakage from hepatocytes to the bloodstream due to the tissue damage [13]. these data were in agreement with other studies revealed that diazepam which is a member of benzodiazipens induce elevation in the enzymes activity [20, 24] and also with Mohammad Azab [5] who stated that long use of diazepam increases the liver enzyme activity (SGPT and SGOT), which might be due to oxidative tissue damage. M. Gogulski and his colleagues reported that repeated diazepam oral administration raise the serum concentrations of SGPT, SGOT, alkaline phosphates, and other enzymes significantly [13].

There was a significant increase in creatinine while there was no significant decrease in B.urea in mice after lorazepam administration. Our findings agreed with Amresh Kumar A. K. et al. [3] whose find a significant increase in serum creatinine and blood urea.

Microscopic examination of the liver specimens showed an elevation of infiltrating immune cells**,** marked congestion was recorded in almost all mice. In group 1 there was hemorrhage, congestion and degenerated cells. These pathological lesions in the liver could attribute to drug toxicant and negative effects of its metabolites and the accumulative ability of diazepam during repeated administration. The present results with the free radical inducing pro-oxidative consequences in the liver and brain cells after benzodiazepens administration suggesting that lorazepam has a crucial effect in the advancement of brains and livers oxidative stress in the lorazepam treated mice groups [11, 34]. Additionally, they showed that ethanol acute hepatic injury induced the up regulation of GABA signaling system in hepatatocytes in mice. So, the modulation of GABA by Lorazepam may lead to accumulation of injuries in hepatocytes. Moreover, our results were coped with another study [5].

Histopathological alterations were obviously increased in group 3 in the form of severe hemorrhage, marked sinusoidal dilatation, and the cells have highly degenerated with an area of inflammation, which highlighted. The abnormal filtration process may be as a result of benzodiazipens modulating postsynaptic GABA transmission effects, which lead to increasing affect blood plasma colloid pressure, capillary pressure and pre-sympatic barriers. These factors have an important function in regulating the filtration rates of the glomeruli, as glomerular filtration rate will be decreasing as a result of the low pressure in the capillaries and osmotic colloid pressure of the plasma [33].

The benzodiazipens are responsible for acute renal injury by two general ways. They are affecting destructing cells and the hemodynamic aspect through their activities and their chemical compounds. Lorazepam can decrease blood flow to the kidney and lower the blood pressure. The kidney ischemic condition can be a result and reduction of

oxygen supplement in renal cortex cells will be resulted from this [21, 27]. The existence of congestion in such cases can resulted in the ischemic condition. Profound congestions will occur in mouse treated with lorazepam. However, congestion is extensive in group 3. Cell damage could not be spare due to hypoxia put several stress conditions on renal cortex cells [28].

The influence of genotoxic chemicals on DNA could be monitored using different molecular markers. RAPD was considered a reliable, sensitive and can swiftly detect a vast amount of DNA damage in addition to different types of genetic alterations, hence it can be implicated in the assessment of genotoxicity and carcinogenic researches [7]. This study used RAPD technique to detect genomic DNA alterations resulted from GABA modulation by lorazepam in male albino mice (*Mus Musculus*) compared with control. The integrity and purity of the extracted DNA was excellent, indicating that the DNA samples were suitable to use in RAPD-PCR.

Following extensive optimization of thermocycling condition, RAPD profiles was detected and implicated to monitor DNA damages due to lorazepam administration. RAPD profiles generated from DNA of rat's brain liver, kidney and blood in the different groups were presented in Fig. 7. The size of all the bands obtained was found in the range of 100-1500 bp. Six random primers were used for detecting the alterations in RAPD patterns of genomic DNA in these samples in comparison to the control group. The profiles obtained by these primers exhibited variations between the control and exposed groups in all samples that had obvious alterations in the quantity and polymorphism of amplified DNA fragments [35]. The total number and number of polymorphic bands exhibited dependence on the primers and treatments used, and displayed a significant degree of variability. The amplified polymorphic bands varied across the treatment groups based on the primer used. The six random primers that were tested yielded definite and consistent results, exhibiting noticeable variations in the quantity of amplified DNA bands. The group that was exposed had polymorphic bands, which varied in their presence or absence, compared to the negative control group.

Results of RAPD profile for all treated and control of rat groups were showed in Table 3, 4 and 5. As can be seen, six primers generated a total of 432 amplified bands, 109 and 167 as a control and polymorphic bands respectively. Compared with the control, the mice (G1) that treated with 1 ml of larazepam for 1 kg recorded highest polymorphic bands as emergence of 41 new loci and the disappearance of 19 loci. While (G3) treated with 1 ml/kg of larazepam shown lowest polymorphic bands (29 presence/19 absence). Primer OP-A-01 gave the highest polymorphic bands (37 bands) while the OP D-03 gave the lowest polymorphic bands (11 bands). According to sample type, highest polymorphic bands (54 bands) was in brain sample while the lowest polymorphic bands (32 bands) was in kidney sample. The blood sample gave highest polymorphic percent (59.65 % bands), while the kidney samples the lowest polymorphic percent (38.09 %). These results indicate that lorazepam causing modulation in DNA mismatch repair leads to DNA damage, such as DNA fragmentation or alterations in the RAPD profile. Hence, the observed DNA fragmentation and genetic polymorphism in the DNA of changes in the RAPD profile in this research may be attributed to strand breaks or variations in the base pairs of genomic DNA, generated by the toxic effects of lorazepam. The lack of a typical RAPD product may be attributed to various point mutations, DNA damage, and/or intricate chromosomal rearrangements caused by numerous factors [4, 34]. The observed changes in RAPD profiles, such as variations in band intensity and the absence of some bands, are likely caused by alterations in the regions where oligonucleotide primers bind, as well as interactions between DNA polymerase and damaged DNA. The lack of bands may be attributed to the presence of photoproducts in DNA, namely pyrimidine dimers. The appearance of additional bands can be ascribed to the existence of oligonucleotide priming sites that become accessible to oligonucleotide primers following a structural modification, or to specific changes in the DNA sequence caused by mutations (leading to new annealing occurrences), large deletions (bringing two existing annealing sites closer), or homologous recombination [3]. Recently, the PCR was applied in many articles in medicine field [8, 23, 32].

The results obtained by RAPD-PCR were used to calculate the percentage of Genomic template stability (GTS %) as a qualitative indicator was calculated for each primer and treatment and presented in Table 5, 6 and Fig. 8. It shown as values decreased gradually obviously according to Cd concentration. In this study the GTS % reflecting changes in the RAPD patterns of rat's brain, liver, kidney and blood for the treated group in comparison with the control group. After exposure to different Lorazepam concentrations, GTS values were changed to lower values for all treated groups in comparison to control group, which indicated that GTS was significantly affected by Lorazepam and the amount of Lorazepam reaching to the treated samples and have been sufficient to produce an increase in the variations of genomic DNA. Especially for the blood and brain that were highly sensitive and GTS values decreased to 30.40 % and 38.89 % respectively for all treatments in comparison with kidney and liver that were less sensitive, GTS values 59.92 % and 46.6 % respectively. Depending on the concentration of the treatment used, the second concentration gave the least value of GTS (39.68 %) compared to the first concentration, which gave the highest value of GTS (48.76 %). GST relates to the efficiency of replication and DNA repair as well as level the level of DNA damage. Thus, an elevated level of DNA turnover may not essentially reduce the stability of the DNA template because the incidence of DNA damage modulates DNA restoration

and duplication [22]. DNA polymorphism identified by RAPD analysis because of the bands occurrence of the bands in the treatments groups can be implied in the environmental toxicity which is consider as a useful biomarker test [18].

Conclusions

A conclusion can be made from the present results that GABA modulation by lorazepam increases the functional and physiological alterations in the kidney and liver of male albino mice and produce variation in the genomic DNA.

References

[1] Abd El-Rahim, A. H., Abd El-Kader, H. A., Abd-El-Moneim, O. M., Radwan, H. A., Fadel, M., & Farag, I. M. (2016). Molecular genetic, cytogenetic and sperm studies on the protective and therapeutic role of vinasse against toxicity of lead acetate in Mice. *Research journal of pharmaceutical biological and chemical sciences*, *7*(4), 2107-2119.

[2] Ali, S. M., Laftah, B. A., Al-Shammary, A. M., & Salih, H. S. (2021). *Study the role of bacterial neuraminidase against adenocarcinoma cells in vivo*. In AIP Conference Proceedings (Vol. 2372, No. 1). AIP Publishing. doi: 10.1063/5.0067193

[3] Amresh Kumar, A. K., Ashok Kumar, A. K., Sukhbir Singh, S. S., & Sandeep Potilya, S. P. (2016). Evaluation of lorazepam as a sedative in buffalo calves. *Haryana Vet*, *55*(1), 53-55.

[4] Atienzar, F. A., Venier, P., Jha, A. N., & Depledge, M. H. (2002). Evaluation of the random amplified polymorphic DNA (RAPD) assay for the detection of DNA damage and mutations. *Mutation Research/Genetic Toxicology and Environmental Mutagenesis*, *521*(1-2), 151-163. doi: 10.1016/S1383-5718(02)00216-4

[5] Azab, M., Khabour, O. F., Alzoubi, K. H., & Almomani, D. H. (2018). Diazepam induced oxidative DNA damage in cultured human lymphocytes. *Journal of King Saud University-Science*, *30*(3), 412-416. doi: 10.1016/j.jksus.2017.03.002

[6] Bancroft, J. D., & Gamble, M. (Eds.). (2008). *Theory and practice of histological techniques*. Elsevier health sciences.

[7] Bartlett, J. M., & Stirling, D. (Eds.). (2003). *PCR protocols* (Vol. 226, pp. 3-525). Totowa, NJ: Humana Press.

[8] Bassi, A. G. H., & Al-Rubaii, B. A. L. (2024). Detection of Pyocin S and the Effects of Lactobacillus Acidophilus Cell-Free Supernatants on Multi-Drug Resistant Pseudomonas Aeruginosa Isolated from Patients of Baghdad Hospitals. *Journal of Communicable Diseases (E-ISSN: 2581-351X & P-ISSN: 0019-5138)*, *56*(1), 135-144. doi: 10.24321/0019.5138.202418

[9] Di Lazzaro, V., Oliviero, A., Saturno, E., Dileone, M., Pilato, F., Nardone, R & Tonali, P. (2005). Effects of lorazepam on short latency afferent inhibition and short latency intracortical inhibition in humans. *The Journal of physiology*, *564*(2), 661-668. doi: 10.1113/jphysiol.2004.061747

[10] Drobny, A., Ngo, P. A., Neurath, M. F., Zunke, F., & Lypez-Posadas, R. (2021). Molecular communication between neuronal networks and intestinal epithelial cells in gut inflammation and Parkinson's disease. *Frontiers in medicine*, *8*, 655123. doi: 10.3389/fmed.2021.655123

[11] Eger, G. A., Ferreira, V. V., Batista, C. R., Bonde, H. L., de Lima, D. D., Rodrigues, A. F., ... & Magro, D. D. D. (2016). Acute administration of diazepam provokes redox homeostasis imbalance in the rat brain: prevention by simvastatin. *Journal of biochemical and molecular toxicology*, *30*(10), 506-512. doi: 10.1002/jbt.21815

[12] Ghit, A., Assal, D., Al-Shami, A. S., & Hussein, D. E. E. (2021). GABAA receptors: structure, function, pharmacology, and related disorders. *Journal of Genetic Engineering and Biotechnology*, *19*(1), 123. doi: 10.1186/s43141-021-00224-0

[13] Gogulski, M., Cieslak, A., Grabska, J., Ardois, M., Pomorska-Myl, M., Koiodziejski, P. A., ... & Szumacher-Strabel, M. (2021). Effects of silybin supplementation on nutrient digestibility, hematological parameters, liver function indices, and liver-specific mi-RNA concentration in dogs. *BMC Veterinary Research*, *17*(1), 228. doi: 10.1186/s12917-021-02929-3

[14] Goldschen-Ohm, M. P. (2022). Benzodiazepine modulation of GABAA receptors: A mechanistic perspective. *Biomolecules*, *12*(12), 1784. doi: 10.3390/biom12121784

[15] Gutiérrez-Castaceda, N. E., González-Corona, J., Griego, E., Galván, E. J., & Ochoa-de la Paz, L. D. (2023). Taurine promotes differentiation and maturation of neural stem/progenitor cells from the subventricular zone via activation of GABAA receptors. *Neurochemical Research*, *48*(7), 2206-2219. doi: 10.1007/s11064-023-03883-2

[16] Harrison, D. J., & Thompson, E. P. (2020). A rapid and low-cost method for genomic DNA extraction from the cyanobacterium Synechocystis. *Biology Methods and Protocols*, *5*(1), bpaa011. doi: 10.1093/biomethods/bpaa011

[17] Hata, T., Rehman, F., Hori, T., & Nguyen, J. H. (2019). GABA, r-aminobutyric acid, protects against severe liver injury. *Journal of surgical research*, *236*, 172-183. doi: 10.1016/j.jss.2018.11.047

[18] Hosseinpour, A., Ilhan, E., Özkan, G., Öztürk, H. I., Haliloglu, K., & Cinisli, K. T. (2022). Plant growth-promoting bacteria (PGPBs) and copper (II) oxide (CuO) nanoparticle ameliorates DNA damage and DNA Methylation in wheat (Triticum aestivum L.) exposed to NaCl stress. *Journal of Plant Biochemistry and Biotechnology*, *31*(4), 751-764. doi: 10.1007/s13562-021-00713-w

[19] Ismael, M. K., Qaddoori, Y. B., Shaban, M. N., & Laftaah AL-Rubaii, B. A. (2023). The Immunohistochemical Staining of Vimentin and E-Cadherin in Bladder Cancer Patients Infected with Hepatitis C Virus. *Journal of Pure & Applied Microbiology*, *17*(2). doi: 10.22207/JPAM.17.2.30

[20] Jeboori, K., & Ali, A. (2014). Adverse effect of diazepam on cytogenetic and biochemical effects in white mice fed diet supplement with chitosan. *GJBB*, *3*, 242.

[21] Khajuria, A., Tay, C., Shi, J., Zhao, H., & Ma, D. (2014). Anesthetics attenuate ischemiareperfusion induced renal injury: Effects and mechanisms. *Acta Anaesthesiologica Taiwanica*, *52*(4), 176-184. doi: 10.1016/j.aat.2014.10.001

[22] Majumdar, S., Chakraborty, B., & Kundu, R. (2018). Comparative analysis of cadmium-induced stress responses by the aromatic and non-aromatic rice genotypes of West Bengal. *Environmental Science and Pollution Research*, *25*, 18451-18461. doi: 10.1007/s11356-018-1966-6

[23] Mohsin, M. R., & Al-Rubaii, B. A. L. (2023). Bacterial growth and antibiotic sensitivity of Proteus mirabilis treated with anti-inflammatory and painkiller drugs. *Biomedicine*, *43*(2), 728-734. doi: 10.51248/.v43i02.2693

[24] Muhsin, H. Y., Al-Humairi, R. M., Alshareef, D. Q., & Ad'hiah, A. H. (2022). Interleukin-22 is up-regulated in serum of male patients with ankylosing spondylitis. *The Egyptian*

Rheumatologist, *44*(4), 351-355. doi: 10.1016/j.ejr.2022.07.002
[25] Oghli, Y. S., Grippe, T., Arora, T., Hoque, T., Darmani, G., & Chen, R. (2023). Mechanisms of theta burst transcranial ultrasound induced plasticity in the human motor cortex. *Brain Stimulation*, *16*(4), 1135-1143. doi: 10.1016/j.brs.2023.07.056
[26] Orlando, L., Tanasijevic, B., Nakanishi, M., Reid, J. C., Garcна-Rodrнguez, J. L., Chauhan, K. D., ... & Bhatia, M. (2021). Phosphorylation state of the histone variant H2A. X controls human stem and progenitor cell fate decisions. *Cell Reports*, *34*(10), 108818. doi: 10.1016/j.celrep.2021.108818
[27] Pae, E. K., Chung, M. K., & Harper, R. M. (2022). Intermittent Hypoxia Interferes with Autocrine Effects of GABA on Insulin Secretion in Postnatal RodentsImplications for Pediatric Obstructive Sleep Apnea. *Children*, *9*(9), 1305. doi: 10.3390/children9091305
[28] Ronco, C., Bellomo, R., & Kellum, J. A. (2019). Acute kidney injury. *The Lancet*, *394*(10212), 1949-1964. doi: 10.1016/S0140-6736(19)32563-2
[29] Saengboonmee, C., Sorin, S., Sangkhamanon, S., Chomphoo, S., Indramanee, S., Seubwai, W., ... & Wongkham, S. (2023). r-aminobutyric acid B2 receptor: A potential therapeutic target for cholangiocarcinoma in patients with diabetes mellitus. *World Journal of Gastroenterology*, *29*(28), 4416. doi: 10.3748/wjg.v29.i28.4416
[30] Sambrook, J., & Russell, D. W. (2001). *Molecular Cloning: Ch. 8. In Vitro amplification of DNA by the polymerase chain reaction* (Vol. 2). Cold Spring Harbor Laboratory Press.
[31] Shen, M. L., Wang, C. H., Lin, C. H., Zhou, N., Kao, S. T., & Wu, D. C. (2016). Luteolin attenuates airway mucus overproduction via inhibition of the GABAergic system. *Scientific reports*, *6*(1), 32756. doi: 10.1038/srep32756
[32] Sigel, E., & Ernst, M. (2018). The benzodiazepine binding sites of GABAA receptors. *Trends in pharmacological sciences*, *39*(7), 659-671. doi: 10.1016/j.tips.2018.03.006
[33] Silva, J. P., Carmo, H., & Carvalho, F. (2022). Drugs of abuse and kidney toxicity. *Current Opinion in Toxicology*, *32*, 100360. doi: 10.1016/j.cotox.2022.100360
[34] Wang, S., Sui, S., Liu, Z., Peng, C., Liu, J., Luo, D. & Lu, W. Y. (2018). Protective roles of hepatic gammaaminobutyric acid signaling in acute ethanol exposureinduced liver injury. *Journal of Applied Toxicology*, *38*(3), 341-350. doi: 10.1002/jat.3544
[35] Wang, S., Xiang, Y. Y., Zhu, J., Yi, F., Li, J., Liu, C., & Lu, W. Y. (2017). Protective roles of hepatic GABA signaling in acute liver injury of rats. *American Journal of Physiology-Gastrointestinal and Liver Physiology*, *312*(3), G208-G218. doi: 10.1152/ajpgi.00344.2016
[36] Wang, S., Zhang, L., Liu, C., & Lu, W. Y. (2017). Protective roles of hepatic GABA signaling in liver injury. *International Journal of Physiology, Pathophysiology and Pharmacology*, *9*(5), 153-156. PMID: 29209452
[37] Williams, J. G., Kubelik, A. R., Livak, K. J., Rafalski, J. A., & Tingey, S. V. (1990). DNA polymorphisms amplified by arbitrary primers are useful as genetic markers. *Nucleic acids research*, *18*(22), 6531-6535. doi: 10.1093/nar/18.22.6531

ВПЛИВ МОДУЛЯТОРІВ РЕЦЕПТОРІВ ГАММА-АМІНОМАСЛЯНОЇ КИСЛОТИ НА ФУНКЦІОНАЛЬНІ, МОЛЕКУЛЯРНІ ТА ГІСТОЛОГІЧНІ ХАРАКТЕРИСТИКИ НИРОК І ПЕЧІНКИ У БІЛИХ САМЦІВ МИШЕЙ

Аль-Аззаві А. Ф., Аджіль М. А., Аль-Байті А. А. Х.

Рецептори гамма-аміномасляної кислоти (ГАМК) вважаються головними рецепторами, що пригнічують нейротрансмітери в мозку ссавців, і доведеним є факт того, що вони існують у ненейрональних клітинах. Мета дослідження – дослідити вплив модуляторів рецепторів гамма-аміномасляної кислоти на функціональні, молекулярні та гістологічні характеристики нирок і печінки при використанні різних доз лоразепаму. Лоразепам, один із препаратів бензодіазепінової групи, відомий своїм модулюючим впливом на ГАМК-рецептори, був використаний як модулятор для визначення впливу модулювання ГАМК на функції нирок та печінки, а також на молекулярні й гістологічні характеристики у 30 білих самців мишей. Було утворено 3 експериментальні групи мишей (всього 21), кожна з яких отримувала різні дози лоразепаму (1 мг/кг, 2 мг/кг та 3 мг/кг маси тіла відповідно). Решта 9 тварин використані у якості контрольної групи. Були досліджені гістологічні та функціональні параметри стану нирок і печінки для оцінки впливу модулювання ГАМК за допомогою лоразепаму. Загальна геномна ДНК була виділена з печінки, мозку, нирок і крові, а метод випадкової ампліфікації поліморфної ДНК (RAPD) був використаний для виявлення молекулярного впливу модулювання ГАМК на геномну ДНК. Дані були проаналізовані за допомогою SPSS версії 20.0 (SPSS Inc.), при цьому для кількісних змінних обчислювалися середні значення та стандартні відхилення (SD), а для порівняння середніх значень між групами використовувався дисперсійний аналіз (ANOVA). Функціональні параметри (сечовина крові, креатинін, АСАТ, АЛАТ, ГГТ) та гістопатологічне дослідження показали значні зміни в оброблених групах порівняно з контрольною групою. Як у печінці так і в нирках мишей зі збільшенням дози лоразепаму відмічалося зростання вираженості застійних явищ у кровоносних судинах з появою крововиливів, ознаками запалення та дегенерацією і некрозом клітин. Молекулярне дослідження виявило суттєві зміни в RAPD-профілях експериментальних груп: нормальні смуги зникли, а нові смуги зявилися на відміну від контрольної групи. RAPD-профілі оброблених і контрольних зразків показали 432 смуги, з яких 109 були контрольними, 167 (втрата нормальних смуг та поява нових) поліморфними, а 156 гомоморфними. Таким чином, зроблено висновок, що модулювання ГАМК лоразепамом викликають функціональні та гістопатологічні зміни в зазначених органах, викликаючи зміни в геномній ДНК.

Ключові слова: *модулювання ГАМК, молекулярні особливості, лоразепам, молекулярний вплив, функціональні характеристики.*

Author's contribution

Al-Azzawie A. F. – research, project administration, and supervision.
Ajeel M. A. – review writing and editing, methodology and writing of the original draft.
Al-Bayti A. A. H. – conceptualization, data visualization, formal analysis, resources, software, and validation.

Signed for print 28.12.2024
Format 60x84/8. Printing offset. Order № 9654. Circulation 100.
Vinnytsia. Printing house “TVORY”, Nemyrivske shose St., 62a,
Vinnytsya, 21034
Phone: 0 (800) 33-00-90, (096) 97-30-934, (093) 89-13-852,
(098) 46-98-043
e-mail: tvory2009@gmail.com
http://www.tvoru.com.ua